SCHOLAR COMMONS
USF UNIVERSITY OF SOUTH FLORIDA

University of South Florida
Scholar Commons

Graduate Theses and Dissertations   Graduate School

2011

Simplified Methodology for Designing Parabolic Trough Solar Power Plants

Ricardo Vasquez Padilla
University of South Florida, rsvasque@mail.usf.edu

Follow this and additional works at: http://scholarcommons.usf.edu/etd

Part of the American Studies Commons, Engineering Commons, and the Oil, Gas, and Energy Commons

Simplified Methodology for Designing Parabolic Trough Solar Power Plants

by

Ricardo Vasquez Padilla

A dissertation submitted in partial fulfillment
of the requirements for the degree of
Doctor of Philosophy
Department of Chemical and Biomedical Engineering
College of Engineering
University of South Florida

Co-Major Professor: D. Yogi Goswami, Ph.D.
Co-Major Professor: Elias Stefanakos, Ph.D.
Muhammad M. Rahman, Ph.D.
John T. Wolan, Ph.D.
Yuncheng You, Ph.D.

Date of Approval:
April 4, 2011

Keywords: Solar radiation, Solar shading, Regenerative Rankine cycle, Levelized cost of electricity, Air cooled condensers

Dedication

Dedicated to Jehovah and my two loves: Jenni and Noah

Acknowledgements

I express my most sincere gratitude to my advisors, Dr. Yogi Goswami and Dr Stefanakos for their guidance, patience, understanding and encouragement throughout this work. I also like to thank the members of my committee, Drs. Muhammad Rahman, John Wolan and Yuncheng You. Special thanks to Ms. Ginny Cosmides, Ms. Barbara Graham and Mr. Charles Garretson who with their advice and kindness were great help during my stay in the Clean Energy Research Center (CERC).

I would like to thank my friends Sesha, Saeb, June, Chennan, Antonio, Jamie, Kofi, Yang and Gokmen, in the CERC, for their help and support, and the Universidad del Norte for the economic support in my doctoral studies. I would also like to thank my friends: Viviana, Homero, Henry, Paula Lezama, Sophia, Cesar, Paula Algarin, Pedro, Cecilia and Mrs. Ena. I can not forget my friend Rolland who is no longer with us but will live forever in my memories. Special acknowledge goes to Ms. Ana Rivera and Alondra for their spiritual support and friendship. I would like to give special thanks to my mother, Nubia, my father, Armando, and my aunt Sara, because they have always believed in me. Thanks to my parents in law Santiago and Maria de Lourdes, without their help this dissertation would not have been written. Finally, I would like to acknowledge Jehovah for giving me strength in moments of weakness and my wife Jennifer and my son Noah for their unwavering support and for being my inspiration.

Table of Contents

List of Tables

List of Figures

List of Symbols

A   Area [m^2]

a$_s$ Azimuth angle [°]

C   Specific heat [kJ/kg K]

D   Diameter [m]

d   Distance between row collectors [m]

$\dot{E}$ Rate of energy transfer by heat, work and mass [kW]

F   Geometric factor for concentric cylinders, View factor

f   Friction factor, Focal length [m]

g   Gravity [m/s^2]

HCE   Heat collection element

h   Enthalpy [kJ/kg], Convective heat transfer coefficient [kW/m^2 K]

HTF   Heat transfer fluid

i   Angle of incidence [°]

K   Incident angle modifier

k   Thermal conductivity [kW/m K]

Kn   Knudsen number

L$_b$ Length between support brackets [m]

L   Axial length of cylinder [m], Projected length [m], Object's length [m]

$\dot{m}$ Mass flow rate [kg/s]

Nu	Nusselt number
P	Pressure [Torr], Annulus gas pressure [Torr], Perimeter [m]
Pr	Prandtl number
PTC	Parabolic trough collector
$\dot{Q}$	Rate of heat transfer [kW]
$\dot{q}$	Radiation heat flux [kW/m^2]
R^2	Coefficient of determination
Ra	Rayleigh number
Re	Reynolds number
R	Gas constant [kJ/kg K]
r	Radius [m], Radial focal distance [m]
t	Time [s]
T	Temperature [°C]
V	Velocity [m/s]
w	Collector width [m]
x	Axial distance [m], Shading distance [m], Cartesian coordinate [m]
y	Cartesian coordinate [m]
z	Axial length [m]

Greek Symbols

α	Altitude angle [°], Accommodation coefficient , Absorptance
β	Volumetric thermal expansion coefficient [K^{-1}]
Δ	Incremental value
δ	Molecular diameter of annulus gas [cm]
ε	Pipe roughness [m], Emissivity

η_o	Pick optical efficiency
γ	Intercep factor
λ	Mean free path [cm]
μ	Absolute viscosity [kg/m s]
ν	Kinematic viscosity [m^2/s]
ρ	Density [kg/m^3], Reflectivity, Tracking angle []
ϕ	Relative humidity
ψ	Collector geometrical end losses
σ	Stefan Boltzmann constant [$5.67 \times 10^{-8}\,W/m^2K^4$]
τ	Transmittance
θ	Ratio of specific heats, Excess temperature of fin [°C]
ε	Sky emissivity
φ	Shading factor
ξ	Variable used in radiation analysis

Subscripts

a-abs	Absorber-absorbed
a	Absorber, Intersection point, Absorber coating
b	Base of fin,
c	Collector surface, Cross area
cl	Clean
cond	Conduction
conv	Convection
ct	Connection tab, Cooling tower
cv,a	Control volume for absorber analysis

cv,e	Control volume for envelope analysis
D	Diameter
e-abs	Envelope-absorbed
e	Glass envelope
es	Envelope-sky
f	Fluid
g	Gas
i,a	Inner, absorber
i-j	From surface i to surface j
L_c	Characteristic length
L	Length of connection tab
m	Partially developed, Mean
SH	Shading
sky-c	From sky to collector surface
w	Wall
wind	Wind
∞	Fully developed, Ambient conditions

Superscripts

‾	Average
′	Per unit of length, Per unit length of aperture area width

Abstract

The performance of parabolic trough based solar power plants over the last 25 years has proven that this technology is an excellent alternative for the commercial power industry. Compared to conventional power plants, parabolic trough solar power plants produce significantly lower levels of carbon dioxide, although additional research is required to bring the cost of concentrator solar plants to a competitive level. The cost reduction is focused on three areas: thermodynamic efficiency improvements by research and development, scaling up of the unit size, and mass production of the equipment. The optimum design, performance simulation and cost analysis of the parabolic trough solar plants are essential for the successful implementation of this technology. A detailed solar power plant simulation and analysis of its components is needed for the design of parabolic trough solar systems which is the subject of this research.

Preliminary analysis was carried out by complex models of the solar field components. These components were then integrated into the system whose performance is simulated to emulate real operating conditions. Sensitivity analysis was conducted to get the optimum conditions and minimum levelized cost of electricity (LCOE). A simplified methodology was then developed based on correlations obtained from the detailed component simulations.

A comprehensive numerical simulation of a parabolic trough solar power plant was developed, focusing primarily on obtaining a preliminary optimum design through the simplified methodology developed in this research. The proposed methodology is used to obtain optimum parameters and conditions such as: solar field size, operating conditions, parasitic losses, initial investment and LCOE. The methodology is also used to evaluate different scenarios and conditions of operation.

The new methodology was implemented for a 50 MWe parabolic trough solar power plant for two cities: Tampa and Daggett. The results obtained for the proposed methodology were compared to another physical model (System Advisor Model, SAM) and a good agreement was achieved, thus showing that this methodology is suitable for any location.

Chapter 1

Introduction

Current world energy consumption shows that approximately 84.7% of the world energy is supplied by fossil fuels, and only 9.9% by renewable energy sources [1]. Figure 1.1 shows that the world energy consumption is projected to increase by 50% from 2005 to 2030. For the specific case of U.S., in 2009 only 8.2% of the energy consumed was produced by renewable sources, and the majority of the renewable energy was coming from biomass and hydroelectric plants [2]. Different factors such as: rising fossil fuel prices, energy security, and greenhouse gas emissions, have encouraged the world to shift
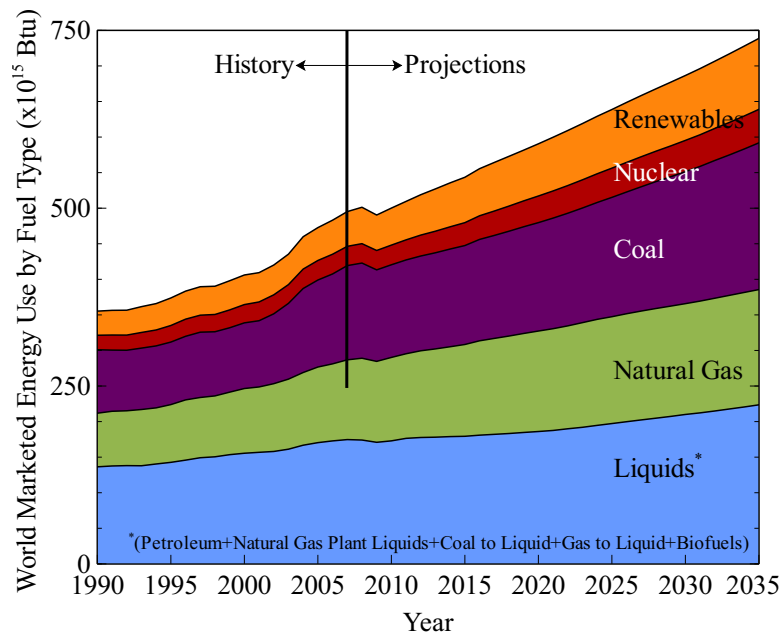
Figure 1.1 Current and projected world energy use by fuel type. Adapted from [1]

1

the energy policy towards renewable sources. Renewable energy sources are attractive for environmental reasons, especially in countries where reducing greenhouse gas emissions is of particular concern.

Power plants with solar concentrators are one of the main renewable energy alternatives for the production of electricity. Currently, four technologies are proposed: Parabolic Trough Collector (PTC), Linear Fresnel Reflector System (LF), Power Tower or Central Receiver System (CRS), and Dish/Engine system (DE). Table 1.1 summarizes the characteristics of each solar technology.

Table 1.1 Characteristics of Concentrating Solar Power (CSP) systems. Adapted from [3]

System	Peak Efficiency (%)	Annual Efficiency (%)	Annual Capacity Factor (%)
Trough/linear Fresnel	21	10–12 (d)	24 (d)
		14–18 (p)	
Power tower	23	14–19 (p)	25–70 (p)
Dish/engine	29	18–23 (p)	25 (p)

(d) demonstrated, (p) Projected, based on pilot-scale testing

This dissertation will focus only on the PTC, which is considered as one of the most mature applications of solar energy in this field [4]. In order to reduce the costs, PTC solar plants should be designed for large sizes or be part of a hybrid system which includes a regular fossil backup. PTCs are composed of parabolic trough-shaped mirrors, which reflect the incident radiation from the sun on the solar receiver tube. The receiver tube is located at the focus of a parabola in whose sides the mirrors are located. As shown in Figure 1.2, the circulating heat transfer fluid (HTF) passes through the receiver and is heated up by the radiant energy absorbed. Then, the HTF is collected to be sent to the

Legend labels:
Parabolic Trough
Collectors (PTC)

Heat Transfer Fluid (HTF)
Working Fluid

Auxiliary Heater

Solar Field

Power
Block

Expansion Tank

Pump

1. Turbine
2. Generator
3. Condenser
4. Pump
5. Preheater
6. Boiler
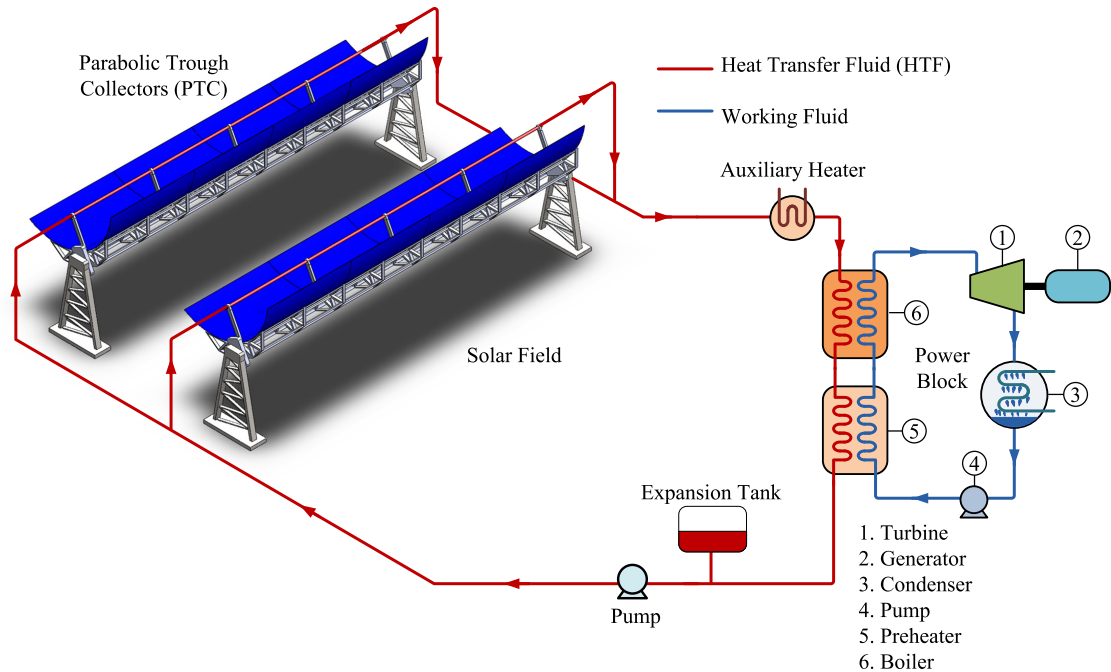
Figure 1.2 Schematic of a PTC solar power plant

power block, where it passes through a series of heat exchangers and produces superheated steam at high temperatures. The superheated steam flows through a steam turbine where rotational mechanical work is then converted into electricity.

A solar field consists of hundreds of Solar Collector Assemblies, which are independently tracking assemblies of parabolic trough solar collectors. Each SCA has the following components: metallic support structure, mirrors, solar receiver, and collector balance of the system. Figure 1.3 shows different parts of a Solar Collector Assembly (SCA) for a LS3 solar collector. In order to reach the operational conditions, the solar collector assemblies (SCA) are arranged in a series configuration normally known as a loop. The length of the loop depends on the PTC performance, but as shown in Figure 1.4, it usually has a U shape to minimize the pressure drop through the pipe header. Usually the PTCs are

3
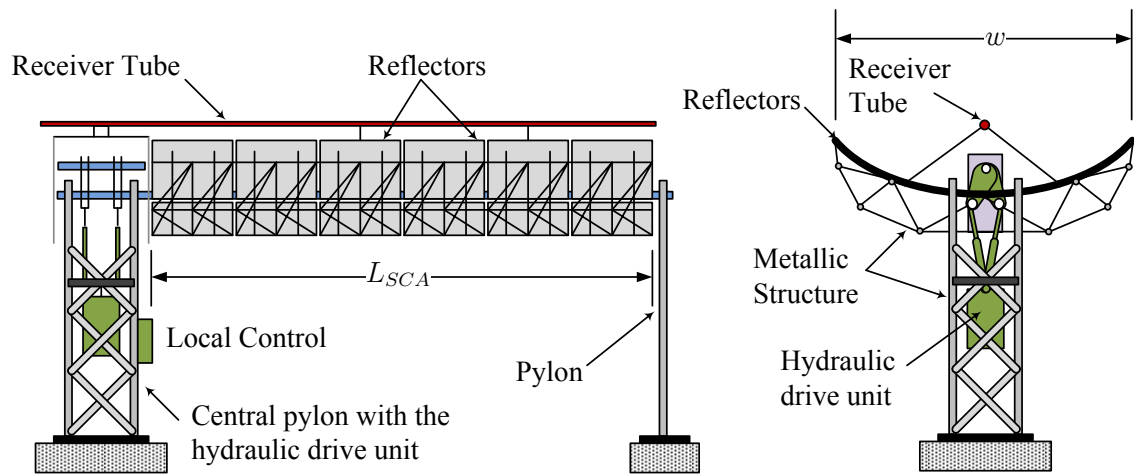
Figure 1.3 Parts of a Solar Collector Assembly (SCA). Adapted from [3]

oriented North-South and tracking the sun from east to west, but this also depends on the land constraints.

The economic feasibility of PTC solar plants is based on finding the optimum size for a given electric output. The preliminary analysis is performed by the integration of the complex models and components, which are integrated to simulate real operating conditions. This dissertation proposes the development of a simple methodology for the initial design of parabolic trough solar systems based on physical models. The methodology is focused in obtaining a preliminary optimum design through a simplified methodology based on correlations obtained from detailed component simulations. This methodology is expected
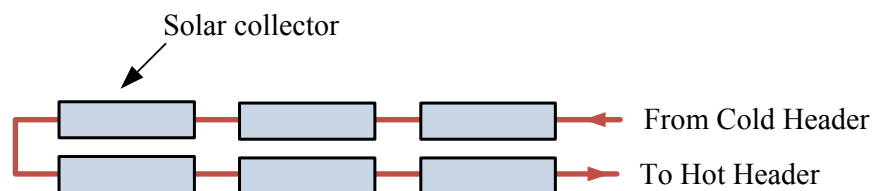
Figure 1.4 Schematic of LS-3 solar collector loop. Adapted from [3]

to be great help for engineers for the design and performance analysis of parabolic trough solar systems.

1.1 Literature Review

One of the first solar power plant simulations was developed by Lippke [5]. A typical 30 MWe SEGS plant was studied using a detailed thermodynamic model. In this model, correlations for the performance of parabolic trough solar collectors were derived based on measured data under different conditions; these correlations were used to calculate the energy obtained from the solar field. The model was used to calculate the gross and net electricity output under different operating conditions.

A detailed heat transfer analysis and modeling of a parabolic trough solar receiver was carried out by Forristall [6]. One and two dimensional energy balances were used for short and long receivers respectively. This model was used to determine the thermal performance of parabolic trough collectors under different operating conditions. Jones et al. [7] accomplished a comprehensive model of the 30 MWe SEGS VI parabolic trough plant in TRNSYS. This model included solar and power cycle performance without fossil backup. The model was created to accurately predict the SEGS VI plant behavior and to examine transient effects such as start up, shutdown, and system response. Likewise, Stuetzle [8, 9] investigated the thermal performance of SEGS VI parabolic trough plant. The analysis consisted of a dynamic model for the collector and a steady-state model for the power plant. This simulation examined the linear model predictive control strategy for maintaining the solar field at a constant outlet temperature, although maximizing of the gross electricity produced was not pursued. Quaschning [10] presented a methodology for economic opti-

5

mization of solar plant design as a function of the solar irradiance. This model is able to find the optimal solar field size for any specific project location.

A complex model for a parabolic trough, including a comprehensive economic analysis, was developed by NREL (National Renewable Energy Laboratory) [11]. The parabolic trough solar technology was modeled using the methodology developed by Stine and Harrigan [12]. The model is capable of modeling a Rankine-cycle parabolic trough plant, with or without thermal storage, and with or without fossil-fuel backup. Another simulation [13] for the solar field based on SEGS VI was modeled in TRNSYS. In this simulation, the Rankine power cycle was separately modeled; the steady-state power cycle performance was regressed in terms of the heat transfer fluid temperature, heat transfer fluid mass flow rate, and condensing pressure, and implemented in TRNSYS. Both the solar field and power cycle models were validated with measured temperature and flow rate data from the SEGS VI plant. A thermal economical model called Solar Advisor Model (SAM) was developed by NREL and Sandia National Laboratory [14, 15]. This model calculates costs, finances, and performance of concentrating solar power and also allows examining the impact of variation in the physical parameters on the costs and overall performance.

A more recent methodology for the economic optimization of the solar area in either parabolic trough or complex solar plants was carried out by Montes et al. [16]. Thermal performance for different solar power plants was analyzed at nominal and load conditions. Once annual electric energy generation is known, levelized cost of energy (LCOE) for the solar plant can be calculated, yielding a minimum LCOE value for a certain optimum solar area. Similarly, an analytic model for a solar thermal electric generating system

6

with parabolic trough collectors was done by Rolim et al. [17]. Three fields of different collectors were considered, the first field with evacuated absorbers, the second with non-evacuated absorbers and the third with bare absorbers. Mittelman and Epstein [18] proposed a new power block by using a bottoming Kalina cycle. This cycle has the advantage that electricity can be produced at low solar insolation (300-400 W/m^2).

As it was shown before, the parabolic trough solar power plant simulation is the result of a combination of complex thermal and cost models. In general the optimizations of these systems require an extensive computational effort and software resources. A simplified conceptual and numerical methodology for designing of parabolic trough solar energy systems was proposed by Stine and Harrigan [19]. This method proposed a design chart called storage sizing graph, which obtains the optimum collector area for certain location. The storage sizing graphs are an excellent initial tool for preliminary design of solar power plants, but they include a simplified thermal models and cost analysis.

Based on the motivation of this dissertation, the chapters follow the following outline. In Chapter 2, a heat transfer analysis of the PTC solar receiver is performed. The new model includes new convective correlations and a comprehensive radiation analysis. A fitting equation for the heat losses is obtained for two solar collectors: LS2 and LS3. Chapter 3 presents the design of typical power block for PTC solar plants. The power block is then simulated under partial load conditions and a fitting equation is obtained to calculate the net cycle power output, condenser heat transfer rate and heat transfer fluid (HTF) return temperature. Chapter 4 shows the design of the solar piping layout and the calculation of the pumping power requirements for circulating the HTF in the solar field. Determination

of thermal losses in pipes and expansion vessel are also included in this chapter. Chapter 5 presents the integration of all previous components and systems and describes the methodology for the initial and optimum design of PTC solar plants. Two distinct sites are used for the application of the proposed methodology, and evaluation of different condenser systems is also carried out. Finally, chapter 6 shows the conclusions and recommendations for further research.

Chapter 2

Solar Radiation

Detailed information about solar radiation availability at any location is essential for the design and economic evaluation of parabolic trough solar power plants. Long term measured data of solar radiation are available for a large number of locations in the United States and other parts of the world. For those locations where long term measured data are not available different physics and satellite models can be used to estimate the solar energy availability.

Solar energy is in the form of electromagnetic radiation with the wavelengths ranging from about 0.3 μm (10^{-6}m) to over 3 μm, which correspond to ultraviolet (less than 0.4 μm), visible (0.4 μm and 0.7 μm), and infrared (over 0.7μm); most of this energy is concentrated in the visible and the near-infrared wavelength range. The incident solar radiation, sometimes called insolation, is measured as irradiance, or the energy per unit time per unit area (kW/m^2). The average amount of solar radiation falling on a surface normal to the rays of the sun outside the atmosphere of the earth, extraterrestrial insolation, at mean earth-sun distance D_o is called the solar constant, I_o. Recently, new measurements have found the value of solar constant to be 1366.1 W/m^2 [20].
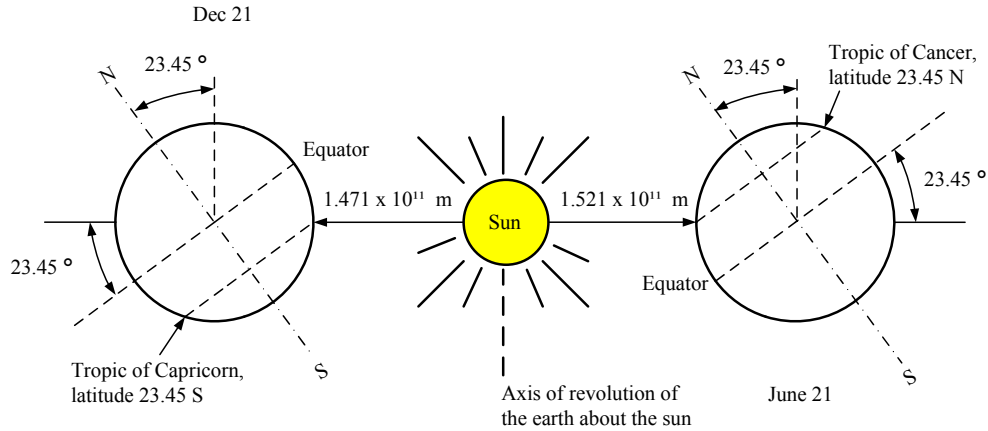
Figure 2.1 Motion of the earth about the sun. Adapted from [21]

2.1 Solar Angles

The variation in seasonal solar radiation availability at the surface of the earth can be understood from the geometry of the relative movement of the earth around the sun. The distance between the earth and the sun changes throughout the year, the minimum being 1.471×10^{11} m at winter solstice (December 21) and the maximum being 1.521×10^{11} m at summer solstice (June 21). The year round average earth sun distance is 1.496×10^{11} m. The amount of solar radiation intercepted by the earth, therefore varies throughout the year, the maximum being on December 21 and the minimum on June 21 (Figure 2.1).

The axis of the earth's daily rotation around itself is at an angle of 23.45 ° to the axis of its ecliptic orbital plane around the sun. This tilt is the major cause of the seasonal variation of the solar radiation available at any location on the earth. The angle between the earth-sun line (through their center) and the plane through the equator is called the solar declination angle, δ_s (Figure 2.2). The declination angle varies between -23.45° on December 21 to +23.45° on June 21. The solar declination is given by:

10
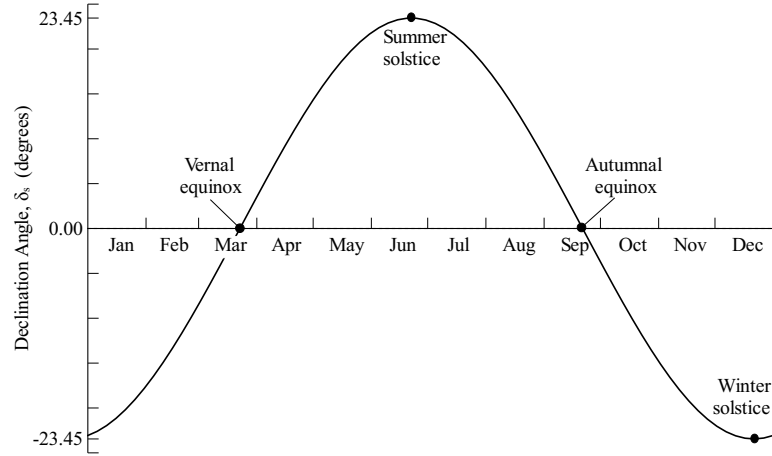
Figure 2.2 Variation of the declination angle, δ_s, throughout the year

$$\delta_s = 23.45° \sin\left[\frac{360\,(284+n)}{365}\right] \qquad (2.1)$$

where n is the day number with January 1 being $n = 1$. In general, the declination is assumed to remain constant during a specific day. The analysis of the sun motion is based on the Ptolemaic theory, which assumes that the earth is fixed and the sun rotates around the earth. The Ptolemaic view describes the relative sun motion with a coordinate system fixed to the earth with its origin at the location of interest.

The position of the sun can be described at any time by two angles, the altitude and azimuth angle (Figure 2.3). The solar altitude angle, α, is the angle between a line collinear with the sun rays and the horizontal plane [21]. The solar azimuth angle, a_s, is the angle between a due south line and the horizontal projection of the line joining the site to the sun [21]. The sign convention used for azimuth angle is positive west of south and negative east of south. The solar zenith angle, z is the angle between the site to sun line and the vertical at the site location:

$$z = 90 - \alpha \qquad (2.2)$$

11
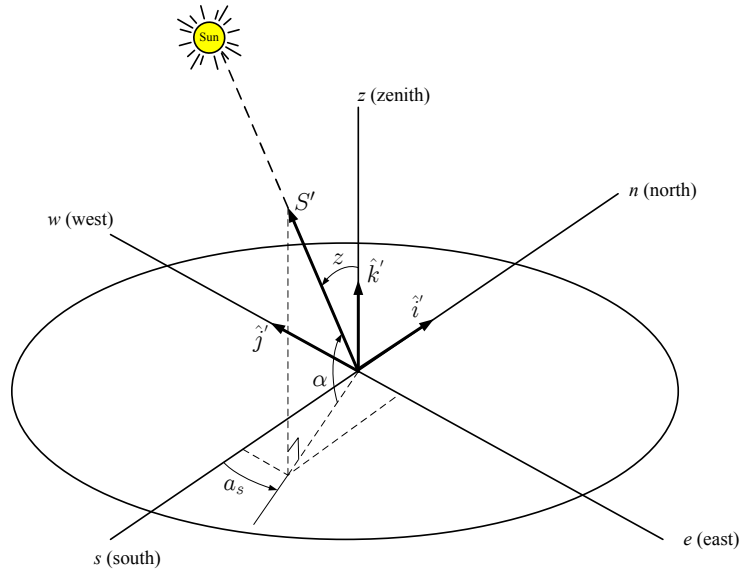
Figure 2.3 Earth surface coordinate system for observer at Q showing the solar azimuth angle (a_s), the solar altitude angle (α) and the solar zenith angle (z) for a central sun ray along direction vector S'. Also shown unit vectors $\hat{i}'$, $\hat{j}'$, $\hat{k}'$ along their respective axes. Adapted from [12]

The solar altitude angle and azimuth angles are not fundamental; hence, they must be related to the fundamental angles (Figure 2.4): hour angle (h_s), latitude (L) and declination angle (δ_s). The solar hour angle is based on the nominal time of 24 hours required for the sun to move 360° around the earth or 15° per hour [21], it is defined as:

$$h = 15° \, (t_s - 12) \tag{2.3}$$

where t_s is the solar time in hours. The solar time is calculated from the local time by the following expression [21]:

$$t_s = t + EOT + (l_{st} - l_{local}) \, 4\,\mathrm{min/degree} \tag{2.4}$$

where l_{st} is the standard time meridian, and l_{local} is the local time meridian. EOT is the equation of time (Figure 2.5), which accounts for the variation of the rotational speed of

12
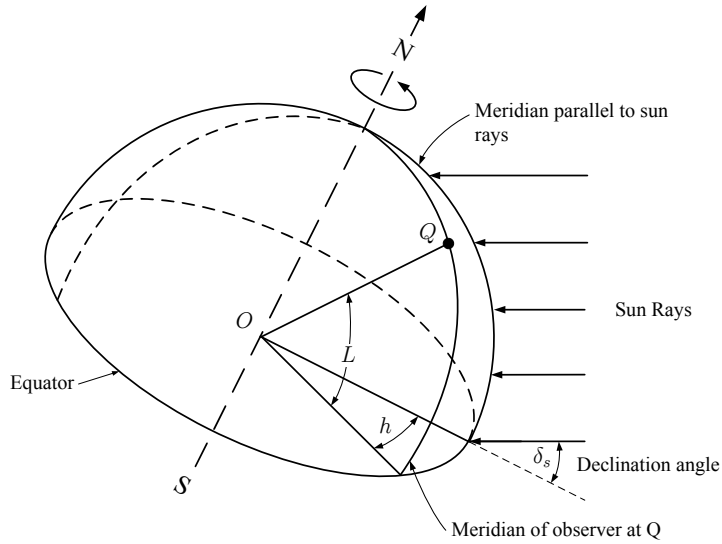
Figure 2.4 Fundamental sun angles: hour angle h, latitude L and declination δ_s. Adapted from [12]

the earth. An approximation for calculating the equation of time, EOT ,in minutes is given by Woolf [22] and is accurate to within about 30 seconds during daylight hours:

$$EOT = 0.258 \cos x - 7.416 \sin x - 3.648 \cos 2x - 9.228 \sin 2x \qquad (2.5)$$

$$x = \frac{360\,(n-1)}{365.242} \qquad (2.6)$$
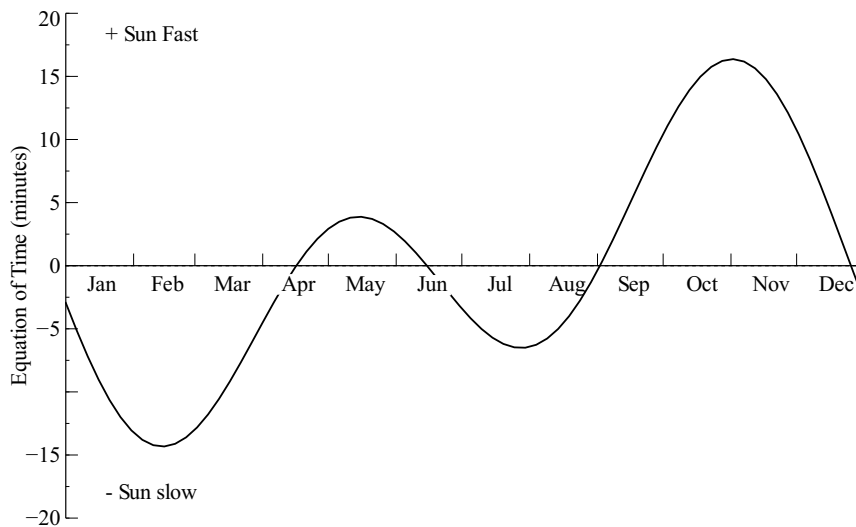
Figure 2.5 Equation of time EOT

13

The latitude angle L (Figure 2.4) is the angle between the line from the center of the earth to site and the equatorial plane. The latitude is considered positive north of the equator and negative south of the equator. Expression for solar altitude and solar azimuth may be defined in terms of latitude (L), hour angle (h), and declination angle (δ_s). As it is shown in Figure 2.3, the unit direction vector S' pointing toward the sun from the observer Q is defined as:

$$S' = S'_i \hat{i'} + S'_j \hat{j'} + S'_k \hat{k'} \tag{2.7}$$

where $\hat{i'}$, $\hat{j'}$, $\hat{k'}$ are unit vectors along n, w, and z axes respectively. The direction cosines corresponding to n, w, and z axes are S'_i, S'_j, and S'_k, respectively. They can be written in terms of the solar altitude and azimuth as:

$$
\begin{aligned}
S'_i &= -\cos\alpha \cos a_s \\
S'_j &= \cos\alpha \sin a_s \\
S'_k &= \sin\alpha
\end{aligned}
\tag{2.8}
$$

Similarly, a direction vector pointing to the sun can be described at the center of the earth as shown in Figure 2.6. Using a new set of coordinates, the direction vector S pointing to the sun may be described in terms of direction cosines S_i, S_j, and S_k as:

$$S = S_i \hat{i} + S_j \hat{j} + S_k \hat{k} \tag{2.9}$$

$$
\begin{aligned}
S_i &= -\cos\delta_s \cos h \\
S_j &= \cos\delta_s \sin h \\
S_k &= \sin\delta_s
\end{aligned}
\tag{2.10}
$$
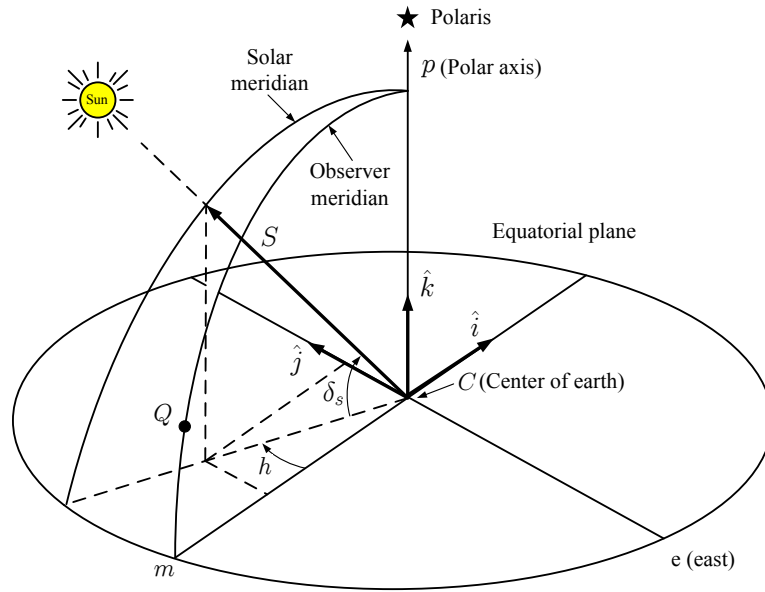
Figure 2.6 Earth center coordinate system for the sun ray direction vector S defined in terms of hour angle (h), and declination angle (δ_s). Adapted from [12]

These two sets of coordinates are interrelated by a rotation about e axis (Figure 2.7) through the complement of the latitude angle $(90 - L)$ and the translation along the earth radius QC. The translation along the earth's radius is negligible since this is about $1/23525$ of the distance from the earth to the sun. Note that the rotation about the e axis is in the negative sense based on the right-hand rule. In matrix rotation this takes the form:

$$
\begin{vmatrix} S'_i \\ S'_j \\ S'_k \end{vmatrix} = \begin{vmatrix} \sin L & 0 & \cos L \\ 0 & 1 & 0 \\ -\cos L & 0 & \sin L \end{vmatrix} \cdot \begin{vmatrix} S_i \\ S_j \\ S_k \end{vmatrix} \tag{2.11}
$$
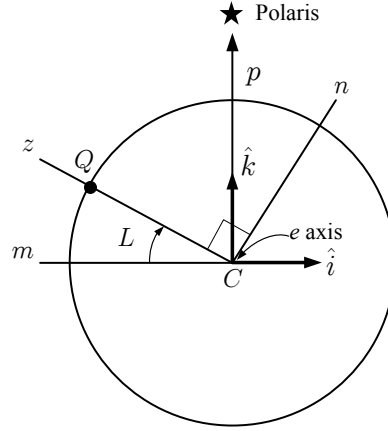
Figure 2.7 Earth surface coordinates after translation from the earth center C to the observer at Q. Adapted from [12]

Solving, it is obtained that:

$$
\begin{aligned}
S'_i &= S_i \sin L + S_k \cos L \\
S'_j &= S_j \\
S'_k &= -S_i \cos L + S_k \sin L
\end{aligned}
\tag{2.12}
$$

After replacing the corresponding direction cosines, the following set of equations are obtained:

$$
-\cos \alpha \cos a_s = -\cos \delta_s \sin L \cos h + \sin \delta_s \cos L \tag{2.13a}
$$

$$
\cos \alpha \sin a_s = \cos \delta_s \sin h \tag{2.13b}
$$

$$
\sin \alpha = \cos \delta_s \cos L \cos h + \sin \delta_s \sin L \tag{2.13c}
$$

Equation (2.13c) is an expression for the solar altitude angle in terms of the observer's location (Latitude angle), the hour angle (time) and the sun's declination (date). Solving for the solar altitude angle:

$$
\alpha = \sin^{-1} \left(\sin \delta_s \sin L + \cos \delta_s \cos L \cos h \right) \tag{2.14}
$$

16

Two expressions for calculating the solar azimuth angle (a_s) from either Equation (2.13a) or (2.13b) were obtained. The solar azimuth angle can be in any of the four trigonometric quadrants depending on the location, time of day, and the season. Both Equations (2.13a) or (2.13b) require a test to know the proper quadrant. For Equation (2.13a) the appropriate procedure for calculating a_s is:

$$a_s = \cos^{-1}\left(\frac{\cos \delta_s \sin L \cos h - \sin \delta_s \cos L}{\cos \alpha}\right) \tag{2.15}$$

$$\text{if} \quad h < 0 \quad \text{then} \quad a_s = -|a_s|$$

For Equation (2.13b), the procedure is as follows:

$$a_s = \sin^{-1}\left(\frac{\cos \delta_s \sin h}{\cos \alpha}\right) \tag{2.16}$$

For $L > \delta_s$:

$$\text{if} \quad \cos h < \left(\frac{\tan \delta_s}{\tan L}\right) \quad \text{then} \quad |a_s| > 90$$

and

$$a_s = \begin{cases} -180 + |a_s| & h < 0 \\[2mm] 180 - |a_s| & h \geq 0 \end{cases} \tag{2.17}$$

$$\text{if} \quad \cos h \geq \left(\frac{\tan \delta_s}{\tan L}\right) \quad \text{then} \quad |a_s| \leq 90$$

and

$$\text{if} \quad h < 0 \quad \text{then} \quad a_s = -|a_s|$$

For $L \leq \delta_s$ the sun remains north of the east-west line ($|a_s| > 90$) and the value of a_s is given by Equation (2.17). The previous procedure is derived from the path of the sun across the sky, which can be viewed as a disc displaced from the observer. This geometric perspective of the sun's path is helpful to visualize the sun movements and obtain expressions for testing the sun angles [12].

The sun may be viewed as traveling about a disc of radius R at a constant rate of 15 degrees per hour. As shown in Figure 2.8(a), the center of this disc appears at different seasonal locations along the polar axis, which passes through the observer at Q and is inclined to the horizon by the latitude angle. The center of the disc is coincident with the observer Q at the equinoxes and is displaced from the observer by a distance of $R \tan \delta_s$ at other times of the year. The extremes of this travel are at the solstices. Figure 2.8(b) is a side view of the sun's disc looking from the east. In the summer, the sun path disc of radius R has its center Y displaced above the observer Q. Point X is defined by a perpendicular from Q. In the n-z plane, the projection of the position S onto the line containing X and Y will be where the hour angle, h, is. The appropriate test for the sun being in the northern sky is then:

$$R \cos h < XY \tag{2.18}$$

The distance XY is:

$$XY = R \frac{\tan \delta_s}{\tan L} \tag{2.19}$$

then

(a) Solar disc

(b) Side view of the sun's disc

Figure 2.8 Geometric view of the sun's path as seen by an observer at Q. Adapted from [12, 21]

$$\cos h < \frac{\tan \delta_s}{\tan L} \tag{2.20}$$

Sunrise and sunset times can be estimated by finding the hour angle at $\alpha = 0$, then:

$$h_{sr} \quad \text{or} \quad h_{ss} = \pm \cos^{-1} \left(-\tan L \tan \delta_s \right) \tag{2.21}$$

2.2 Hourly Solar Radiation Models

The average amount of solar radiation falling on a surface normal to the rays of the sun outside the atmosphere of the earth (extraterrestrial) at mean earth-sun distance is called the solar constant, I_o. In this simulation the solar constant has a value of 1366.1 W/m^2 as calculated by Gueymard [20]. Figure 2.9 shows the extraterrestrial solar radiation spec-
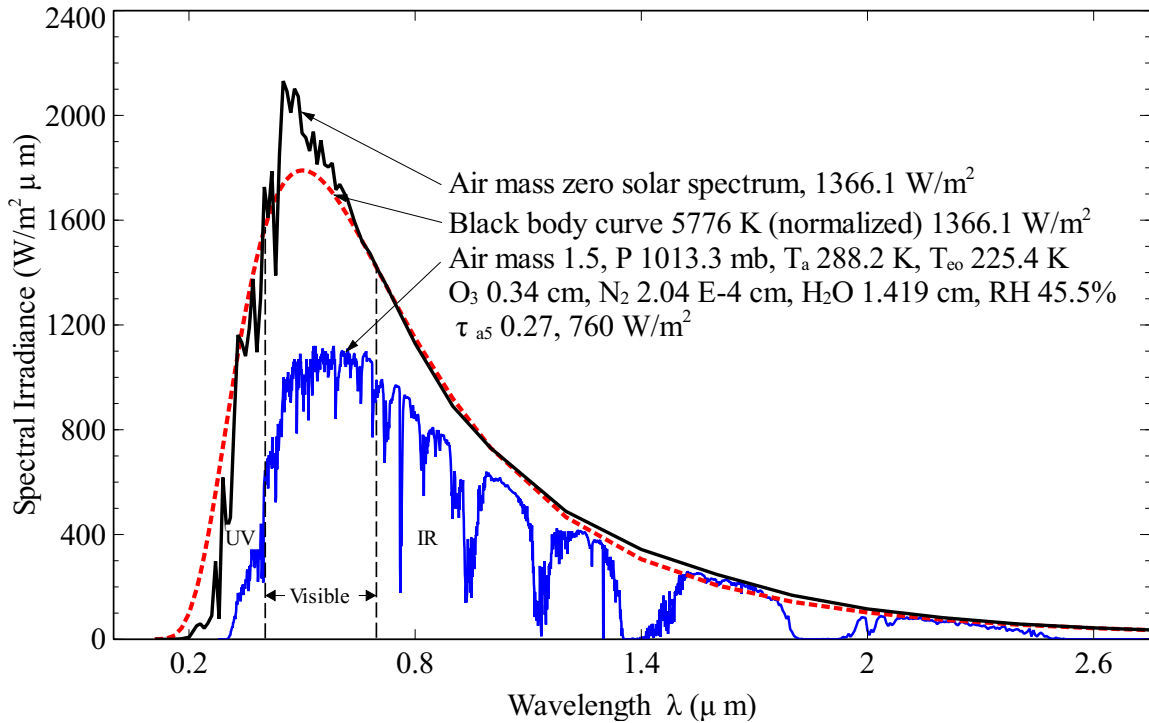
Figure 2.9 Extraterrestrial solar radiation spectrum (in vacuum below 280 nm, in air above 280 nm); also shown are equivalent black body and atmosphere-attenuated spectra (SMARTS2, U.S. Standard Atmosphere USSA, rural aerosol model, Z=48.19° (Air mass 1.5)). Adapted from [20, 23]

trum, with the solar constant of 1366.1 W/m^2, with the equivalent black body (normalized) curve and the atmosphere attenuated spectrum for air mass of 1.5. The seasonal variation of extraterrestrial solar radiation at the surface of the earth is well understood from the relative movement of the earth around the sun. The extraterrestrial radiation varies by the inverse distance square from the earth to the sun as:

$$I = I_o \left(D_o / D \right)^2 \qquad (2.22)$$

where D is the distance between the sun and the earth, and D_o is the yearly mean earth-sun distance (1.496×10^{11}m). The factor $\left(D_o/D \right)^2$ is calculated as [21]:

$$\left(D_o/D \right)^2 \;=\; 1.00011 + 0.034221 \cos\left(x\right) + 0.00128 \sin\left(x\right)$$
$$+0.000719 \cos\left(2\,x\right) + 0.000077 \sin\left(2\,x\right) \qquad (2.23)$$

$$x = 360 \left(n - 1\right) / 365°$$

Figure 2.10 shows the variation of the factor $\left(D_o/D \right)^2$ throughout the year. As extraterrestrial solar radiation, I, passes through the atmosphere, a part of it is reflected back into
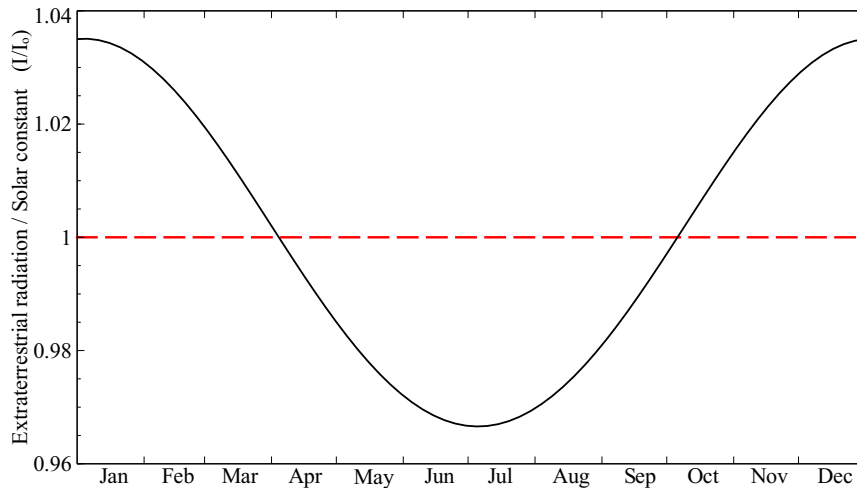
Figure 2.10 Variation of $\left(D_o/D \right)^2$ throughout the year

the space, a part is absorbed by the air and water vapor, and some gets scattered by the molecules of air, water vapor, aerosols and dust particles (Figure 2.11) [21]. The part of solar radiation that reaches the surface of the earth with essentially no change in direction is called direct or beam radiation. The scattered diffuse radiation reaching the surface from the sky is called sky diffuse radiation.
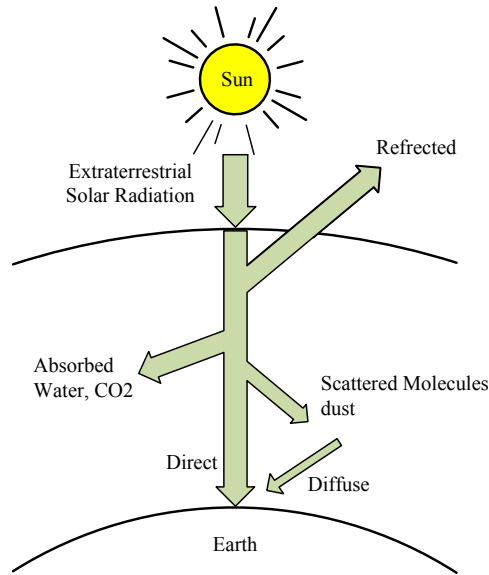
Figure 2.11 Attenuation of solar radiation as it passes through the atmosphere. Adapted from [21]

Determination of the hourly solar radiation received during the average day of each month is primordial for calculating the solar collector performance throughout the day. The long term models provide the mean hourly distribution of global radiation over the average day of each month. Given the long term average daily total and diffuse irradiation on a horizontal surface, $\overline{H}_h$ and $\overline{D}_h$ respectively, it is possible to find the long term hourly solar radiation: I_h and $I_{d,h}$. Values of $\overline{H}_h$ and $\overline{D}_h$ can be obtained from either ground measurement data or satellite data [24]. Satellite data provide information about solar

radiation and meteorological conditions in locations where ground measurement data are not available.

For solar radiation calculation, Daily integration approach (Model DI) [25] was used as the hourly radiation model. Gueymard [25] developed the Daily integration approach to predict the monthly-average hourly global irradiation by using a large data set of 135 stations with diverse geographic locations (82.58 N to 67.68 S) and climates. Gueymard compared his proposed model with previous hourly radiation models, Collares-Pereira and Rabl Model CP&R [26] and Collares-Pereira and Rabl Model modified by Gueymard [27], and concluded that the daily integration model is the most accurate compared to the other models.

Total instantaneous solar radiation on a horizontal surface, I_h, is the sum of the beam or direct radiation, $I_{b,h}$, and the sky diffuse radiation $I_{d,h}$:

$$I_h = I_{b,h} + I_{d,h} \tag{2.24}$$

Referring to Figure 2.12, I_h may be expressed as:

$$I_h = I_{b,N} \cos z + I_{d,h} \tag{2.25}$$

or

$$I_h = I_{b,N} \sin \alpha + I_{d,h} \tag{2.26}$$

The hourly beam radiation, $I_{b,h}$ is obtained from Equation (2.24):

$$I_{b,h} = I_h - I_{d,h} \tag{2.27}$$
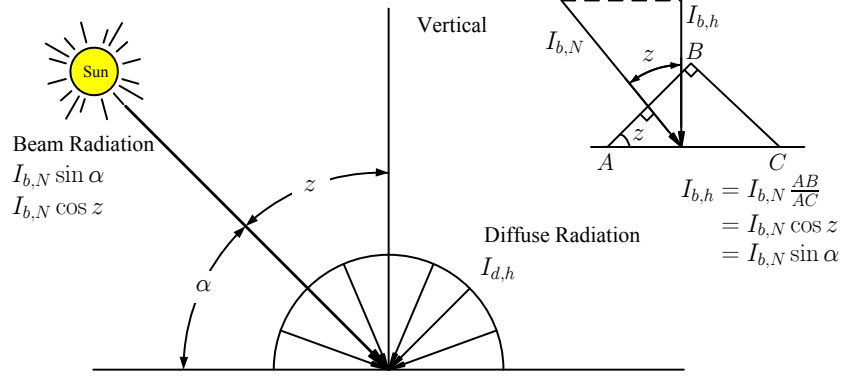
Figure 2.12 Solar radiation on a horizontal surface. Adapted from [21]

Introducing the hourly to daily ratios r_d and r_t as:

$$r_d = \frac{I_{d,h}}{\overline{D}_h} \tag{2.28}$$

$$r_t = \frac{I_h}{\overline{H}_h} \tag{2.29}$$

Then, the beam radiation is:

$$I_{b,h} = r_t \overline{H}_h - r_d \overline{D}_h \tag{2.30}$$

Liu and Jordan [28] showed that r_d is well expressed by (Figure 2.13):

$$r_d = \frac{\pi}{T} \frac{\cos h - \cos h_{ss}}{\sin h_{ss} - h_{ss} \cos h_{ss}} \tag{2.31}$$

The daily-average extraterrestrial irradiation on a horizontal surface, H_o, may be calculated as a function of the solar constant, E_{sc}, as:

$$H_o = \frac{24}{\pi} h_{ss} R E_{sc} \sin h_o \tag{2.32}$$

24
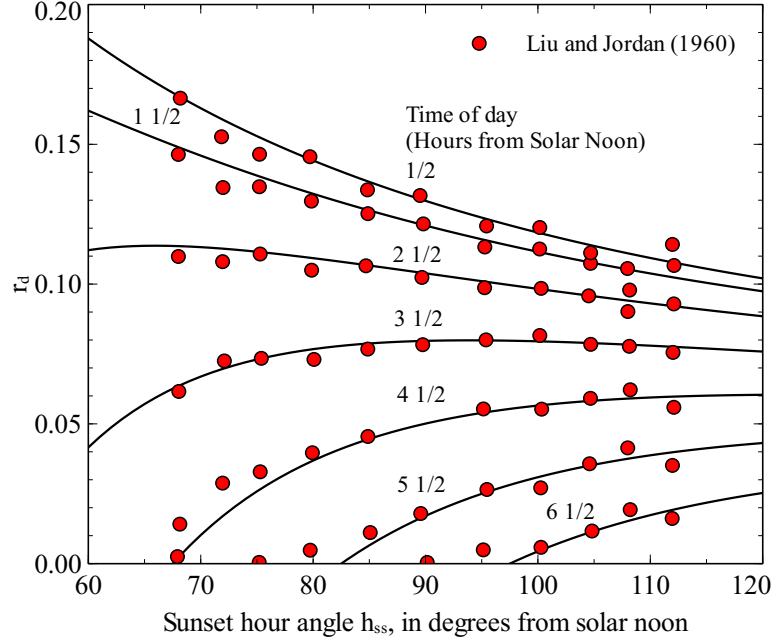
Figure 2.13 Variation of r_d, diffuse conversion factor, with the sunset hour angle for different times of the day. Adapted from [26, 28]

where h_{ss} is the sunset hour angle $(+)$ in radians defined by Equation 2.21. During polar days and nights, the value of h_{ss} is given by:

$$h_{ss} = \begin{cases} 0 & \text{if } -\tan L \tan \delta_s > 1 \\ \\ \pi & \text{if } -\tan L \tan \delta_s < -1 \end{cases} \tag{2.33}$$

where h_o is the daily average solar elevation outside of the atmosphere, defined by:

$$h_o = qA(h_{ss})/h_{ss} \tag{2.34}$$

and

$$q = \cos L \cos \delta_s \tag{2.35}$$

$$A(h_{ss}) = \sin h_{ss} - h_{ss} \cos h_{ss} \tag{2.36}$$

The solar geometry need be determined for only an average day of each month. The monthly average declination, δ_s, and the monthly average sun–earth correction factor, $R = (D_o/D)^2$, are shown in Table 2.1.

Table 2.1 Monthly average solar declination angle, δ_s, and sun–earth distance correction factor, R. Adapted from [25, 29]

Month	δ_s	R
1	-20.71	1.032
2	-12.81	1.025
3	-1.80	1.011
4	9.77	0.994
5	18.83	0.978
6	23.07	0.969
7	21.16	0.967
8	13.65	0.975
9	2.89	0.99
10	-8.72	1.007
11	-18.37	1.022
12	-22.99	1.031

The daily average clearness index, K_t, is given by [30]:

$$K_t = \frac{\overline{H}_h}{H_o} \tag{2.37}$$

The day length (in hours) is obtained as:

$$S_o = \frac{24}{\pi} h_{ss} \tag{2.38}$$

The ratio of the horizontal hourly radiation to the total horizontal daily radiation, r_t, is given by:

$$r_t = r_d \frac{1 + q\,(a_2/a_1)\,A\,(h_{ss})\,r_d\,(24/\pi)}{1 + q\,(a_2/a_1)\,B\,(h_{ss})\,/A\,(h_{ss})} \qquad (2.39)$$

where (a_2/a_1) represents the atmospheric extinction effect. a_1 and a_2 were obtained from a multiple least-squares fit:

$$a_1 = 0.41341\,K_t + 0.61197\,K_t^2 - 0a.01886\,K_t\,S_o + 0.00759\,S_o \qquad (2.40)$$

$$a_2 = \text{Max}\left(0.054,\ 0.28116 + 2.2475\,K_t - 1.7611\,K_t^2 - 1.84535\,\sin h_o\right.$$

$$\left. + 1.681\,\sin^3 h_o\right) \qquad (2.41)$$

and $B\,(h_{ss})$ is defined as:

$$B\,(h_{ss}) = \omega_s\,\left(0.5 + \cos^2 h_{ss}\right) - 0.75\,\sin\,(2\,h_{ss}) \qquad (2.42)$$

For a parabolic trough solar collector, only the beam radiation on the aperture area, $I_{b,c}$, is needed [21]. The beam radiation, $I_{b,c}$, is calculated as:

$$I_{b,c} = \left(r_t\,\overline{H}_h - r_d\,\overline{D}_h\right)\,\frac{\cos i}{\sin \alpha} \qquad (2.43)$$

where i is the angle of incidence, which depends on the tracking mode and the position of the sun. In order to optimize the PTC performance, two different tracking mode are used (Figure 2.14): North-South (East-West axis tracking) and East-West (North-South axis tracking). The next section shows how to calculate $\cos i$ for single axis tracking.

(a) East-West (North-South axis tracking)   (b) North-South (East-West axis tracking)
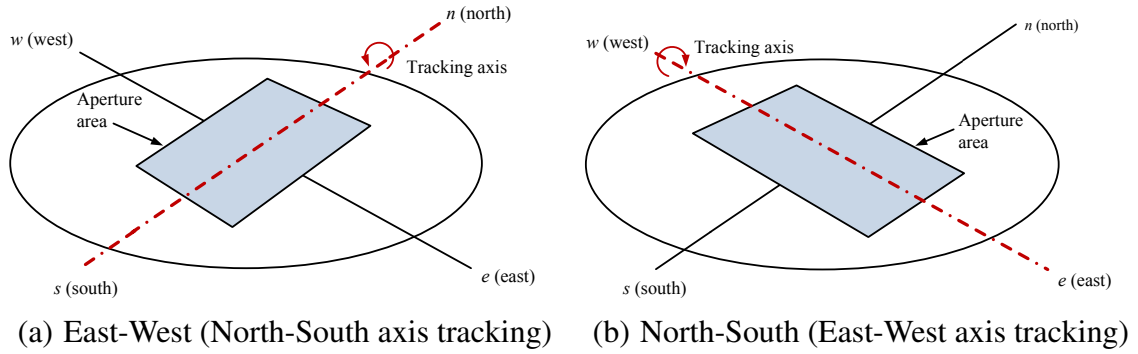
Figure 2.14 Tracking mode for PTCs

2.3 Single Axis Tracking

As it was mentioned before, PTCs are designed to operate with tracking about only one axis. A tracking drive system rotates the collector about an axis of rotation until the sun central ray and the aperture normal area are coplanar. Figure 2.15 shows how the rotation of a collector aperture about a tracking axis r. The tracking angle, ρ, brings the central ray unit vector S into the plane formed by the aperture normal and the tracking axis. To write expressions for i and ρ in terms of the collector orientation and solar angles, it is necessary to transform the initial coordinates , x', y', z' (Figure 2.3) to a new coordinate system that has the tracking axis as one of its three orthogonal axes. The other two axes are oriented
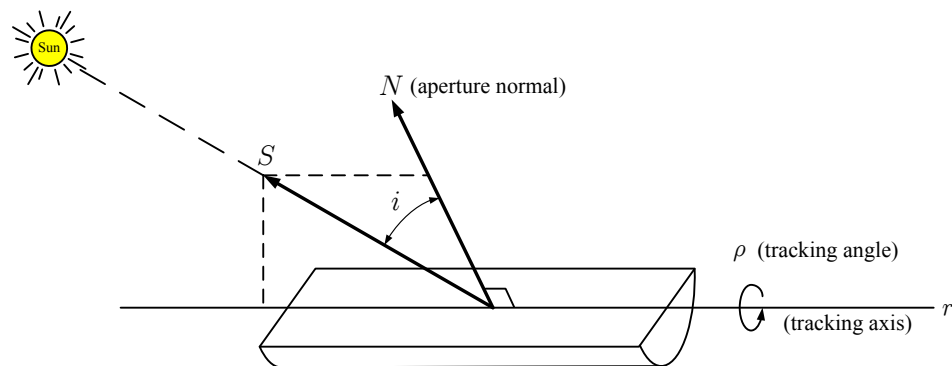
Figure 2.15 A single-axis tracking aperture. Adapted from [12]
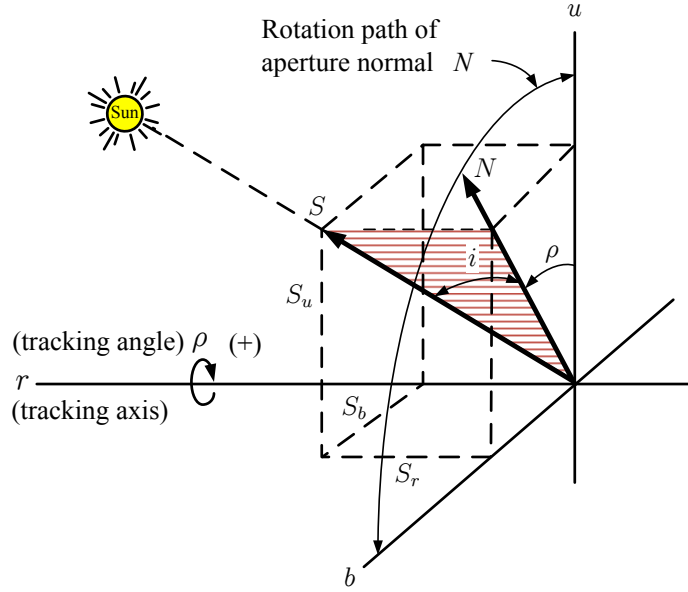
Figure 2.16 Single-axis tracking system coordinate. Adapted from [12]

such as that one axis is parallel to the surface of the earth. Figure 2.16 shows the new coordinate system, where r is the tracking axis, b is the axis that always remains parallel to the earth surface and u is the third orthogonal axis. Note that the aperture normal N rotates in the $u - b$ plane. Both i and ρ can be defined in terms of the direction cosines of the central ray unit vector S along the u, b, and r axes. The tracking angle is defined by[1]:

$$\tan \rho = -\frac{S_u}{S_b} \tag{2.44}$$

and the cosine of incidence angle, i, is given by:

$$\cos i = \sqrt{S_b^2 + S_u^2} \tag{2.45}$$

or

$$\cos i = \sqrt{1 - S_r^2} \tag{2.46}$$

---

[1]The sign minus is based on the right hand rule

2.3.1 Horizontal Tracking Axis

To describe this category, we must rotate the u, b, and r coordinates by an angle γ from the z, w, and n coordinates that were previously used to describe the sun ray unit vector (Figure 2.16). Since the axis tracking remains parallel to the earth surface, the rotation takes place about the z axis as shown in Figure 2.17. The direction cosines of S (new coordinate system) are calculated as[2]:

$$
\begin{vmatrix} S_r \\ S_b \\ S_u \end{vmatrix} = \begin{vmatrix} \cos\gamma & -\sin\gamma & 0 \\ \sin\gamma & \cos\gamma & 0 \\ 0 & 0 & 1 \end{vmatrix} \cdot \begin{vmatrix} S'_i \\ S'_j \\ S'_k \end{vmatrix}
\tag{2.47}
$$
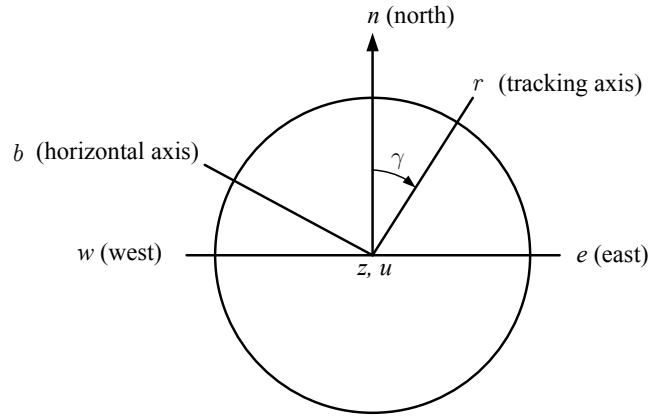
Figure 2.17 Rotation of u, b, and r from z, w, and n coordinates about the z axis. Adapted from [12]

Substituting into Equation (2.44), it is obtained that the tracking angle is:

$$
\tan\rho = \frac{\sin(\gamma - a_s)}{\tan\alpha}
\tag{2.48}
$$

---

[2]Note that this rotation is in the negative direction based on the right-hand rule

The angle of incidence for a single axis, horizontal tracking collector is:

$$\cos \theta_i = \sqrt{1 - \cos^2 \alpha \cos^2 (\gamma - a_s)} \qquad (2.49)$$

When the tracking axis is oriented in the north-south direction ($\gamma = 0$), the equations above reduce to:

$$\tan \rho = -\frac{\sin a_s}{\tan \alpha} \qquad (2.50)$$

and

$$\cos i = \sqrt{1 - \cos^2 \alpha \cos^2 a_s} \qquad (2.51)$$

When the tracking axis is oriented in the east-west direction ($\gamma = 90$), the Equations (2.48) and (2.49) become:

$$\tan \rho = \frac{\cos a_s}{\tan \alpha} \qquad (2.52)$$

and

$$\cos i = \sqrt{1 - \cos^2 \alpha \sin^2 a_s} \qquad (2.53)$$

2.4 Results

For the design of parabolic trough solar plants, two locations were selected: Tampa and Daggett. The latitude and longitude of these locations are specified in Table 2.2.

Table 2.2 Locations used for the design of parabolic trough solar plants

Location	Latitude	Longitude
Tampa, Fl	27.97°	-82.53°
Daggett, CA	34.85°	-116.80°

The results obtained for solar radiation calculations, using two different radiation data sources: TMY3 [32] and Surface meteorology and Solar Energy (NASA-SSE) [24], are shown in Figures 2.18 and 2.20. Figure 2.18 shows the comparison of the three hourly solar radiation models: CP&R, CP&RG and DI model. The three model show minor differences for the monthly average beam radiation. This agrees with the results obtained by Gueymard [25], who found that DI model showed better performance at high latitudes than the other models but at low latitudes the differences were small. Figures 2.19 and 2.20 show the effect of the tracking axis on the beam radiation. As it was expected, for both locations, the North-South axis tracking presents better performance during most of the year. For that reason most of the PTCs are oriented with their tracking axis in the North-South direction. Figure 2.21 shows the annual total radiation obtained for each tracking axis, again the new results are more favorable for the North-South axis tracking, therefore this configuration will be adopted for the calculation of solar radiation in this dissertation.

(a) Tampa   (b) Daggett
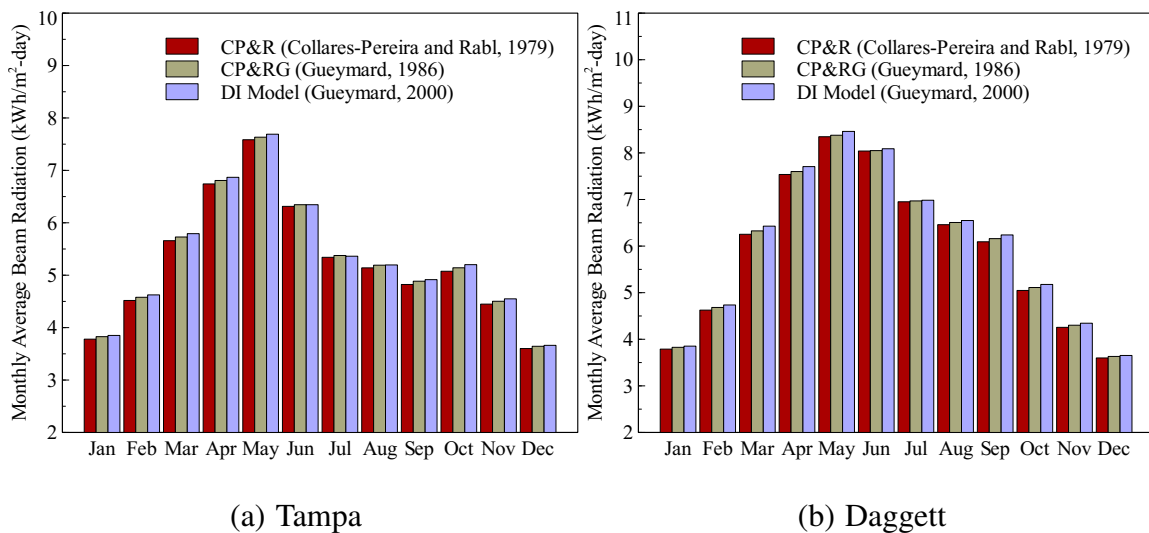
Figure 2.18 Comparison of different hourly radiation models. Radiation data source: NASA-SSE [24], hourly radiation model: CP&R [31], CP&RG [27] and DI model [25]

(a) North-South Axis Tracking (b) East-West Axis Tracking
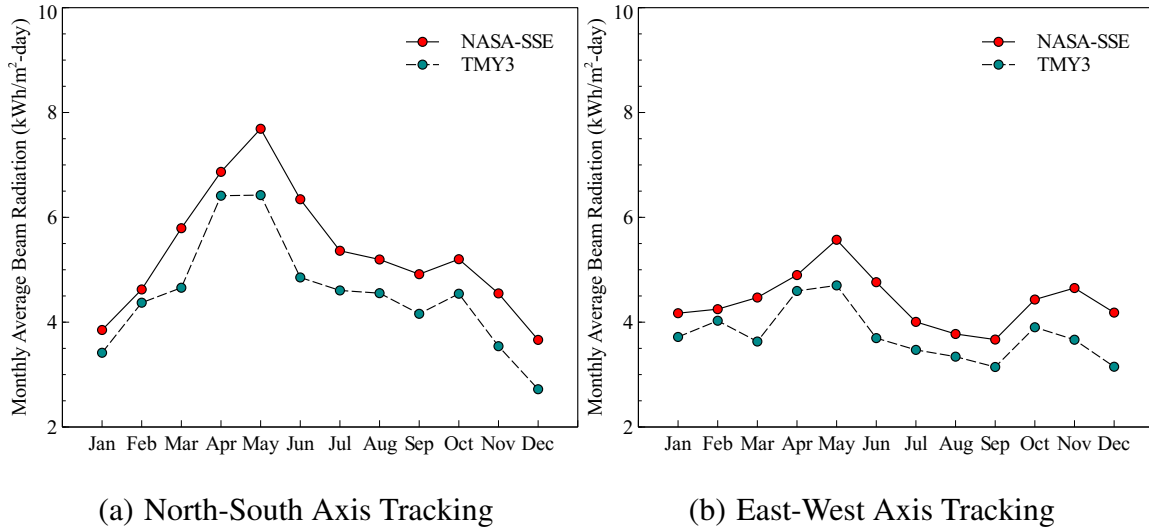
Figure 2.19 Effect of tracking axis and data radiation source on the monthly average beam radiation for Tampa. Radiation data source: NASA-SSE [24] and TMY3 [32], hourly radiation model: DI model [25]

(a) North-South Axis Tracking (b) East-West Axis Tracking
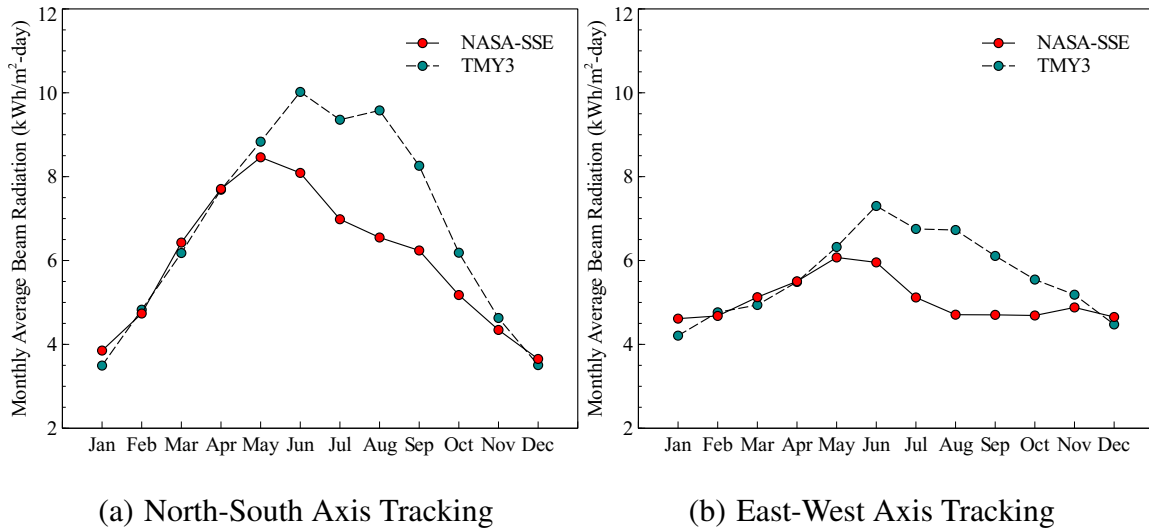
Figure 2.20 Effect of tracking axis and data radiation source on the monthly average beam radiation for Daggett. Radiation data source: NASA-SSE [24] and TMY3 [32], hourly radiation model: DI model [25]

The DI model, along with radiation data from NASA-SSE were used to map the direct and beam radiation. The maps were plotted using the Matplotlib Basemap Toolkit [33] in Python 2.6 [34]. Given the resolution of the radiation data obtained from NASA-SSE

33
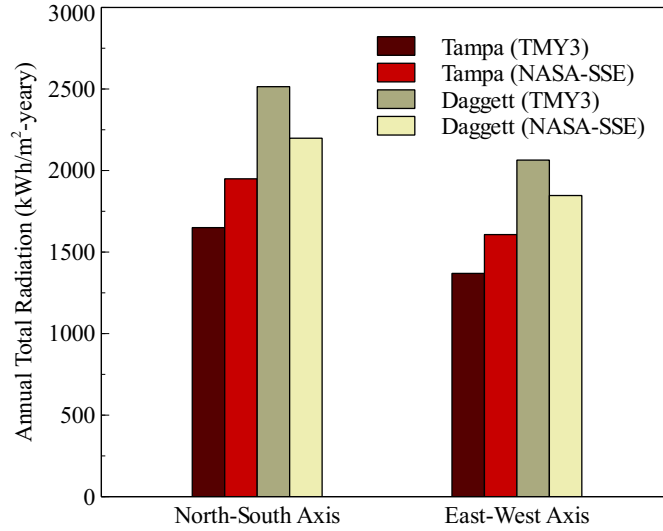
Figure 2.21 Comparison of the annual total beam radiation for different tracking axis and solar radiation data source. Radiation data source: NASA-SSE [24] and TMY3 [32], location: Tampa and Daggett, hourly radiation model: DI model [25]
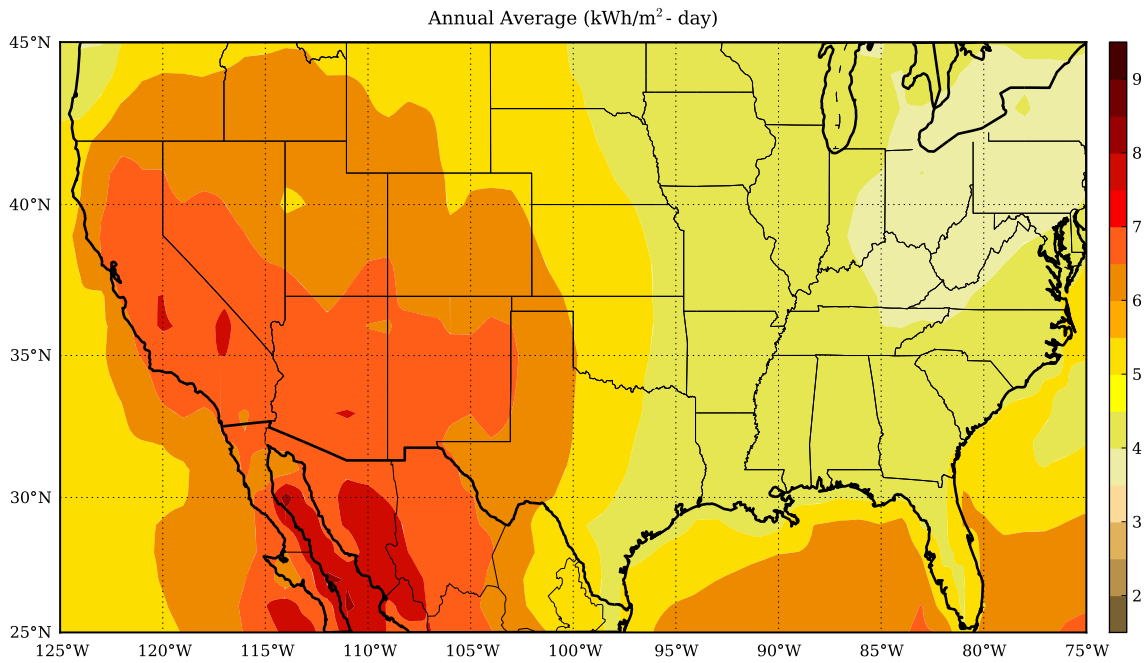
Figure 2.22 Solar direct beam radiation map for USA. Radiation data source: NASA-SSE [24], hourly radiation model: DI model [25]
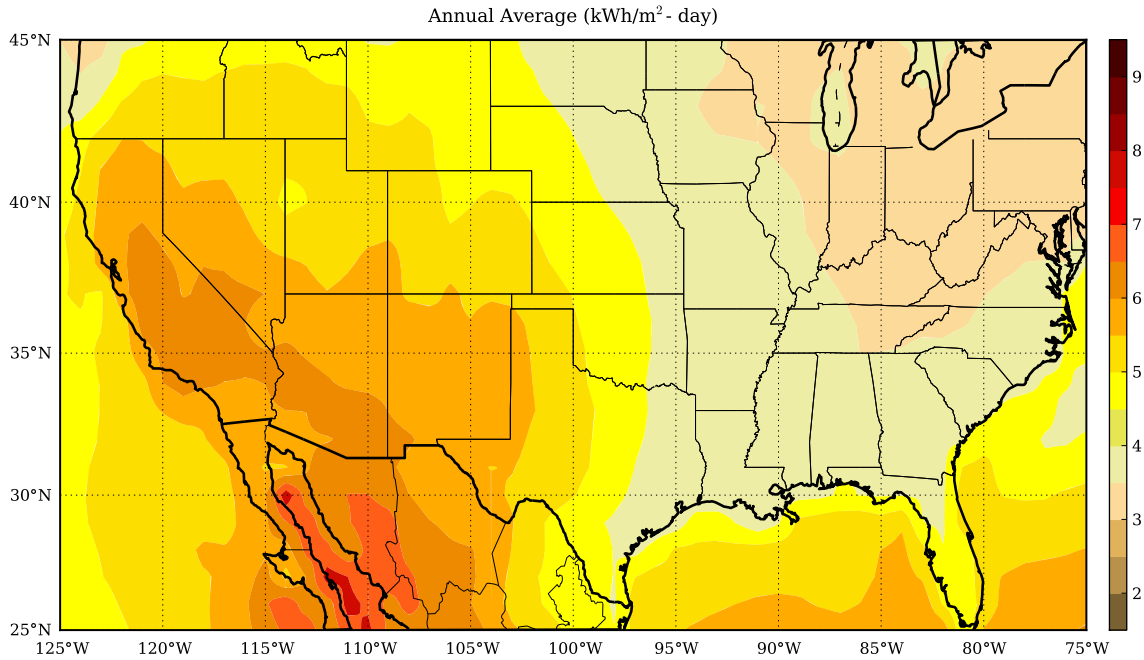
Figure 2.23 Solar beam radiation map (North-South axis tracking) for USA. Radiation data source: NASA-SSE [24], hourly radiation model: DI model [25]

(a) Direct Beam Radiation

(b) Beam Radiation for North-South Axis Tracking
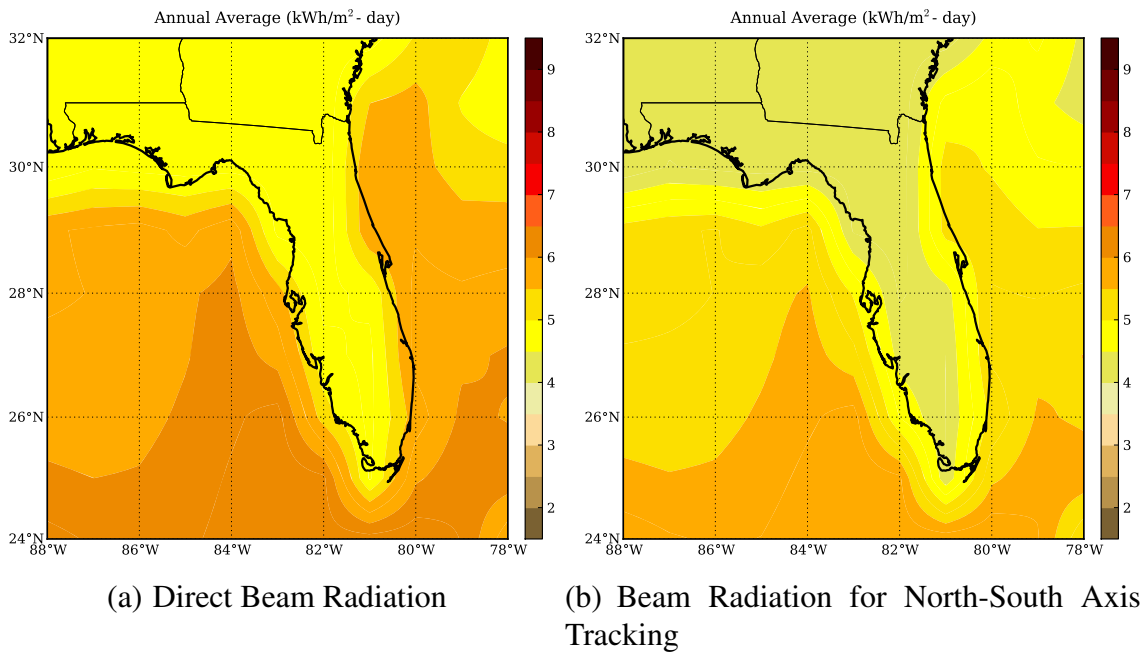
Figure 2.24 Solar radiation map for Florida. Radiation data source: NASA-SSE [24], hourly radiation model: DI model [25]

($1° \times 1°$), it was necessary to use a bilinear interpolation [33] for obtaining data at higher resolution. Figures 2.22 and 2.23 show the maps obtained for the North-South axis tracking beam radiation for USA, while Figure 2.24 shows the results for Florida. The results showed that in general Florida has acceptable levels of beam radiation. Lower levels of radiation increase the cost of the Concentrated Solar Power (CSP) plants and therefore their economic viability.

2.5 Solar Shading

The solar shading on PTC (Parabolic trough collector) was initially solved using only one concentrating collector (Figure 2.25).
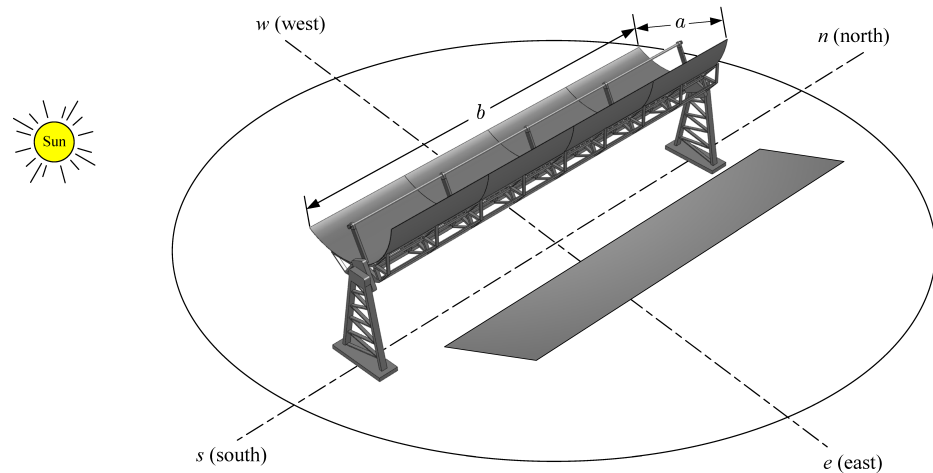
Figure 2.25 Solar shading problem with only one concentrating collector

For a simple object, its shadow is defined by (Figure 2.26):

$$L_{SH} = \frac{L}{\tan \alpha} \tag{2.54}$$

where L is the length of the object, and L_{SH} is the length of the object's shadow. For a PTC, the shading was calculated with the projected area (rectangular projected section) and each
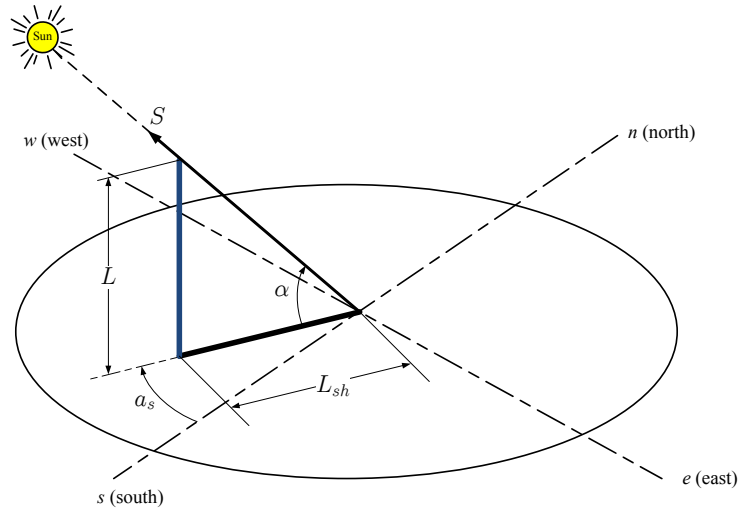
Figure 2.26 Geometry used to calculate the shadow of an object

shadow projection was assumed to be parallel. Figure 2.27 shows the geometry used to

solve the problem. Using the previous expression, it is obtained:

$$L_{S1} = \frac{d_1 - \dfrac{a}{2}\sin\zeta}{\tan\alpha} \tag{2.55}$$
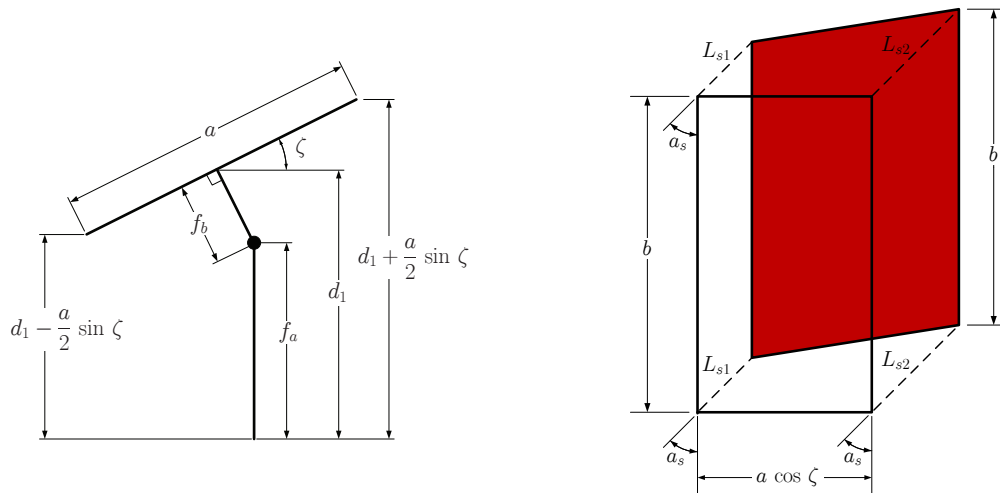
Figure 2.27 Simplified geometry used for one concentrating collector

37

$$L_{S2} = \frac{d_1 + \dfrac{a}{2}\sin\zeta}{\tan\alpha} \tag{2.56}$$

with

$$d_1 = f_a + f_b\cos\zeta$$

As seen in Figure 2.27, the shading area is given by:

$$A_{SH} = b \cdot a \left[a\cos\zeta + \frac{\sin\zeta\,\sin a_s}{\tan\alpha}\right] \tag{2.57}$$

It is also important to obtain an expression for σ (Figure 2.28):

$$K = a\left[\cos^2\zeta + \frac{\sin^2\zeta}{\tan^2\alpha} + \frac{\sin 2\zeta}{\tan\alpha}\sin a_s\right]^{1/2} \tag{2.58}$$
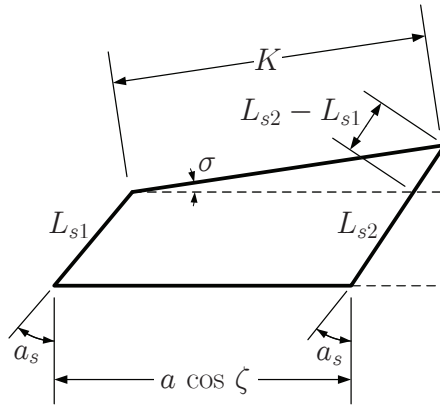
Figure 2.28 Geometry used in a solar shading problem with only one concentrating collector

Using sine law:

$$\sin\sigma = \frac{a}{K}\frac{\sin\zeta}{\tan\alpha}\cos a_s \tag{2.59}$$

The next expression for σ is obtained:

$$\sigma = \sin^{-1} \left[\frac{\sin \zeta \cos a_s}{\tan \alpha \left(\cos^2 \zeta + \dfrac{\sin^2 \zeta}{\tan^2 \alpha} + \dfrac{\sin 2\zeta}{\tan \alpha} \sin a_s \right)^{1/2}} \right] \qquad (2.60)$$

After solving for the shadow of one concentrating collector, the problem with two or more concentrating collector was then solved. Figure 2.29 shows the geometry used for this problem. Two variables, b' and x_s, were found. Referring to Figure 2.29, in order to calculate x_s, it is necessary to obtain θ first . The angle θ (Figure 2.30(a)) is given by:

$$\tan \theta = \tan \zeta \cos \sigma \qquad (2.61)$$

x_s is obtained from the following expression:

$$x_s = \frac{a \sin \zeta - \left(\dfrac{d - a \cos \zeta}{\cos \sigma} \right) \tan \alpha}{\cos \theta \tan \alpha + \sin \theta} \qquad (2.62)$$

The second collector is not shaded when:

$$a \sin \zeta \leq \left(\frac{d - a \cos \zeta}{\cos \sigma} \right) \tan \alpha \qquad (2.63)$$

or

$$\tan \alpha \geq \tan \alpha_{cr} \qquad (2.64)$$

α_{cr} is defined as:

$$\tan \alpha_{cr} = \frac{\sin \zeta \cos \sigma}{d/a - \cos \zeta}$$

39
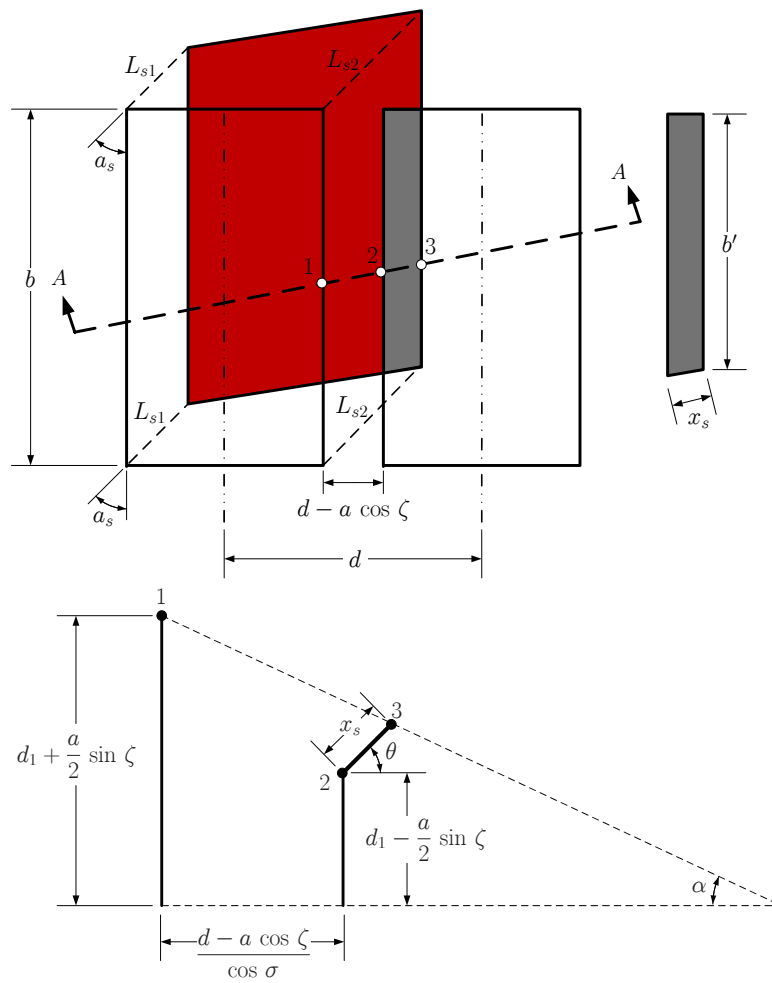
Figure 2.29 Solar shading problem with two concentrating collectors
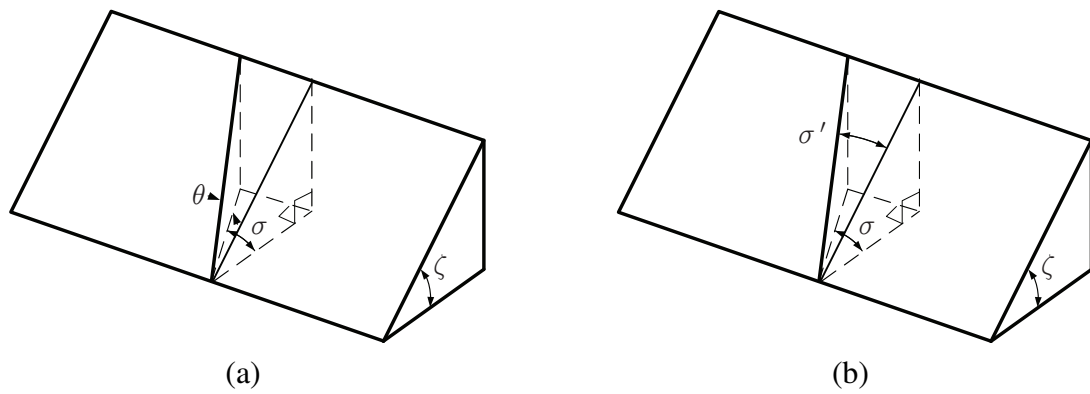
Figure 2.30 Geometry used to calculate θ and σ'

Because $0 \leq \alpha \leq 90^o$, the last expression can be rewritten as:

$$\alpha \geq \alpha_{cr} \qquad (2.65)$$

In order to calculate the shading area, it is necessary to calculate σ' (Figure 2.30(b)):

$$\tan \sigma' = \tan \sigma \cos \zeta \qquad (2.66)$$

Now, it is necessary to define some conditions based on points P_1 and P_2 (Figure 2.31). Point P_1 is defined by:

$$P_1 = (x_1, y_1) \qquad (2.67)$$

$$x_1 = L_{s2} \sin a_s + \frac{a}{2} \cos \zeta \qquad (2.68)$$

$$y_1 = L_{s2} \cos a_s \qquad (2.69)$$
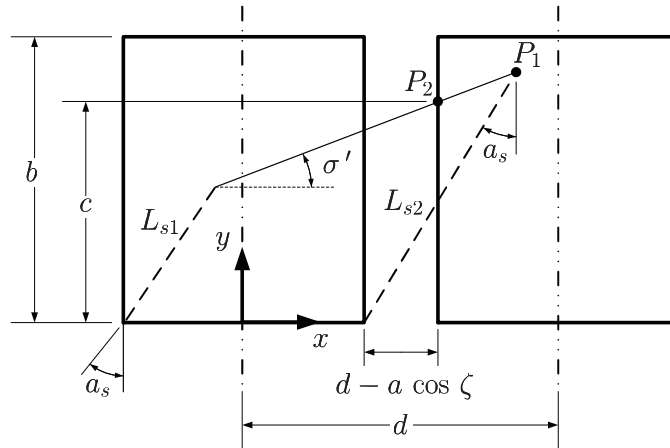
Figure 2.31 Interception of the solar shading with the projected area of the parabolic trough

The equation of a straight line is given by:

$$y - y_1 = \tan \sigma \ (x - x_1) \qquad (2.70)$$

Point P_2 is defined as follows:

$$P_2 = (x_2, y_2) \tag{2.71}$$

$$x_2 = d - \frac{a}{2} \cos \zeta \tag{2.72}$$

$$y_2 = y_1 + m\,(x_2 - x_1) \tag{2.73}$$

$$c = y_2 \tag{2.74}$$

where $x_2 - x_1$ is given by:

$$x_2 - x_1 = d - a \cos \zeta - \left(d_1 + \frac{a}{2} \sin \zeta\right) \frac{\sin a_s}{\tan \alpha}$$

then

$$y_2 = \left(d_1 + \frac{a}{2} \sin \zeta\right) \frac{\cos a_s}{\tan \alpha} + \tan \sigma \left[d - a \cos \zeta - \left(d_1 + \frac{a}{2} \sin \zeta\right) \frac{\sin a_s}{\tan \alpha}\right] \tag{2.75}$$

There is no shadow when:

$$y_2 \geq b$$

which is equivalent to:

$$y_2' \geq R$$

with

$$y_2' = \frac{y_2}{a} \qquad \text{and} \qquad R = \frac{b}{a}$$
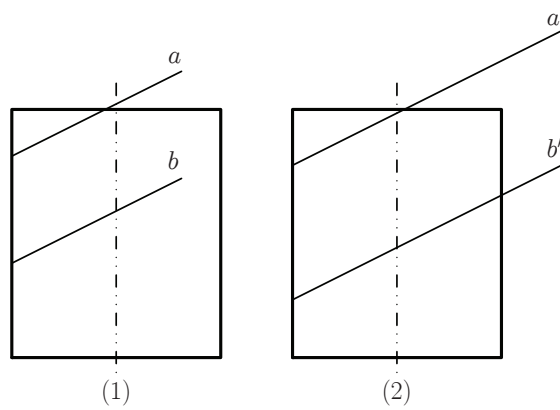
Figure 2.32 Different configurations for the solar shading area

When there is shading, as seen in Figure 2.32, different configurations can be observed.

For case (1):

$$x_s' \cos \sigma' < 1 \qquad (2.76)$$

and

$$\begin{cases} x_s' \sin \sigma' + c' > R & Case\ (a) \\ \\ x_s' \sin \sigma' + c' < R & Case\ (b) \end{cases} \qquad (2.77)$$

$$x_s' = \frac{x_s}{a}$$

For case (2):

$$x_s' \cos \sigma' > 1 \qquad (2.78)$$

and

$$\begin{cases} x_s' \sin \sigma' + c' > R & Case\ (a) \\ \\ x_s' \sin \sigma' + c' < R & Case\ (b) \end{cases} \qquad (2.79)$$

43

For cases 1-a and 2-a', the shading area (Figure 2.33) is given by:

$$A_{sh} = \frac{(b-c)^2}{2 \tan \sigma'}$$ (2.80)
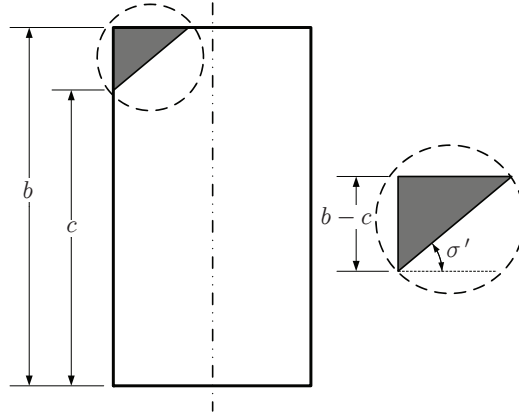
Figure 2.33 Shading area for configuration 1-a and 2-a'

The expression for c (Figure 2.31) was previously obtained as:

$$c = \left(d_1 + \frac{a}{2} \sin \zeta\right) \frac{\cos a_s}{\tan \alpha} + \tan \sigma \left[d - a \cos \zeta - \left(d_1 + \frac{a}{2} \sin \zeta\right) \frac{\sin a_s}{\tan \alpha}\right]$$ (2.81)

The fraction of shading area is:

$$SH = \frac{A_{sh}}{ab} = \frac{(b-c)^2}{2ab \tan \sigma'}$$ (2.82)

Manipulating the last expression:

$$SH = \frac{(R-c')^2}{2R \tan \sigma'}$$ (2.83)

with

$$R = \frac{b}{a} \quad \text{and} \quad c' = \frac{c}{a}$$

For case 1-b, the shading area (Figure 2.34) is given by:

44

$$A_{sh} = \left(b - c - \frac{x_s}{2} \sin \sigma'\right) x_s \cos \sigma' \tag{2.84}$$
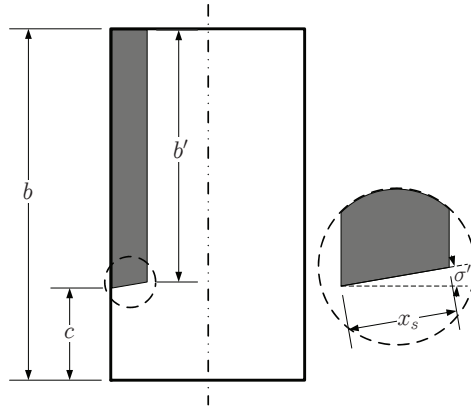
Figure 2.34 Shading area for configuration 1-b

The fraction of shading area is:

$$SH = \frac{A_{sh}}{ab} = \left(R - c' - \frac{x_s'}{2} \sin \sigma'\right) \frac{x_s'}{R} \cos \sigma' \tag{2.85}$$

$$x_s' = \frac{x_s}{a}$$

For case 2-b', the shading area (Figure 2.35) is calculated as:

$$A_{sh} = \left(b - c - \frac{a}{2} \tan \sigma'\right) a \tag{2.86}$$

In this case x_s is given by the next expression:

$$x_s \cos \sigma' = a \tag{2.87}$$

The fraction of shading area is:

$$SH = \frac{A_{sh}}{ab} = \frac{1}{R}\left(R - c' - \frac{1}{2} \tan \sigma'\right) \tag{2.88}$$
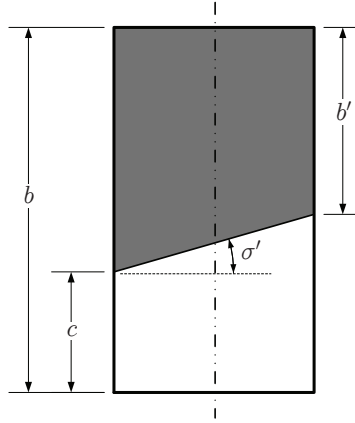
Figure 2.35 Shading area for configuration 2-b'

The shading factor is defined by:

$$\varphi_{SH} = 1 - SH \qquad (2.89)$$

The procedure for solar shading calculations is shown in Figure 2.36. In order to validate the shading model, it was compared with the model developed by Stuetzle [8] which assumes that the shadow covers the entire length of the PTC. Table 2.3 shows the input parameters used for the simulation of the solar shading.

Table 2.3 Input parameters for solar shading simulation

Dimension	Value	Reference
a	5 m	[4]
b	400 m	[13]
d	15 m	[13]
Focal Length (f)	1.49 m	[4]
f_a	$a/2$	[12]
f_b	$a^2/(16f)$	[12]

The simulation was carried out by June 21 and December 21 at SEGS VI location (latitude 37.21°N and longitude 117.022°W), the results are shown in Figure 2.37. The results obtained show that the model developed by Stuetzle is more conservative, although
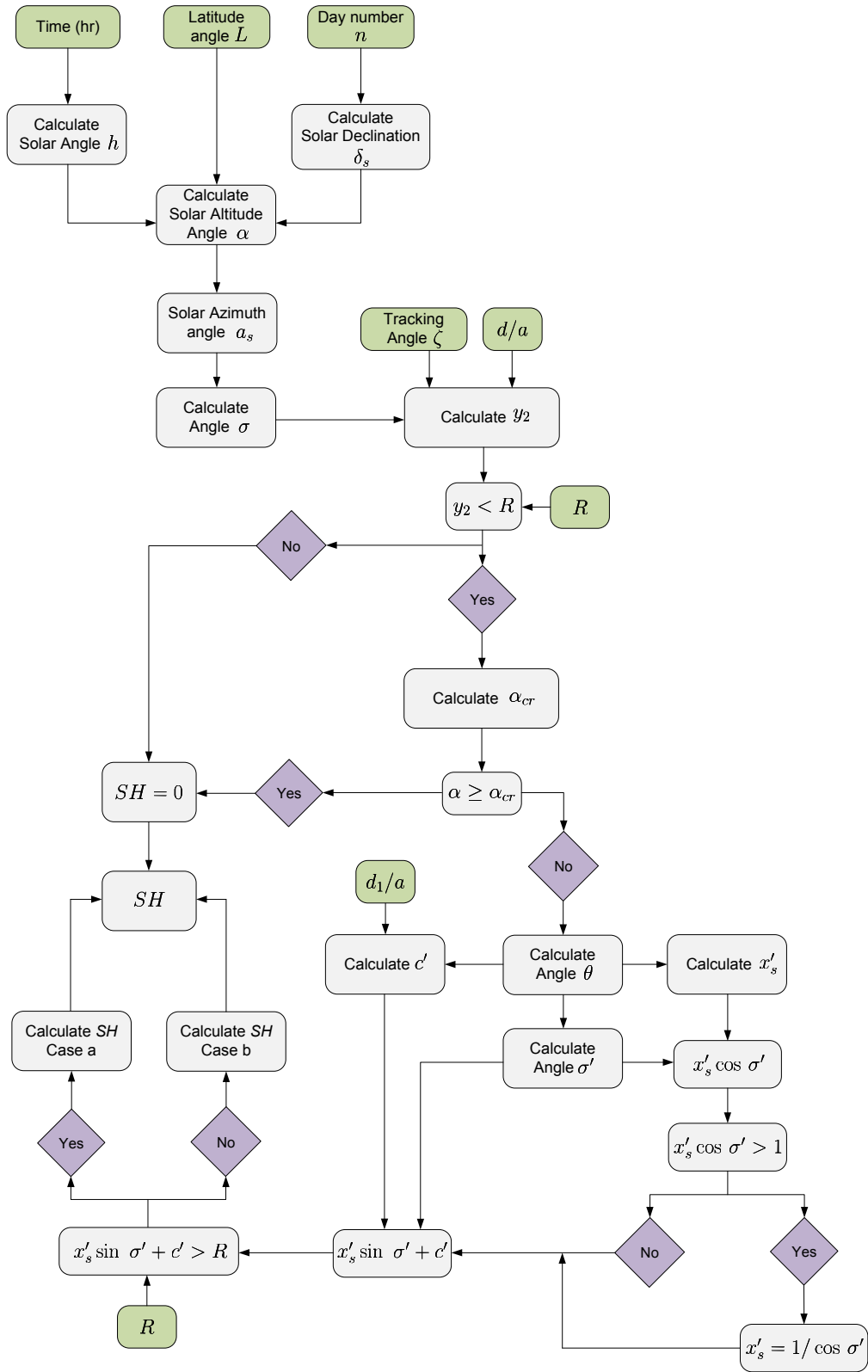
Figure 2.36 Logic flow for calculation of solar shading

47

there are small differences between the models owing to the dimensions of the PTC. For smaller systems, like small collectors for heating and electricity production, the proposed model seems to be more appropriate.
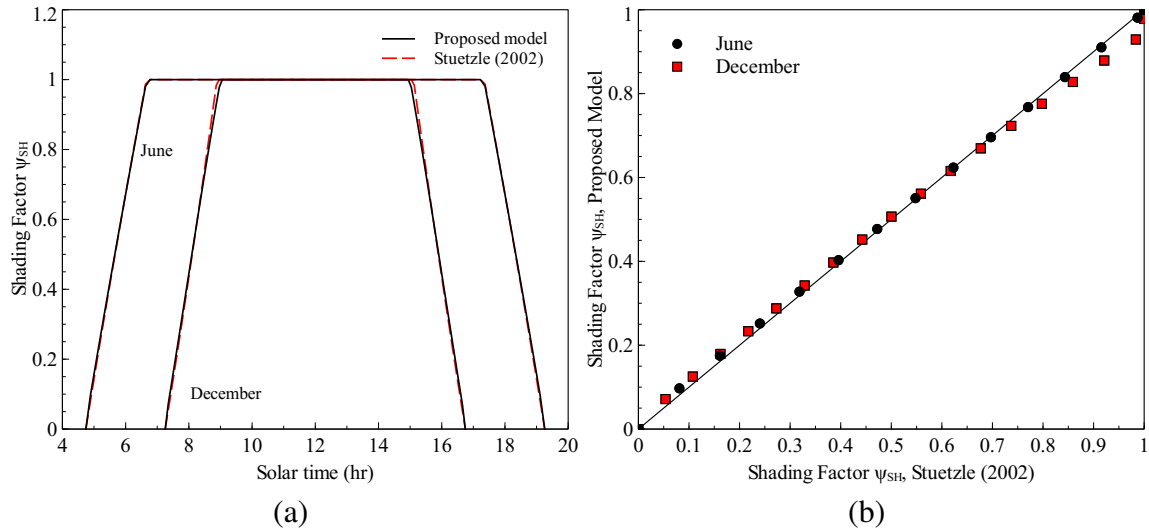
Figure 2.37 Comparison between the proposed shading model and the model developed by Stuetzle [8]. Input parameters are given in Table 2.3

2.6   Conclusions

DI model was selected as the hourly radiation model. The inputs for this model can be measured data or satellite data, which gives certain flexibility to those locations where measured radiation data are not available. The results show that North-South axis tracking is the best tracking configuration for the locations analyzed: Tampa and Daggett.

The solar radiation maps obtained can be an aid to find preliminary locations around the world where optimum levels of radiation are present, although it is important to emphasize that solar radiation is only one of the criteria to find optimum locations for Concentrated Solar Power plants (CSP).

A solar shading model was developed; the results showed that the proposed model is suitable for any PTC dimensions.

Chapter 3

Heat Transfer Analysis of Parabolic Trough Solar Receiver

3.1 Introduction

Parabolic trough power plants currently represent the most mature technology for solar thermal power production. A parabolic trough solar collector (PTC) takes the radiant energy from the sun and converts it to useful thermal energy in the heat transfer fluid (HTF) that circulates through the solar field. Once the geometry and thermal properties are defined, the thermal performance and energy gained by the HTF can be calculated under different configurations and meteorological conditions. PTCs are typically operated at up to temperatures of 400 °C and synthetic oil is commonly used as HTF. The heat transfer analysis of these collectors is important for the calculation of thermal losses and sizing of the solar power plant during preliminary design and also permits to evaluate the effects of collector degradation, and HTF flow rate control strategies on the overall plant performance [13]. Given the importance of the heat transfer analysis in PTCs, since the 1970s numerous models have been proposed.

Edenburn [35] predicted the efficiency of a PTC by using an analytical heat transfer model for evacuated and non evacuated cases. The results showed good agreement with measured data obtained from Sandia National Laboratories (SNL) collector test facility [36]. Ratzel et al. [37] carried out both analytical and numerical study of the heat

conduction and convective losses in an annular receiver for different geometries. Three techniques were proposed to reduce the conduction heat loss: evacuation, oversizing the annular receiver while keeping the Rayleigh number below 1000 over the range of operation and use of gases with low thermal conductivity. Clark [38] analyzed the effects of design and manufacturing parameters that influenced the thermal and economical performance of parabolic trough receivers. Dudley et al. [39] developed an analytical model of SEGS LS-2 parabolic solar collector. The thermal loss model for the heat collection element was one dimensional steady state model based on thermal resistance analysis. This model was validated with experimental data collected by SNL for different receiver annulus conditions: vacuum intact, lost vacuum (air in annulus), and broken annulus cover (bare tube). The results showed a reasonable agreement between the theoretical and experimental heat losses. Thomas and Thomas [40] developed a set of curve-fitting equations based on a numerical heat transfer model for the heat losses in the receiver of a PTC for different geometries, radiative properties and meteorological conditions. A detailed heat transfer model for the solar receiver was developed by Forristall [6]. One dimensional energy balance for several segments was used for short and long receivers respectively. This model was used to determine the thermal performance of parabolic trough collectors under different operating conditions. Stuetzle [8] proposed an unsteady state analysis of solar collector receiver to calculate the collector field outlet temperature. The model was solved by discretizing the partial differential equations obtained by energy balance. The results obtained showed that the overall match between the calculated and measured outlet temperatures was good. García-Valladares and Velásquez [41] developed a detailed numerical model for

51

a single pass solar receiver and validated it. Then they extended the model to a double pass receiver. Their results showed that the proposed configuration enhances the thermal efficiency of the solar collector compared with the single pass. Recently, three dimensional heat transfer analysis of PTCs was performed by combining the Monte Carlo Ray Trace Method (MCRT) and CFD analysis [42–44]. The results indicated that the flange (support bracket) and bellow under non-vacuum conditions bring a high conductive heat loss.

In the middle 90s, Cohen and Kerney [45] proposed the use of direct steam generation (DSG) collector as a future development of the Solar Electric Generating Station (SEGS) in order to eliminate the costly synthetic oil, intermediate heat transport piping loop and the heat exchanger between the solar field and the power block. Heidemann et al. [46] formulated a two dimensional heat transfer model for calculating the absorber wall temperature of a DSG collector under steady and unsteady conditions. The numerical solution showed that a sudden drop of irradiation induces a very high temperature gradient inside the absorber tube in a short period of time. Odeh et al. [47] carried out a model for heat loss of a DSG collector in terms of wall temperature rather than working fluid temperature. The results were compared with the Sandia test data and the results showed that the model underestimates the measured loss. This underestimation was attributed to omission of heat loss from the receiver tube vacuum bellows. Odeh et al. [48] studied the thermal performance of parabolic trough solar collector used as direct steam generator for different solar radiation levels and geometric configurations. This heat transfer model showed better agreement with the in focus test results than the polynomial curve fit equation obtained by Dudley et al. [39]. The thermal losses calculated for water were based on the receiver

wall temperature and the results showed that thermal losses calculated for steam as the heat transfer fluid were lower than those obtained for synthetic oil.

In this chapter a detailed one dimensional heat transfer analysis of a PTC is presented. The existing models published previously assume that there is no thermal interaction between the neighboring surfaces (absorber-envelope, and envelope-envelope) for thermal radiation losses. Although this assumptions simplifies the analysis, it underestimates the radiation losses at high absorber temperatures. To account for the thermal interaction between adjacent surfaces, a comprehensive radiative analysis was implemented in our study for the heat losses in the absorber and the glass envelope. A review of the correlations for convective heat transfer losses was performed as well and new correlations were used in this model. The receiver and envelope were divided into several segments, and mass and energy balance were carried out in each control volume. The partial differential equations were discretized by using the finite difference method and the set of nonlinear algebraic equations were solved simultaneously. In order to validate the proposed numerical model, it was compared with the experimental data obtained from Sandia National Laboratories (SNL), Dudley et al. [39], and other heat transfer models [6, 41] as well.

3.2 Solar Receiver Model

The heat collection element (HCE) consists of an absorber surrounded by a glass envelope (Figure 3.1). The absorber is typically stainless steel tube with a selective absorber surface which provides the required optical and radiative properties. Selective surfaces combine a high absorptance for solar radiation with low emittance for the temperature range in which the surface emits radiation. This combination of surface characteristics is
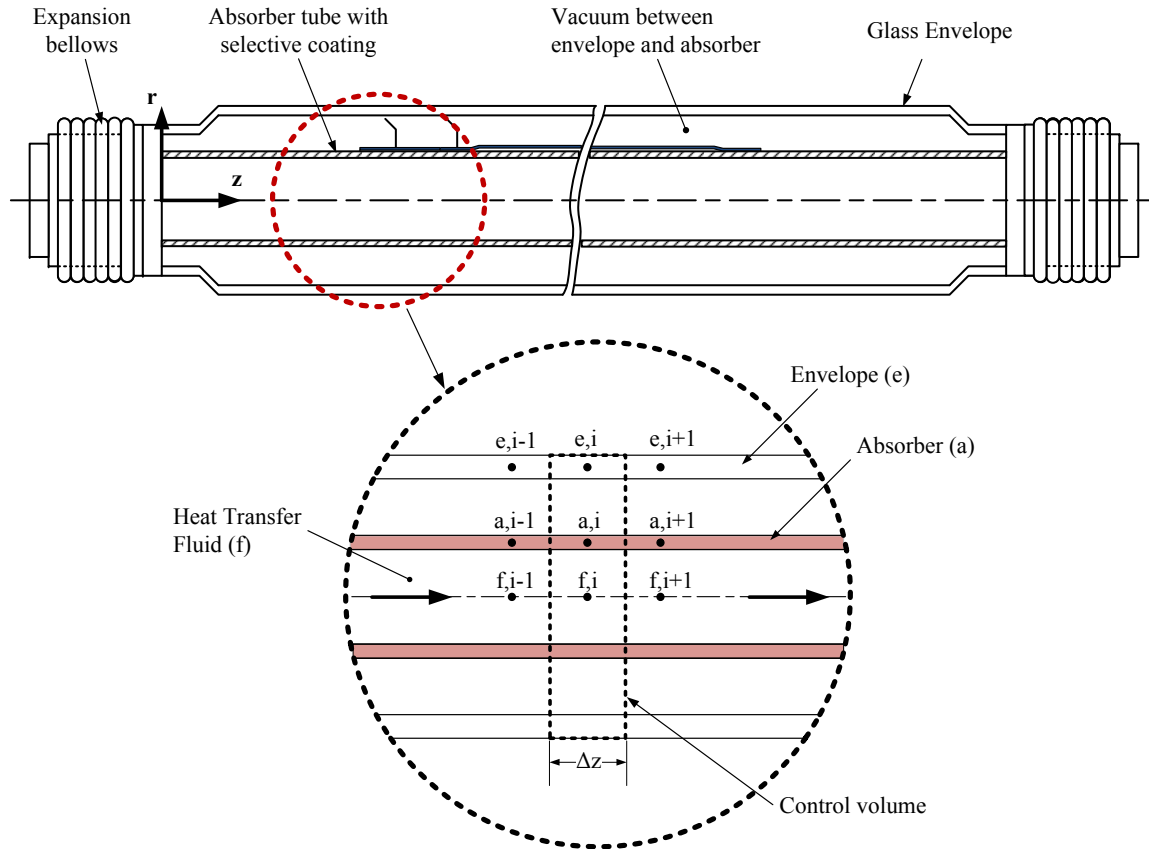
Figure 3.1 Parts of a heat collection element (HCE) and control volume used for the heat transfer analysis. Adapted from [49]

possible because 98 percent of the energy in incoming solar radiation is contained within wavelengths below 3 μm [21]. The glass envelope is an anti reflective evacuated glass tube which protects the absorber from degradation and reduces the heat losses. The vacuum enclosure is used primarily to reduce heat losses at high operating temperatures and to protect the solar-selective absorber surface from oxidation. The HCE uses conventional glass to metal seals and metal bellows at either end to achieve the necessary vacuum enclosure and for thermal expansion difference between the steel tubing and the glass envelope [4]. The bellows also allow the absorber to extend beyond the glass envelope so that the Heat

Collection Elements can form a continuous receiver. The space between bellows provides a place to attach the HCE support brackets [6]. Chemical getters are placed in the annulus to absorb hydrogen, which comes from the HTF and decreases the PTC performance.

The heat transfer model is based on an energy balance between the heat transfer fluid and the surroundings. Figure 3.2 shows the heat transfer in a cross section at the solar collector and the thermal resistance model used in the heat transfer analysis.
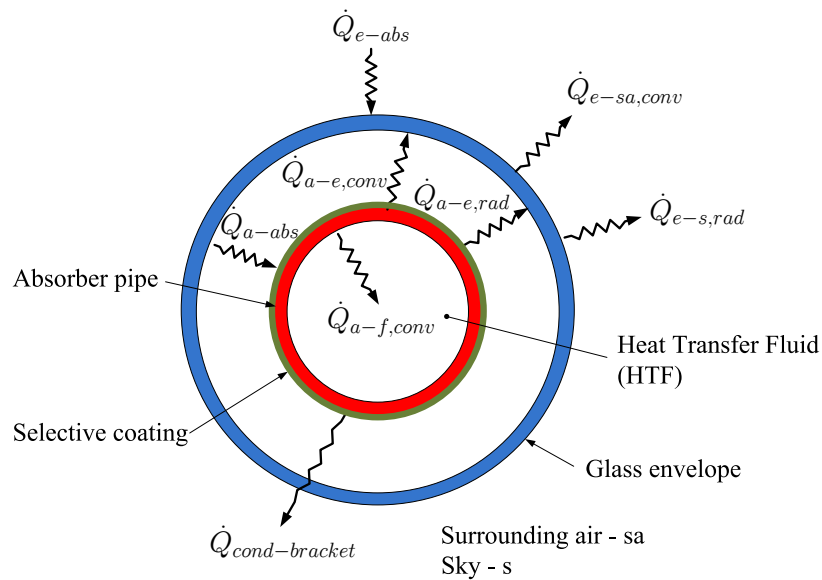
(a) Heat transfer
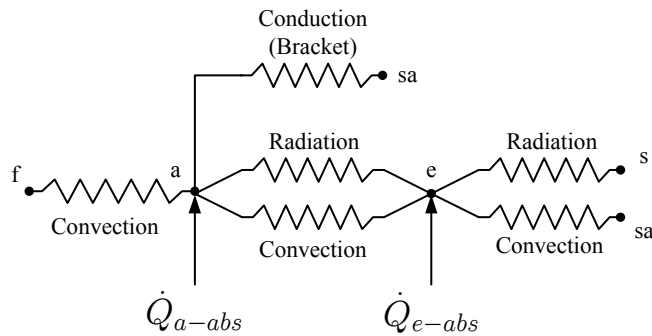
(b) Thermal circuit

Figure 3.2 Heat transfer and thermal resistance model in a cross section at the heat collection element (HCE). Adapted from [6, 39]

The solar energy reflected by the mirrors is absorbed by the glass envelope $\dot{Q}_{e-abs}$ and the absorber surface $\dot{Q}_{a-abs}$. A part of the energy absorbed in the absorber is transferred to the HTF by forced convection $\dot{Q}_{a-f,conv}$, remaining energy is transferred back to the glass envelope by radiation $\dot{Q}_{a-e,rad}$ and natural convection $\dot{Q}_{a-e,conv}$ and lost through the support brackets by conduction $\dot{Q}_{cond,bracket}$ as well. The heat loss coming from the absorber (radiation and natural convection) passes through the glass envelope by conduction and along with the energy absorbed by the glass envelope $\dot{Q}_{e-abs}$ is lost to the environment by convection $\dot{Q}_{e-sa,conv}$ and to sky by radiation $\dot{Q}_{e-s,rad}$ [6]. In this heat transfer model the absorbed radiation was assumed as a heat flux term. In most of the surfaces the thickness of the surface layer over which absorption is taking place is very small compared with the overall dimensions, therefore the error associated with this assumption is very low [50,51]. In order to obtain the partial differential equations that govern the heat transfer phenomena, an energy balance was applied over a section of the solar receiver (Figure 3.1). The equations obtained for each component are showed below.

3.2.1 Heat Transfer from Absorber to Heat Transfer Fluid

Referring to the control volume in Figure 3.3, a uniform temperature and heat flux distribution around the receiver is assumed. After applying the energy balance on this control volume, assuming unsteady state and incompressible fluid with [52], $h \approx C_p T$, the following partial differential equation (PDE) is obtained:

$$A_{i,a}\rho_f C_{p,f} \frac{\partial T_f}{\partial t} = -\dot{m}_f \frac{\partial}{\partial z}\left(C_{p,f} T_f + \frac{V_f^2}{2}\right) + \dot{Q}'_{a-f,conv} \tag{3.1}$$
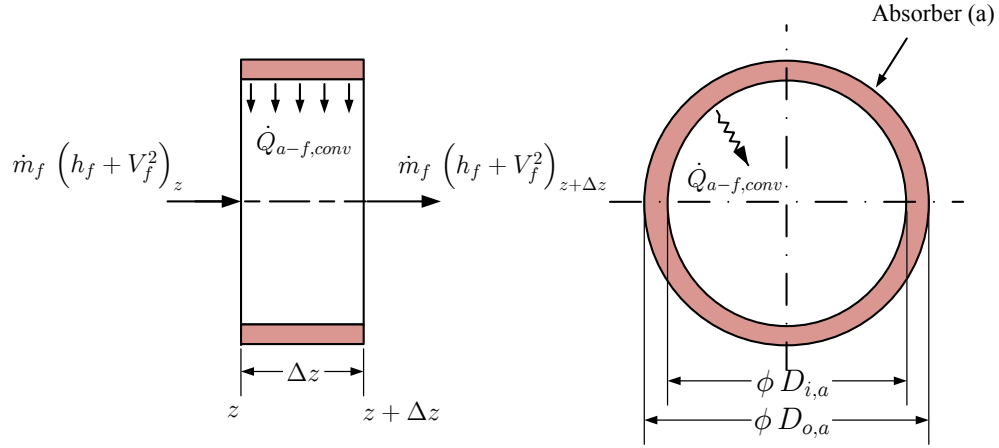
Figure 3.3 Control volume of the heat transfer fluid

$$V_f = \frac{\dot{m}_f}{\rho_f A_{i,a}} \qquad (3.2)$$

where $A_{i,a}$ is the internal cross sectional area of the absorber, $A_{i,a} = (\pi/4)\,D_{i,a}^2$, and $\dot{Q}'_{a-f,conv}$ is the heat transfer by convection from the absorber to HTF per unit length. The convective heat transfer is given by:

$$\dot{Q}'_{a-f,conv} = \pi\,Nu_f\,k_f\,(T_a - T_f) \qquad (3.3)$$

where Nu_f is the Nusselt number, k_f is the thermal conductivity of HTF, and T_a is the absorber wall temperature. Two cases are considered in this chapter: circular pipe and concentric annulus.

3.2.1.1 Circular Pipe

The recommended correlation [53] for fully developed turbulent flow ($Re_D > 2300$) convective heat transfer in circular ducts is given by Gnielinski correlation [54]:

$$Nu_f = \frac{(C_f/2)\,(Re_D - 1000)\,Pr}{1 + 12.7\,(C_f/2)^{\frac{1}{2}}\,(Pr^{2/3} - 1)}\left(\frac{Pr}{Pr_w}\right)^{0.11} \qquad (3.4)$$

$$Re_D = \frac{V_f D_{i,a}}{v_f}$$

where C_f is the friction coefficient (Fanning friction factor), Re_D is the Reynolds number based on the absorber inner pipe diameter, Pr is the Prandtl number, and v_f is the kinematic viscosity of HTF. This correlation is valid for $2300 \leq Re_D \leq 5 \times 10^6$ and $0.5 \leq Pr \leq 2000$. The thermal properties should be evaluated at the bulk mean heat transfer fluid temperature, except Pr_w which is evaluated at the absorber wall temperature. The friction coefficient is calculated from the Filonenko correlation [53] for isothermal flows in smooth tubes:

$$C_f = (1.58 \, Ln \, Re_D - 3.28)^{-2} \qquad 10^4 \leq Re_D \leq 10^7 \qquad (3.5)$$

The convection heat transfer coefficient for rough tubes can be calculated approximately by using the friction coefficient determined from the Colebrook and White equation [53]:

$$\frac{1}{\sqrt{C_f}} = 3.48 - 1.7372 \, Ln \left(\frac{2\,\varepsilon}{D_{i,a}} + \frac{9.35}{Re_D \, \sqrt{C_f}} \right) \qquad 5 \leq Re_\varepsilon \leq 70 \qquad (3.6)$$

with

$$Re_\varepsilon = \frac{V_f \, \varepsilon}{v_f} \qquad (3.7)$$

The best explicit correlation for practical friction coefficient computations in a rough circular duct is given by Chen [53]:

$$\frac{1}{\sqrt{C_f}} = 3.48 - 1.7372 \, Ln \left(\frac{2\,\varepsilon}{D_{i,a}} - \frac{16.2426}{Re_D} \, Ln \, A_2 \right) \qquad (3.8)$$

$$A_2 = \frac{(2\,\varepsilon/D_{i,a})^{1.1098}}{6.0983} + \left(\frac{7.149}{Re_D} \right)^{0.8981}$$

for $4000 \leq Re_D \leq 10^8$ and $2 \times 10^{-8} \leq 2\,\varepsilon/D_{i,a} \leq 0.1$. For the transition flow $2100 \leq Re_D \leq 4000$ the formula developed by Bhatti and Shah can be used to calculate the friction coefficient [55]:

$$C_f = 0.0054 + \frac{2.3 \times 10^{-8}}{Re_D^{-3/2}} \tag{3.9}$$

Since entry lengths for turbulent flow are typically short $10 \leq z/D \leq 60$, it is often reasonable to assume that the average Nusselt number for the entire tube is equal to the value associated with the thermally fully developed turbulent flow [56]. However, for short tubes the mean Nusselt number for thermally developing flow can be calculated using Al-Arabi's correlation [55]:

$$\frac{Nu_{f,m}}{Nu_{f,\infty}} = 1 + \frac{C}{z/D} \tag{3.10}$$

where Nu_∞ stands for the fully developed Nusselt number and:

$$C = \frac{(z/D)^{0.1}}{Pr^{1/6}} \left(0.68 + \frac{3000}{Re_D^{0.81}} \right) \tag{3.11}$$

For laminar flow, $(Re_D \leq 2300)$, the Nusselt number on walls with uniform temperature is given by:

$$Nu_f = 3.66 \tag{3.12}$$

For a circular tube subjected to constant surface temperature, the average Nusselt number for the thermal entrance region can be determined from Hausen's correlation [55]:

$$Nu_f = 3.66 + \frac{0.0668}{z^{*1/3} \left(0.04 + z^{*2/3} \right)} \tag{3.13}$$

59

where $z^* = (z/D) / (Re_D Pr)$. The thermal properties should be evaluated at the bulk mean fluid temperature. The fully developed conditions are reached for [57]:

$$\frac{z/D}{Re_D Pr} \approx 0.05$$

The friction coefficient for fully developed laminar flow in a circular duct is given by:

$$C_f = \frac{16}{Re_D} \tag{3.14}$$

3.2.1.2 Concentric Annulus

The Nusselt number in this case can be determined from a suitable turbulent flow correlation [58, 59] (Equation (3.4)) by using a hydraulic diameter of $D_h = D_{i,a} - D_{plug}$. Petukhov and Roizen [60] recommend to include the following correction factor to improve the accuracy of Nusselt number obtained from Gnielinski correlation:

$$F = 1 - 0.14 \, r^{*0.6} \tag{3.15}$$

The friction coefficient is calculated from Filonenko correlation [53] for isothermal flows in smooth tubes:

$$C_f = \left(1.58 \, Ln \, Re_{D_l} - 3.28\right)^{-2} \tag{3.16}$$

In order to get more accurate friction coefficients. Jones et al. [61] recommend to use the laminar equivalent diameter for concentric annular ducts rather than the hydraulic diameter. The laminar equivalent diameter is defined as:

$$\frac{D_l}{D_h} = \frac{1 + r^{*2} + \left(1 - r^{*2}\right) / \ln r^*}{\left(1 - r^*\right)^2} \tag{3.17}$$

60

For short segments the mean Nusselt number for thermally developing flow can be calculated using Al-Arabi's correlation (Equation (3.10)). For laminar flow, Table 3.1 shows the Nusselt number for fully developed flow.

Table 3.1 Nusselt number for concentric annulus under laminar flow. Adapted from [62]

$r*$	Nu_{oo}
0.00	3.6568
0.02	3.9934
0.05	4.0565
0.10	4.1135
0.25	4.2321
0.50	4.4293
1.00	4.8608

For the case when the fluid is thermally developing for a fully developed laminar profile, Table 3.2 shows the values obtained of the Nusselt number for different values of r^* and x^*, which are defined as:

$$r^* = \frac{D_{i,a}}{D_{plug}} \qquad\qquad z_h^* = \frac{z}{D_h \, Re_{D_h} \, Pr}$$

Table 3.2 Nusselt number for concentric annulus under laminar flow for developing temperature and developed velocity profile. Adapted from [62]

x^*	z_h^*					
	0.02	0.05	0.10	0.25	0.5	1.0
0.010	5.217	5.287	5.359	5.518	5.762	6.260
0.015	4.732	4.796	4.862	5.005	5.232	5.705
0.025	4.298	4.359	4.419	4.548	4.757	5.207
0.050	4.031	4.093	4.150	4.269	4.468	4.902
0.100	3.994	4.057	4.114	4.233	4.430	4.861
0.150	3.993	4.057	4.114	4.232	4.429	4.861
0.250	3.993	4.057	4.114	4.232	4.429	4.861
0.500	3.993	4.057	4.114	4.232	4.429	4.861
1.000	3.993	4.057	4.114	4.232	4.429	4.861
∞	3.993	4.057	4.114	4.232	4.429	4.861

3.2.2 Heat Transfer from Absorber to Glass Envelope

Two heat transfer mechanisms occur between the absorber and the glass envelope: convection heat transfer and thermal radiation. Convection heat transfer depends on the annulus pressure; experimental work has shown that heat transfer losses are independent of the annulus vacuum pressure for pressures above 1 Torr [37]. At pressures below 1 Torr, molecular conduction is the heat transfer mechanism while for pressure above 1 Torr, natural convection takes place. After applying the energy balance (Figure 3.4), the next PDE is obtained:

$$
A_a \rho_a C_{p,a} \frac{\partial T_a}{\partial t} = A_a \frac{\partial}{\partial z} \left(k_a \frac{\partial T_a}{\partial z} \right) + \dot{Q}'_{a,abs} - \dot{Q}'_{a-f,conv} - \dot{Q}'_{a-e,conv}
$$

$$
- \dot{Q}'_{a-e,rad} - \dot{Q}'_{cond,bracket} \tag{3.18}
$$

where A_a is the cross sectional area of the absorber, $A_a = (\pi/4)\left(D_{o,a}^2 - D_{i,a}^2\right)$, $\dot{Q}'_{a,abs}$ is the solar absorption in the absorber per receiver length, $\dot{Q}'_{a-f,conv}$ is the heat transfer by convection from absorber to HTF per unit length, $\dot{Q}'_{a-e,conv}$ is the heat transfer by convection from absorber to envelope per unit length, $\dot{Q}'_{a-e,rad}$ is the heat transfer by radiation
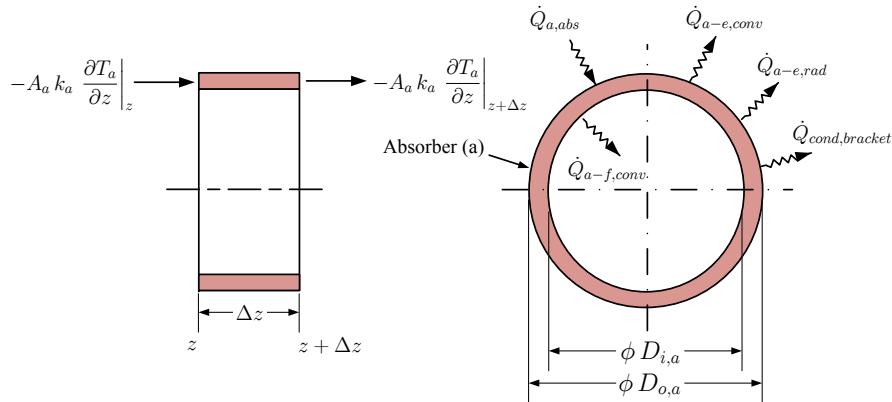
Figure 3.4 Control volume used for the absorber analysis

from absorber to glass envelope per unit length, and $\dot{Q}'_{cond,bracket}$ is the heat conduction through support brackets per unit length. Stainless steel is normally used as the absorber tube material. Table 3.3 presents the properties of three stainless steel commonly used as the absorber tube material.

Table 3.3 Thermal conductivity, density and specific heat for 304L, 316L and 321H stainless steel, temperature in ºC. Data taken from [63]

Material	k (W/m K)	ρ (kg/m^3)	C_p (kJ/kg K)
304L	$0.0130\,T + 14.9732$	8027.17	0.5024
316L	$0.0130\,T + 14.9732$	8027.17	0.5024
321H	$0.0151\,T + 14.5837$	8027.17	0.5024

3.2.2.1 Vacuum in Annulus (P < 1 Torr)

Heat conduction in gases at various pressures occurs in four distinct regimes; these regimes are determined by Knudsen number (Kn), which is the ratio of the molecular mean free-path, λ, to a characteristic dimension of the system L_c. At very low pressures ($K_n > 10$) collisions between molecules are relatively rare; this is known as the free molecule regime. At normal pressures ($K_n < 0.01$) the gas may be assumed as a continuum. Between these extremes lie the transition ($0.1 < K_n < 10$) and the temperature jump ($0.01 < K_n < 0.1$). The Knudsen number ranges are approximated since they are somewhat geometry dependent and also depend on the accommodation coefficients. The goal of evacuating a collector is to make the heat losses by conduction and convection insignificant, therefore the vacuum in the HCE must be in the free molecule regime or near free molecule conditions. The

pressure associated with this regime is approximately 0.0001 Torr (0.013 Pa) [4, 64]. The heat transfer coefficient for the annular space is given by [65]:

$$h_{a-e} = \frac{k_g}{\frac{D_{o,a}}{2} Ln\,(D_{i,e}/D_{o,a}) + b\lambda\,(D_{i,e}/D_o + 1)} \qquad (3.19)$$

$$\dot{Q}'_{a-e,conv} = h_{a-e}\,\pi\,D_{o,a}\,(T_a - T_e) \qquad (3.20)$$

where k_g is the mean conductivity of the gas in the annular place evaluated at $\overline{T}_{a-e} = (T_a + T_e)/2$, $D_{o,a}$ is the diameter of the receiver tube, $D_{i,e}$ is the inner diameter of the glass envelope, T_a is the temperature of the receiver tube, T_e is the temperature of the glass envelope, and λ is the mean free path (m). The coefficient b is defined by [65]:

$$b = \frac{2 - \alpha}{\alpha}\left[\frac{9\gamma - 5}{2\,(\gamma + 1)}\right] \qquad (3.21)$$

where α is the accommodation coefficient, and γ is the ratio of specific heats. The mean free path (m) is calculated by using the next expression [65]:

$$\lambda = 2.331 \times 10^{-20}\frac{\overline{T}_{a-e}}{P\delta^2} \qquad (3.22)$$

where $\overline{T}_{a-e}$ is the average annulus gas temperature (K^{-1}), P is the annulus gas pressure (Torr or mm Hg), and δ is the molecular diameter of annulus gas (cm). The molecular diameters for different gases are shown in Table 3.4.

Experimental studies have reported the values for the thermal accommodation coefficient, α, from 0.01 to nearly unity [68]. This value depends on either the gas surface arrangement or the level of contaminant gas layers adsorbed on the surface. Qualitative theoretical arguments predict that thermal accommodation tends to increase with the in-

Table 3.4 Molecular diameter of different gases

Gas[1]	$\delta \times 10^8$ (cm)
Air	3.66 [2]
Hydrogen	2.97 [3]
Argon	3.42 [3]

[1] The molecular diameters were obtained from measured gas viscosity

[2] [66]

[3] [67]

creasing gas molecular weight and with roughness for a given surface [69]. Since the exact nature of the thermal accommodation coefficient is still an active problem; almost all the evidence indicates that for most gas-solid interactions a value of $\alpha = 1$ could be assumed in the absence of well documented information [70–72].

3.2.2.2 Pressure in Annulus (P > 1 Torr)

The conduction layer model has shown to accurately predict the heat transfer for horizontal cylinders [55]. Kakaç et al. [53] recommend a correlation given by Kuehn and Goldstein [73]. This correlation uses an iterative method to obtain the mean bulk temperature and is based on extensive experimental and numerical heat transfer results. This numerical model assumes that the conduction layers do not overlap. The convective heat transfer is given by:

$$\dot{Q}'_{a-e,conv} = \pi k_g Nu_{a-e} \left(T_a - T_e \right) \qquad (3.23)$$

The correlation for the convection part is written as [73]:

$$Nu_{D_i conv} = \frac{hD_i}{k_g} = \frac{2}{\ln\left(\frac{1+2/Nu_i}{1-2/Nu_o)}\right)} \tag{3.24}$$

with

$$Nu_i = \left\{ \left[0.518 \, Ra_{D_i}^{1/4} \, f_2\left(Pr\right)\right]^{15} + \left(0.1 \, Ra_{D_i}^{1/3}\right)^{15} \right\}^{1/15} \tag{3.25}$$

$$Ra_{D_i} = \frac{g\,\beta\,\left(T_a - \bar{T}_b\right) D_i^3}{v^2} Pr \tag{3.26}$$

where g is the Earth's gravity, β is the volumetric thermal expansion coefficient, and v is the kinematic viscosity. For an ideal gas:

$$\beta = \frac{1}{\bar{T}_{a-e}}$$

$$Nu_o = \left(\left\{ \left[\left(\frac{1}{1-e^{-\frac{1}{4}}}\right)^{\frac{5}{3}} + \left[0.587 \, f_3\left(Pr\right) \, Ra_{D_o}^{1/4}\right]^{\frac{5}{3}} \right]^{\frac{3}{5}} \right\}^{15} + \left(0.1 \, Ra_{D_o}^{1/3}\right)^{15} \right)^{\frac{1}{15}} \tag{3.27}$$

$$Ra_{D_o} = \frac{g\,\beta\,\left(\bar{T}_b - T_e\right) D_o^3}{v^2} Pr \tag{3.28}$$

with

$$f_2\left(Pr\right) = \left[1 + \left(\frac{0.559}{Pr}\right)^{3/5}\right]^{-5/12}$$

$$f_3\left(Pr\right) = \left[\left(1 + \frac{0.6}{Pr^{0.7}}\right)^{-5} + \left(0.4 + 2.6 \, Pr^{0.7}\right)^{-5}\right]^{-1/5}$$

For the conduction part, which prevails as the Rayleigh number approaches zero, the heat transfer by conduction is given by:

$$Nu_{D_i cond} = \frac{2}{\cosh\left\{\left[D_i^2 + D_o^2\right]/2D_i D_o\right\}}$$ (3.29)

The overall Nusselt number valid for any Rayleigh number is:

$$Nu_{a-e} = \left[\left(Nu_{D_i conv}\right)^{15} + \left(Nu_{D_i cod}\right)^{15}\right]^{1/15}$$ (3.30)

Fluid properties are evaluated at the average temperature of $\overline{T} = (T_a + T_e)/2$, $D_i = D_{o,a}$ and $D_o = D_{i,e}$. The average bulk temperature is obtained from:

$$\frac{\overline{T}_b - T_e}{T_a - \overline{T}_b} = \frac{\overline{Nu_{D_i conv}}}{\overline{Nu_{D_o conv}}}$$ (3.31)

and

$$\overline{Nu_{D_i conv}} = \frac{2}{\ln\left[1 + 2/Nu_i\right]}$$ (3.32)

$$\overline{Nu_{D_o conv}} = \frac{2}{-\ln\left[1 - 2/Nu_o\right]}$$ (3.33)

3.2.2.3 Radiation Heat Transfer from Receiver to Envelope

Thermal radiation analysis for one surface implies that all surfaces that can exchange radiative energy with the surface must be considered simultaneously. How much energy two surfaces exchange depends on their size, separation distance, and orientation [51]. In order to carry out the radiative heat transfer analysis some view factors must be calculated.
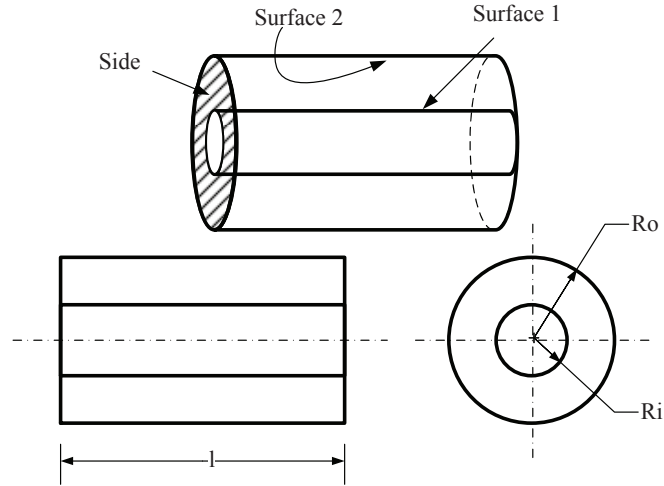
Figure 3.5 Annulus geometry

The view factors for a short annulus [51, 74] (Figure 3.5) are given by:

$$
\begin{aligned}
F_{2-1} = & \frac{1}{R} - \frac{1}{\pi R}\left\{ \cos^{-1}\left(\frac{B}{A}\right) - \frac{1}{2L}\left[\sqrt{(A+2)^2 - (2R)^2}\cos^{-1}\left(\frac{B}{RA}\right) \right.\right. \\
& \left.\left. + B\sin^{-1}\left(\frac{1}{R}\right) - \frac{\pi A}{2}\right] \right\}
\end{aligned}
\tag{3.34}
$$

$$
F_{1-2} = \left(\frac{D_0}{D_i}\right) F_{2-1}
\tag{3.35}
$$

$$
F_{1-s} = \frac{1}{2}\left(1 - F_{1-2}\right)
\tag{3.36}
$$

$$
\begin{aligned}
F_{2-2} = & 1 - \frac{1}{R} + \frac{2}{\pi R}\tan^{-1}\left(\frac{2\sqrt{R^2-1}}{L}\right) \\
& - \frac{L}{2\pi R}\left\{ \frac{\sqrt{4R^2+L^2}}{L}\sin^{-1}\left[\frac{4\left(R^2-1\right) + \left(L^2/R^2\right)\left(R^2-2\right)}{L^2+4\left(R^2-1\right)}\right]\right. \\
& \left. - \sin^{-1}\left(\frac{R^2-2}{R^2}\right) + \frac{\pi}{2}\left(\frac{\sqrt{4R^2+L^2}}{L}-1\right) \right\}
\end{aligned}
\tag{3.37}
$$

68

$$F_{2-s} = \frac{1}{2}\left(1 - F_{2-1} - F_{2-2}\right) \qquad (3.38)$$

with

$$R = R_o/R_i$$

$$L = l/R_i$$

$$A = L^2 + R^2 - 1$$

$$B = L^2 - R^2 + 1$$

The view factors for neighboring surfaces (Figure 3.6) on shell interior coaxial cylinder are as follows ($F_{21'}$ [75], $F_{22'}$ [76]):

$$
\begin{aligned}
F_{2-1'} &= \frac{1}{R\delta^*}\int_0^c \left\{ \frac{B^*}{a^{*3/2}}\left[(L-\delta^*)\, tan^{-1}\left(\frac{L-\delta^*}{a^{*1/2}}\right)\right.\right.\\
&\left.\left. + (L+\delta^*)\, tan^{-1}\left(\frac{L+\delta^*}{a^{*1/2}}\right) - 2L\, tan^{-1}\left(\frac{L}{a^{*1/2}}\right)\right]\right\} d\theta \qquad (3.39)
\end{aligned}
$$

with

$$R = R_o/R_i$$

$$L = l/R_i$$

$$a^* = R^2 + 1 - 2R\, Cos\,\theta$$

$$
\begin{aligned}
B^* &= \frac{R}{\pi\,(R-1)^2}\left[R^2 + 1 - R\,(1+Cos\,\theta) - 2\,Sin^2\frac{\theta}{2}\right]\cdot\left[R^2+1\right.\\
&\left. -R\,(1+Cos\,\theta) - 2R^2\,Sin^2\frac{\theta}{2}\right]
\end{aligned}
$$
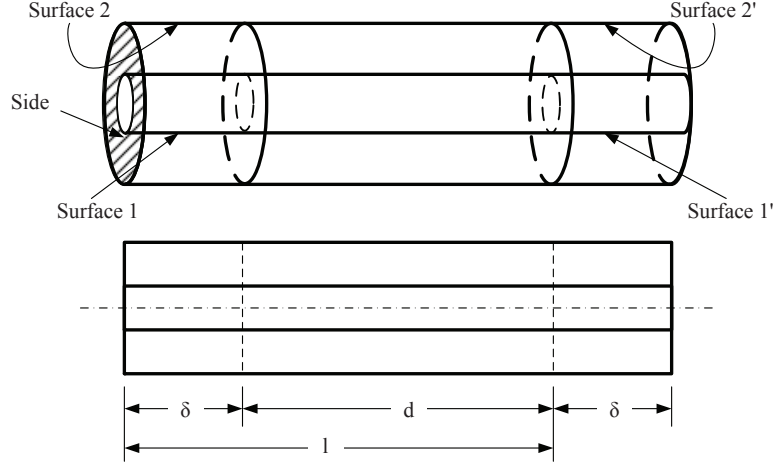
Figure 3.6 Surfaces on a coaxial cylinder

$$c = cos^{-1}\left(R_i/R_o\right)$$

$$\delta^* = \delta/R_i$$

$$F_{2-2'} = \left(1 + \frac{N}{2}\right) F_{22}\Big|_{\delta^*(2+N)} - (1+N)\, F_{22}\Big|_{\delta^*(1+N)} + \frac{N}{2} F_{22}\Big|_{\delta^* N} \qquad (3.40)$$

with

$$N = d/\delta$$

$$\delta^* = \delta/R_i$$

$$F_{2-2}\Big|_{\xi} = F_{2-2}\Big|_{L=\xi}$$

$$F_{2'-s} = (N+2)\, F_{2-s}\Big|_{\delta^*(2+N)} - (N+1)\, F_{2-s}\Big|_{\delta^*(1+N)} \qquad (3.41)$$

with

$$N = d/\delta$$

70

$$\delta^* = \delta/R_i$$

$$F_{2-s}\Big|_{\xi} = F_{2s}\Big|_{L=\xi}$$

$$F_{1'-s} = (N+2)\, F_{1-s}\Big|_{\delta^*(2+N)} - (N+1)\, F_{1-s}\Big|_{\delta^*(1+N)} \tag{3.42}$$

with

$$N = d/\delta$$

$$\delta^* = \delta/R_i$$

$$F_{1-s}\Big|_{\xi} = F_{1-s}\Big|_{L=\xi}$$

The view factors $F_{1-2'}$, $F_{2-1'}$, and $F_{2-2'}$ F_{1-s} were calculated for different points (Figure 3.7). The results are shown in Figure 3.8 and Figure 3.9. The results show that view factors for closest node are high but as the nodal distance increases the view factors approach zero.

(a) Intermediate position (b) Side position
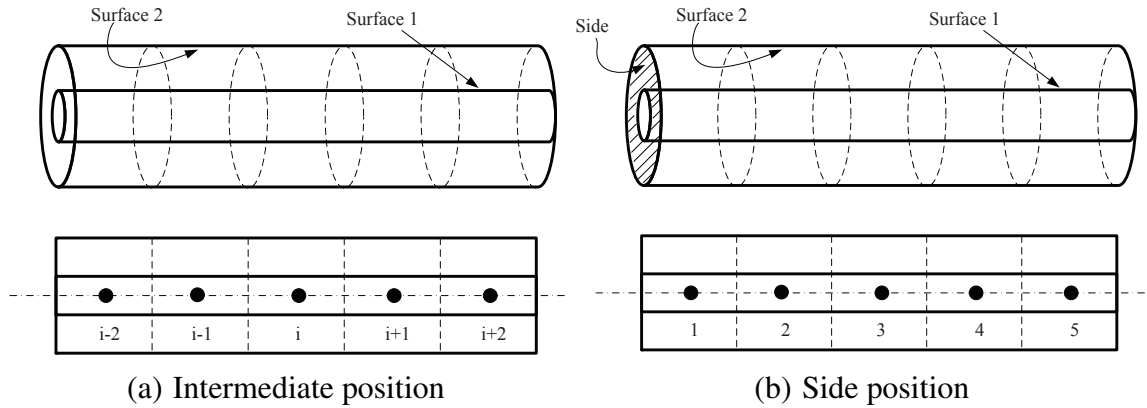
Figure 3.7 Node position for coaxial cylinders

(a) $F_{1-2'}$

(b) $F_{2-1'}$

(c) $F_{2-2'}$

(d) F_{1-s}
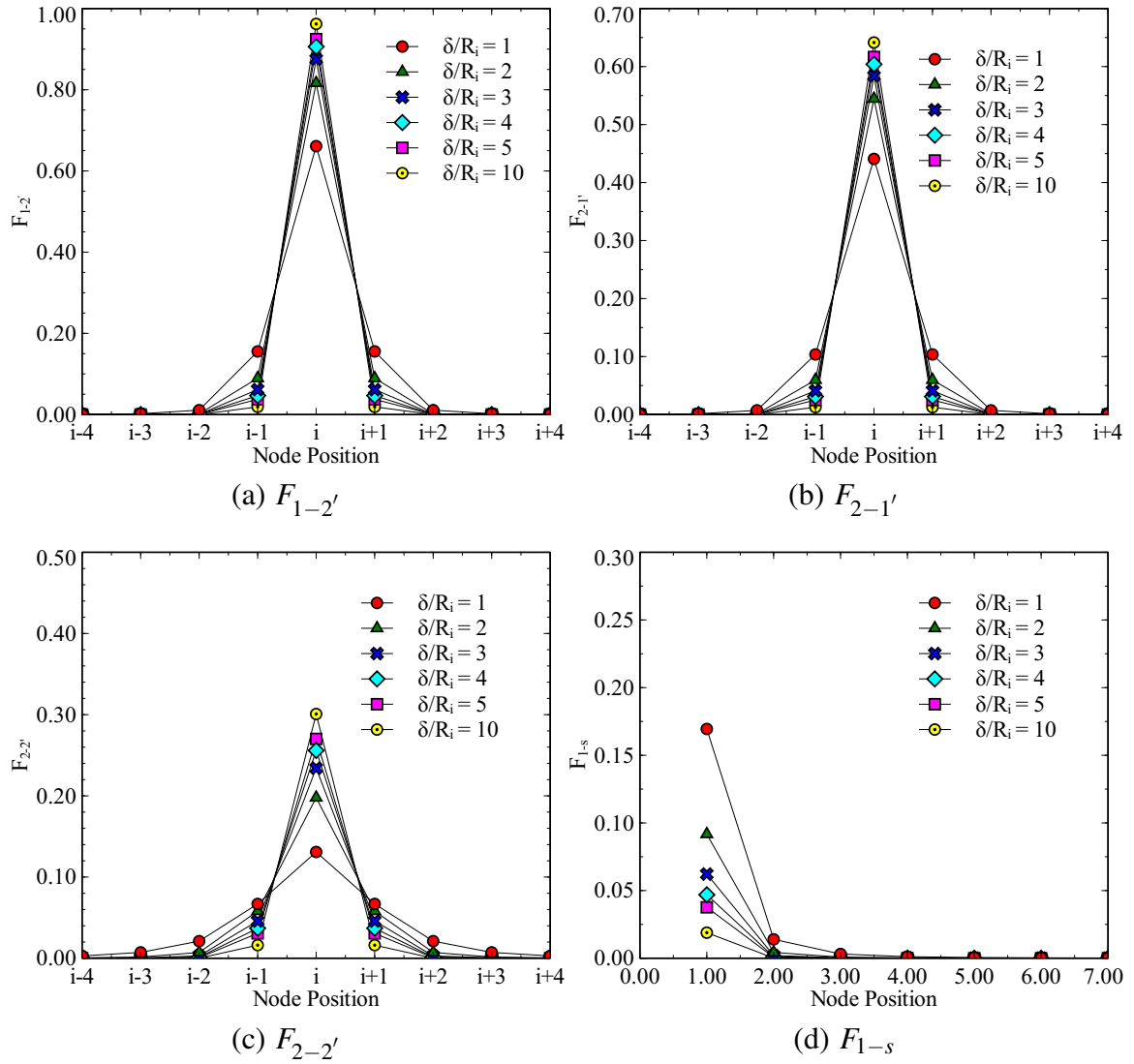
Figure 3.8 View factors for neighboring surfaces on shell interior of coaxial cylinders, $R = 1.5$

(a) $F_{1-2'}$

(b) $F_{2-1'}$

(c) $F_{2-2'}$

(d) F_{1-s}
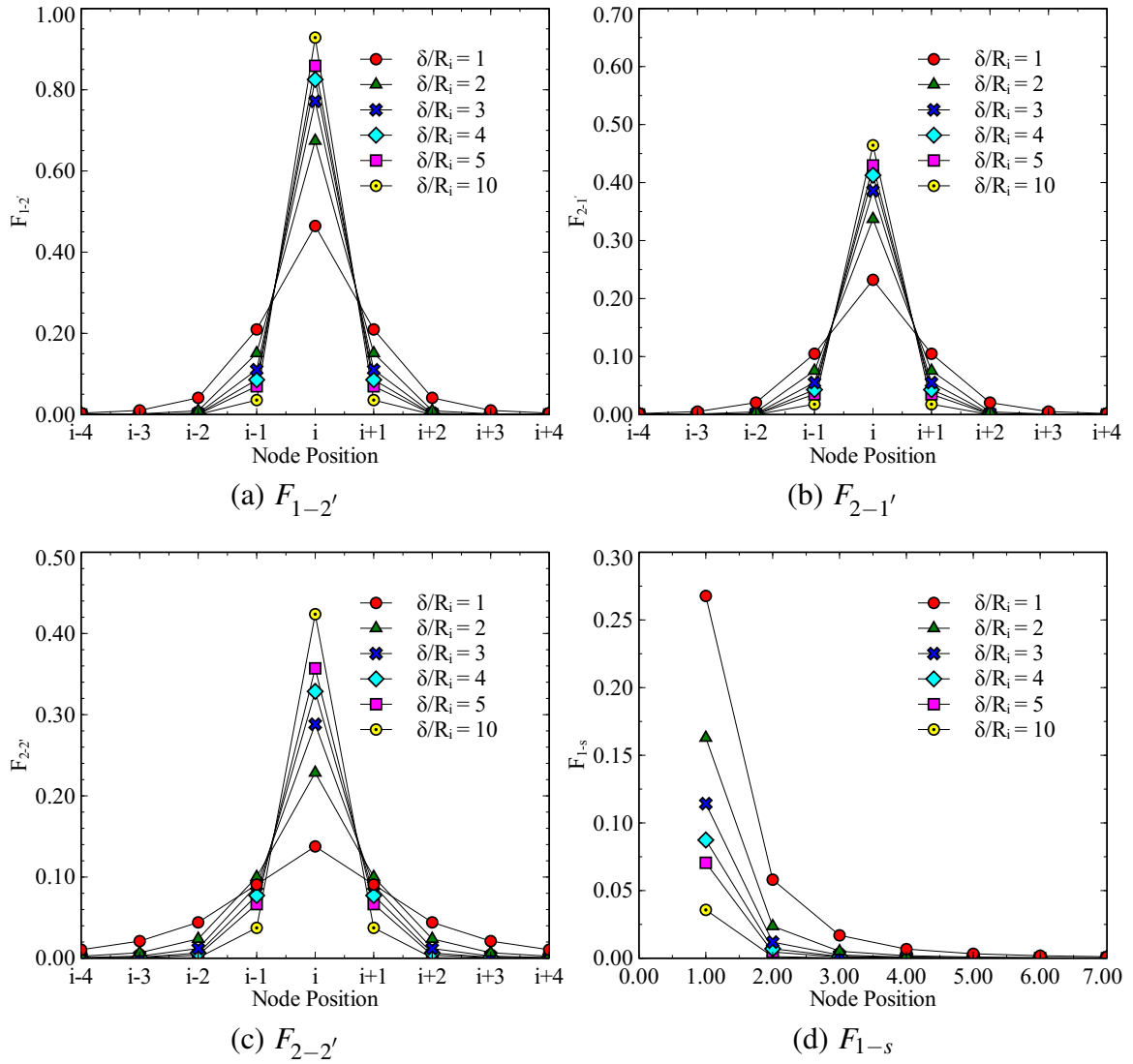
Figure 3.9 View factors for neighboring surfaces on shell interior of coaxial cylinders, $R = 2.0$

The radiation heat transfer calculation is simplified by assuming the glass envelope is opaque to infrared radiation and assuming gray surfaces $(\alpha = \varepsilon)$. Making an energy balance to calculate the radiative heat transfer rate between surfaces, the next expression is obtained [50]:

$$\dot{q}_i = R_i - \sum_{j=1}^{N} R_j F_{i-j} \qquad i = 1, 2, 3, \ldots N \tag{3.43}$$

where R_i is the radiosity, which is the total heat flux leaving the surface i. Radiosity is defined as [50]:

$$R_i = \varepsilon_i \sigma T_i^4 + \rho_i \sum_{j=1}^{N} R_j F_{i-j} \qquad i = 1, 2, 3, \ldots N \tag{3.44}$$

where ε_i is the emissivity of surface i, F_{i-j} is the view factor between surface i and j, $\dot{q}_i$ is the net radiative heat flux on the surface i, and σ is the Stefan Boltzmann constant equal to $5.67 \times 10^{-8}\, W/m^2 K^4$.

For the particular case of the thermal radiation between the receiver and the envelope, four surfaces are included (Figure 3.5). For simplification, it is assumed that the right side and left side are adiabatic surfaces, which means that they may reflect all incoming but do not emit any radiant heat. These requirements are satisfied if $\rho_r = \rho_l = 1.0$ and $\varepsilon_r = \varepsilon_l = 0$ [77]. The radiative heat transfer rate and radiosity for each surface are shown below. For the external surface of receiver, surface a and node i:

$$R_{a_i} = \varepsilon_{a_i} \sigma T_{a_i}^4 + \rho_{a_i} \left[\sum_{j=1}^{N} F_{a_i - a_j} R_{a_j} + \sum_{j=1}^{N} F_{a_i - e_j} R_{e_j} + F_{a_i - r} R_r + F_{a_i - l} R_l \right] \tag{3.45}$$

$$\dot{q}_{a_i} = R_{a_i} - \left[\sum_{j=1}^{N} F_{a_i - a_j} R_{a_j} + \sum_{j=1}^{N} F_{a_i - e_j} R_{e_j} + F_{a_i - r} R_r + F_{a_i - l} R_l \right] \tag{3.46}$$

$$F_{a_i-a_j} = 0 \quad F_{a_i-e_j} = F_{1-2'} \quad F_{a_i-r} = F_{1'-s} \quad F_{a_i-l} = F_{1'-s}$$

For the internal surface of the envelope, surface e and node i:

$$R_{e_i} = \varepsilon_{e_i} \sigma T_{e_i}^4 + \rho_{e_i} \left[\sum_{j=1}^{N} F_{e_i-a_j} R_{a_j} + \sum_{j=1}^{N} F_{e_i-e_j} R_{e_j} + F_{e_i-r} R_r + F_{e_i-l} R_l \right] \tag{3.47}$$

$$\dot{q}_{e_i} = R_{e_i} - \left[\sum_{j=1}^{N} F_{e_i-a_j} R_{a_j} + \sum_{j=1}^{N} F_{e_i-e_j} R_{e_j} + F_{e_i-r} R_r + F_{e_i-l} R_l \right] \tag{3.48}$$

$$F_{e_i-a_j} = F_{2-1'} \quad F_{e_i-e_j} = F_{2-2'} \quad F_{e_i-r} = F_{2'-s} \quad F_{e_i-l} = F_{2'-s}$$

For the right side, surface r:

$$R_r = \left[\sum_{j=1}^{N} F_{r-a_j} R_{a_j} + \sum_{j=1}^{N} F_{r-e_j} R_{e_j} + F_{r-l} R_l \right] \tag{3.49}$$

$$F_{r-a_j} = F_{s-1'} \quad F_{r-e_j} = F_{s-2'} \quad F_{r-r} = 0 \quad F_{r-l} = F_{s-s}$$

For the left side, surface l:

$$R_l = \left[\sum_{j=1}^{N} F_{l-a_j} R_{a_j} + \sum_{j=1}^{N} F_{l-e_j} R_{e_j} + F_{l-r} R_r \right] \tag{3.50}$$

$$F_{l-a_j} = F_{s-1'} \quad F_{l-e_j} = F_{s-2'} \quad F_{l-r} = F_{s-s} \quad F_{l-l} = 0$$

Equations (3.45) and (3.47) can be written in a compact way by introducing Kronecker's delta function [51]. The Kronecker's delta function is defined as [51]:

$$\delta_{ij} = \begin{cases} 1 & i = j \\ 0 & i \neq j \end{cases} \tag{3.51}$$

The simplified equations are as follows:

$$\sum_{j=1}^{N} \left(\frac{\delta_{ij}}{\varepsilon_{a_i}} R_{a_j} - \frac{\rho_{a_i}}{\varepsilon_{a_i}} F_{a_i-e_j} R_{e_j} \right) - \frac{\rho_{a_i}}{\varepsilon_{a_i}} \left(F_{a_i-r} R_r + F_{a_i-l} R_l \right) = \sigma T_{a_i}^4 \qquad (3.52)$$

$$\sum_{j=1}^{N} \left(\frac{R_{e_j}}{\varepsilon_{e_i}} \left(\delta_{ij} - \rho_{e_i} F_{e_i-e_j} \right) - \frac{\rho_{e_i}}{\varepsilon_{e_i}} F_{e_i-a_j} R_{a_j} \right) - \frac{\rho_{e_i}}{\varepsilon_{e_i}} \left(F_{e_i-r} R_r + F_{e_i-l} R_l \right) = \sigma T_{e_i}^4 \qquad (3.53)$$

The heat transfer loss by radiation per unit length on the external absorber surface is:

$$\dot{Q}'_{a-e,rad} = \dot{q}_{a_i} \pi D_{o,a} \qquad (3.54)$$

The heat transfer gained by radiation per unit length on the internal envelope surface is given by:

$$\dot{Q}'_{a-e,rad'} = \dot{q}_{e_i} \pi D_{i,e} \qquad (3.55)$$

3.2.2.4   Heat Conduction Through Support Brackets

The solar receiver is placed at the collector focal line by support brackets supported on the collector structure and located at each end of every solar receiver. For this analysis, the support brackets are divided into two segments connected in series. The first segment is a connection tab (rectangular cross section) that connects the base of the solar receiver and the metallic support and the second segment is a metallic support (square tube) that connects the connection tab to the collector structure (Figure 3.10).

76
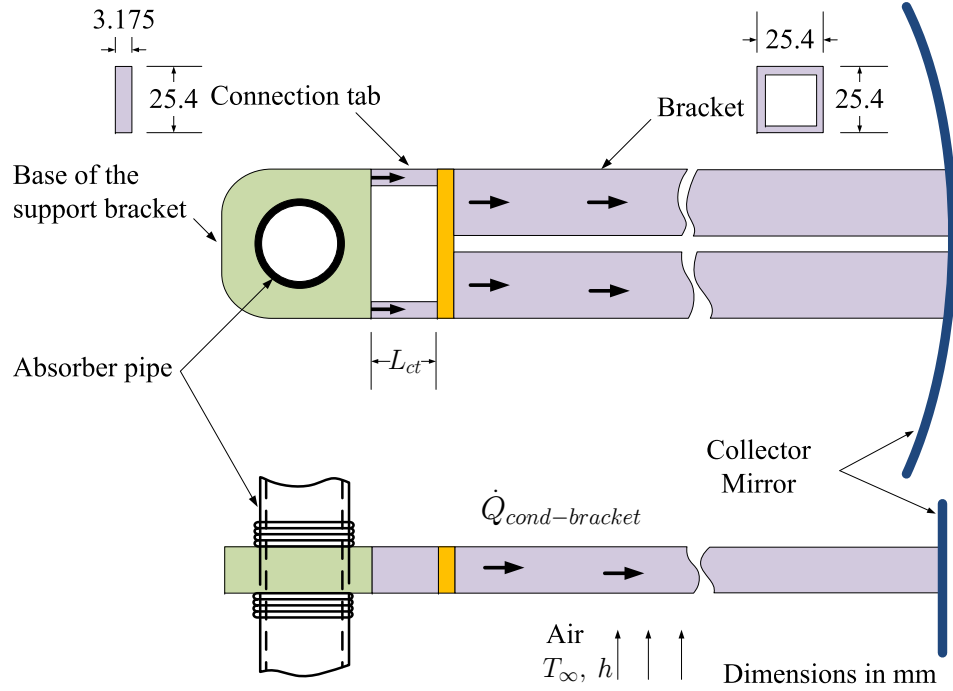
Figure 3.10 Support bracket. Adapted from [6]

Initially, a heat conduction analysis for a fin with a prescribed temperature at the tip is studied. The temperature distribution in the fin is given by [78]:

$$\frac{\theta}{\theta_b} = \frac{\sinh m\,(L-x) + (\theta_L/\theta_b)\,\sinh mx}{\sinh mL} \tag{3.56}$$

with

$$\theta = T - T_\infty$$

$$m^2 = \frac{h_b P}{k_b A_c}$$

where θ_b is the excess temperature at the base of the fin, θ_L is the excess temperature at the tip of the fin, P is the fin perimeter, and A_c is the cross sectional area of the fin. For this configuration, It will be assumed that the convective heat transfer coefficient is uniform

77

over the length of the fin. Using this approximation, the temperature at the intersection point is obtained as:

$$\frac{\theta_a}{\theta_b} = \frac{1}{\cosh m_1 L_{ct} + \dfrac{\zeta_2}{\zeta_1} \sinh m_1 L_{ct}} \tag{3.57}$$

with

$$\zeta_i = \sqrt{h_b k_b P_i A_{c,i}}$$

The base temperature is assumed to be the absorber temperature at the point where the bracket is located.

$$\theta_b = T_a - T_\infty$$

The heat losses by conduction are given by [78]:

$$\dot{Q}_{cond-bracket} = 2\,\zeta_1\,\theta_b\,\frac{\cosh m_1 L_{ct} - \dfrac{\theta_a}{\theta_b}}{\sinh m_1 L_{ct}} \tag{3.58}$$

and

$$\dot{Q}'_{cond,bracket} = \dot{Q}_{cond,bracket}/L_b \tag{3.59}$$

where L_b is the length between the support brackets. Based on the geometric information given in the heat transfer model developed by Forristall [6], the connection tab has a length in the range of $25.4 \leq L_{ct} \leq 50.8$ mm. A comparison of the results obtained from Equation (3.58), for connection tabs with different lengths, and the conduction model used by Forristall [6] is shown in Figure 3.11.

78
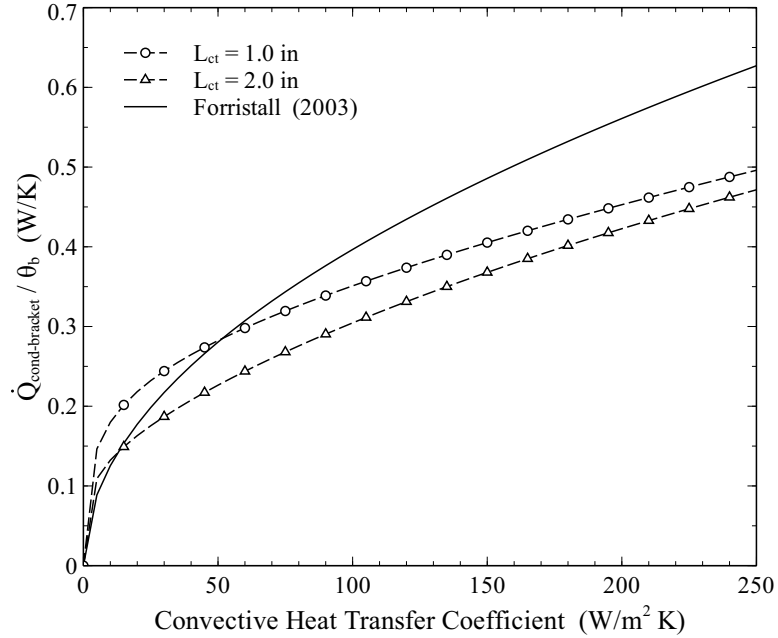
Figure 3.11 Comparison of the heat losses through support brackets for different connection tab lengths, and the model used by Forristall [6]

The results show that the model used by Forristall is more conservative, which means higher heat losses from support brackets. For the current conduction analysis, a connection tab with a length of 25.4 mm will be assumed, this assumption is based on the maximum heat transfer losses obtained from Equation (3.58). For simplification, the convective heat transfer coefficient is calculated for the square tube because this part of the support bracket has more than 99% of the area exposed to the environment. The convective coefficient is obtained from:

$$h_b = \frac{Nu_L k_b}{L} \tag{3.60}$$

The thermal properties of air are evaluated at the film temperature [78] $T_f = (T_a + T_\infty)/2$ and the average surface temperature of the fin is:

$$\overline{T}_{fin} \approx \frac{T_a + (m_2 L - 1)\, T_\infty}{m_2 L} \tag{3.61}$$

The thermal conductivity, k_b (kW/m $^\circ C$), for the support bracket, plain carbon steel, at certain film temperature (ºC) was obtained by fitting the data [56] to a straight line ($R^2 = 0.998$):

$$k_b = -0.0419\, T_f + 73.2357 \tag{3.62}$$

Two convective heat transfer modes are used to calculate the heat transfer coefficient: natural convection ($V_{wind} = 0$) and forced convection ($V_{wind} > 0$).

For long cylinders in still air, heat losses by natural convection are greater in or close to the horizontal, than in inclined [79, 80], because when tubes are inclined the abnormal flow pattern decreases the heat transfer, although this difference is negligible for a cylinder in vertical position. It is assumed that the previous analysis can be extrapolated for non circular cylinders; this assumption is particularly true for long bodies of arbitrary cross section [81], in which the geometry configuration can be approximated as a cylindrical shape. For this analysis, the convective heat transfer coefficient is calculated in the horizontal position since this position leads to the highest values. For a square cross sectional area the average Nusselt number is given by [55]:

$$Nu_L = [(Nu_l)^m + (Nu_t)^m]^{1/m} \tag{3.63}$$

$$Nu^T = G\bar{C}_L Ra^{1/4} \tag{3.63a}$$

80

$$Nu_l = \frac{C_2}{\ln\left(1 + C_2/Nu^T\right)} \tag{3.63b}$$
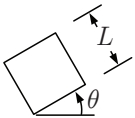
$$Nu_t = \bar{C}_t\,Ra^{1/3} \tag{3.63c}$$

The constant $\bar{C}_L$ is defined as follows [55]:

$$\bar{C}_L = \frac{0.671}{\left[1 + (0.492/Pr)^{9/16}\right]^{4/9}} \tag{3.64}$$

The others constants G, C_2, $\bar{C}_t$ and m are shown in Table 3.5. Given the geometry of the support bracket, an inclination angle of 0° was selected for calculating the average Nusselt number.

Table 3.5 Constants for use in Equation (3.63) for long horizontal square cylinders in an isothermal environment [55]. Original data taken from Clemens et al. [82] for air. Correlation is validated for $10^3 \le Ra \le 10^8$

Geometry	θ	G	C_2	$\bar{C}_t\ (Pr = 0.71)$	m
$Nu = \bar{h}L/k$	0°	0.735	1.3	0.087	4.5
$Ra = \dfrac{g\beta\Delta T L^3}{\nu\alpha}$	15°	0.720	1.3	0.102	4.5
	30°	0.786	1.3	0.106	4.5
$P = 4L$	45°	0.797	1.3	0.108	4.5

The Nusselt number for a square cylinder subjected to a cross flow of air is defined by [83]:

$$Nu_L = C\,Re_L^m \tag{3.65}$$
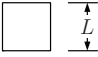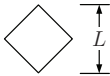
The constants C, m recommended by Sparrow et al. [83] for use in Equation (3.65) are shown in Table 3.6. Based on the previous correlation, it can be demonstrated that [83]:

$$\frac{\bar{h}_{square}}{\bar{h}_{diamond}} = 0.6 \left(\frac{U_\infty L}{v_\infty} \right)^{0.07} \tag{3.66}$$

$$5000 \leq \frac{U_\infty L}{v_\infty} \leq 42000$$

It was found that square orientation has higher convective heat transfer coefficients than the diamond orientation, therefore a square orientation was selected for the heat transfer analysis under forced convection.

Table 3.6 Constants for use in Equation (3.65) for long horizontal square cylinders [84] subjected to a cross flow of air

Geometry			Re_L	C	m
Square	$\rightarrow$ □	L	$5000 - 60000$	0.14	0.666
Diamond	$\rightarrow$ ◇	L	$6000 - 60000$	0.27	0.59

3.2.3 Heat Transfer from Glass Envelope to the Ambient

The heat transfer from the glass envelope to the surroundings is by convection and radiation. Convection heat transfer has two cases: with wind (forced convection) and no wind (natural convection). The radiation heat transfer is basically between the glass envelope and either the sky or the collector surface, but the maximum radiation heat losses take place when the solar receiver is assumed to be surrounded only by the sky surface.

The energy balance on the control volume (Figure 3.12) leads to the next PDE:

$$A_e \, \rho_e \, C_{p,e} \, \frac{\partial T_e}{\partial t} \;=\; A_e \frac{\partial}{\partial z}\left(k_e \frac{\partial T_e}{\partial z}\right) + \dot{Q}'_{e,abs} + \dot{Q}'_{a-e,conv} + \dot{Q}'_{a-e,rad'}$$

$$-\dot{Q}'_{e-sa,conv} - \dot{Q}'_{e-s,rad} \tag{3.67}$$

where $\dot{Q}'_{e,abs}$ is the solar absorption in the envelope per receiver length, $\dot{Q}'_{e-sa,conv}$ is the heat transfer by convection from the glass envelope to the surrounding air per unit length, and $\dot{Q}'_{e-s,rad'}$ is the heat transfer by radiation from the glass envelope to the sky per unit length.
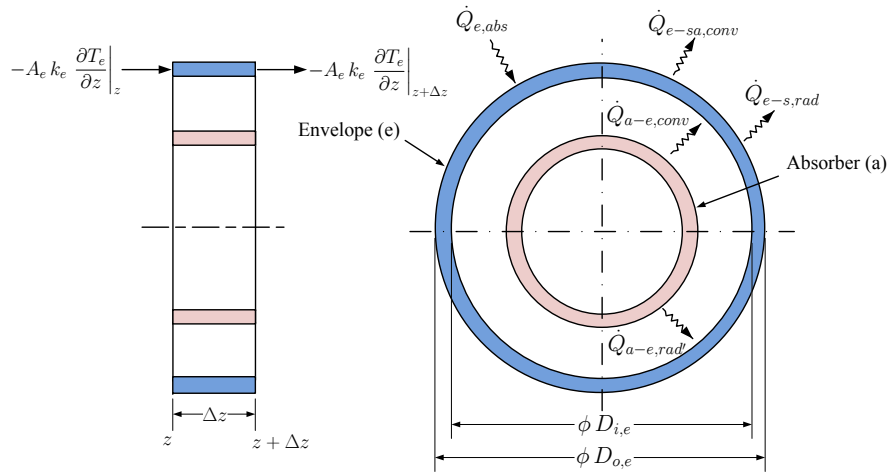
Figure 3.12 Control volume of glass envelope

Borosilicate glass is used commonly as the glass envelope material. The thermal conductivity and the volumetric heat capacity ($\rho \, C_p$) are calculated by using a polynomial fit obtained from [85]:

$$k_e = k_{e,o} \sum_i a_i \left(\frac{T}{298.15}\right)^i \tag{3.68}$$

83

$$(\rho C_p)_e = (\rho C_p)_{e,o} \sum_i b_i \left(\frac{T}{298.15} \right)^i \tag{3.69}$$

The coefficients for these equations are presented in Table 3.7.

Table 3.7 Polynomial coefficients for thermal conductivity and volumetric heat capacity. Data taken from [85]

Coefficient	Value	Coefficient	Value
$k_{e,o}$	1.15	$(\rho C_p)_{e,o}$	1770
a_0	0.7688	b_0	0.8716
a_1	0.2158	b_1	0.1634
a_2	0.0157	b_2	-0.035

3.2.3.1 Heat Convection

The heat transfer by convection per unit length from the glass envelope to the surrounding air is calculated as:

$$\dot{Q}'_{e-sa,conv} = h_e \pi D_{o,e} (T_e - T_\infty) \tag{3.70}$$

with

$$h_e = \frac{Nu_e k_e}{D_{o,e}} \tag{3.71}$$

For no wind conditions, the expression given by Churchill and Chi [53] is recommended for horizontal cylinder under natural convection:

$$Nu_e = \left[0.60 + 0.387 \left\{ \frac{Ra_D}{\left[1 + (0.559/Pr)^{\frac{9}{16}} \right]^{\frac{16}{9}}} \right\}^{\frac{1}{6}} \right]^2 \tag{3.72}$$

For wind conditions, the average Nusselt number recommended for a cylinder in cross flow [53] is given by:

$$Nu_e = c\,Re_D^m\,Pr^n\left(\frac{Pr}{Pr_w}\right)^p \tag{3.73}$$

The constants suggested for this equation are tabulated in Table 3.8. The value of p depends on the heat flux direction: $p = 0.25$ for fluid heating and $p = 0.2$ for fluid cooling. Fluid properties are evaluated at the average temperature of $\bar{T} = (T_o + T_\infty)/2$, except Pr_w which is valuated at the wall temperature.

Table 3.8 Constants for Equation (3.73) for a cylinder in cross flow [53]

c	m	n	Re_D
0.76	0.4	0.37	$1 - 4 \times 10^1$
0.52	0.5	0.37	$4 \times 10^1 - 10^3$
0.26	0.6	0.37	$10^3 - 2 \times 10^5$
0.023	0.8	0.4	$2 \times 10^5 - 10^7$

3.2.3.2 Radiation Heat Transfer (Sky and Collector Surface)

In this analysis the solar receiver is surrounded by either the collector or the sky. In order to simplify the model, it is assumed that half of the receiver surface is surrounded by the mirror and the other half by the sky (Figure 3.13). The heat flux and radiosity are calculated for each surface. For the external surface of the envelope at node i:

$$\dot{q}_{es_i} = R_{es_i} - F_{es_i-sky}R_{sky} - F_{es_i-rs}R_{rs} - F_{es_i-ls}R_{ls} - F_{es_i-c}R_c \tag{3.74}$$

For the sky surface:

$$\dot{q}_{sky} = R_{sky} - \sum_{i=1}^{N} F_{sky-es_i}R_{es_i} - F_{sky-sky}R_{sky} - F_{sky-rs}R_{rs} - F_{sky-ls}R_{ls} - F_{sky-c}R_c \tag{3.75}$$
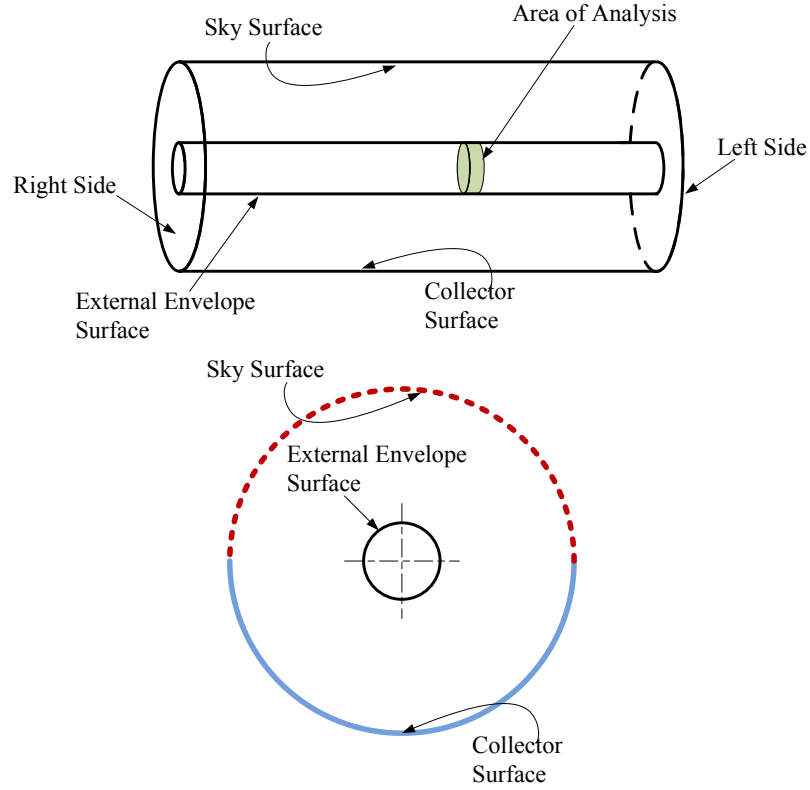
Figure 3.13 Zone analysis of the radiation heat loss from the receiver to the ambient

For the collector surface:

$$\dot{q}_c = R_c - \sum_{i=1}^{N} F_{c-es_i} R_{es_i} - F_{c-sky} R_{sky} - F_{c-rs} R_{rs} - F_{c-ls} R_{ls} - F_{c-c} R_c \qquad (3.76)$$

The view factor F_{sky-es_j} is given by:

$$F_{sky-es_j} = F_{es_j-sky} \frac{A_{es_j}}{A_{sky}} \qquad (3.77)$$

where A_{es_j} is the area of analysis (envelope), and A_{sky} is the sky area. Simplifying:

$$F_{sky-es_j} = F_{es_j-sky} \left(\frac{2\Delta z}{L} \right) \left(\frac{D_{o,e}}{D_c} \right) \qquad (3.78)$$

where L is the length of the collector. Since $\Delta z/L$ and $D_{o,e}/D_c$ and are very small, $(\Delta z/L)(D_{o,e}/D_c) \approx 0$, F_{sky-es_j} approaches zero ($F_{sky-es_j} \approx 0$). Using the previous simplification, it can be determined that:

$$F_{sky-rs} \approx 0 \tag{3.79}$$

$$F_{sky-ls} \approx 0 \tag{3.80}$$

The view factors $F_{sky-sky}$ and F_{sky-c} for an infinitely long cylinder are calculated by the following expressions [86]:

$$F_{sky-sky} = 1 - \frac{2}{\pi}\left[\left(1-R^2\right)^{1/2} + R\sin^{-1}R\right] \tag{3.81}$$

$$F_{sky-c} = \frac{2}{\pi}\left[\left(1-R^2\right)^{1/2} + R\sin^{-1}R\right] - R \tag{3.82}$$

and

$$R = D_{o,e}/D_c$$

Figure 3.14 shows the variation of $F_{sky-sky}$ and F_{sky-c} with the parameter R. For this particular analysis R is small, and therefore $F_{sky-sky}$ and F_{sky-c} can be approximated by:

$$F_{sky-sky} \approx 1 - \frac{2}{\pi} \tag{3.83}$$

$$F_{sky-c} \approx \frac{2}{\pi} \tag{3.84}$$
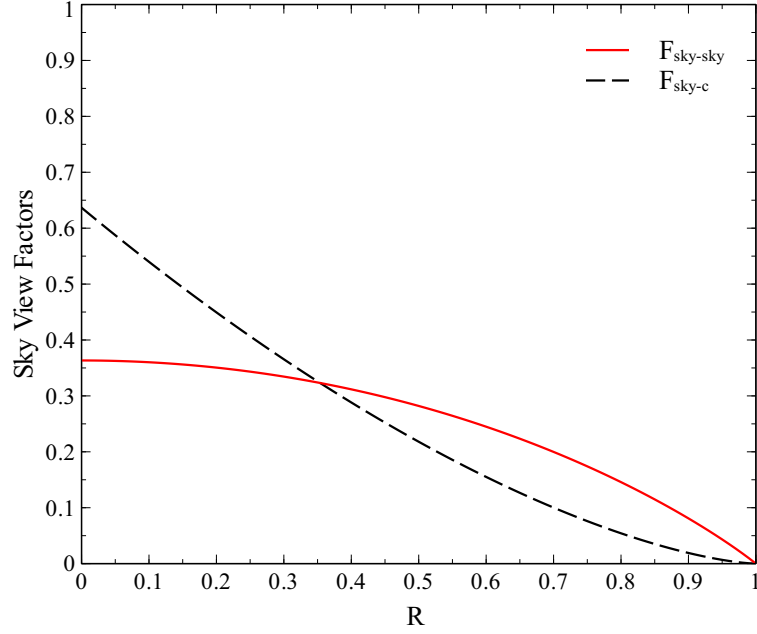
Figure 3.14 Sky view factors, $F_{sky-sky}$ and F_{sky-c}

The values of the view factors for the solar collector, F_{c-sky} and F_{c-c}, are calculated by using symmetry.

$$F_{c-c} \approx 1 - \frac{2}{\pi} \qquad (3.85)$$

$$F_{c-sky} \approx \frac{2}{\pi} \qquad (3.86)$$

The sky is often considered as a global black body [30,87], defined in terms of an equivalent sky temperature [88–90], which is not true but useful for practical calculations of heat exchange between the sky and any surface at ground level. Using the last approximation, $\varepsilon_{sky} = 1$, equations for sky and collector surface can be simplified as:

$$\dot{q}_{sky} = R_{sky} - F_{sky-sky} R_{sky} - F_{sky-c} R_c \qquad (3.87)$$

$$\dot{q}_c = R_c - F_{c-sky} R_{sky} - F_{c-c} R_c \qquad (3.88)$$

$$R_{sky} = \sigma T_{sky}^4 \tag{3.89}$$

$$R_c = \varepsilon_c \sigma T_c^4 + (1 - \varepsilon_c) \left[F_{c-sky} R_{sky} + F_{c-c} R_c \right] \tag{3.90}$$

Adding Equations (3.87) and (3.88) for the sky and the collector surface, the following equation is obtained:

$$\dot{q}_{sky} + \dot{q}_c = 0 \tag{3.91}$$

Substituting Equation (3.91) into Equation (3.87), the heat flux for the sky is obtained:

$$\dot{q}_{sky} = \frac{\sigma \left(T_{sky}^4 - T_c^4 \right)}{\frac{\pi}{2} + \left(\frac{1}{\varepsilon_c} - 1 \right)} \tag{3.92}$$

The heat flux for the area of analysis can be calculated by substituting Equation (3.92) into Equation (3.74). After several simplifications the following expression is obtained:

$$\frac{\dot{q}_{es_i}}{\varepsilon_{es_i}} = \sigma T_{es_i}^4 - \sigma T_{sky}^4 \left[F_{es_i-sky} (\xi_c + 1) + F_{es_i-rs} + F_{es_i-ls} \right] - \sigma T_c^4 F_{es_i-sky} \left[1 - \xi_c \right] \tag{3.93}$$

with

$$\xi_c = \frac{\left(\frac{1}{\varepsilon_c} - 1 \right)}{\frac{\pi}{2} + \left(\frac{1}{\varepsilon_c} - 1 \right)} \tag{3.94}$$

$$F_{es_i-sky} = \frac{1}{2} \sum_{j=1}^{N} F_{1_i-2'_j} \tag{3.95}$$

In this analysis, it is assumed that the collector mirror temperature is approximately the ambient temperature [91]. For the case when the collector surface is not included in the analysis (maximum heat transfer losses by radiation [6]), which means that glass envelope

is assumed to be totally covered by the sky surface, the heat flux for the area of analysis is given by:

$$\dot{q}_{es_i} = \sigma \, \varepsilon_{es_i} \left(T_{es_i}^4 - T_{sky}^4 \right) \qquad (3.96)$$

The last equation is similar to that used in other heat transfer models [8, 13, 21, 41, 92]. The heat transfer loss by radiation on external glass envelope surface per unit length is:

$$\dot{Q}'_{e-e,rad} = \dot{q}_{es_i} \, \pi \, D_{o,e} \qquad (3.97)$$

Several relations have been proposed to relate T_{sky}, for clear skies, to other measured meteorological variables . In the absence of meteorological data such as: relative humidity, dew point temperature, etc, a simple relation given by Swinbank [93] may be used:

$$T_{sky} = 0.0553 \, T_\infty^{1.5} \qquad (3.98)$$

3.2.4   Solar Energy Absorption

In order to calculate the heat transfer losses through the solar receiver, optical efficiency terms and solar radiation absorption are determined. The energy absorbed in the solar receiver is affected by the optical properties and imperfections of the solar collector ensemble. The imperfections in either the reflector or shape of the concentrator are accounted by the intercept factor, γ, which is a fraction of the direct solar radiation reflected by mirrors that does not reach the glass cover [3]. The factors that affect the intercept factor are [6, 13]:

- Heat collection element shadowing (bellows, shielding, supports), γ_1

- Twisting and tracking error, γ_2

- Geometry accuracy of the collector mirrors, γ_3

- Clean mirror reflectivity, ($\rho_{cl} \approx 0.935$ [6])

- Mirror clearness, γ_4

- Dirt on heat collection element, γ_5

- Miscellaneous factors, γ_6

The values for γ_i are shown in Table 3.9. The intercept factor is then defined as:

$$\gamma = \prod_{i=1}^{6} \gamma_i \tag{3.99}$$

Table 3.9 Effective optical efficiency terms. Adapted from [6, 13, 15]

Factor and Optical properties	Value
Luz Black Chrome (γ_1)	0.974
Luz Cermet (γ_1)	0.971
Twisting and tracking error (γ_2)	0.994
Geometry accuracy of the collector mirrors (γ_3)	0.980
Mirror clearness (γ_4)	0.950
Dirt on HCE (γ_5)	0.980
Miscellaneous factor (γ_6)	0.960

For a concentrating collector, the effective optical efficiency is defined as long as the direct beam radiation is normal to the collector aperture area. When the beam radiation is not normal, a factor called incident angle modifier, $K(i)$, is included to account for all optical and geometric losses due to an incident angle greater than 0º [3]. The incident angle

91

modifier, depends on the geometry and the optical characteristics of the solar collector. The incident angle modifier is defined as [94]:

$$K = \frac{\eta_o(i)}{\eta_o(i=0)} \tag{3.100}$$

The incident angle modifier function is defined by:

$$K = \max(0, K(i)) \tag{3.101}$$

The incident angle modifier depends on the geometry and optics of the concentrator. Table 3.10 shows the incident angle modifier function for different solar collectors. These functions were plotted and are shown in Figure 3.15.

Table 3.10 Incident angle modifier for different solar collectors

Solar Collector	Incident Angle Modifier function[1], $K(i)$
LS-2 [39]	$1 + 0.000884 \dfrac{i}{\cos i} - 0.00005369 \dfrac{i^2}{\cos i}$
LS-3 [3]	$1 - 2.2307 \times 10^{-4} i - 1.1 \times 10^{-4} i^2$ $+3.18596 \times 10^{-6} i^3 - 4.85509 \times 10^{-8} i^4$
IST [95]	$1 + 0.0003178 \dfrac{i}{\cos i} - 0.00003985 \dfrac{i^2}{\cos i}$
Euro Trough [16, 96]	$1 - 5.25097 \times 10^{-4} \dfrac{i}{\cos i} - 2.859621 \times 10^{-5} \dfrac{i^2}{\cos i}$

[1] i incident angle in degrees

Another geometric factor is called the collector geometrical end losses, $\psi(i)$. This factor accounts for the fraction of a receiver length which is not illuminated by the rays
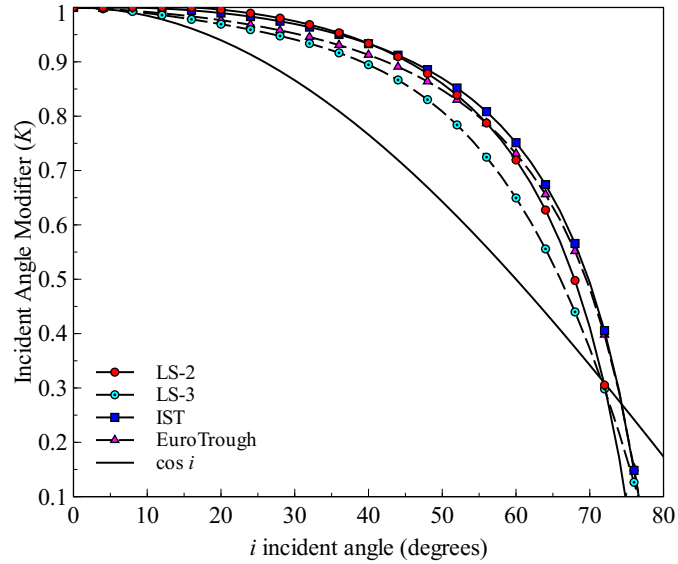
Figure 3.15 Incident angle modifier for different solar collectors. LS-2 [39], LS-3 [3], IST [95] and Euro Trough [16, 96]

incident on the aperture [94, 97]. As it is shown in Figure 3.16, the part of the receiver that

is not illuminated (z) is as follows:

$$z = r \tan i \qquad (3.102)$$

The distance r is shown in Figure 3.17 and is defined by [12]:

$$r = f + \frac{x^2}{4f} \qquad (3.103)$$
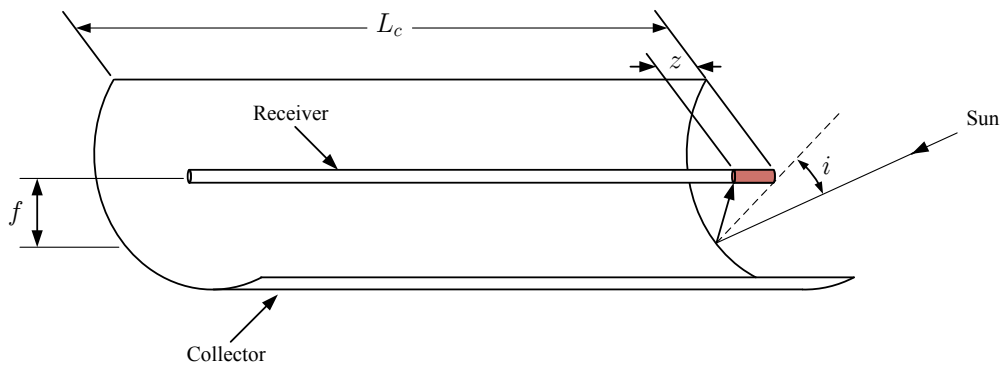
Figure 3.16 Collector geometrical end losses
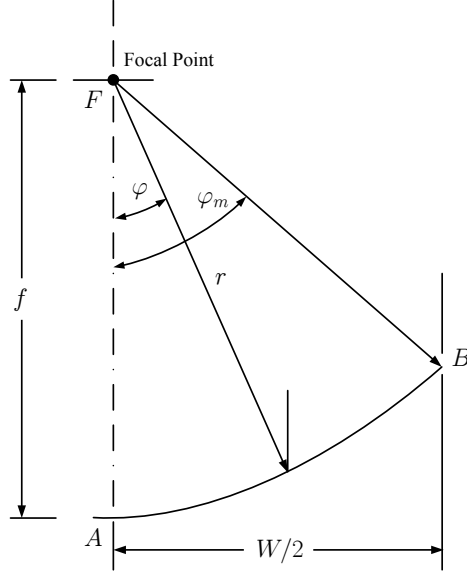
Figure 3.17 Parabola geometry for a rim angle of φ_m. Adapted from [30]

The fraction of the receiver that is illuminated is:

$$\psi(i) = 1 - \frac{r}{L_c} \tan i \tag{3.104}$$

Lippke et al. [5] proposed to take $r = f$. This assumption is widely used in other models [8, 13] and leads to minimum end losses for certain geometric configuration. A previous work developed by Gaul and Rabl [94] suggests the use of an average value of r. This value is used in the present work and is given by:

$$\bar{r} = \frac{1}{w/2} \int_0^{w/2} \left(f + \frac{x^2}{4f} \right) dx = f \left(1 + \frac{w^2}{48 f^2} \right) \tag{3.105}$$

Replacing the value of $\bar{r}$, then, the collector geometrical end loss [94, 97] is:

$$\psi(i) = \max \left(0, \ 1 - \frac{f}{L_c} \left(1 + \frac{w^2}{48 f^2} \right) \tan i \right) \tag{3.106}$$

94

Figure 3.18 compares the end loss factor for the model of Lippke et al. [5] and the model of Gaul and Rabl [94] for two collector geometries. The model of Gaul and Rabl shows lower end loss factor than the model of Lippke, which means that a higher fraction of the receiver is not illuminated.
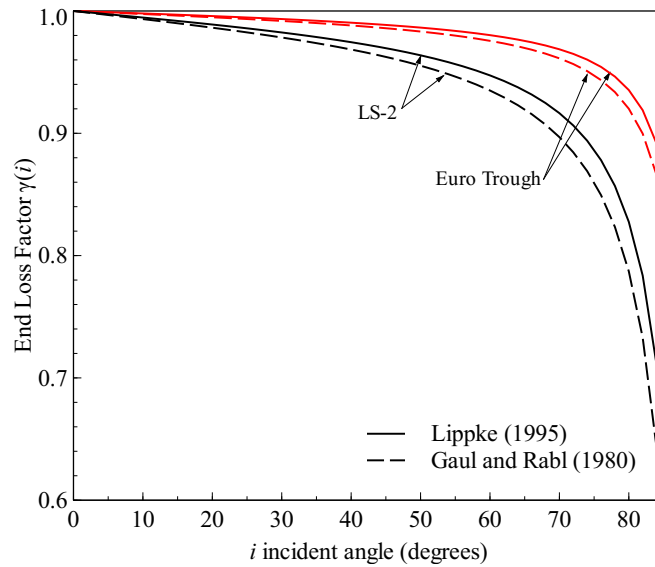
Figure 3.18 End loss factor for different collectors and assumptions. Lippke (1995) [5], Gaul and Rabl (1980) [94]

The peak optical efficiency of the parabolic trough collector is [3]:

$$\eta_o = \rho_{cl} \, \gamma \, (\tau_e \, \alpha_a)_n \qquad (3.107)$$

where τ_e is the envelope transmittance, and α_a is the coating absorptance. Due to re-reflections and subsequent transmissions, a modified value of $(\tau_e \, \alpha_a)_n$ as $1.01 \, (\tau_e \, \alpha_a)_n$ is recommended by Stuetzle [8]. Table 3.11 shows the radiative properties of the heat collection element, and the envelope transmittance, it is assumed that both the envelope transmittance and the coating absorptance are independent of the temperature. In order to account for the effect of temperature on the radiation heat losses through the solar receiver, coat-

ing emittance was approximated by a polynomial function obtained by Forristall [6]. The polynomial coefficients are shown in Table 3.12.

Other important properties for solar radiation losses are the glass envelope absorptance and emissivity. In this models it is assumed that both of these radiative properties are independent of the temperature; the envelope absorptance has a value of $\alpha_e = 0.023$ [100], while the emissivity has an average value of $\varepsilon_e = 0.90$ [100]. Figure 3.19 shows the values

Table 3.11 Radiative properties of different heat collection elements (HCE). Adapted from [6]

Selective Coating	Envelope Transmittance	Coating Absorptance	Coating Emittance	
			100 °C	400 °C
Luz Black Chrome	0.935	0.940	0.110	0.27
Luz Cermet	0.935	0.920	0.060	0.15
Solel UVAC Cermet a	0.965	0.960	0.070	0.13
Solel UVAC Cermet b	0.965	0.950	0.080	0.15
Solel UVAC Avg	0.965	0.955	0.076	0.14
Schott PTR®70 [98]	0.96	0.95	–	0.1

Table 3.12 Coating emittance of different solar receivers. Adapted from [6]

Selective Coating	Coating Emittance [1]
Luz Black Chrome	$5.333 \times 10^{-4} \, (T + 273.15) - 0.0856$
Luz Cermet	$3.27 \times 10^{-4} \, (T + 273.15) - 0.065971$
Solel UVAC Cermet a	$2.249 \times 10^{-7} T^2 + 1.039 \times 10^{-4} T + 0.05599$
Solel UVAC Cermet b	$1.565 \times 10^{-7} T^2 + 1.376 \times 10^{-4} T + 0.06966$
Solel UVAC Avg	$1.907 \times 10^{-7} T^2 + 1.208 \times 10^{-4} T + 0.06282$
Schott PTR®70 [2] [99]	$2.00 \times 10^{-7} T^2 + 0.062$

[1] Temperature in °C

[2] At an absorber temperature of 400 °C the emittance uncertainty was ± 0.005
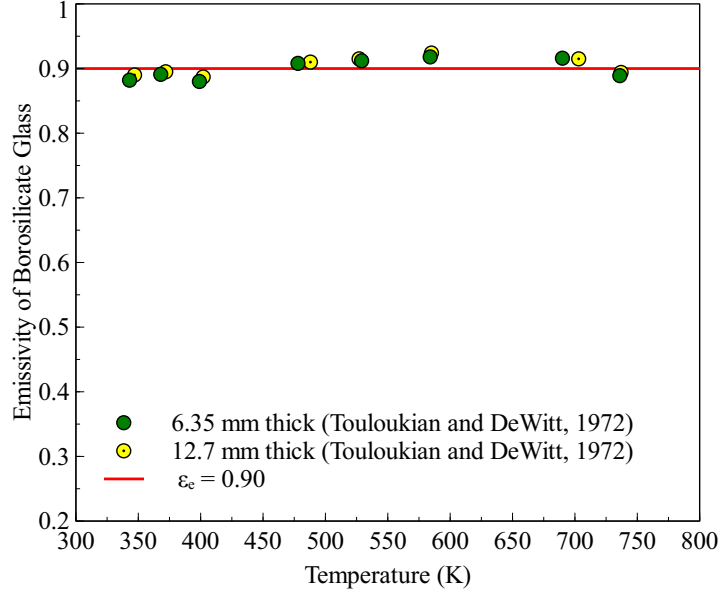
Figure 3.19 Effect of temperature on the emissivity of borosilicate glass for two thicknesses (6.35 and 12.7 mm). Values taken from [100]

of the emissivity for borosilicate glass at different thicknesses. The energy absorbed on the solar receiver and the glass envelope is given by:

$$\dot{Q}_{a-abs} = \eta_o \, K\left(i\right) \varphi\left(i\right) SH \, I'_{bn} \tag{3.108}$$

and

$$\dot{Q}_{e-abs} = \rho_{cl} \, \gamma \, \alpha_e \, K\left(i\right) \varphi_{SH} \, \varphi\left(i\right) I'_{bn} \tag{3.109}$$

where φ_{SH} is the shading factor, with $\varphi_{SH} = 0$ for the collector aperture area totally shaded.

3.3 Numerical Solution

The partial differential equations (PDE) were discretized for steady state conditions by using the finite difference method and taking into account the dependence of the thermal

properties on the temperature [101]. For the heat transfer fluid, the discretization by using backward difference gave the following algebraic equation:

$$\gamma_{i-1} T_{f,i-1} - \beta_i T_{f,i} + \tau_i = 0 \qquad i = 1, 2, \ldots N \qquad (3.110)$$

with

$$\gamma_{i-1} = \frac{\dot{m}_f}{\Delta z} C_{p,f,i-1}$$

$$\beta_i = \frac{\dot{m}_f}{\Delta z} C_{p,f,i} + \pi N u_{f,i} k_{f,i}$$

$$\tau_i = \frac{\dot{m}_f}{\Delta z} \left[\left(\frac{V_f^2}{2} \right)_{i-1} - \left(\frac{V_f^2}{2} \right)_i \right] + \pi N u_{f,i} k_{f,i} T_{a,i}$$

Boundary nodes:

$$i = 0, \ T_{f,0} = T_e \qquad (3.111)$$

For the absorber, the discretization was carried out by using central difference. The algebraic equation obtained was as follows:

$$\alpha_i T_{a,i-1} - \alpha_i^+ T_{a,i} + \alpha_i' T_{a,i+1} + \lambda_{q,i} = 0 \qquad i = 1, 2, \ldots N \qquad (3.112)$$

with

$$\alpha_i = A_a \frac{k_{a,i}}{\Delta z^2}$$

$$\alpha_i' = A_a \frac{k_{a,i+1}}{\Delta z^2}$$

$$\alpha_i^+ = \alpha_i + \alpha_i'$$

98

$$\lambda_{q,i} = \left(\sum_j \dot{Q}'_{a,j} \right)_i$$

$$\sum_j \dot{Q}'_{a,j} = \dot{Q}'_{a,abs} - \dot{Q}'_{a-f,conv} - \dot{Q}'_{a-e,conv} - \dot{Q}'_{a-e,rad} - \dot{Q}'_{cond,bracket}$$

Boundary nodes:

$$i = 1, \quad T_{a,0} = T_{a,1} \tag{3.113}$$

$$i = N, \quad T_{a,N+1} = T_{a,N} \tag{3.114}$$

For the envelope, using central difference, it was obtained that:

$$\Gamma_i T_{a,i-1} - \Gamma_i^+ T_{a.i} + \Gamma_i' T_{a,i+1} + \Delta_{q,i} = 0 \qquad i = 1, 2, \ldots N \tag{3.115}$$

with

$$\Gamma_i = A_e \frac{k_{e,i}}{\Delta z^2}$$

$$\Gamma_i' = A_e \frac{k_{e,i+1}}{\Delta z^2}$$

$$\Gamma_i^+ = \Gamma_i + \Gamma_i'$$

$$\Delta_{q,i} = \left(\sum_j \dot{Q}'_{e,j} \right)_i$$

$$\sum_j \dot{Q}'_{e,j} = \dot{Q}_{e,abs} + \dot{Q}_{a-e,conv} + \dot{Q}_{a-e,rad'} - \dot{Q}_{e-sa,conv} - \dot{Q}_{e-s,rad}$$

Boundary nodes:

$$i = 1, \quad T_{e,0} = T_{e,1} \tag{3.116}$$

$$i = N, \quad T_{e,N+1} = T_{e,N} \tag{3.117}$$

The nonlinear algebraic equations were written in Python 2.6 [34] and solved simultaneously by using a wrapper around MINPACK's "hybrd" and "hybrj" algorithms [102]. The collector efficiency and thermal losses are calculated as follows:

$$\eta_c = \frac{\dot{m}\left(h_{o,f} - h_{i,f}\right)}{I_b A_{ap}} \tag{3.118}$$

$$\text{Thermal Loss} = \left[\sum_i \left(\dot{Q}'_{a-e,conv}\right)_i + \sum_i \left(\dot{Q}'_{a-e,rad}\right)_i + \sum_j \left(\dot{Q}'_{cond,bracket}\right)_j\right] \frac{\Delta z}{I_b A_{ap}} \tag{3.119}$$

3.4 Model Validation

In order to validate the heat transfer model, it was compared with experimental data obtained from Sandia National Laboratories (SNL) [39]. In addition, to corroborate the improvement in the correlations and radiation analysis proposed in this chapter, the numerical model was also compared with the other solar receiver heat transfer models [6, 41]. The experimental results were for a solar collector assembly (LS-2) module placed at the AZTRAK rotating platform at the SNL. Due to limitations in the experimental set up, a 2 inch diameter flow restriction device (solid plug) was centered in the inside diameter of the absorber tube. Two different selective coatings were used in this test: black chrome and cermet. Cermet has better radiative properties (low emissivity) at high temperatures than black chrome, and does not oxidize if the vacuum is lost [39]. The Sandia test was performed for both full sun and no sun condition and different scenarios for the annulus of the heat collection element (HCE) : vacuum intact (the evacuated annulus pressure was 10^{-4} Torr), lost vacuum (annulus filled with ambient air), and glass cover completely removed (bare tube). The three previous conditions were tested with the cermet coating but broken annulus was not included for the black chrome coating case. All the conditions and

Table 3.13 Specifications for a SEGS LS-2 parabolic trough solar collector test. Data taken from [39]

Module Size	7.8×5 m
Rim angle	$70°$
Reflectors	12 thermally sagged panels Second surface silvered Low iron glass ($\varepsilon_c = 0.86$ [103])
Aperture Area	39.2 m^2
Focal Length	1.84 m
Concentration Ratio	71
Receiver (HCE)	Evacuated tube design, metal bellows at each end Absorber diameter: 70 mm Length: 4 m (2 per module at Sandia) Pyrex glass envelope : 115 mm diameter Selective coating: Cermet and Black chrome $i = 0$, $K(i) = 1$, $\varphi(i) = 1$
Conditions of HCE Annulus	Vacuum intact (the evacuated annulus pressure was 10^{-4} Torr) Lost vacuum (annulus filled with ambient air) Glass cover completely removed (bare tube)
Atmospheric Air Pressure	0.83 atm
Heat Transfer Fluid	Syltherm 800

specifications used in the experimental test are summarized in Table 3.13. A silicone heat transfer fluid (Syltherm 800) was used in the experimental set up. The properties for this working fluid were fitted to the experimental data from [104] and a polynomial regression was obtained for each property. The equations used for this fitting were:

$$C_{p,s800} = \sum_{n=0}^{3} C_{p,n} T^n \tag{3.120}$$

$$\rho_{s800} = \sum_{n=0}^{3} \rho_n T^n \tag{3.121}$$

$$k_{s800} = \sum_{n=0}^{3} k_n T^n \qquad (3.122)$$

The coefficient obtained by the polynomial regression are shown in Table 3.14.

Table 3.14 Coefficients obtained by polynomial regression of thermal properties of Syltherm 800. Experimental data taken from [104]

Property	Coefficients, n				R^2
	0	1	2	3	
$C_{p,n}$	1.574	1.707E-03	0.000	0.000	0.99
ρ_n	953.164	-0.916	4.211E-04	-1.670E-06	0.99
k_n	0.138	-1.880E-04	0.000	0.000	0.99

All the results in this chapter were obtained by dividing the solar receiver into 12 segments, $\Delta x = 2/3$ m. This number of segments was selected according to a grid-independent solution analysis. Figure 3.20 shows the results obtained for different collector segments
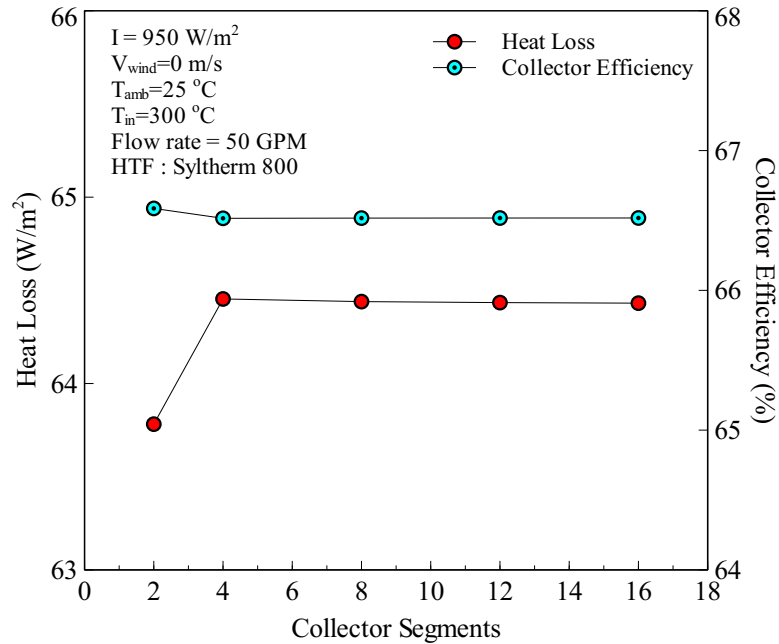
Figure 3.20 Grid independent analysis for different collector segments, case: air in the annulus

with cermet coating as selective coating and air in the annulus. The results show that 12 elements are suitable for validation of the proposed heat transfer analysis.

3.5   Results and Discussion

The results obtained for the collector efficiency and thermal losses are shown in Figures 3.21-3.23. For the collector efficiency (Figure 3.21), the model follows the trends of the experimental values and all the results are always inside the experimental error bars. As it was expected, the higher efficiencies are obtained when the annulus is under vacuum, but in both cases (air and vacuum) at high temperatures the collector efficiency drops gradually, which is more notable for the black chrome coating as it is shown in Figure 3.21(b). This is explained by the radiative properties of black chrome coating at high temperatures. For the case of cermet coating, Figure 3.21(a), the model developed by Garcia-Valladares and Velásquez [41] shows some discrepancies at low temperatures in the collector efficiency due to their assumptions : negligible conduction at the ends of each trough and only radiation heat losses take place between the receiver and the glass envelope for the case of vacuum in the annular space (refer to [41] for more details). Those assumptions were not made in the current model or NREL model. The proposed model and NREL model [6] seem to obtain similar collector efficiencies values, but a detailed root mean square error calculation (Table 3.15 and 3.16) shows that the proposed model achieved an improvement as compared with the NREL and Garcia-Valladares and Velásquez models. The only case without improvement was for black chrome coating with air in the annulus (RMSE of 0.855 % and 0.808 % for the proposed model and NREL model respectively), where there is not much difference between the proposed and the NREL models.
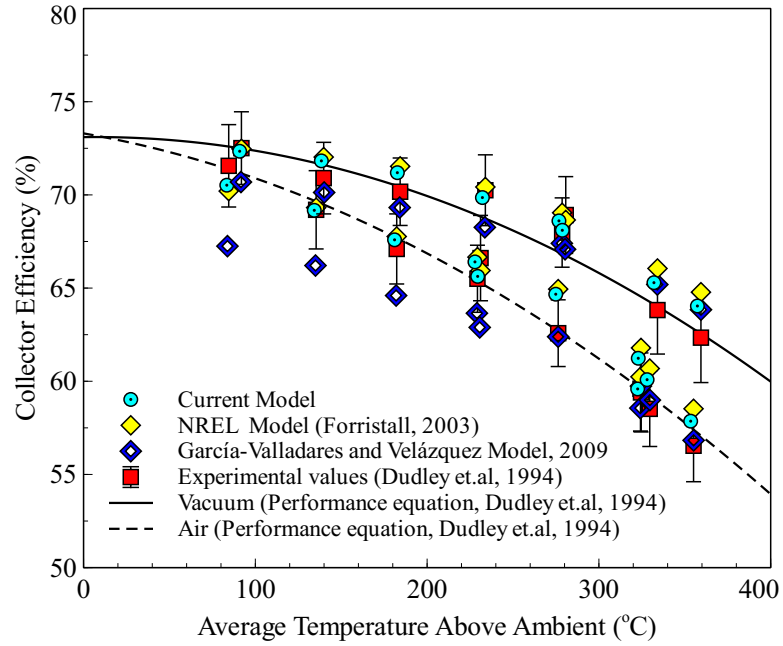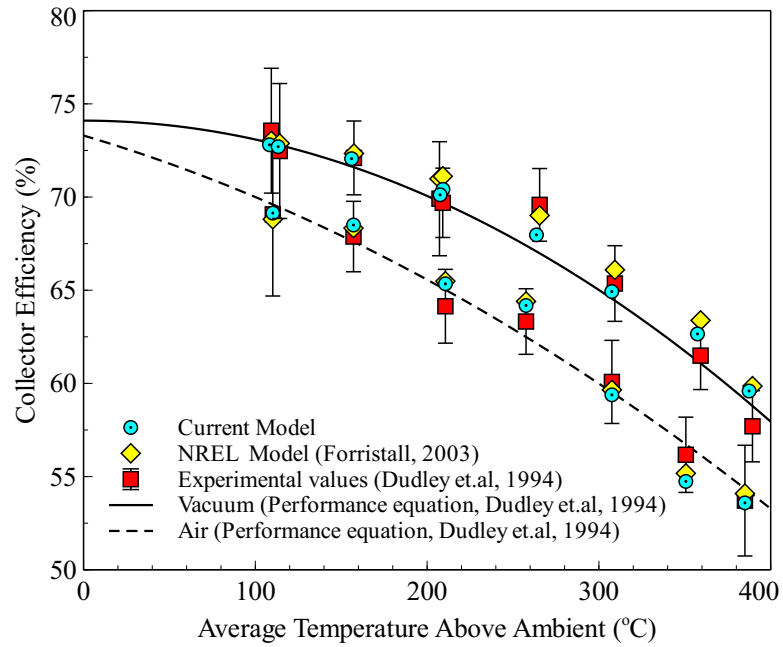
Figure 3.21 Comparison of collector efficiency calculated from the proposed model with experimental data [39] and other solar receiver models [6, 41]
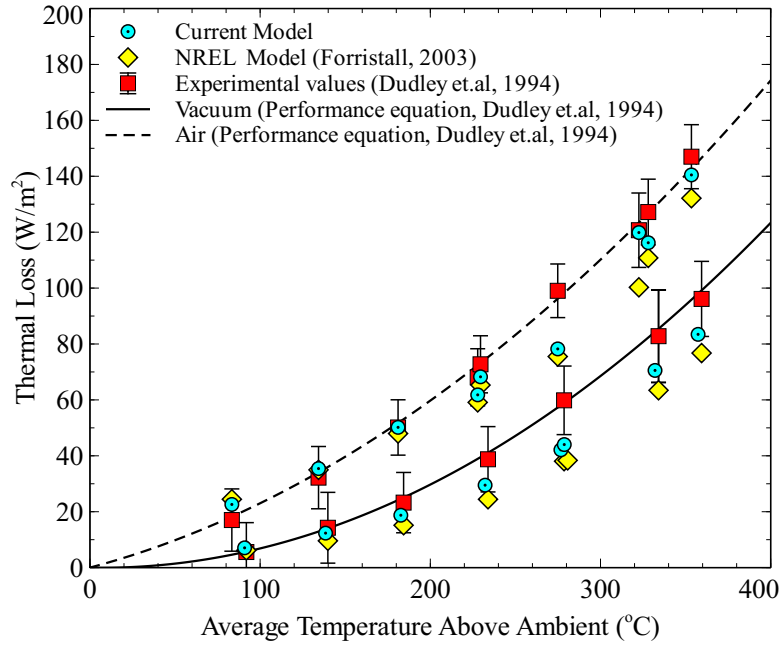
(a) Cermet coating
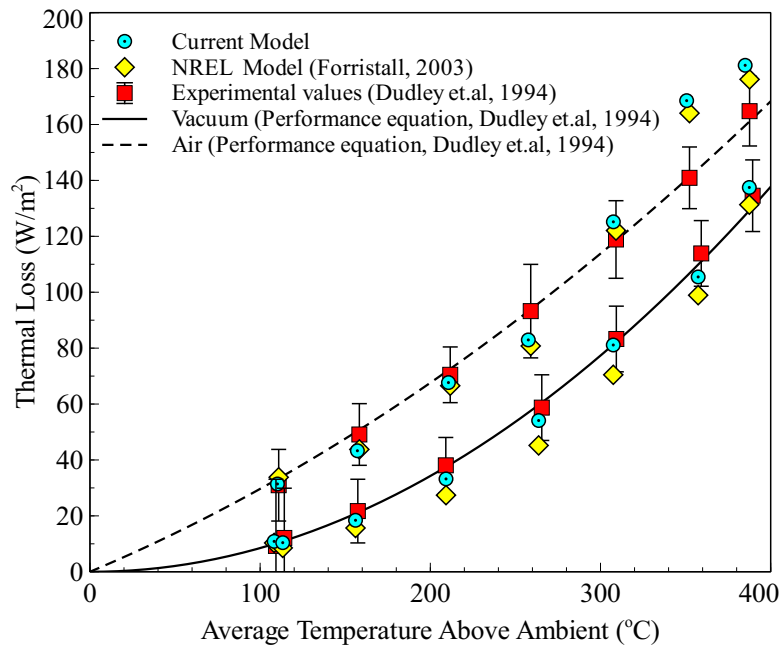
(b) Black chrome coating

Figure 3.22 Comparison of thermal losses calculated from the proposed model with experimental data [39] and other solar receiver models [6, 41], on-sun case
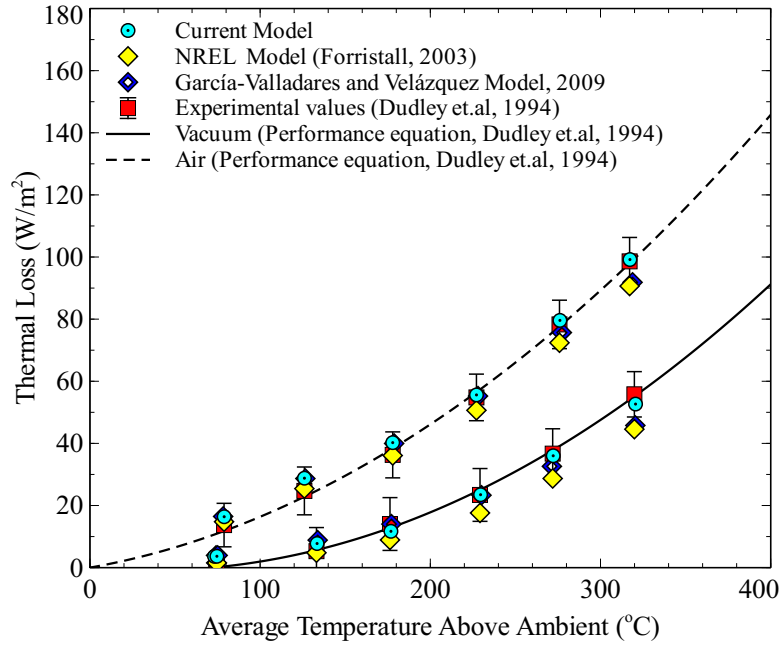
(a) Cermet coating
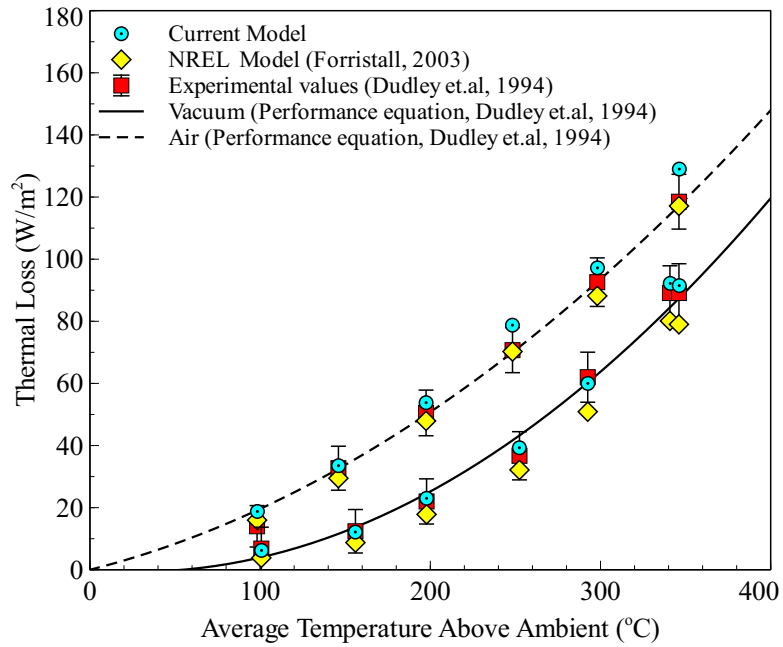
(b) Black chrome coating

Figure 3.23 Comparison of thermal losses calculated from the proposed model with experimental data [39] and other solar receiver models [6, 41], off-sun case

Table 3.15 Comparison of root mean square error (RMSE) between the proposed heat transfer model and other numerical models for the cermet coating case. Experimental data taken from [39], NREL model [6], García-Valladares and Velázquez Model [41]

Model	RMSE	
	η_c (%)	Heat Losses (W/m^2)
Vacuum (Sun)		
Current model	1.012	10.255
NREL model	1.382	14.718
García-Valladares and Velázquez Model	1.433	—
Vacuum (Off Sun)		
Current model	—	2.414
NREL model	—	6.004
García-Valladares and Velázquez Model	—	4.671
Air (Sun)		
Current model	1.225	8.959
NREL model	1.562	13.594
García-Valladares and Velázquez Model	2.292	—
Air (Off Sun)		
Current model	—	2.651
NREL model	—	4.416
García-Valladares and Velázquez Model	—	3.865

Figures 3.22 and 3.23 show the thermal losses calculated for the different models and compared with the experimental values. As in the case of collector efficiency, the thermal losses also showed a good agreement with the experimental results and most of the values are inside the experimental error bars. The RMSE analysis shows that the proposed model gave thermal loss values closest to the experimental results as compared to those obtained from the NREL and Garcia-Valladares and Velásquez models. The only excep-

Table 3.16 Comparison of root mean square error (RMSE) between the proposed heat transfer model and other numerical models for the black chrome coating case. Experimental data taken from [39], NREL model [6]

Model	RMSE	
	η_c (%)	Heat Losses (W/m^2)
Vacuum (Sun)		
Current model	0.926	4.260
NREL model	1.191	9.650
Vacuum (Off Sun)		
Current model	—	1.978
NREL model	—	7.230
Air (Sun)		
Current model	0.855	13.196
NREL model	0.808	11.225
Air (Off Sun)		
Current model	—	4.714
NREL model	—	2.667

tion was again for the black chrome coating, for which the NREL model achieved better RMSE (11.225 W/m^2 and 2.667 W/m^2 for on-sun and off-sun case respectively, air in the annulus scenario) than the proposed model (13.196 W/m^2 and 4.714. W/m^2 for the current model respectively). In this case our model shows higher heat losses at temperatures above ambient of 350 °C or higher. It is difficult to say which model is more accurate, although we feel our model is more conservative.

The third scenario, with the glass envelope removed (bare tube) and the surrounding air in direct contact with the absorber tube, leads to highest thermal losses as expected. This scenario is possible in the solar power plants during regular operation when the glass tube

gets broken. The heat transfer analysis for this scenario quantifies how much the collector efficiency is degraded. For this case, wind speed takes an important role in the thermal losses and therefore in the collector efficiency as well. Naeeni and Yaghoubi [105, 106] analyzed the wind flow and thermal field around the receiver tube. They concluded that the local Nusselt distribution around the receiver tube is different from the cross flow condition. Given that in the proposed model, the convective heat losses were calculated for a cylinder in cross flow, it can be concluded that for forced convection ($V_{wind} > 0$) , the model will overpredict thermal losses and underpredict collector efficiency. This can be seen in Figure 3.24 ($\varsigma = 1$). Forristall [6] recommended to include in his model half of the convective losses ($\varsigma = 0.5$) to reduce the overestimation of thermal losses by convection. In this paper, after a fitting analysis, it was found that a reduction of 41.8 % in heat convection losses ($\varsigma = 0.582$) leads to good results. Figure 3.24 compares the results obtained for different heat convection factors. In order to compare the different heat convection factors, RMSE was calculated for each factor. The results obtained are shown in Table 3.17; the lowest RMSE was obtained for the factor proposed in this study, $\varsigma = 0.582$.

Table 3.17 Comparison of root mean square error (RMSE) for different heat loss convection factors

ς		Heat Loss (W/m^2)	η_c (%)
1.0	Regular model	91.62	13.12
0.5	Recommended by Forristall [6]	32.75	5.78
0.582	Proposed model	27.80	3.92
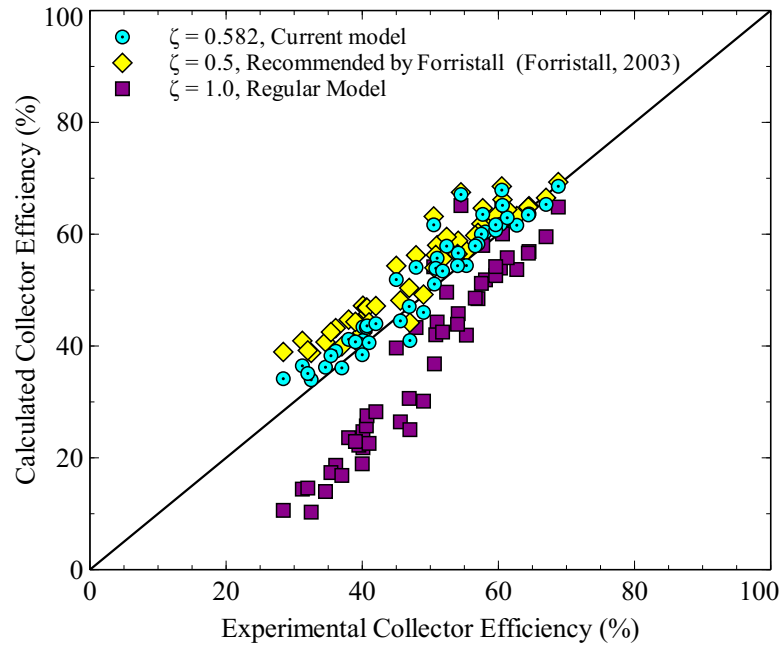
(a) Collector efficiency
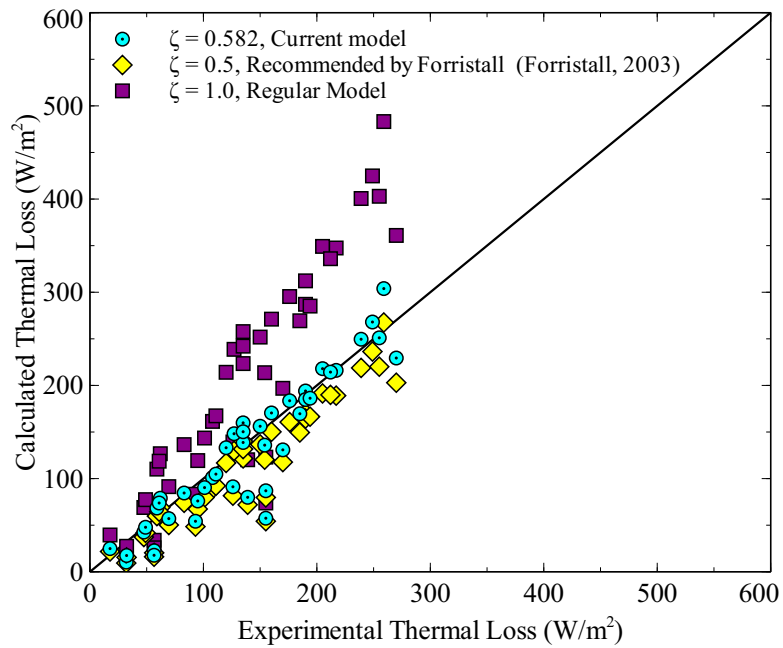
(b) Thermal loss

Figure 3.24 Comparison of theoretical and experimental [39] collector efficiency and thermal losses obtained for different heat convection loss factors

110

3.6 Non-Linear Regression Heat Loss Model

The proposed equation for the heat losses model is as follow:

$$\dot{Q}_{HL} \quad (\text{W/m}) = \quad \psi_o + \psi_1 \left(T_f - T_\infty\right) + \psi_2 T_f^2 + \psi_3 T_f^3$$

$$+ I_{bn} K \cos i \left[\psi_4 + \psi_5 T_f^2\right] + V_{wind}^n \left[\psi_6 + \psi_7 \left(T_f - T_\infty\right)\right] \quad (3.123)$$

with

$$T_f = \frac{T_{f,i} + T_{f,o}}{2} \quad\quad\quad\quad (3.124)$$

This equation is based on the correlation proposed by Price [11], although slight modifications were introduced in the original equation. The conditions and parameters used for the heat losses calculation are presented in Table 3.18.

Table 3.18 Specifications used for the heat loss model

Solar Collectors	LS-2 and LS-3
Inlet Temperature ($^\circ C$)	50, 100,150,…400
Beam Radiation (W/m^2)	0, 250, 500, 750, 1000
Ambient Temperature ($^\circ C$)	15, 30, 45
Receiver (HCE)	Selective coating: Universal Vacuum Air Collector (UVAC) [6] $i = 0^\circ$, 15°, 30°, 45°, 60°, 75°, 90° $SH = 1$
Conditions of HCE Annulus	Vacuum intact (the evacuated annulus pressure was 10^{-4} Torr) Lost vacuum (annulus filled with ambient air)
Atmospheric Air Pressure	1 atm
Heat Transfer Fluid	VP-1
Mass Flor rate (kg/s)	8

Table 3.19 Heat loss correlation coefficients

Coefficients	LS-2		LS-3	
	Vacuum	Air	Vacuum	Air
ψ_o	1.868	-2.720	1.930	-3.229
ψ_1	2.515×10^{-1}	1.028	2.498×10^{-1}	1.033
ψ_2	-1.080×10^{-3}	-1.165×10^{-3}	-1.097×10^{-3}	-1.201×10^{-3}
ψ_3	6.639×10^{-6}	6.700×10^{-6}	6.671×10^{-6}	6.747×10^{-6}
ψ_4	1.771×10^{-4}	-3.541×10^{-3}	8.556×10^{-5}	-4.596×10^{-3}
ψ_5	4.398×10^{-8}	1.771×10^{-8}	5.569×10^{-8}	2.784×10^{-8}
ψ_6	-8.087×10^{-1}	-3.686	-8.401×10^{-1}	-3.503
ψ_7	3.543×10^{-2}	1.605×10^{-1}	3.555×10^{-2}	1.603×10^{-1}
n	3.598×10^{-1}	3.536×10^{-1}	3.537×10^{-1}	3.533×10^{-1}
R^2	0.9998	0.9996	0.9998	0.9996
RMSE	1.64	4.00	1.69	4.01

The correlation coefficients for different conditions in the receiver annulus are shown in Table 3.19. Table 3.19 also shows the coefficient of determination, R^2, which is a measure of how well the heat losses can be predicted by the proposed correlation, and the root mean square error (RMSE). The results show that the proposed fitting Equation 3.123 predicts the heat losses for LS-2 and LS-3 solar collectors very accurate. This is corroborated in Figure3.25 by plotting the heat losses obtained from the non-linear regression and the proposed model.

3.7 Conclusions

A comprehensive heat transfer model for thermal analysis of parabolic trough solar receivers was developed. The proposed model included a detailed radiative heat transfer analysis and more accurate heat transfer correlations. The results obtained showed good agreement with experimental data and in comparison with other heat transfer models, the proposed model presented in general lower RMSE values and better performance, espe-
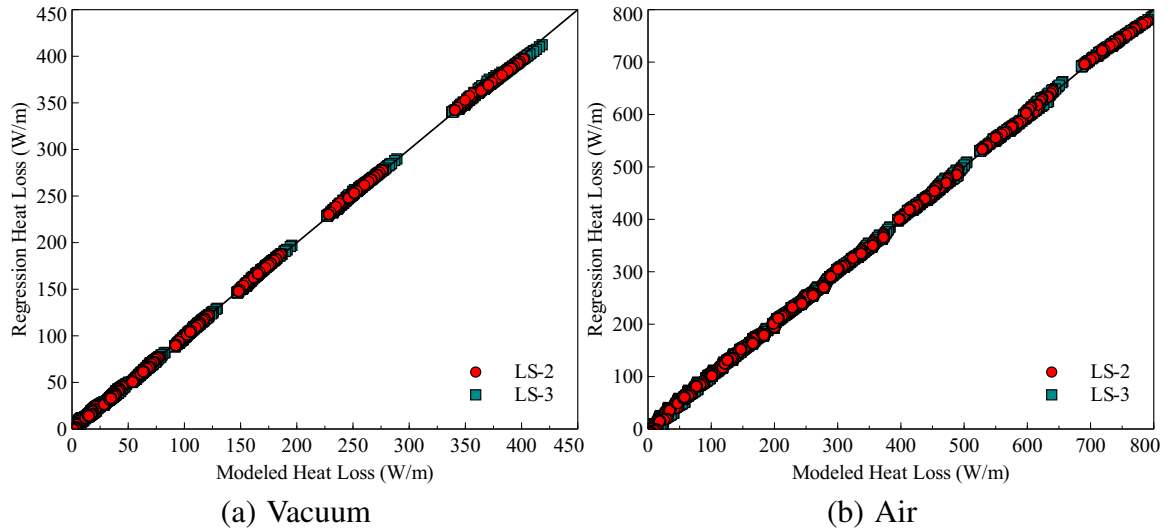
Figure 3.25 Comparison of heat losses obtained from the non-linear correlation (Equation 3.123) and the proposed model

cially for the heat transfer losses. For the case of bare tube (glass envelope broken), it was found that a factor of 0.418 in convective heat losses leads to improvement in the performance of the heat transfer model. Based on the results obtained, it is concluded that this model is suitable for the calculation of heat losses and collector efficiency under different flow, selective coating and operating conditions.

A non-linear regression model was obtained for LS-2 and LS-3 solar collectors. This model is very useful for predicting the heat losses in a solar collector under different radiation and meteorological conditions without using the proposed comprehensive model.

<center>Chapter 4</center>

<center>**Power Block**</center>

4.1 Introduction

The power block commonly used in concentrating solar thermal power plants is a Regenerative Rankine Cycle [13, 16]. The thermodynamic cycle is shown in Figure 4.1. The heat transfer fluid (HTF) passes through three heat exchangers (simplified model): superheater, boiler and preheater. In the preheater, which is normally a shell and tube type heat exchanger, compressed water coming from closed feedwater heater (CF-1) is heated up until saturated liquid condition is reached. Then, the saturated liquid flows through the boiler where a change of phase from liquid to vapor occurs. The boiler (steam generator) is a shell-and-tube heat exchanger with the HTF entering the tube side and liquid feedwater flowing through the shell side. After the boiler, the saturated vapor goes to the superheater where additional energy is added to the steam, bringing it to a superheated vapor condition. This heat exchanger is a shell-and-tube type as well. The superheated steam (10) is expanded through the high pressure turbine.

Two extractions, 11 and 12, are taken from the high pressure turbine to the closed feedwaters (CF-1, CF-2). Closed feedwater heaters are shell-and-tube-type recuperators [52], which are used to increase the feedwater temperature through condensation of the extracted steam.

<center>114</center>
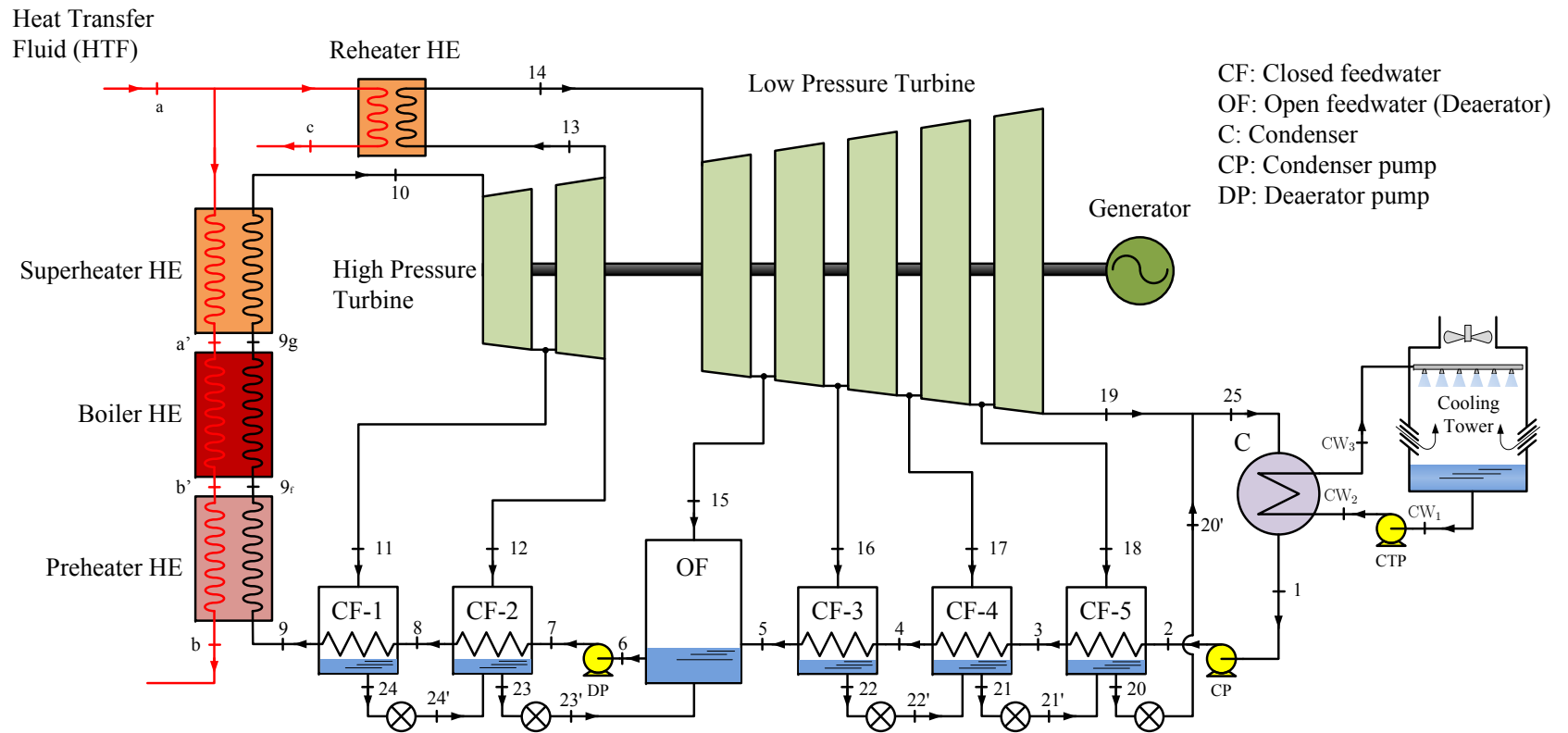
Figure 4.1 Regenerative Rankine cycle configuration

The thermal efficiency of the cycle is increased by including closed feedwaters, but the optimum number of heaters is based on economical optimization, and for this case an optimum of five heaters is recommended [107, 108]. The remaining steam (13) is reheated; the reheat is used to allow higher boiler pressures without low-quality steam problems at the turbine exhaust pressure and therefore an increase in the overall thermal efficiency of the cycle is achieved. The reheated steam (14) is then expanded into the low pressure turbine; four extractions, (15)-(18), are bled to the closed feedwaters (CF-3, CF-4, CF-5) and an open feedwater (OF). Open feedwaters are a direct contact-type heat exchanger [52] in which streams at different temperatures are mixed to form a stream at an intermediate temperature at saturated liquid condition (6).Open feedwaters are also used for removing air and other dissolved gases which can cause corrosion problem or decrease the performance of the cycle. The exhaust turbine stream (19) is mixed with the feedwater coming from the trap in the closed feedwater 5 (CF-5). A trap is a valve that permits only liquid to pass through to a region of lower pressure [52]. The mixture goes to the condenser, a shell-and-tube heat exchanger, where a change of phase from mixture to saturated liquid takes places. The feedwater (1) leaving the condenser (Saturated liquid condition) is pumped to the open feedwater pressure though the condenser pump. The feedwater is preheated by the closed feedwaters (CF3, CF4 and CF5) until it reaches the open feedwater (5). Saturated liquid at the exit of the open feedwater (6) is pumped at boiler pressure and preheated by closed feedwaters (CF1 and CF2) and finally returns to the preheater (9).

Initially, mass and energy balance, under steady state conditions, was carried out in each component of the cycle and mass flow rate, temperature and pressure were obtained

for each stream. The thermodynamic cycle was then modeled for partial load conditions. These partial load conditions are present throughout the day due to the intermittent energy absorbed by the solar field. These conditions affect the temperature and mass flow rate of the HTF entering the power block. The mass flow rate is varied for the cases in which the HTF temperature is held constant. For partial load conditions in heat exchangers the approximation developed by Patnode [13] was used:

$$\frac{UA}{UA_{ref}} = \left(\frac{\dot{m}_o}{\dot{m}_{o,ref}} \right)^{0.8} \tag{4.1}$$

where UA and UA_{ref} are the product of the overall heat transfer coefficient, U, and the heat transfer area, A, for the current and reference conditions respectively, and $\dot{m}_o$ and $\dot{m}_{o,ref}$ are the mass flow rates of the outer fluid in the heat exchanger for the current and reference conditions respectively. This approach is based on Colburn equation for fluids with constants properties and it assumes that the mass flow rates of the inner and outer fluids remain in the same proportion at partial load conditions as at the reference load.

$$\frac{\dot{m}_i}{\dot{m}_o} = \frac{\dot{m}_{i,ref}}{\dot{m}_{o,ref}} \tag{4.2}$$

The thermodynamic properties of water and steam were implemented in Python 2.6 [34] by using the international-standard IAPWS-IF97 steam tables [109]. The analysis for each component of the cycle is developed below. For all the heat exchangers it is assumed that:

- The heat exchangers operate under steady state and steady flow conditions

- Heat transfer losses to the ambient are negligible

- There is no heat generation in the heat exchangers

- Pressure drop is negligible

4.2 Reheater and Superheater

Superheater and reheater increase the temperature of the saturated or near saturated steam in order to increase the thermodynamic efficiency of the Rankine cycle [110]. They are shell-and-tube heat exchangers whose main difference is the operating pressure. In the superheater, thermal energy is added to the steam coming from the boiler to bring it to superheated conditions. For the reheater, steam coming from the high pressure turbine exit is reheated to avoid problems with the steam quality leaving the low pressure turbine and increase the overall efficiency of the Rankine cycle. The following assumptions are made for the superheater and reheater heat exchangers:

- The steam entering the superheater (stream 9_g) is at saturated vapor conditions

- The temperature of the stream leaving the superheater is given by: $T_{10} = T_a - \Delta T_{pinch}$ (Figure 4.2)

- The temperature of the stream leaving from the reheater is : $T_{14} = T_a - \Delta T_{pinch}$

Figure 4.3 shows a schematic of the reheater and superheater. The heat transfer fluid (HTF) coming from the solar field heats up the steam leaving the boiler (superheater) or high pressure turbine (reheater). Counterflow arrangement, (one-shell pass and one-tube pass) is assumed and the effectiveness–NTU method is used for all the heat exchangers.

118
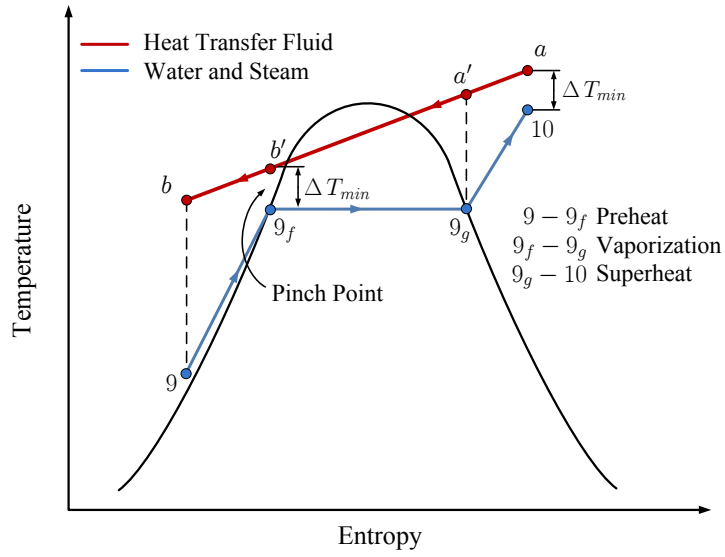
Figure 4.2 Steam generation process

This method is based on a dimensionless parameter called the heat transfer effectiveness ,

defined as [111]:

$$\varepsilon = \frac{\dot{Q}}{\dot{Q}_{max}} = \frac{\text{Actual heat transfer rate}}{\text{Maximum posible heat transfer rate}} \quad (4.3)$$
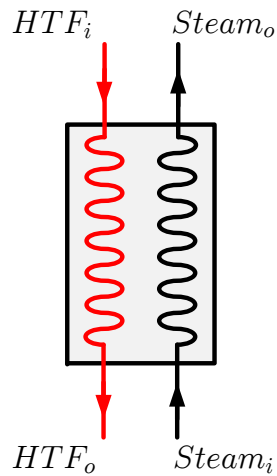
Figure 4.3 Reheater and superheater heat exchanger

The actual heat transfer rate can be determined from the energy balance on the hot (HTF) and cold (steam) fluids as follows:

$$\dot{Q} = C_{HTF} \left(T_{HTF_i} - T_{HTF_o} \right) \tag{4.4}$$

$$\dot{Q} = C_{Steam} \left(T_{Steam_o} - T_{Steam_i} \right) \tag{4.5}$$

with the heat capacity rates defined as:

$$C_{HTF} = \frac{\dot{m}_{HTF} \left(h_{HTF_i} - h_{HTF_o} \right)}{T_{HTF_i} - T_{HTF_o}} \tag{4.6}$$

$$C_{Steam} = \frac{\dot{m}_{Steam} \left(h_{Steam_o} - h_{Steam_i} \right)}{T_{Steam_o} - T_{Steam_i}} \tag{4.7}$$

where $\dot{m}_{HTF}$ is the mass flow rate of the heat transfer fluid, and $\dot{m}_{Steam}$ is the mass flow rate of the steam. The mass balance for this feedwater heater is:

$$\dot{m}_{HTF_o} = \dot{m}_{HTF_i} \tag{4.8}$$

$$\dot{m}_{Steam_o} = \dot{m}_{Steam_i} \tag{4.9}$$

The maximum temperature difference in a heat exchanger is the difference between the inlet temperatures of the heat transfer fluid (hot) and the inlet steam (cold).

$$\Delta T_{max} = T_{HTF_i} - T_{Steam,i} \tag{4.10}$$

The maximum heat transfer rate in a heat exchanger is reached when the steam is heated to the inlet temperature of the hot fluid or the HTF is cooled to the inlet temperature of the steam. These two limiting conditions will not be reached simultaneously unless the heat capacity rates of the HTF and steam are identical ($C_{HTF} = C_{Steam}$) [111]. The fluid with

120

the smaller heat capacity rate will reach the larger temperature difference, therefore, the maximum possible heat transfer rate in a heat exchanger is given by:

$$\dot{Q}_{max} = C_{min} \left(T_{HTF_i} - T_{Steam,i} \right) \tag{4.11}$$

and

$$C_{min} = \min \left(C_{HTF}, C_{Steam} \right) \tag{4.12}$$

Then, once the effectiveness of the heat exchanger is known, the actual rate of heat transfer is as follows:

$$\dot{Q} = \varepsilon \, C_{min} \left(T_{HTF_i} - T_{Steam,i} \right) \tag{4.13}$$

The effectiveness of a heat exchanger depends on the geometry of the heat exchanger as well as the flow arrangement [111]. Two parameters typically involved in the effectiveness relation of a heat exchanger are:

$$\varepsilon = f \left(\frac{UA}{C_{min}}, \frac{C_{min}}{C_{max}} \right) \tag{4.14}$$

where UA/C_{min}, also known as the number of transfer units NTU, is a measure of the heat transfer surface area A, and C_{min}/C_{max} is the dimensionless capacity ratio, c. For a counterflow arrangement (one-shell pass and one-tube pass) the effectiveness is as follows [111]:

$$\varepsilon = \frac{1 - \exp\left[-NTU \left(1 - c \right) \right]}{1 - c \, \exp\left[-NTU \left(1 - c \right) \right]} \tag{4.15}$$

A special case it is presented when $c = 1$, for this case the effectiveness is simplified as [56]:

$$\varepsilon = \frac{NTU}{1 + NTU} \tag{4.16}$$

The effectiveness can be also expressed in terms of the maximum heat transfer rate:

$$\varepsilon = \frac{C_{HTF} \left(T_{HTF_i} - T_{HTF_o} \right)}{C_{min} \left(T_{HTF_i} - T_{Steam,i} \right)} \tag{4.17}$$

or

$$\varepsilon = \frac{C_{Steam} \left(T_{Steam_o} - T_{Steam_i} \right)}{C_{min} \left(T_{HTF_i} - T_{Steam,i} \right)} \tag{4.18}$$

At partial load conditions the product of the overall heat transfer coefficient, U, and the heat transfer area, A, is given by [112]:

$$UA' = UA \left(\frac{\dot{m}'_{HTF_i}}{\dot{m}_{HTF_i}} \right)^{0.8} \tag{4.19}$$

where UA' is the new product of the overall heat transfer coefficient and the heat transfer area calculated at the new mass flow rate $\dot{m}'_{HTF_i}$.

4.3 Boiler

The boiler is a heat exchanger in which the feedwater changes phase from liquid to vapor at constant temperature and pressure [111]. The boiler (Figure 4.4) is shell-and-tube type heat exchanger with the HTF entering the tube side and liquid feedwater flowing through the shell side. The following assumptions are made to the analysis of the boiler heat exchanger:

- The feedwater stream entering the boiler (stream 9_f) is at saturated liquid conditions

- The temperature of the HTF stream leaving the boiler is given by: $T_{b'} = T_{sat \; @ T = T_9} + \Delta T_{pinch}$ (Figure 4.2)
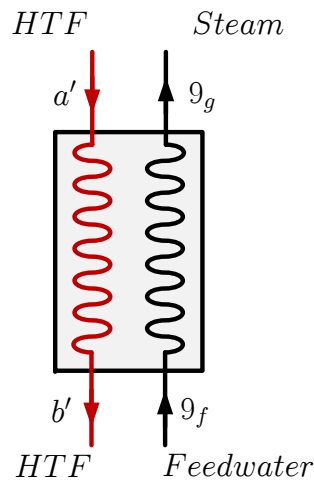
Figure 4.4 Boiler heat exchanger

The actual heat transfer rate at the boiler is as follows:

$$\dot{Q}_{boiler} = C_{HTF} \left(T_{HTF_{a'}} - T_{HTF_{b'}} \right) \tag{4.20}$$

or

$$\dot{Q}_{boiler} = \dot{m}_{Feedwater} \left(h_{Steam} - h_{Feedwater} \right) = \dot{m}_{Feedwater} \, h_{fg \; @ T = T_9} \tag{4.21}$$

The feedwater coming from the preheater absorbs a large amount of heat at constant temperature during the phase-change process. The heat capacity rate of the steam during the phase-change process approaches infinity since the temperature change is zero [111].

The minimum heat capacity rate is obtained from the HTF and the dimensionless capacity ratio is defined as:

$$c_{boiler} = \frac{C_{min,boiler}}{C_{max,boiler}} = 0 \tag{4.22}$$

with C_{min} defined as:

$$C_{min,boiler} = C_{HTF} = \frac{\dot{m}_{HTF} \left(h_{HTF_{a'}} - h_{HTF_{b'}}\right)}{T_{HTF_{a'}} - T_{HTF_{b'}}} \tag{4.23}$$

The mass balance for the boiler is as follows:

$$\dot{m}_{HTF_{b'}} = \dot{m}_{HTF_{a'}} \tag{4.24}$$

$$\dot{m}_{Steam} = \dot{m}_{Feedwater} \tag{4.25}$$

The maximum heat transfer rate is given by:

$$\dot{Q}_{boiler,max} = C_{min} \left(T_{HTF_{a'}} - T_{sat\,@T=T_9}\right) \tag{4.26}$$

The effectiveness is as follows [111]:

$$\varepsilon_{boiler} = 1 - \exp\left(-NTU_{boiler}\right) \tag{4.27}$$

or

$$\varepsilon_{boiler} = \frac{C_{HTF} \left(T_{HTF_{a'}} - T_{HTF_{b'}}\right)}{C_{min} \left(T_{HTF_{a'}} - T_{sat\,@T=T_9}\right)} \tag{4.28}$$

$$\varepsilon_{boiler} = \frac{\dot{m}_{Feedwater}\, h_{fg\,@T=T_9}}{C_{min} \left(T_{HTF_{a'}} - T_{sat\,@T=T_9}\right)} \tag{4.29}$$

At partial load conditions the product of the overall heat transfer coefficient, U_{boiler}, and the heat transfer area, A_{boiler}, is given by [112]:

$$(UA)'_{boiler} = (UA)_{boiler} \left(\frac{\dot{m}'_{HTF_{a'}}}{\dot{m}_{HTF_{a'}}} \right)^{0.8} \tag{4.30}$$

where $(UA)'_{boiler}$ is the new product of the overall heat transfer coefficient and the heat transfer area of the boiler calculated at the new mass flow rate $\dot{m}'_{HTF_{a'}}$. The HTF return temperature and mass flow rate are calculated as:

$$\dot{m}_{HTF,rec} = \dot{m}_{HTF} + \dot{m}_{HTF,superheater} \tag{4.31}$$

$$h_{HTF,rec} = \frac{\dot{m}_{HTF}\, h_{HTF,a} + \dot{m}_{HTF,superheater}\, h_{HTF,c}}{\dot{m}_{HTF} + \dot{m}_{HTF,superheater}} \tag{4.32}$$

$$T_{HTF,rec} = f\left(h_{HTF,rec} \right) \tag{4.33}$$

4.4   Preheater

The preheater (Figure 4.5) is a shell and tube exchanger whose main goal is to bring the entering feedwater to saturated liquid conditions. In order to simplify the analysis, the preheater is assumed to be of variable area (this assumption is also adopted by Patnode [13]) at partial load conditions so that the exiting stream 9_f is always at saturated liquid condition. This assumption reduces the number of guess variables to be solved at partial load conditions and does not have much effect on the performance of the cycle.
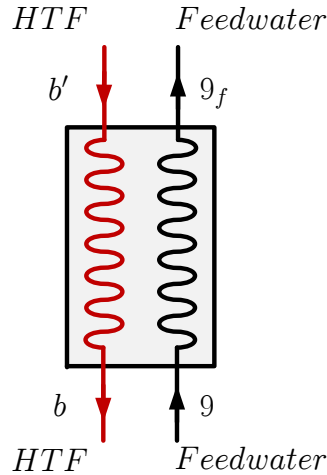
Figure 4.5 Preheater heat exchanger

The actual heat transfer rates for the hot (HTF) and cold (feedwater) fluids is as follows:

$$\dot{Q}_{preheater} = \dot{m}_{HTF}\left(h_{HTF_{b'}} - h_{HTF_b}\right) \tag{4.34}$$

$$\dot{Q}_{preheater} = \dot{m}_F\left(h_{9_f} - h_9\right) \tag{4.35}$$

where $h_{9_f} = h_{f@P=P_{10}}$ and $\dot{m}_F$ is the mass flow rate of the feedwater. The mass balance for

the preheater is:

$$\dot{m}_{HTF_b} = \dot{m}_{HTF_{b'}} \tag{4.36}$$

$$\dot{m}_{Feedwater,9} = \dot{m}_{Feedwater,9_f} \tag{4.37}$$

4.5   Closed Feedwater

Closed feedwater heaters are shell and tube heat exchangers, in which the steam bled

from the turbine condenses on the shell side whereas the feedwater stream is heated on the

tube side. The condensate is removed by using a trap and is allowed to pass to a feedwater

heater operating at lower pressure or into the condenser (stream 20') [52]. Normally closed feedwaters include three heat transfer zones as follows [113]:

- Desuperheating zone where the steam is cooled to its saturation temperature

- Condensing zone where the steam is condensed to saturated liquid condition at constant pressure and temperature

- Subcooling zone where the liquid is cooled below its saturation temperature

It is assumed that the closed feedwater heaters are always working at the condensing zone and the condensed water leaving the closed feedwater is at the saturated liquid condition. The terminal temperature difference, which is the temperature difference between the saturation temperature at the extraction pressure and the feedwater temperature leaving the closed feedwater heater, is assumed as 2.8 °C at reference conditions [114]. The energy and mass balance for the closed feedwater heater 2 (CF-2, Figure 4.6) are detailed below. Initially thermodynamic properties of the stream 12' (mixture) are calculated as:

$$h_{12'} = \frac{1}{\dot{m}_{12'}} \left[h_{24'} \dot{m}_{24'} + h_{12} \dot{m}_{12} \right] \tag{4.38}$$

$$\dot{m}_{12'} = \dot{m}_{24'} + \dot{m}_{12} \tag{4.39}$$

The temperature of stream 12' is given by:

$$T_{12'} = T \left(P_{12}, h_{12'} \right) \tag{4.40}$$
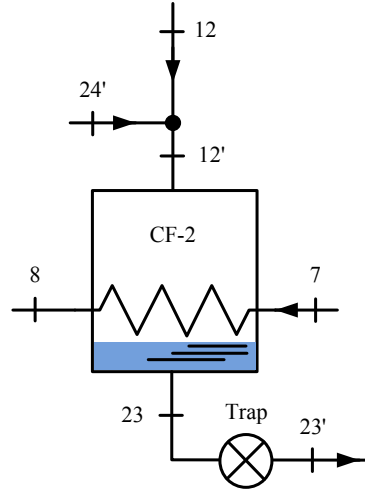
Figure 4.6 Closed feedwater heater

The mass balance shows that $\dot{m}_8 = \dot{m}_7$, $\dot{m}_{23} = \dot{m}_{12'}$, and $\dot{m}_{23'} = \dot{m}_{23}$. For the stream after the trap, stream 23', the enthalpy is $h_{23'} = h_{f@P=P_{12}}$ and the energy balance is as follows:

$$\dot{m}_{12'}\, h_{12'} + \dot{m}_7\, h_7 - \dot{m}_8\, h_8 - \dot{m}_{23}\, h_{23} = 0 \tag{4.41}$$

The actual heat transfer rate at the closed feedwater is then calculated as:

$$\dot{Q}_{CF-2} = C_{F,7-8}\,(T_8 - T_7) \tag{4.42}$$

$$\dot{Q}_{CF-2} = \dot{m}_{12'}\,(h_{12'} - h_{23}) \tag{4.43}$$

The analysis for the closed feedwater is similar to the boiler analysis previously performed.

$$c_{CF-2} = \frac{C_{min,CF-2}}{C_{max,CF-2}} = 0 \tag{4.44}$$

with C_{min} defined as:

$$C_{min,CF-2} = C_{F,7-8} = \frac{\dot{m}_7\,(h_8 - h_7)}{T_8 - T_7} \tag{4.45}$$

128

The maximum heat transfer rate is given by:

$$\dot{Q}_{CF-2,max} = C_{min} \left(T_{12'} - T_7\right) \tag{4.46}$$

The effectiveness is as follows [111]:

$$\varepsilon_{CF-2} = 1 - \exp\left(-NTU_{CF-2}\right) \tag{4.47}$$

or

$$\varepsilon_{CF-2} = \frac{C_{F,7-8} \left(T_8 - T_7\right)}{C_{min} \left(T_{12'} - T_7\right)} \tag{4.48}$$

$$\varepsilon_{CF-2} = \frac{\dot{m}_{12'} \left(h_{12'} - h_{23}\right)}{C_{min} \left(T_{12'} - T_7\right)} \tag{4.49}$$

At partial load conditions the product of the overall heat transfer coefficient, U_{CF-2}, and the heat transfer area, A_{CF-2}, is given by [13]:

$$(UA)'_{CF-2} = (UA)_{CF-2} \left(\frac{\dot{m}'_7}{\dot{m}_7}\right)^{0.8} \tag{4.50}$$

where $(UA)'_{CF-2}$ is the new product of the overall heat transfer coefficient and the heat transfer area of the closed feedwater (CF-2) calculated at the new mass flow rate $\dot{m}'_7$.

4.6 Open Feedwater (Deaerator)

Open feedwater heaters are direct contact-type heat exchangers [52], which are more efficient than closed feedwaters (Figure 4.7). In this feedwater heater, streams at different temperatures and same pressure are mixed to achieve stream exiting at the saturation condition corresponding to the inlet pressure. Open feedwater heaters (Deaerator) are also used

for removing the air and other dissolved gases which can cause corrosion problems. The mass and energy balance are obtained as:

$$\dot{m}_6 = \dot{m}_{15} + \dot{m}_5 + \dot{m}_{23'} \tag{4.51}$$

$$h_{15}\,\dot{m}_{15} + h_5\,\dot{m}_5 + h_{23'}\,\dot{m}_{23'} - h_6\,\dot{m}_6 = 0 \tag{4.52}$$
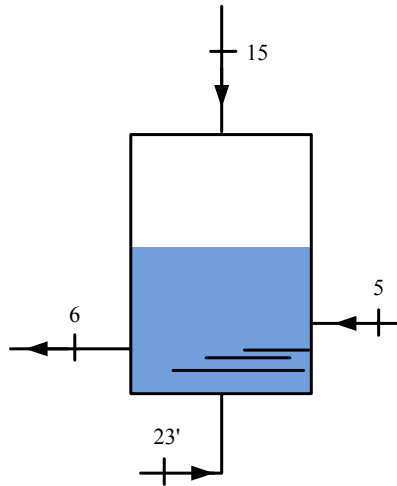
Figure 4.7 Open feedwater heater

4.7 Turbine

The proposed regenerative Rankine cycle uses two turbines: high pressure and low pressure turbine; the high pressure turbine has two stages while the low pressure turbine has five stages. Reheat is applied between the last stage of the high pressure turbine and the first stage of the low pressure turbine. The reheat pressure was selected based on the optimization analysis carried by Habib et al. [115] and Dincer and Al-Muslin [116]. They concluded that the optimum reheat pressure should be between 19-20% of the boiler pressure.

For both turbines the constant efficiency method [114] was employed to calculate the entropy at the exiting stream of each stage. The optimum pressure at each extraction was determined by dividing the total isentropic drop in equal parts according to the number of stages (Figure 4.8). This configuration leads to optimum turbine performance [108, 113].
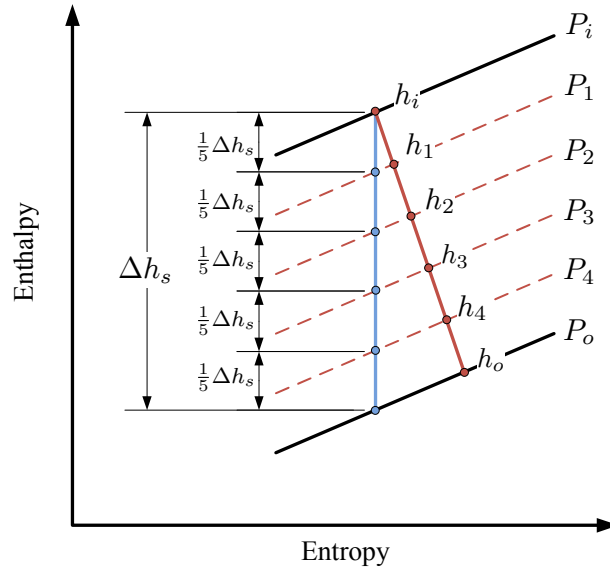
Figure 4.8 Enthalpy-entropy diagram of steam expansion in a multi-stage turbine (5 stages)

The procedure for modeling the high pressure turbine is shown below (Figure 4.9). Initially, the properties at the inlet stream are calculated. The exit pressure is determined from the optimum reheat pressure as previously explained.

$$P_{13} = f_b P \tag{4.53}$$

with $0.19 \leq f_b \leq 0.2$. The value of f_b is selected so that the minimum steam quality at the exit is $x_{19} \geq 0.9$.

The isentropic enthalpy drop is calculated as:

$$\Delta h_{s,T} = h_{10} - h_{12,s} \tag{4.54}$$

131

From Boiler

To Reheater HE
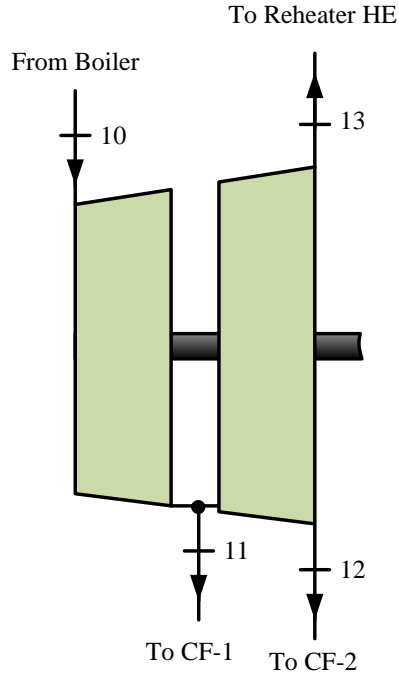
Figure 4.9 High pressure turbine (2 stages)

The isentropic enthalpy drop in each stages is calculated by dividing the total isentropic enthalpy drop by the number of stages. The isentropic enthalpy is calculated at each extraction as:

$$h_{11,s} = h_{10} - \Delta h_{s,T}/2 \tag{4.55}$$

$$h_{12,s} = h_{13,s} = h_{11} - \Delta h_{s,T}/2 \tag{4.56}$$

The optimum extraction pressures are given by:

$$P_{11} = P\left(h_{11,s}, s_{10}\right) \tag{4.57}$$

$$P_{12} = P_{13} = P\left(h_{12,s}, s_{10}\right) \tag{4.58}$$

The enthalpy at each exiting stream is calculated by using the constant efficiency method [114].

$$h_{11} = h_{10} - \eta_{H,T} \left(h_{10} - h_{11,s} \right) \tag{4.59}$$

$$h_{12} = h_{13} = h_{10} - \eta_{H,T} \left(h_{10} - h_{12,s} \right) \tag{4.60}$$

The steam flow to the steam turbine is controlled by the steam control valves. There are two main methods to vary the steam flow though the steam turbine [117]:

- changing the position of the turbine control valves

- changing the steam pressure upstream from the turbine valves by keeping them in a fixed position

In the fixed boiler pressure control the turbine governor valve is used to control the power output while boiler pressure is kept almost constant. This method works under rapid load changes but large thermal stresses are induced due to the inlet steam temperature fluctuation [118]. For sliding pressure control, boiler pressure is used to control the output power while the turbine governor valves is kept wide open. Although this control strategy produces minimal thermal stress, the response of the system is slow and the thermal efficiency is lower compared to the fixed boiler pressure control method [16]. In this analysis, sliding pressure control is assumed since it has better performance for large load changes [16], which is commonly the case in solar power plants owing to the intermittency of the solar irradiation.

The calculation of the transient operating conditions for each stage of the turbine is done starting with the last stage and up to the first stage. At partial load conditions, the pressure drop at each stage is calculated by using Stodola Law[1] [107]:

$$\frac{P_i^2 - P_o^2}{P_{i,ref}^2 - P_{o,ref}^2} = \left(\frac{\dot{m}}{\dot{m}_{ref}}\right)^2 \tag{4.61}$$

where P_i is the inlet pressure of the stage, P_o is the outlet pressure of the stage, $P_{i,ref}$ is the inlet pressure of the stage at reference conditions, $P_{o,ref}$ is the outlet pressure of the stage at reference conditions, and $\dot{m}/\dot{m}_{ref}$ is the throttle flow ratio. The turbine efficiency is affected at partial load conditions as well, specifically there is a reduction in the turbine efficiency given by:

$$\eta_t = (1 - R)\,\eta_{t,ref} \tag{4.62}$$

The reduction factor R (Figure 4.10) is as follows[2] [119]:

$$R = 0.191 - 0.409 \left(\frac{\dot{m}}{\dot{m}_{ref}}\right) + 0.218 \left(\frac{\dot{m}}{\dot{m}_{ref}}\right)^2 \tag{4.63}$$

4.8 Pump

A pump is a device to move or compress liquids [52]. The proposed thermodynamic cycle has two pumps: condenser pump and open feedwater pump. The condenser pump increases the pressure from the cycle low pressure to the open feedwater pressure while the open feedwater pump increases the pressure from the open feedwater pressure to the boiler

[1]No correction factor for temperature is included because the sliding pressure keeps the steam inlet temperature almost constant

[2]Condensing turbine with one governing stage and 3600 rpm
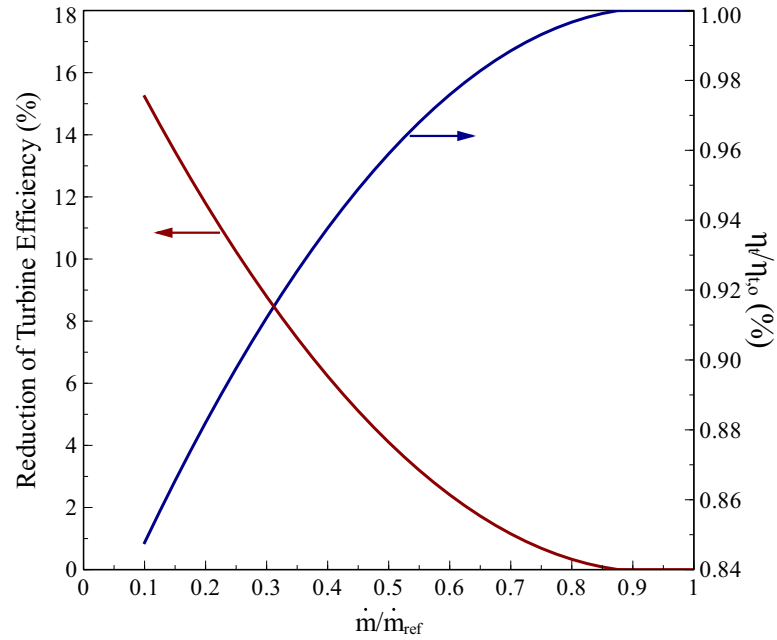
Figure 4.10 Effect of throttle flow ratio on the turbine efficiency

pressure. The work input required to compress the feedwater is taken into consideration for calculation of the net work obtained from the thermodynamic cycle, since this electric work is subtracted from the net electric work obtained from the turbines.

The pumps are assumed to work under steady conditions and heat losses to the surroundings are negligible. The mass and energy balance are as follows (Figure 4.11):

$$\dot{m}_{Feedwater_i} = \dot{m}_{Feedwater_o} \tag{4.64}$$
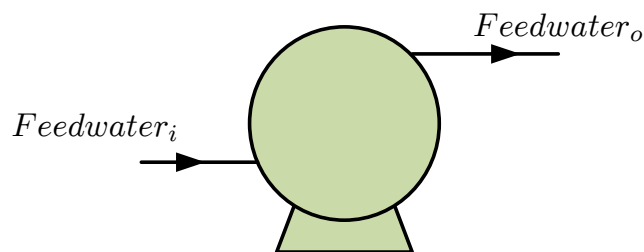
Figure 4.11 Pump

The exiting enthalpy is given by:

$$h_{Feedwater_o} = h_{Feedwater_{i_i}} + \frac{\left(h_{Feedwater_{o,s}} - h_{Feedwater_{i_i}} \right)}{\eta_{pump}} \tag{4.65}$$

with $h_{Feedwater_{o,s}} = h\left(P_{Feedwater_o}, s_{Feedwater_i} \right)$. The pump work is then:

$$\dot{W}_{pump} = \dot{m}_{Feedwater_i} \left(h_{Feedwater_o} - h_{Feedwater_{i_i}} \right) \tag{4.66}$$

At partial load conditions the efficiency of the pump is affected by the variation of mass flow rate. The pump efficiency is defined by [5]:

$$\frac{\eta_{pump}}{\eta_{pump,ref}} = e_{mo} + 2\left(1 - e_{mo} \right) \frac{\dot{m}_{Feedwater_i}}{\dot{m}_{Feedwater_{i,ref}}} - \left(1 - e_{mo} \right) \left(\frac{\dot{m}_{Feedwater_i}}{\dot{m}_{Feedwater_{i,ref}}} \right)^2 \tag{4.67}$$

where $\eta_{pump,ref}$ is the efficiency of the pump at reference conditions. For constant speed, Lippke [5] recommends to use a value of $e_{mo} = 0$. Figure 4.12 shows the effect of throttle flow ratio on the pump efficiency.
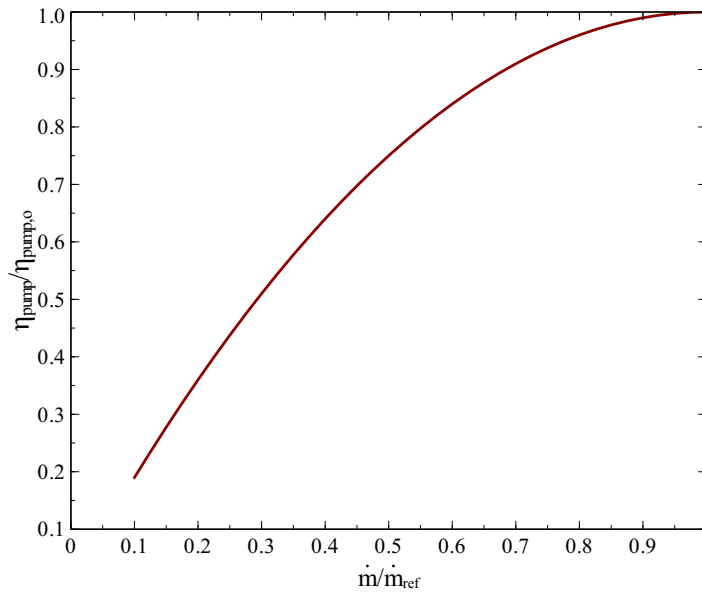
Figure 4.12 Effect of throttle flow ratio on the pump efficiency

136

4.9 Condenser

The condenser is a two phase flow heat exchanger. The heat generated by the steam phase change from vapor to liquid is removed by a coolant. The shell and tube condenser has the coolant flowing on the tube side and the steam on the shell side. Cooling water is commonly used as the coolant in the solar power plants although problems with water shortages have brought air cooled condensers as an alternative [120]. The mass and energy balance for the condenser are as follows (Figure 4.13):

$$\dot{Q}_c = \dot{m}_{25}\left(h_{25} - h_1\right) \tag{4.68}$$

$$\dot{m}_{25} = \dot{m}_1 \tag{4.69}$$

where $h_1 = h_{sat@P=P_{25}}$. The efficiency of the Rankine cycle is affected by the condenser pressure; at a fixed boiler pressure the condenser pressure should be kept as low as possible [52]. The condenser temperature depends on the cooling method employed to remove the latent heat to the surroundings. The minimum ambient temperature is given by the wet bulb temperature; thus, most of the solar power plants use cooling tower which keeps the
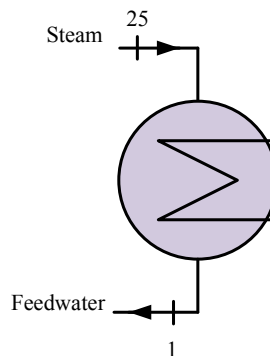
Figure 4.13 Schematic of the condenser

cooling water temperature at values near this temperature by evaporation process. For sites with water shortages, air cooled condensers can be used. Air cooled condensers are limited to the dry bulb temperature of the air which decreases the thermal efficiency of the power block. Two types of coolants were considered in this study: water and air. For both cooling fluids, preliminary design to meet the thermal requirements of the condenser and hourly simulations of operations were performed. A detailed analysis of the cooling methods and their integration with the condenser is shown below.

4.9.1 Cooling Tower

Cooling towers are widely used in industrial processes to remove waste heat. Two types of cooling towers exist: natural and mechanical draft. In this simulation mechanical draft cooling tower with air and water in counterflow is analyzed.

A cooling tower cools water by a combination of heat and mass transfer. The hot water coming from the condenser is sprayed in the tower in order to expose a large surface of water to the atmospheric air. Due to the low humidity of the air entering at the cooling tower, a part of the falling water evaporates [52], taking its latent from the remaining water in the liquid state. The net effect is a temperature drop in the exiting water. This temperature drop in the cooling water is known as the temperature range (Figure 4.14). Another factor is the "cooling tower approach" (Figure 4.14) which is the difference between the cold water temperature leaving the tower and the ambient wet bulb temperature [121]. A minimum value of 5 °F is recommended for this factor since the size of the tower varies widely with the approach temperature [122].
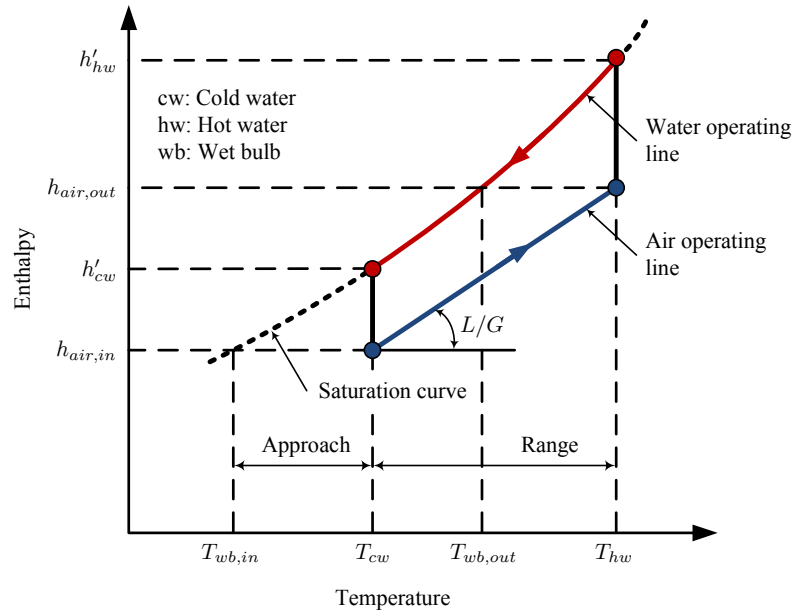
Figure 4.14 Cooling tower process heat. Adapted from [121]

The wet bulb temperature is an important variable of design for cooling towers since the condenser pressure is a direct function of the cold water temperature. The design wet bulb temperature is commonly selected as the 5% ambient wet bulb temperature, which is the wet bulb temperature that has historically been exceeded, on the average, by only 5% of the hours in the warmest summer months [123].

4.9.1.1   Design Procedure

For a given set of design conditions, there is an optimum design for the cooling tower. The optimum design conditions are related to minimum construction and operation cost. The optimum outlet air temperature is given by [124]:

$$T_{air,o} = \frac{T_{cw_3} + T_{cw_2}}{2} \tag{4.70}$$

For this approximation, the air flow rate will be within $\pm 10\%$ of the optimum design. As shown in Figure 4.15, the cool water leaving the tower is pumped to the condenser. During this process the temperature rise is negligible [125], that is $T_{cw_2} \approx T_{cw_1}$. The water inlet and outlet temperatures are defined by:

$$T_{cw_3} = T_{sat@P=P_1} - \Delta T_{pinch,c} \tag{4.71}$$

$$T_{cw_1} = T_{wb,in} + \Delta T_{approach} \tag{4.72}$$

where $\Delta T_{pinch,c}$ is the pinch point temperature between the steam and the cooling water and $T_{wb,in}$ is the design wet bulb temperature. Although the water mass flow rate is not constant, the evaporation rate is small and is commonly neglected [124]. From the energy balance the mass flow ratio of the water (L_w) to the air (G) is given by:

$$\frac{L_w}{G} = \frac{h_{air,o} - h_{air,i}}{C_{p,w}\left(T_{CW_3} - T_{CW_2}\right)} \tag{4.73}$$
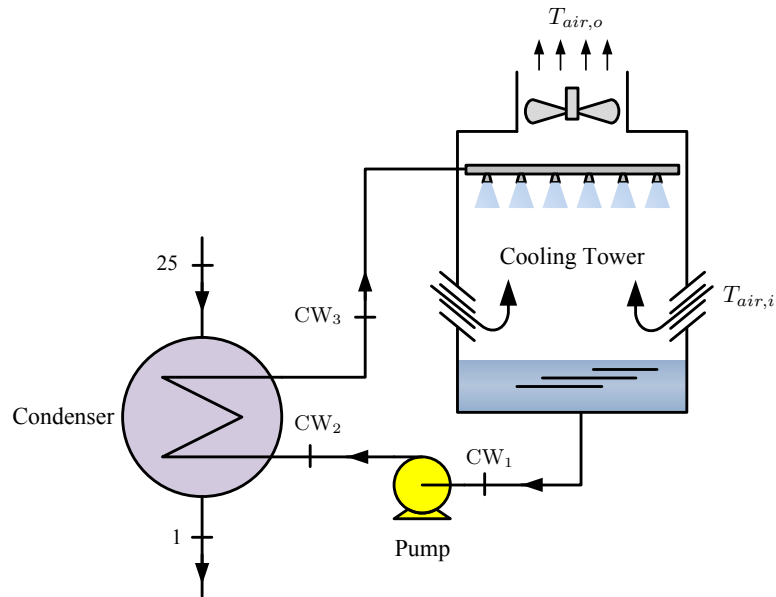
Figure 4.15 Schematic of a cooling tower

The air leaving the tower is assumed to be at saturated conditions. The tower charac-

teristic $ka\bar{V}/\bar{L}_w$ for counterflow tower is given by the Merkel equation [121]:

$$\frac{ka\bar{V}}{\bar{L}_w} = \int_{T_{cw_1}}^{T_{cw_3}} C_{p,air} \frac{dT}{h_s - h_{air}} \tag{4.74}$$

where k is the mass transfer coefficient in kg/hr-m^2, a is the contact area in m^2/m^3, $\bar{V}$ is

the active cooling volume in m^3/m^2, $\bar{L}_w$ is the water mass flow rate per unit of tower cross

sectional area in kg/hr-m^2, h_s is the enthalpy of the saturated air at water temperature in

kJ/kg$_{air}$, h is the enthalpy of the air stream in kJ/kg$_{air}$, and $C_{p,air}$ is the specific heat of the

air in kJ/Kg-K.

The performance of a cooling tower is affected by the water and air mass flow rates.

Optimum capital and fan power costs are obtained at $\bar{G}$ less than 8800 kg/hr-m^2, while a

poor water distribution is obtained at greater than 15000 kg/hr-m^2. Mohiuddin and Kant

[126] recommend the following procedure to determine the water and air flow rates for

mechanical draught cooling towers:

- Calculate the ratio of the water to the air mass flow rate $L_w/G = \bar{L}_w/\bar{G}$ from Equation

  (4.73)

- Determine $\bar{G}$ for a value of $\bar{L}_w$ of 12000 kg/hr-m^2

- If the resulting value of $\bar{G}$ exceeds 7800 kg/hr-m^2, it is necessary to determine the

  value of $\bar{L}_w$ that corresponds to $\bar{G} = 7800$ kg/hr-m^2

The required fill height, Z_{tower}, is calculated from the tower characteristics $(ka\bar{V}/\bar{L}_w)$ as:

$$Z_{tower}\,(\text{m}) = \bar{V} = \left(\frac{ka\bar{V}}{\bar{L}_w}\right)\frac{\bar{L}_w}{ka} \tag{4.75}$$

In order to calculate Z_{tower}, Leeper [124] suggests a value of $ka = 1600$ kg/hr-m^3 and the value of $\bar{L}_w$ is calculated from the procedure recommended by Mohiuddin and Kant [126]. The pump power is determined from the following equation:

$$\dot{W}_{CT,pump}\,(\text{kW}) = \frac{\rho_w\,g\,L_w\,H_p}{1000\,\eta_{ct,pump}} \tag{4.76}$$

where ρ_w is the density of the water, H_p is the pump head in m, and $\eta_{ct,pump}$ is the efficiency of the cooling tower pump. A good approximation for the pump head is [124]:

$$H_p\,(\text{m}) = Z_{tower} + 3 \tag{4.77}$$

Fan power requirement is calculated based on an empirical correlation which assumes that one horse power (1 hp $\simeq$ 0.75 kW) is required per each 226.5 m^3/min of air moved by the fan [126]. The air flow rate is calculated based on the position of the fan. For forced draft tower is calculated at the inlet air stream while for induced draft tower is calculated at the exit air stream. The density (kg$_{d,air}$/m^3) of the air water vapor mixture is given by [127]:

$$\rho_{air} = \frac{P}{R_{air}\,T_{air}\,(\text{K})\,(1 + 1.6078\,\omega)} \tag{4.78}$$

where ω is the humidity ratio , defined as the ratio of the mass of the water vapor in the air to the mass of dry air, M_{air}/M_v is the ratio of the molecular weight of the air to the

molecular weight of the water vapor, $M_{air}/M_v = 1.6078$, R_{air} is the gas constant for dry air, $R_{air} = 0.287$ kJ/kg-K, and P is the total pressure in kPa. The air flow rate is given by:

$$F \left(m^3/\text{min} \right) = \frac{G}{60 \, \rho_{air,o}} \tag{4.79}$$

where $\rho_{air,o}$ is calculated at the outlet air stream. The fan power is then calculated as:

$$\dot{W}_{ct,fan} \left(\text{kW} \right) = \frac{F \left(m^3/\text{min} \right)}{226.5} 0.75 \tag{4.80}$$

The NTU_c (number of transfer units) and effectiveness, ε_c, are calculated as below. The heat removed from the condenser is given by:

$$\dot{Q}_c = L_w C_{p,w} \left(T_{CW_3} - T_{CW_2} \right) \tag{4.81}$$

The minimum heat capacity rate is obtained from the cooling water and the dimensionless capacity ratio is $c_c = 0$, with C_{min} defined as:

$$C_{min,c} = L_w C_{p,w} \tag{4.82}$$

The maximum heat transfer rate is given by:

$$\dot{Q}_{c,max} = C_{min,c} \left(T_1 - T_{CW_2} \right) \tag{4.83}$$

The effectiveness is as follows [111]:

$$\varepsilon_c = 1 - \exp \left(-NTU_c \right) \tag{4.84}$$

or

$$\varepsilon_c = \frac{\dot{m}_{25} \left(h_{25} - h_1 \right)}{C_{min,c} \left(T_1 - T_{CW_2} \right)} \tag{4.85}$$

143

$$\varepsilon_c = \frac{L_w C_{p,w} (T_{CW_3} - T_{CW_2})}{C_{min,c} (T_1 - T_{CW_2})} \tag{4.86}$$

The NTU_c is calculated as :

$$NTU_c = \frac{(UA)'_c}{C_{min,c}} \tag{4.87}$$

At partial load conditions the product of the overall heat transfer coefficient, U_c, and the heat transfer area, A_c, is given by [13]:

$$(UA)'_c = (UA)_c \left(\frac{L'_w}{L_w}\right)^{0.8} \tag{4.88}$$

where $(UA)'_c$ is the new product of the overall heat transfer coefficient and the heat transfer area of the condenser calculated at the new mass flow rate L'_w.

4.9.2 Cooling Tower Performance at Off Design Conditions

The change in the water temperature across the tower, for negligible water loss due to evaporation, is given by [128]:

$$\frac{dT_w}{dV} = \frac{G}{L_w C_{pw}} \frac{dh_{air}}{dV} \tag{4.89}$$

Above equation can be rewritten in terms of only air enthalpies [128]:

$$\frac{dh_{sw}}{dV} = \frac{G C_s}{L_w C_{pw}} \frac{dh_{air}}{dV} \tag{4.90}$$

with

$$C_s = \frac{dh_s}{dT}\bigg|_{T=T_w} \tag{4.91}$$

Equation (4.90) can be solved analytically by making an analogy with heat exchangers [129]. The air side effectiveness for a cooling tower is defined as the ratio of the actual heat

transfer to the maximum air side heat transfer that would occur if the exiting air stream were saturated at the temperature of the incoming water ($h_{air,o} = h_{s,wi}$).

$$\varepsilon_{air} = \frac{\dot{Q}}{G\left(h_{s,cw_3} - h_{air,i}\right)} \tag{4.92}$$

Then, the actual heat transfer is:

$$\dot{Q} = \varepsilon_{air} \, G \left(h_{s,cw_3} - h_{air,i}\right) \tag{4.93}$$

Making an analogy with a counterflow heat exchanger, ε_{air} is defined as [128]:

$$\varepsilon_{air} = \frac{1 - \exp\left[NTU_{ct}\left(1 - m'\right)\right]}{1 - m' \exp\left[NTU_{ct}\left(1 - m'\right)\right]} \tag{4.94}$$

with

$$m' = \frac{G C_s}{L_w C_{pw}} \tag{4.95}$$

and

$$NTU_{ct} = \frac{k \, a \, V}{G} \tag{4.96}$$

The exit air enthalpy is determined by replacing $\dot{Q}$ from the energy balance of the air:

$$h_{air,o} = h_{air,i} + \varepsilon_{air} \left(h_{s,wi} - h_{air,i}\right) \tag{4.97}$$

The outlet water temperature and the water loss by evaporation are calculated as [128]:

$$T_{cw_2} = \frac{L_{w,i} C_{pw} T_{cw_3} - G \left(h_{air,o} - h_{air,i}\right)}{L_{w,o} C_{pw}} \tag{4.98}$$

The average saturation specific heat, C_s, is estimated as the average slope between the inlet and outlet water conditions:

$$C_s = \frac{h_{s,cw_3} - h_{s,cw_1}}{T_{cw_3} - T_{cw_1}} \tag{4.99}$$

The water loss is obtained from the overall mass balance:

$$L_{wo} = L_{wi} - G\left(\omega_{air,o} - \omega_{air,i}\right) \tag{4.100}$$

where $\omega_{air,o}$ is calculated by using an averaged value over the entire tower [128]:

$$\omega_{air,o} = \omega_{air,e} + \left(\omega_{air,i} - \omega_{air,e}\right) \exp\left(-NTU_{ct}\right) \tag{4.101}$$

The effective saturation humidity ratio, $\omega_{air,e}$, is associated with the effective saturation enthalpy $h_{s,e}$:

$$h_{s,e} = h_{air,i} + \frac{h_{air,o} - h_{air,i}}{1 - \exp\left(-NTU_{ct}\right)} \tag{4.102}$$

The cooling tower performance is affected by the changes in operational parameters. One of the parameters which changes most often is the ambient wet bulb temperature. A change in the inlet wet bulb temperature does not affect the tower characteristics but rather affects the approach temperature. When air and water flow rate are adjusted, the NTU_{ct} of the cooling tower is affected. The effect of the flow rates on NTU_{ct} is as follows:

$$NTU_{ct} = c \left[\frac{L_w}{G}\right]^{1+n} \tag{4.103}$$

where c and n are constants for a given cooling tower. Leeper [124] suggests a value of $c = -0.6$ and the value of n is obtained from the design conditions.

4.9.3 Air Cooled Condensers

Traditional cooling methods for condensers in thermal power plants are water intensive processes. An alternative to these processes is the use of dry cooling condensers, which completely eliminates the need for makeup cooling water. Dry cooling is attractive because of the necessity to reduce the consumption for the limited water resources for an expanding world population. If dry cooling is used rather than water cooling, it is possible to save water for fifty thousand inhabitants per each 100 MWe capacity [130]. Some of the advantages of air cooled condensers are [130, 131]:

- Elimination of water consumption for cooling water makeup

- No icing or fogging problems

- Reduced maintenance costs (no chemical additives or periodic cleaning is required)

- Elimination of the cooling tower plume

- Reduction of condensation on the mirrors closest to the cooling tower plume (this condensation affects the optical performance of PTC)

- Dry cooled plants offer potential economic and collateral advantages due to plant siting flexibility

- Dry cooling systems emit only warm and clean air, without adverse environmental effects

On the other hand, air cooled systems have also some disadvantages:

- Heat transfer by forced air is a less effective process than evaporative heat transfer

- Larger heat exchanger areas are required to achieve the equivalent the heat rejection

- Greater fan power will be required to achieve the equivalent the heat rejection

- The performance of the air cooled condenser is strongly influenced by the ambient conditions (dry bulb temperature)

There are two basic types of dry cooling towers: direct and indirect. The indirect system is similar to a wet tower except that the cooling element consists of a large finned cooling coil that does not allow the cooling media (water) to be in contact with the air. In the direct air cooled condenser, the steam flows through a bank of finned tubes , and the ambient air is blown across the tubes by one or more axial fans [133]. An A frame (Figure 4.16) is often
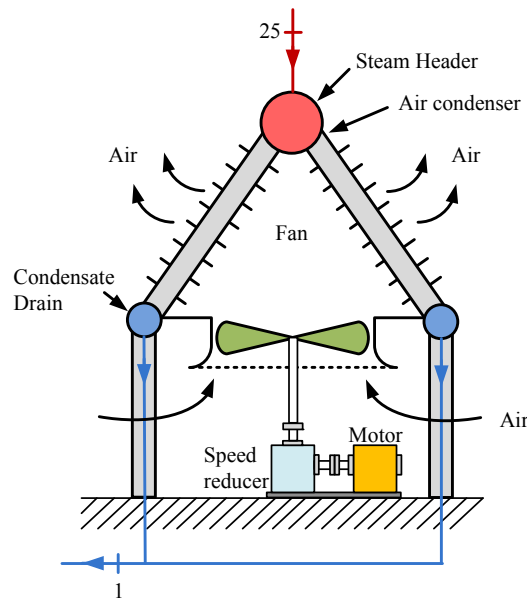
Figure 4.16 Configuration of an A frame air cooled condenser. Adapted from [132]

used where the condensing steam flows through the tubes which are orientated at angles of 45° or 60° with the horizontal [133].

For air cooled heat exchangers using horizontal tubes, two configurations are possible: forced and induced draft. In the forced draft configuration (Figure 4.17(a)) the fan is located below the tube bundle, while for the induced draft it is located above. Although the forced
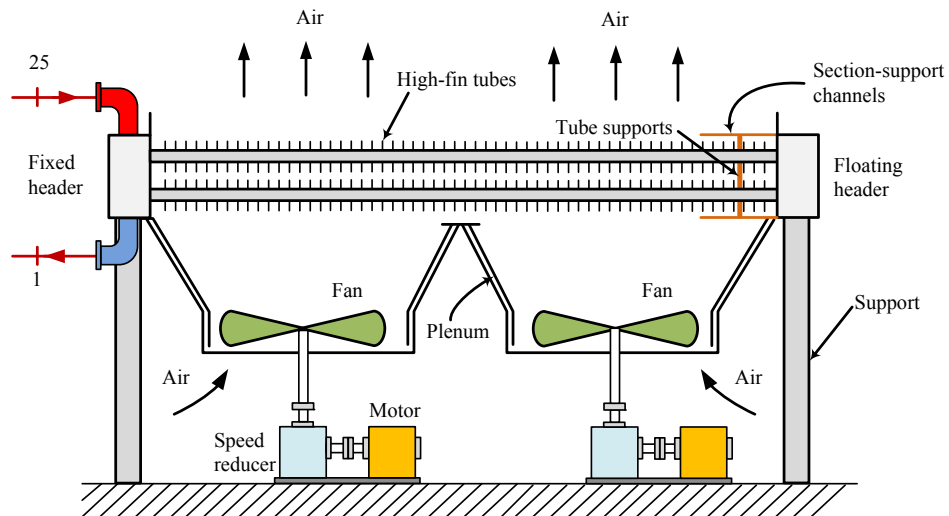
(a) Forced-draft
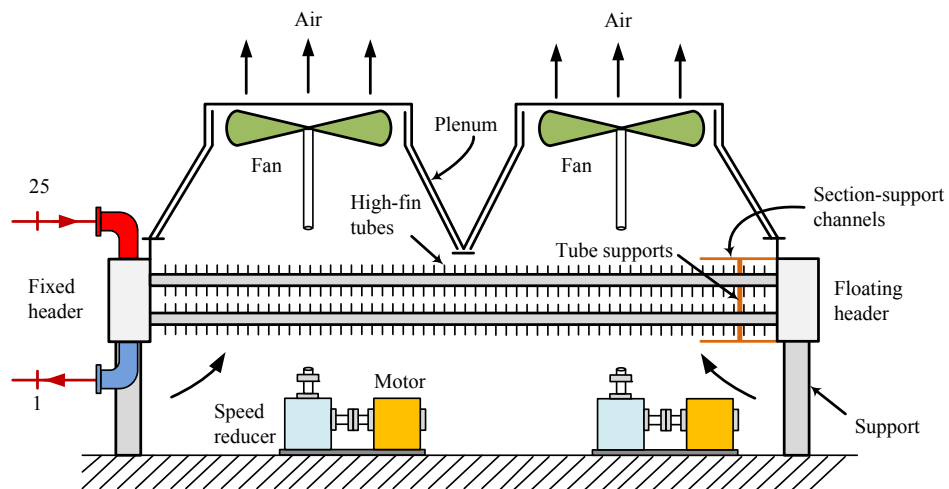
(b) Induced-draft

Figure 4.17 Configuration of forced and induced draft air cooled heat exchanger. Adapted from [133]

draft is the simplest, some problems with the recirculating hot air are present because of the low velocity of the air stream leaving the heat exchanger. This problem can be reduced by using an induced draft configuration (Figure 4.17(b)) in which the air flow is more uniform and the velocity of the stream leaving the tube bundle is higher than in the forced draft operation. Recirculating hot air decreases the performance of the air cooled heat exchanger and more heat transfer area and air mass flow rate are required. This explains why induced draft air cooled units usually do not require significantly more power than the induced draft units [133].

An air cooled heat exchanger consists of one or more fan bays. A bay consists of one or more tube bundles placed side by side in the bay, the fans, drive system, framework and the support structure. Tube bundles are rectangular in shape and usually 6-12 ft wide. Axial flow fans have diameters of 6-18 ft and their size is generally 50 hp (37 kW) or less. The design guidelines for air cooled heat exchangers are as follows [133]:

- Tubing selection is based on the tube side fluid temperature and corrosion resistance. It is recommended to choose one of the tubing configurations presented in Table 4.1

- In order to obtain uniform distribution of air flow cross the tube bundle, the fan area should be at least 40% of the bundle face area. A minimum of four tube rows is suggested.

- For two fan bays, the ratio of the tube length to bundle width should be in the range of 3-3.5

Table 4.1 Typical high-fin tube data. Adapted from [133, 134]

Fin and Tube Dimensions	1/2 in. by 9	5/8 in. by 10
Root tube OD (in)	1.000	1.000
Fin height (in)	0.500	0.625
Fin (OD)	2.000	2.250
Average Fin height (in)		
Tension wound or embedded	0.012 - 0.014	0.012 - 0.014
Bimetallic or integral	0.015 - 0.025	0.015 - 0.025
Fins per inch	9	10
Tube layout angle	30	30
Tube Pitch (in)	2.25 △	2.5 △
A_{Tot}/L	3.80	5.58
A_{Tot}/A_o	14.50	21.40
A_{Tot}/A_i		
13 BWG	17.9	26.3
14 BWG	17.4	25.6
16 BWG	16.7	24.5
External surface are per unit bundle face area, A/A_{face}		
Three tube rows	60.6	80.4
Four tube rows	80.8	107.2
Five tube rows	101.0	134.0
Six tube rows	121.2	160.8

- The air cooled heat exchanger should be design to operate at the summer conditions. Usually the temperature selected is 3-5% dry bulb temperature. This dry bulb temperature is the air temperature that has historically been exceeded an average of only 3-5% for the whole year

- For induced draft operation, the outlet air temperature is limited to about 104.5°C in order to prevent damage in the fan. Forced draft unit should be considered if the outlet air temperature is greater than 177°C

- The air velocity based on the bundle area and standard air conditions is usually in the range of 400-800 ft/min

151

4.9.3.1 Design of the Air Cooled Condensers

For the air cooled condenser design a cross flow air cooled heat exchanger (horizontal tube position) is assumed, a simple design as compared to the A frame air cooled condensers. Preliminary design using air cooled heat exchangers is a good starting point to calculate the fan power requirements (parasitic losses) and the effect of environmental conditions (air temperature) on the net power output without compromising the accuracy of the results[3].

Two cities were selected for the design of air cooled condenser unit; for both units 5/8 in. by 10 tube configuration was selected (Table 4.1). The dry bulb design temperature was calculated based on 3-5% dry bulb temperature suggested by the design guidelines. Figure 4.18 shows the accumulative frequency distribution of hourly dry bulb temperature corresponding to Tampa and Daggett.

A layout with 10-two fan bays is analyzed here (Figure 4.19). For this configuration, the load is divided into 10 equal parts.

An initial temperature difference (ITD), which is the temperature difference between the saturated steam vapor temperature and the dry bulb design temperature, is assumed. Typically ITD is in the range of 14- 33.3°C (25-60°F) [120, 136]. In this design ITD is assumed to be 22.2 °C (40 °F). Then, the condenser temperature is given by:

$$T_{sat,c} = T_{air,d} + ITD \qquad (4.104)$$

---

[3]This simplified design procedure was also assumed by [135]

(a) Tampa, Fl   (b) Daggett, CA
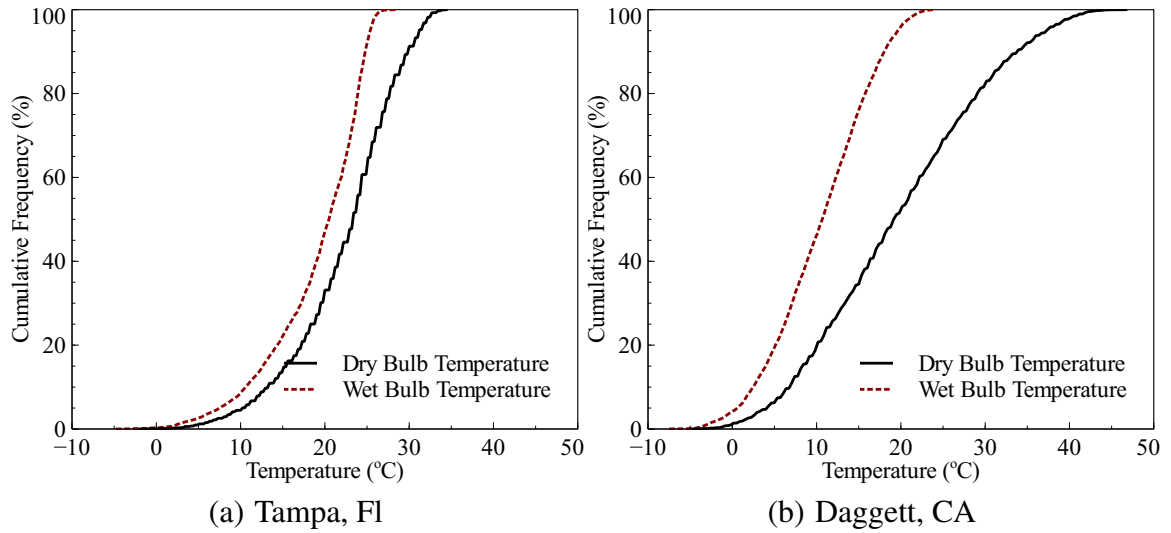
Figure 4.18 Cumulative frequency distribution of the dry bulb temperature. Data taken from [32]

The air temperature rise ΔT_{air} can be approximated by [134]:

$$\Delta T_{air}\,(^{\circ}\mathrm{F}) = \left(\frac{U_D + 1}{5.55}\right)\left(T_{sat,c} - T_{air,d}\right) \tag{4.105}$$

where $T_{sat,c}$ is the condenser temperature, $T_{air,d}$ is the dry bulb design temperature, and U_D

is the overall heat transfer coefficients in the air cooled heat exchangers in W/m^{2}K. Typical
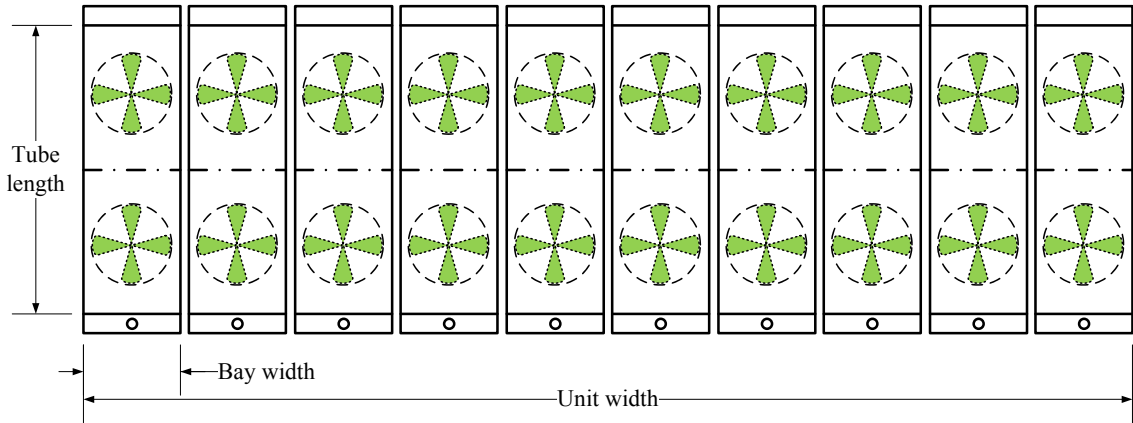
Figure 4.19 Air cooled condenser layout

values of U_D are shown in Table 4.2. For pure steam the overall heat transfer coefficient in air cooled heat exchangers is in the range of $U_D \approx 35.78 - 53.38 \text{ W}/\text{m}^2\text{K}$.

Table 4.2 Typical values of overall heat transfer coefficient in air cooled heat exchangers. Adapted from [133, 134]

Service	U_D W/m^{2}K (Btu/h·ft^2·°F)
Light hydrocarbons	25.55 - 28.39 (4.5 - 5.0)
Light Gasoline	25.55 (4.5)
Light naphtha	21.58 - 26.69 (3.8 - 4.7)
Heavy naphtha	18.74 - 23.85 (3.3 - 4.2)
Reactor effluent	21.58 - 26.69 (3.8 - 4.7)
Ammonia	28.39 - 33.50 (5.0 - 5.9)
Amine reactivator	26.69 - 32.37 (4.7 - 5.7)
Freon 12	19.88 - 23.85 (3.5 - 4.2)
Pure steam (0-20 Psig)	35.78 - 53.38 (6.3 - 9.4)
Steam with non-condensables	18.74 (3.3)

The air mass flow rate is determined from:

$$\dot{m}_{air} = \frac{\dot{Q}/n_{bay}}{C_{p,air}\,\Delta T_{air}} \tag{4.106}$$

where n_{bay} is the number of bays and $\dot{m}_{Tot,air} = \dot{m}_{air} \cdot n_{bay}$. The Logarithmic Mean Temperature Difference (LMTD) is:

$$\Delta T_{ln} = \frac{\left(T_{sat} - T_{air,d}\right) - \left(T_{sat} - T_{air,o}\right)}{\ln\left(\dfrac{T_{sat} - T_{air,d}}{T_{sat} - T_{air,o}}\right)} = \frac{\Delta T_{air}}{\ln\left(\dfrac{ITD}{ITD - \Delta T_{air}}\right)} \tag{4.107}$$

In order to determine the heat transfer surface area, a LMTD correction factor is assumed to be $F \approx 1.0$. With more than four tubes , the F factor is nearly the same as for unmixed -unmixed cross flow.

The heat transfer rate is calculated as:

$$\dot{Q} = A \, U_D \, F \, \Delta T_{ln} \times 10 \tag{4.108}$$

therefore

$$A = \frac{\dot{Q}/10}{U_D \, F \, \Delta T_{ln}} \tag{4.109}$$

The next step is to determine the number of tube rows, tube length and the number of tubes. The bundle face area required for a given face velocity (standard) is [133]:

$$A_{face} = \frac{\dot{m}_{air}}{\rho_{std} \, V_{face}} \tag{4.110}$$

where ρ_{std} is the air density at standard conditions, $\rho_{std} = 1.2013$ kg/m^3. The face velocity is usually in the range of $2.54 - 3.56$ m/s, a face velocity of 3.05 m/s can be assumed. The ratio of heat transfer surface area to bundle face area is then calculated. The $\left(A/A_{face}\right)_{cal}$ value is compared to the values shown in Table 4.1 and the closest value based on the number of tube rows is selected as $(A/A_{face})_d$. Using this value, the required face area is recalculated:

$$A_{face} = A/(A/A_{face})_d \tag{4.111}$$

A tube length, L, of three times the bundle width, W, based on the design guidelines, is assumed.

$$A_{face} = W \, L = 3 \, W^2 \tag{4.112}$$

The number of tubes is calculated using the value of $(A_{Tot}/L)_d$ obtained from Table 4.1:

$$n_t = \frac{A}{(A_{Tot}/L)_d \, L} \tag{4.113}$$

The number of tubes is selected based on the closest integer divisible by the number of tube rows previously calculated with $(A/A_{face})_d$. The corresponding bundle width is given by:

$$W_{actual} = D_{tube,pitch} \, n_{t,row} + \Delta x \tag{4.114}$$

where $n_{t,row} = n_t / n_{tube\,rows}$, and the side clearance Δx is assumed to be 2 in. The actual bundle face area and standard face velocity are :

$$A_{face,actual} = W_{actual} \, L_{actual} \tag{4.115}$$

$$V_{face,std} = \frac{\dot{m}_{air}}{\rho_{std} \, A_{face,actual}} \tag{4.116}$$

For this case the temperature change of the condensing steam is negligible and therefore $F \approx 1$ [137]. The required overall coefficient is:

$$U_{req} = \frac{\dot{Q}}{A \, F \, \Delta T_{ln}} \tag{4.117}$$

The overall heat transfer coefficient U_D' is calculated below. At high vapor velocity the gravitational effects can be neglected, and the condensate collects as a thin annular film around the inside of the tube walls, with no stratification. Most condensers operate in this flow regime [55]. The model for the local Nusselt number is given by:

$$Nu = Nu_l \, F(x) \tag{4.118}$$

156

Kröger [138] recommends to use the correlation obtained by Shah [62]:

$$Nu_{cx} = 0.023 \, Re_c^{0.8} \, Pr_c^{0.4} \left[(1 - x_x)^{0.8} + \frac{3.8 \, x^{0.76} \, (1 - x_x)^{0.04}}{p_r^{0.38}} \right] \qquad (4.119)$$

$$p_r = P/P_c$$

where P_c is the critical pressure, x_x is the local quality, and A_{ts} is the tube cross sectional area. By integrating Equation (4.119) for the case when $x_{x,i} = 1$ and $x_{x,o} = 0$, the mean condensation Nusselt number is:

$$Nu_c = 0.023 \, Re_c^{0.8} \, Pr_c^{0.4} \left[0.55 + \frac{2.09}{p_r^{0.38}} \right] \qquad (4.120)$$

All the properties are calculated at saturated liquid conditions. The Reynolds number Re_c is given by:

$$Re_c = \frac{\dot{m} \, D_i \, (n_p/n_t)}{A_{ts} \, \mu_c} \qquad (4.121)$$

If Re_c is in the range of $350 \leq Re_c \leq 6300$, the configuration is satisfactory. One pass, $n_p = 1$, is recommended for air cooled condensers [132]. The convective heat transfer coefficient is calculated as:

$$h_i = k_c \, Nu_c / D_i \qquad (4.122)$$

with $D_i = 0.021 \, \text{m}$ (0.81 in). For the convective heat transfer coefficient for air side, h_o, the maximum air velocity in the tube bank is

$$V_{max}/V_{face} = A_{face}/A_{min} \qquad (4.123)$$

where A_{min} is the minimum area in the tube bank, and A_{face} is the face area. For equilateral triangular pitch, the minimum area is given by:

$$A_{min} = (P_T - D_r) L - 2 \eta_f L b \tau \tag{4.124}$$

where D_r is the root diameter, P_T is the tube pitch, L is the tube length and $2 \eta_f L b \tau$ is the approximate area occupied by the fins. Then:

$$V_{max} = \frac{P_T V_{face}}{(P_T - D_r) - 2 \eta_f b \tau} \tag{4.125}$$

The Nusselt number is calculated by [133]:

$$Nu = 0.38 \, Re^{0.6} \, Pr^{1/3} \, (A_{Tot}/A_o)^{-0.15} \tag{4.126}$$

This equation is valid for:

$$1800 \leq Re \leq 10^5$$

$$0.011 \, \text{m} \leq D_r \leq 0.051 \, \text{m}$$

$$0.006 \, \text{m} \leq b \leq 0.019 \, \text{m}$$

$$0.0003 \, \text{m} \leq \tau \leq 0.0005 \, \text{m}$$

$$0.0274 \, \text{m} \leq P_T \leq 0.0986 \, \text{m}$$

$$1 \leq A_{Tol}/A_o \leq 50$$

$$275.6 \leq \text{fins per meter} \leq 433.1$$

The value of A_{Tot}/A_o is obtained from Table 4.1. The Reynolds number is calculated as:

$$Re = \frac{D_r \, V_{max} \, \rho_{air}}{\mu_{air}} \tag{4.127}$$

The air density should be corrected for the elevation of the air cooled unit location. The corrected atmospheric pressure is:

$$\frac{\rho}{\rho_o} = \frac{P}{P_o} = \exp\left[-\frac{M \, (g/g_c) \, z}{RT}\right] \tag{4.128}$$

where M is the molecular weight of air $\cong 29.87$, R is the gas constant, $8314 \, \text{J/kg mol} \cdot \text{K}$, T is the absolute temperature in K, z is the elevation above mean sea level in m, P_o, ρ_o are the pressure and density of air at temperature T and sea level, $P_o \approx 1$ atm, and P, ρ are the pressure and density of air at temperature T and elevation z.

The overall design heat transfer coefficient for high fin tubing is as follows:

$$U_D = \left[\left(\frac{1}{h_i} + R_{D_i}\right)\frac{A_{Tot}}{A_i} + \frac{A_{Tot}}{L}\frac{\ln\,(D_o/D_i)}{2\,\pi\,k_{tube}} + R_{con}\frac{A_{Tot}}{A_{con}} + \frac{1}{\eta_w\,h_o} + \frac{R_{D_o}}{\eta_w}\right]^{-1} \tag{4.129}$$

where R_{con} is the contact resistance between fin and tube wall, A_{con} is the contact area between fin and tube wall, R_{D_i} is the thermal resistance of the inner fouling layer, $R_{D_{oi}}$ is the thermal resistance of the outer fouling layer, $\eta_w\,h_o$ is the convective resistance of the fins, k_{tube} is the thermal conductivity of the wall tube.

Equation (4.129) is applicable to all types of tubing with the exception of bimetallic tubes. For bimetallic tubes, the thermal resistance of the outer tube must also be accounted.

In the absence of available data for the contact resistance, this term is usually neglected, $R_{cond} = 0$. The procedure to obtain the weighted efficiency of the fin is:

$$\psi = (r_{2c} - r_1) \left[1 + 0.35 \ln (r_{2c}/r_1)\right] \tag{4.130}$$

with

$$r_1 = D_r/2$$

$$r_2 = r_1 + b$$

$$r_{2c} = r_2 + \tau/2$$

The fin efficiency is given by:

$$\eta_f = \frac{\tanh (m\,\psi)}{m\,\psi} \tag{4.131}$$

$$m = (2\,h_o/k\,\tau)^{0.5}$$

The extended and prime surface areas per inch of the tube length are calculated as:

$$A_{fins} = 2\,N_f\,\pi\,\left(r_{2c}^2 - r_1^2\right) \tag{4.132}$$

$$A_{prime} = 2\,\pi\,r_1\,\left(L - N_f\,\tau\right) \tag{4.133}$$

The weighted efficiency of the finned surface is given by:

$$\eta_w = \left(\frac{A_{prime}}{A_{prime} + A_{fins}}\right) + \eta_f \left(\frac{A_{fins}}{A_{prime} + A_{fins}}\right) \tag{4.134}$$

The pressure drop, in Pa, for flow across a bank of high finned tubes is given by [133]:

$$\Delta P_{air} = \frac{f \, N_r \, G^2}{\rho_{air}} \tag{4.135}$$

$$G = \rho_{air} \, V_{max}$$

where f is the Fanning friction factor, N_r is the number of tube rows. The friction factor is calculated by the following expression:

$$f = \left[1 + \frac{2 \, e^{-(a/4)}}{1+a} \right] \left[0.021 + \frac{27.2}{Re_{eff}} + \frac{0.29}{Re_{eff}^{0.2}} \right] \tag{4.136}$$

with

$$a = \left(P_T - D_f \right) / D_r$$

$$Re_{eff} = Re \, (l/b)$$

$$D_f = D_r + 2b$$

$$l = \frac{1}{\eta_f} - \tau$$

The fans should covert at least 40% of the bundle area. For a two fan bay, the fan diameter is:

$$D_{fan} \geq \left[\frac{0.8}{\pi} A_{face,actual} \right]^{1/2} \tag{4.137}$$

The volumetric air flow, per fan in acfm is:

$$\dot{v}_{fan} = \frac{0.5 \, \dot{m}_{air}}{\rho_{air}} \tag{4.138}$$

The total pressure change, in Pa, in across the fan is given by:

$$\Delta P_{total,fan} = \Delta P_{air} + \alpha_{fr} \rho_{fr} \frac{V_{fr}^2}{2} \qquad (4.139)$$

where α_{fr} is the kinetic energy correction factor, $\alpha_{fr} \approx 1$, and V_{fr} is the air velocity in the fan ring, $V_{fr} = \dot{v}_{fan} / \left(\pi D_{fr}^2 / 4 \right)$. The brake power is calculated by:

$$\dot{W}_{fan} \text{(kW)} = \frac{\Delta P_{total,fan} \, \dot{v}_{fan}}{1000 \, \eta_{fan}} \qquad (4.140)$$

where η_{fan} is the fan efficiency. The power supplied by the motor is:

$$\dot{W}_{motor} = \frac{\dot{W}_{fan}}{\eta_{sr}} \qquad (4.141)$$

where η_{sr} is the speed reducer efficiency.

The following assumptions were used for the preliminary design of the air cooled condenser:

- Tubing type: G tube fitting with steel tubes and aluminum fins

- Tube size:0.0254 m (1 in) OD, 16 BWG, 393.7 fins per meter (10 fins per inch), fin height 0.0016 m (0.625 in)

- Tube layout is triangular (30°) with a tube pitch of 0.0635 m (2.5 in)

- Draft type: Induced Draft, the condenser operates below 177 °C (350 °F)

- Headers: Plug type

Tables 4.3 and 4.4 show the specifications and the design summary of the air cooled condenser obtained for Tampa and Daggett respectively.

Table 4.3 Air cooled condenser parameters for Tampa

Parameter	Value	Units
$\dot{Q}_{total}$	10	MW
n_{bay}	10	—
$T_{air,d}$	32	°C
ITD	22.2	°C
$T_{air,out}$	47.49	°C
$T_{sat,c}$	54.22	°C
$\dot{m}_{Tot,air}$	641.6	kg/s
$(A/A_{face})_{cal}$	129.87	—
$(A/A_{face})_d$	134	—
Tube rows	5	—
n_t	180	—
n_p	2	—
W_{actual}	2.33	m
L_{actual}	7.31	m
$A_{face,actual}$	17.09	m^2
$V_{face,std}$	3.12	m/s
h_i	6301.94	W/m^{2}K
h_o	54.34	W/m^{2}K
$k_{aluminum}$	238.5	W/m K
η_w	0.848	—
k_{tube}	45.0	W/m K
R_{D_i}	8.80×10^{-5}	$(\text{W/m}^2\text{K})^{-1}$
R_{D_o}	0	$(\text{W/m}^2\text{K})^{-1}$
R_{con}	0	$(\text{W/m}^2\text{K})^{-1}$
U_d	34.47	W/m^{2}K
U_{req}	34.45	W/m^{2}K
D_{fan}	2.13	m
ΔP_{air}	133.90	Pa
$\Delta P_{total,fan}$	170.50	Pa
η_{fan}	0.7	—
η_{sr}	0.95	—
$\dot{W}_{motor}$	7.53	kW
$\dot{W}_{motor,bay}$ (2 fans)	15.07	kW
$\dot{W}_{Tot,motor}$ (10 bay)	150.7	kW

Table 4.4 Air cooled condenser parameters for Daggett

Parameter	Value	Units
$\dot{Q}_{total}$	10	MW
n_{bay}	10	—
$T_{air,d}$	39.11	°C
ITD	22.2	°C
$T_{air,out}$	54.49	°C
$T_{sat,c}$	61.33	°C
$\dot{m}_{Tot,air}$	646.3	kg/s
$\left(A/A_{face}\right)_{cal}$	129.16	—
$(A/A_{face})_d$	134	—
Tube rows	5	—
n_t	180	—
n_p	2	—
W_{actual}	2.33	m
L_{actual}	7.31	m
$A_{face,actual}$	17.09	m^2
$V_{face,std}$	315	m/s
h_i	5877.18	W/m^{2}K
h_o	54.57	W/m^{2}K
$k_{aluminum}$	238.5	W/m K
η_w	0.847	—
k_{tube}	45.0	W/m K
R_{D_i}	8.80×10^{-5}	$\left(\text{W/m}^2\text{K}\right)^{-1}$
R_{D_o}	0	$\left(\text{W/m}^2\text{K}\right)^{-1}$
R_{con}	0	$\left(\text{W/m}^2\text{K}\right)^{-1}$
U_d	34.22	W/m^{2}K
U_{req}	34.21	W/m^{2}K
D_{fan}	2.13	m
ΔP_{air}	139.38	Pa
$\Delta P_{total,fan}$	176.71	Pa
η_{fan}	0.7	—
η_{sr}	0.95	—
$\dot{W}_{motor}$	7.85	kW
$\dot{W}_{motor,bay}$ (2 fans)	15.69	kW
$\dot{W}_{Tot,motor}$ (10 bay)	156.9	kW

The effectiveness of the air cooled condenser units is given by:

$$\varepsilon_{ACC} = \frac{\dot{Q}}{\dot{m}_{Tot,air}\, C_{P,air}\left(T_{sat,c} - T_{air,d}\right)} \tag{4.142}$$

The number of transfer units (NTU) is calculated based on the relation for heat exchangers with phase change:

$$NTU_{ACC} = -\ln\left(1 - \varepsilon_{ACC}\right) \tag{4.143}$$

The UA_{ACC} of the air cooled condenser is:

$$UA_{ACC} = NTU\,\dot{m}_{Tot,air}\, C_{P,air} \tag{4.144}$$

For the hourly simulations the following assumptions are made [13]:

- Fluid properties remain constant during the operation of the air cooled condenser unit

- The air mass flow rate calculated in the preliminary design is assumed to be constant

- The UA of the air cooled condenser unit does not change during the operation of the power block, since the effect of the heat transfer coefficient of the condensing steam on UA is relatively small compared to the heat transfer coefficient on the air side

- The final condenser heat exchanger is sized by adding identical air cooled condenser units N_{units}

The last assumption implies that NTU and the effectiveness of the air cooled condenser unit remain constant. Using these assumptions, it is found that:

$$\varepsilon = \frac{\dot{m}_{steam,unit}\left(h_{25} - h_1\right)}{\dot{m}_{Tot,air}\, C_{p,air}\left(T_{sat@P=P_1} - T_{air}\right)} \tag{4.145}$$

The steam mass flow rate is distributed uniformly in the condenser units as:

$$\dot{m}_{steam,unit} = \dot{m}_{steam}/N_{units} \tag{4.146}$$

The total parasitic losses in the air cooled condenser are:

$$\dot{W}_{Tot,ACC} = \dot{W}_{Tot,motor}\,N_{units} \tag{4.147}$$

The heat exchanger parameters obtained from the preliminary design are shown in Table 4.5.

Table 4.5 Heat exchanger parameters calculated for the air cooled condenser

Tampa, FL	
ε	0.696
NTU	1.192
UA	770.35 kW/K
Daggett, CA	
ε	0.691
NTU	1.175
UA	765.20 kW/K

4.10   Net Electric Work

The total turbine work is given by:

$$\dot{W}_{HP,t} = \dot{m}_{10}\,h_{10} - \dot{m}_{11}\,h_{11} - \dot{m}_{12}\,h_{12} - \dot{m}_{13}\,h_{13} \tag{4.148}$$

$$\dot{W}_{LP,t} = \dot{m}_{14}\,h_{14} - \dot{m}_{15}\,h_{15} - \dot{m}_{16}\,h_{16} - \dot{m}_{17}\,h_{17} - \dot{m}_{18}\,h_{18} - \dot{m}_{19}\,h_{19} \tag{4.149}$$

$$\dot{W}_t = \dot{W}_{HP,t} + \dot{W}_{LP,t} \tag{4.150}$$

The pump work is found as follows:

$$\dot{W}_{pump,cond} = \dot{m}_2\,h_2 - \dot{m}_1\,h_1 \tag{4.151}$$
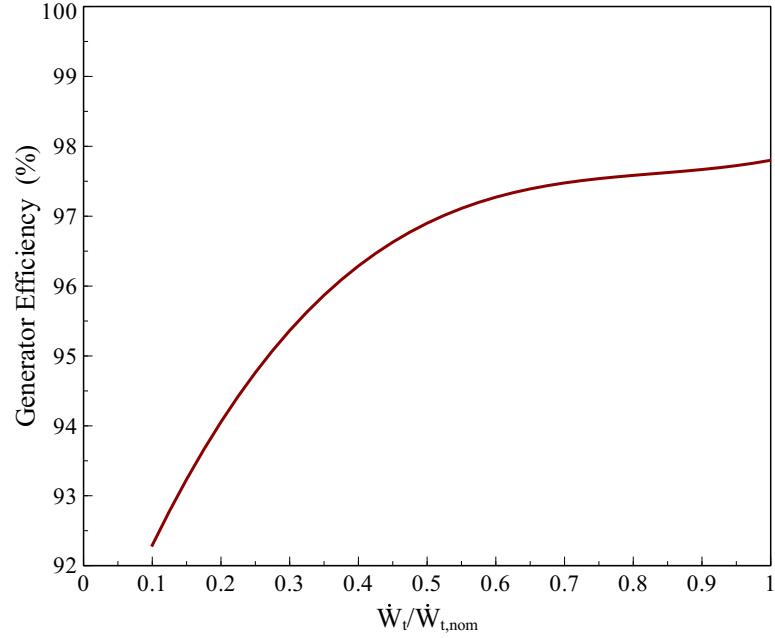
Figure 4.20 Effect of turbine work on the generator efficiency

$$\dot{W}_{pump,OF} = \dot{m}_7 \, h_7 - \dot{m}_6 \, h_6 \qquad (4.152)$$

The gross electric power output, $\dot{W}_e$, is calculated by multiplying the net power of the cycle

by the generator efficiency:

$$\dot{W}_e = \dot{W}_t \, \eta_{generator} \qquad (4.153)$$

Then the net work is:

$$\dot{W}_{net} = \dot{W}_e - \dot{W}_{pump,cond} - \dot{W}_{pump,OF} \qquad (4.154)$$

At partial load conditions, the generator efficiency varies with the load ($\dot{W}_t / \dot{W}_{t,nom}$,

Figure 4.20) as follows [13]:

$$\eta_{generator} = 0.90 + 0.258 \, \text{Load} - 0.3 \, \text{Load}^2 + 0.12 \, \text{Load}^3 \qquad (4.155)$$

$$\text{Load} = \frac{\dot{W}_t}{\dot{W}_{t,nom}}$$

167
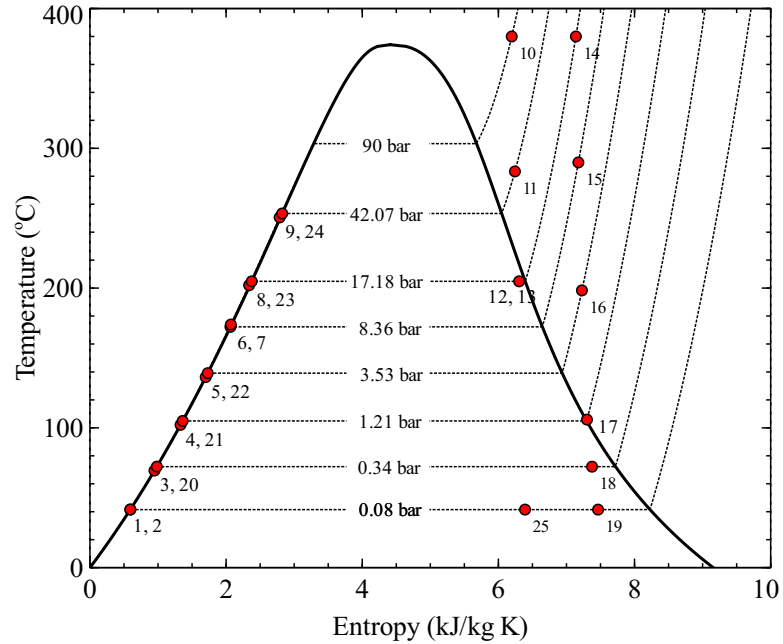
Figure 4.21 Temperature - entropy diagram of the regenerative Rankine cycle

4.11 Results

The thermodynamic properties of water and steam were implemented in Python 2.6 [34] by using the international-standard IAPWS-IF97 steam tables [109]. The input parameters used in the simulation are shown in Table 4.6. The results obtained at nominal conditions are presented in Table 4.7, and the temperature-entropy diagram of the regenerative cycle is shown in Figure 4.21.

The nonlinear algebraic equations for heat and mass balance were solved simultaneously by using a wrapper around MINPACK's hybrd and hybrj algorithms [102, 139]. In order to obtain a general solution for the power block at partial load conditions, normalized variables were used. The normalized variables were obtained by dividing the output cycle parameters by their respective values at nominal conditions:

$$\dot{W}_{net}/\dot{W}_{net,nom} \tag{4.156}$$

Table 4.6 Cycle parameters assumed for the simulation

Parameter	Value	Reference
Heat Transfer Fluid (HTF)		
Inlet Temperature	390 °C	[13]
Fluid	VP-1, Hitec	[4]
Rankine Cycle		
Gross Electric Power, $\dot{W}_e$	50 MW$_e$	[16]
High Pressure	90 bar	[16]
High pressure turbine efficiency	85.50 %	[16]
Low pressure turbine efficiency	89.50 %	[16]
Reheat Pressure	0.19 P_{high}	[115, 116]
Condenser Pump Efficiency	75 %	[16]
Open Feedwater Pump Efficiency	78 %	[16]
Terminal Temperature difference Closed Feedwater	2.8 °C	[122]
Condenser Pressure	0.08 bar	
ΔT_{pinch}	10 °C	[122]

Table 4.7 Cycle parameters obtained at nominal conditions

Variable	Value	Units
Cycle		
$\dot{W}_{HP,t}$	15778.3	kW
$\dot{W}_{LP,t}$	35242.1	kW
$\dot{W}_{pump,cond}$	47.6	kW
$\dot{W}_{pump,OF}$	639.6	kW
$\dot{W}_{net}$	48385.9	kW
$\dot{Q}_{boiler} + \dot{Q}_{superheater}$	128713.5	kW
η_{cycle}	37.6	%
$\dot{Q}_c$	78380.3	kW
$\dot{m}_{steam}$	54.8	kg/s
Heat Transfer Fluid		
$\dot{m}_{HTF,VP1}$	491.3	kg/s
$\dot{m}_{HTF,VP1,superheater}$	50.8	kg/s
$T_{HTF,VP1,ret}$	292.6	°C
$\dot{m}_{HTF,Hitec}$	776.4	kg/s
$\dot{m}_{HTF,Hitec,superheater}$	75.7	kg/s
$T_{HTF,Hitec,ret}$	293.2	°C
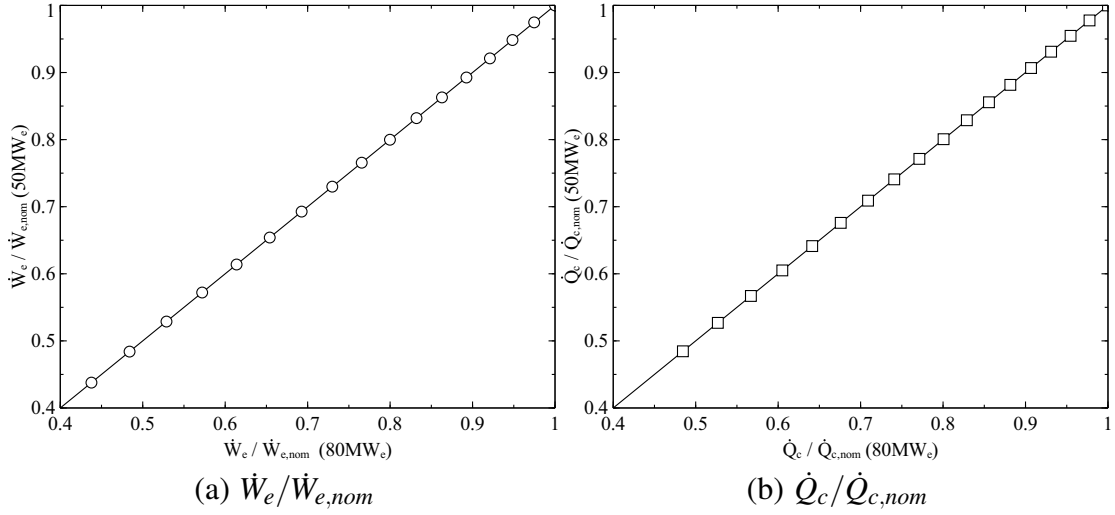
Figure 4.22 Effect of the power plant size on the normalized electric output $\dot{W}_e/\dot{W}_{e,nom}$ and the normalized condenser heat transfer rate $\dot{Q}_c/\dot{Q}_{c,nom}$, HTF: VP-1

$$\dot{Q}_c/\dot{Q}_{c,nom} \tag{4.157}$$

$$T_{HTF,rec}/T_{HTF,rec,nom} \tag{4.158}$$

Figure 4.22 shows the results obtained for 50 MW$_e$ and 80 MW$_e$. The results demonstrate that the normalized behavior is independent of the power block size. In order to corroborate the last conclusion, the proposed power model (50 MW$_e$) was compared with other simulation carried out by Patnode [13] for a power block of 35 MW$_e$. As seen in Figure 4.23, two different boiling pressures, 90 and 100 bar, were used as input to the proposed power block model. 90 bar is the nominal boiler pressure, while 100 bar is the boiler pressure used by Patnode [13]. The results show that the boiling pressure affects slightly the normalized gross electric output but in both cases the values are close to the results obtained by Patnode. It is concluded that the proposed model can be used at different power size, and it is recommended to use the same input parameters as given in Table 4.6, since
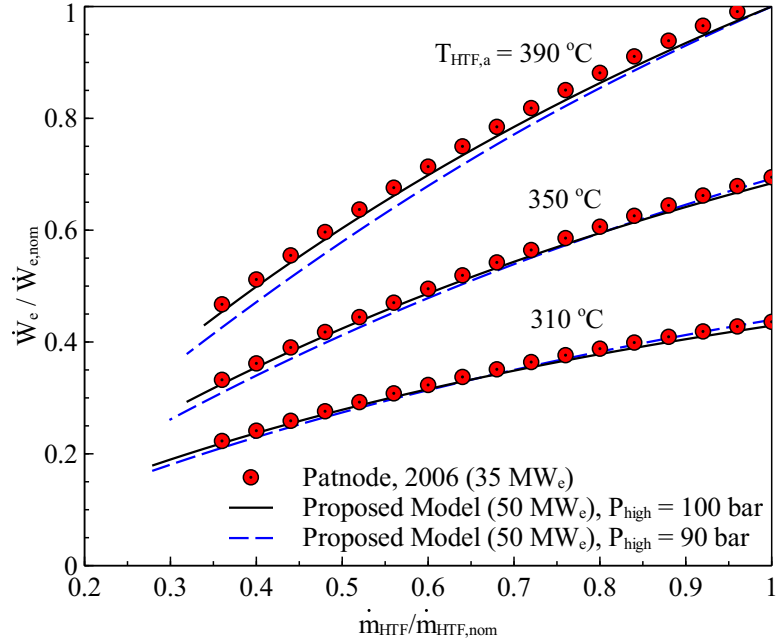
Figure 4.23 Comparison of the normalized electric output $\dot{W}_e/\dot{W}_{e,nom}$ obtained by the proposed power block model and the model developed by Patnode [13]

any change in the input parameters will affect the accuracy of the results presented by this simulation.

Figure 4.24 shows the results obtained for the normalized net work output with VP-1 as the heat transfer fluid. The condenser pressure and the normalized steam mass flow rate affect adversely the normalized net work output. As shown in Figure 4.24, the normalized steam mass flow rate can be decreased down to a certain value, below which no feasible solutions are reached. This limiting value is due to the restrictions on the mass and energy balance at the open feedwater heater and closed feedwater heater 5 (CF-5). Figure 4.25 shows the effect of normalized steam mass flow rate and condenser pressure on the normalized turbine extraction mass flow rates $\dot{m}_{15}/\dot{m}_{10}$ and $\dot{m}_{18}/\dot{m}_{10}$ at 390 °C. As it was mentioned before, in order to satisfy the mass and energy balance, the mass flow rates $\dot{m}_{15}$ and $\dot{m}_{18}$
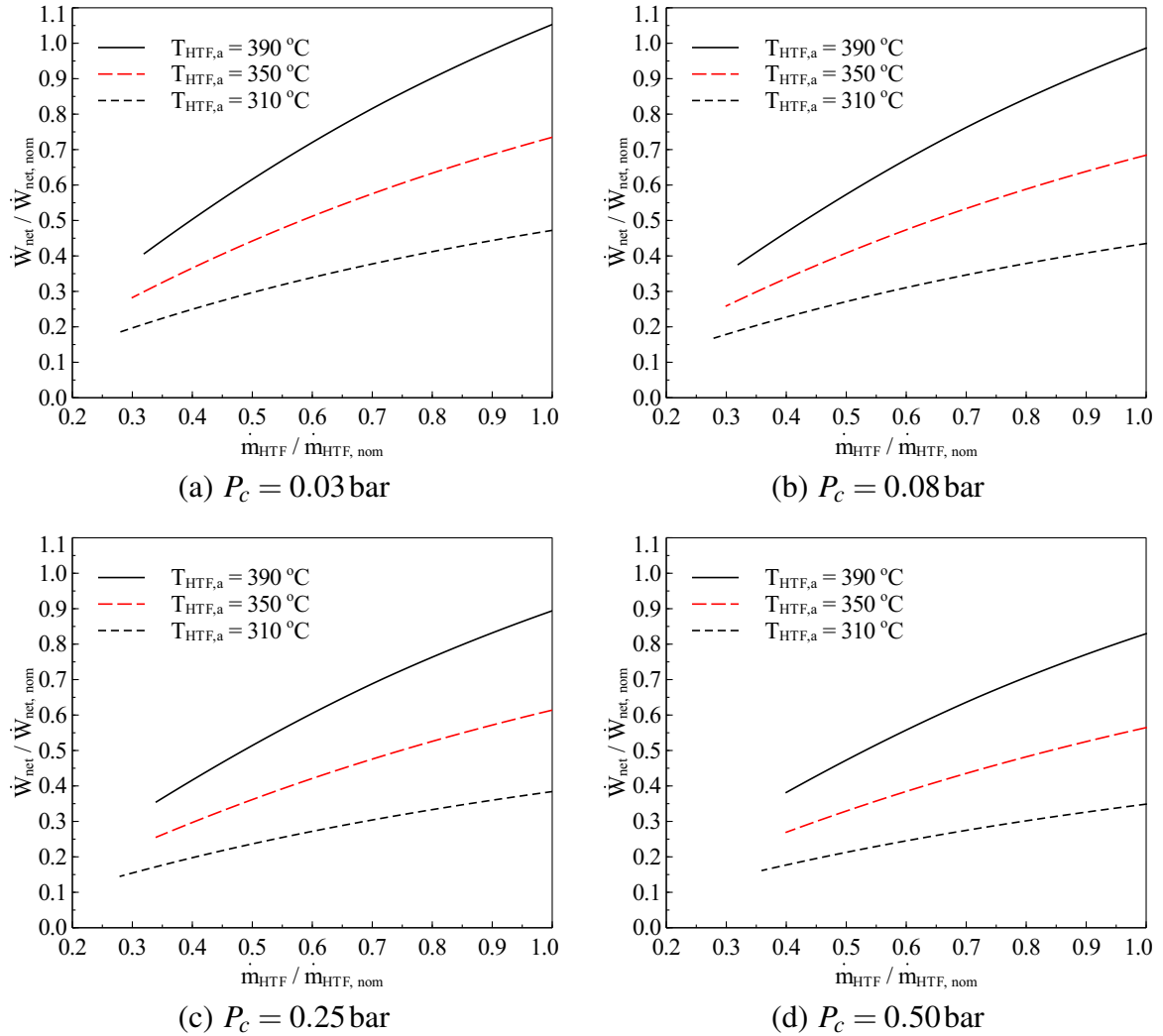
Figure 4.24 Effect of the normalized steam mass flow rate $\dot{m}_{steam}/\dot{m}_{steam,nom}$, condenser pressure and HTF inlet temperature $T_{HTF,a}$ on the normalized net work output $\dot{W}_{net}/\dot{W}_{net,nom}$, HTF: VP-1
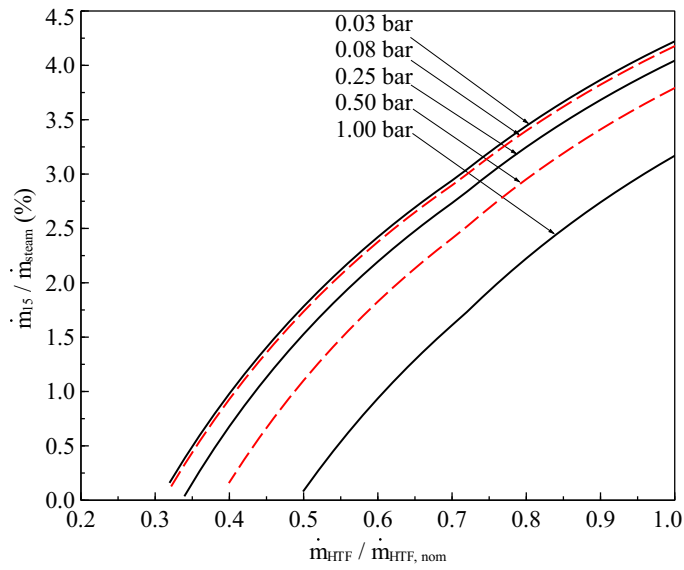
(a) $\dot{m}_{15}/\dot{m}_{10}$
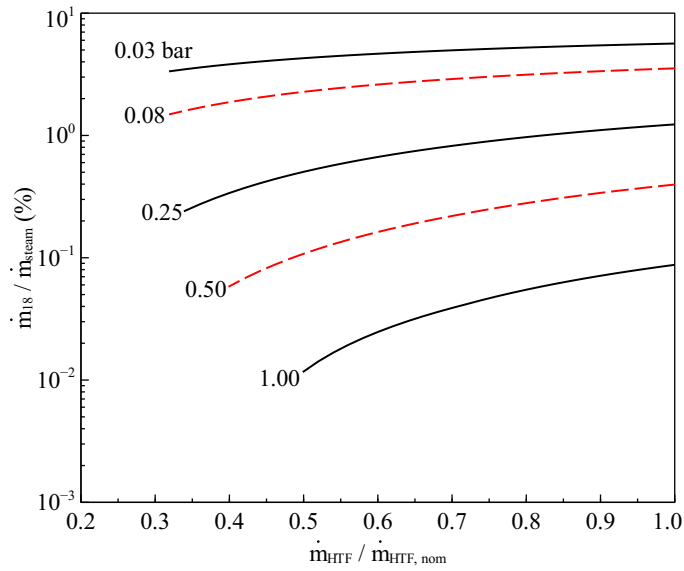
(b) $\dot{m}_{18}/\dot{m}_{10}$

Figure 4.25 Effect of the normalized steam mass flow rate $\dot{m}_{steam}/\dot{m}_{steam,nom}$ and condenser pressure on the normalized turbine extraction mass flow rates $\dot{m}_{15}/\dot{m}_{10}$ and $\dot{m}_{18}/\dot{m}_{10}$, $T_{HTF,a} = 390\,°C$, HTF: VP-1

should decrease as the normalized steam mass flow rate $\dot{m}_{steam}/\dot{m}_{steam,ref}$ decreases. This tendency is owing to the increase in enthalpy associated with the sliding pressure control method [108]. Figure 4.26 shows a comparison of the normalized net work output obtained for two different HTFs VP-1 and Hitec. The results show that the difference between these two HTFs is negligible. The maximum normalized net work output is obtained at a low condenser pressure and high heat transfer fluid inlet temperature. Therefore, to optimize the net power output at a given condenser pressure, the HTF inlet temperature should be kept at the nominal conditions[4] by adjusting the HTF mass flow rate. Figure 4.27 shows the results obtained for the normalized condenser heat transfer rate $\dot{Q}_c/\dot{Q}_{c,nom}$. The trend obtained is similar to the normalized net work output. Another important variable in the analysis is the return HTF temperature, Figure 4.28 shows the normalized return HTF temperature for the condenser pressure at nominal conditions (0.08 bar). The results show that the normalized return HTF temperature is independent of the condenser pressure and is affected by the HTF inlet temperature and the normalized steam mass flow rate.

4.12 Linear Regression Model

The proposed equation for the linear regression of the parameters obtained from the power block modeling is as follows:

$$
\begin{aligned}
\ln \Phi \;=\; & \psi_0 + \psi_1 \ln m^*_{HTF} + \psi_2 \left[\ln m^*_{HTF}\right]^2 + \psi_3 T^*_{HTF,i} + \psi_4 \left(T^*_{HTF,i}\right)^2 \\
& + \psi_5 \ln P^*_{cond} + \psi_6 \left[\ln P^*_{cond}\right]^2 + \psi_7 \ln m^*_{HTF} \ln P^*_{cond} \\
& + \psi_8 \ln m^*_{HTF} T^*_{HTF,i} + \psi_8 \ln T^*_{HTF,i} \ln P^*_{cond}
\end{aligned}
\tag{4.159}
$$

---

[4]This control strategy is also used by Montes et al. [16]
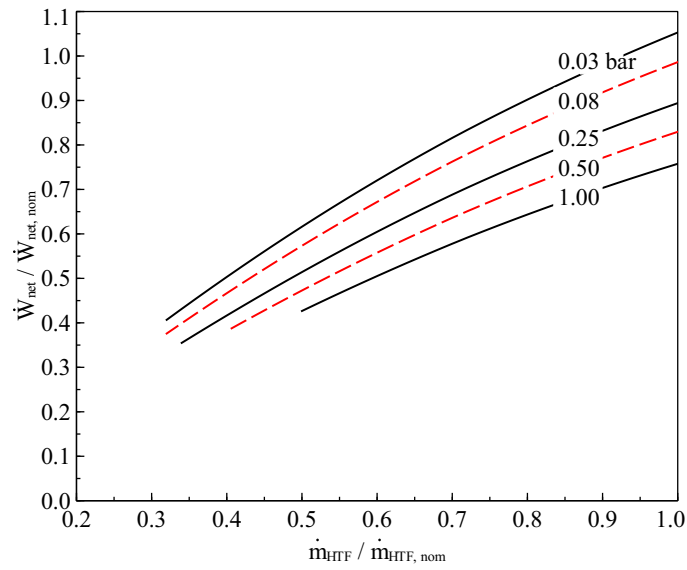
(a) VP-1
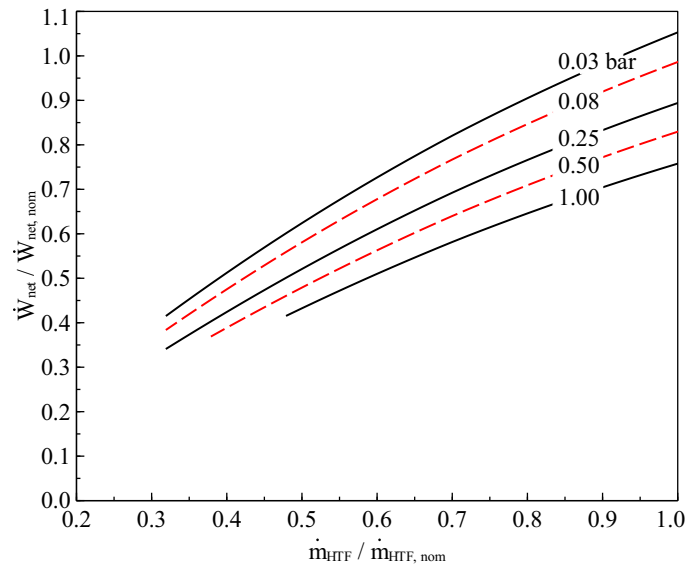
(b) Hitec

Figure 4.26 Effect of normalized steam mass flow rate $\dot{m}_{steam}/\dot{m}_{steam,nom}$ and condenser pressure on the normalized net work output $\dot{W}_{net}/\dot{W}_{net,nom}$, $T_{HTF,a} = 390\,^{\circ}\mathrm{C}$
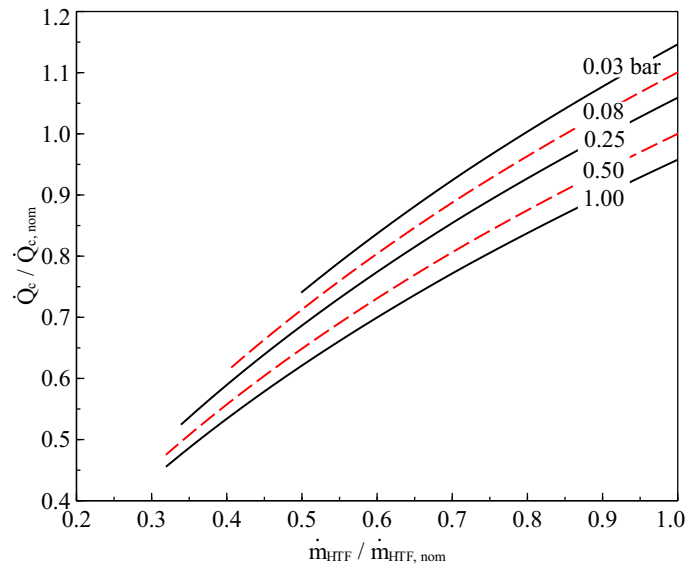
(a) VP-1
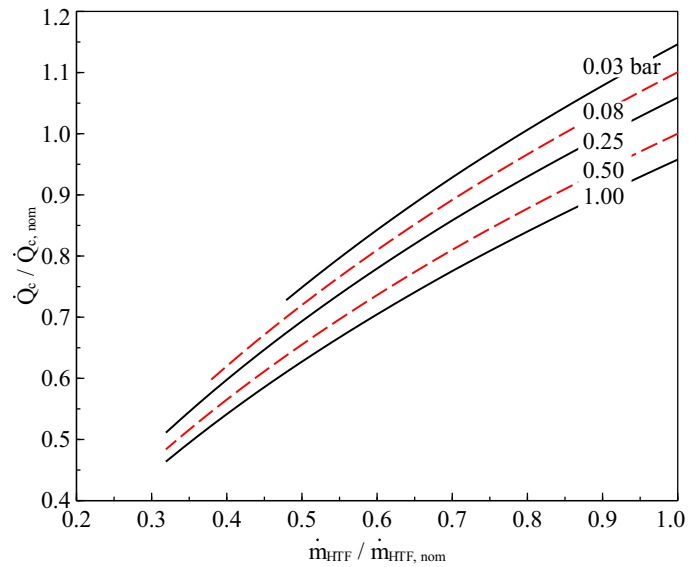
(b) Hitec

Figure 4.27 Effect of normalized steam mass flow rate $\dot{m}_{steam}/\dot{m}_{steam,nom}$ and condenser pressure on the normalized condenser heat transfer rate $\dot{Q}_c/\dot{Q}_{c,nom}$, $T_{HTF,a} = 390\,^{\circ}\mathrm{C}$
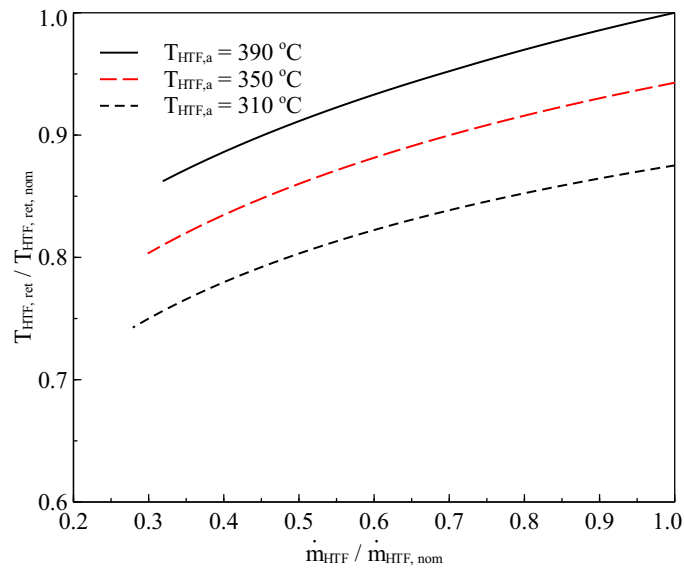
(a) VP-1
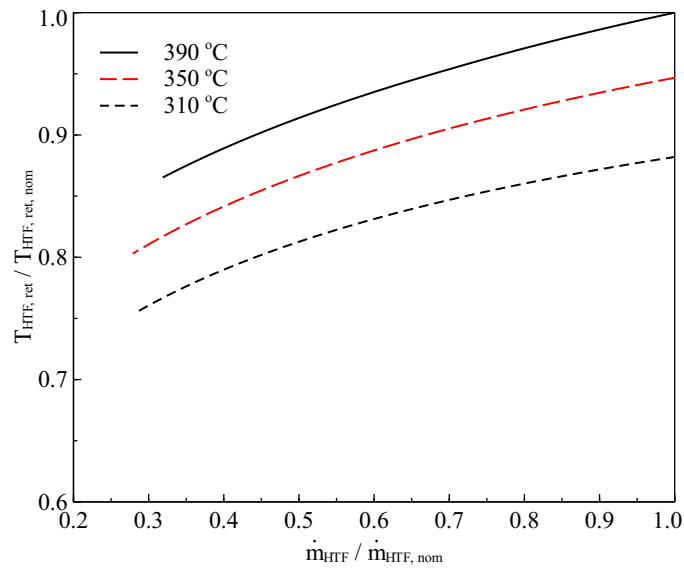
(b) Hitec

Figure 4.28 Effect of normalized steam mass flow rate $\dot{m}_{steam}/\dot{m}_{steam,nom}$ and condenser pressure on the return HTF temperature, $P_c = 0.08$ bar

The normalized input parameters are as follows:

$$m^*_{HTF} = \frac{\dot{m}_{HTF}}{\dot{m}_{HTF,nom}} \qquad T^*_{HTF,i} = \frac{T_{HTF,i}}{T_{HTF,i,nom}} \qquad P^*_{cond} = \frac{P_{cond}}{P_{cond,nom}}$$

and

$$\Phi = \frac{\dot{W}_{net}}{\dot{W}_{net,nom}}, \quad \frac{\dot{Q}_c}{\dot{Q}_{c,nom}}, \quad \frac{T_{HTF,ret}}{T_{HTF,ret,nom}}$$

The regression model was written in Python 2.6 by using "leastsq" module, which is a wrapper around MINPACK lmdif and lmder algorithms [102]. The input parameters used for the power block simulation are described in Table 4.8. Tables 4.9 and 4.10 show the coefficients obtained for the proposed linear regression. Values of the coefficient of determination, R^2, and root mean square error RMSE are also shown in Tables 4.9 and 4.10.

The results show that the linear regression accurately represents the behavior of the parameters ($\dot{W}_{net}/\dot{W}_{net,nom}$, $\dot{Q}_c/\dot{Q}_{c,nom}$, $T_{ret,HTF}/T_{ret,HTF,nom}$), obtained from the power block model. This is corroborated by the Figure 4.29, which shows a comparison of the parameters obtained from the linear regression with the power block model.

Table 4.8 Inputs parameters for the power block simulation

Inlet HTF Temperature, $T_{HTF,i}$ (°C)	290 - 390
Nominal Inlet HTF Temperature, $T_{HTF,i,nom}$ (°C)	390
Dimensionless HTF mass flow rate, $\dot{m}_{HTF}/\dot{m}_{HTF,nom}$	0.3 - 1.0
Condenser Pressure, P_{cond} (bar)	0.03 - 1 bar
Nominal condenser Pressure, $P_{cond,nom}$ (bar)	0.08
Power Block	50 MW$_e$

Table 4.9 Coefficients used for the proposed linear correlation given by Equation 4.159, HTF: VP-1

Coefficients	$\dot{W}_{net}/\dot{W}_{net,nom}$	$\dot{Q}_c/\dot{Q}_{c,nom}$	$T_{ret,HTF}/T_{ret,HTF,nom}$
ψ_0	-7.118	-4.473	-1.172
ψ_1	8.864×10^{-2}	-5.732×10^{-2}	9.454×10^{-2}
ψ_2	-1.228×10^{-1}	-8.135×10^{-2}	$-3.832 \times 10^{-3}3$
ψ_3	10.957	6.579	1.836
ψ_4	-3.839	-2.111	-6.643×10^{-1}
ψ_5	-2.202×10^{-1}	4.075×10^{-2}	7.979×10^{-4}
ψ_6	-1.477×10^{-2}	2.196×10^{-3}	5.431×10^{-5}
ψ_7	1.567×10^{-2}	2.934×10^{-3}	-4.768×10^{-6}
ψ_8	6.326×10^{-1}	6.154×10^{-1}	3.602×10^{-2}
ψ_9	1.532×10^{-1}	8.269×10^{-3}	-8.791×10^{-4}
R^2	0.9995	0.9999	0.9998
RMSE	0.0101	0.0035	0.0011

Table 4.10 Coefficients used for the proposed linear correlation given by Equation 4.159, HTF: Hitec

Coefficients	$\dot{W}_{net}/\dot{W}_{net,nom}$	$\dot{Q}_c/\dot{Q}_{c,nom}$	$T_{ret,HTF}/T_{ret,HTF,nom}$
ψ_0	-7.123	-4.485	-1.157
ψ_1	1.798×10^{-2}	-1.055×10^{-1}	7.796×10^{-2}
ψ_2	-1.210×10^{-1}	-7.624×10^{-2}	-5.264×10^{-3}
ψ_3	11.185	6.754	1.847
ψ_4	-4.063	-2.274	-6.911×10^{-1}
ψ_5	-2.056×10^{-1}	3.859×10^{-2}	8.678×10^{-4}
ψ_6	-1.492×10^{-2}	2.294×10^{-3}	5.863×10^{-5}
ψ_7	1.589×10^{-2}	2.721×10^{-3}	-2.678×10^{-7}
ψ_8	6.842×10^{-1}	6.532×10^{-1}	4.800×10^{-2}
ψ_9	1.385×10^{-1}	1.023×10^{-2}	-9.883×10^{-4}
R^2	0.9999	1.0000	0.9997
RMSE	0.0045	0.0014	0.0011

(a) $\dot{W}_{net}/\dot{W}_{net,nom}$ (b) $\dot{Q}_c/\dot{Q}_{c,nom}$
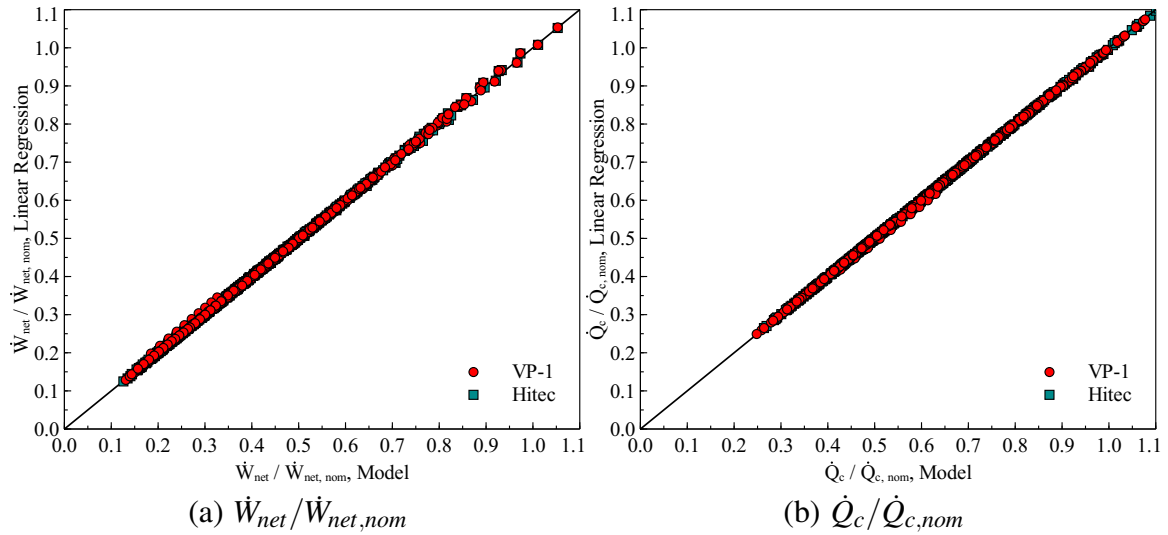
Figure 4.29 Comparison of the dimensionless net work output and condenser heat transfer rate obtained from the linear correlation with the proposed power block model, HTF: VP-1 and Hitec

4.13 Conclusions

A comprehensive model for the simulation of a regenerative Rankine cycle was developed. The results obtained showed that the output power from the cycles is affected mainly by: the inlet heat transfer fluid (HTF) temperature, mass flow rate of the HTF and the condenser pressure. The cycle parameters were normalized and it was found that the performance was independent of the power block size.

A linear regression was proposed by using the normalized variables, the results showed that the linear equation represents accurately the trend given by the results obtained in the simulation.

Chapter 5

Solar Field Piping and Thermal Losses

5.1 Solar Field Layout

The solar piping system circulates the heat transfer fluid (HTF) in a closed loop to and from the power block and solar field. This system is designed to maintain an equally distributed flow through all the solar collector loops and thus to avoid hot spots or cold spots [140]. The solar piping model in this chapter is based on the model developed by National Renewable Laboratory (NREL) [141]. In this model two layouts were proposed: an H field layout for collectors areas greater than 400000 m^2, and an I layout for areas less than 400000 m^2.

5.1.1 H Field Layout

As shown in Figure 5.1, in this layout the solar field is divided into 4 header pairs, with the power block located at the center of the solar field. Cold fluid is distributed from the cold header to each solar loop and returns to the hot header where it goes back to the power block. Each collector loop consists of 6 LS-3 solar collectors which are arranged in series to increase the temperature of the HTF to the operating conditions. In a solar collector loop, the solar collectors are connected by ball joints, which are used to allow independent rotation of the adjacent solar collectors [3].
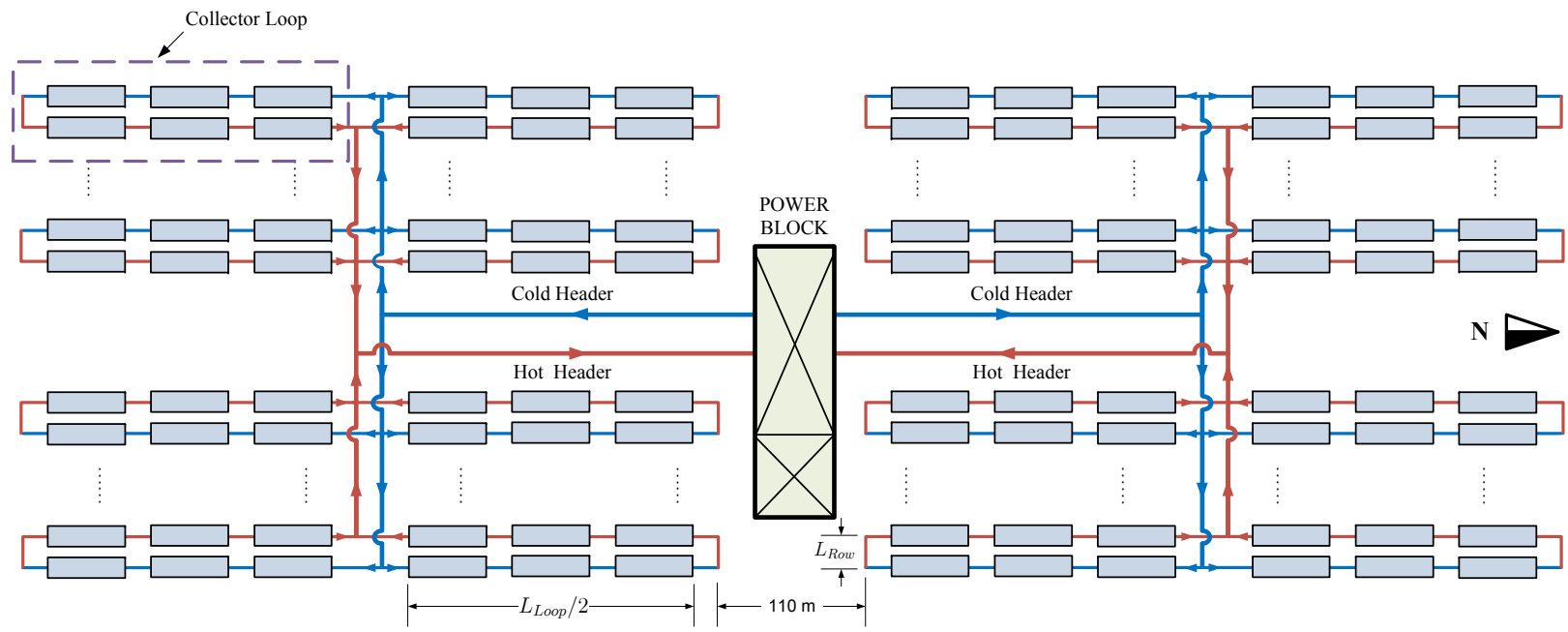
Figure 5.1 H solar field layout. Adapted from [3]

The ball joints are preferred over flexible hoses due to their advantages which include: lower cost, reduced pressure drop, and reduced heat losses [3]. In order to reduce the land requirements and piping power, the collector loop has two rows such that the cold and hot headers are located in the same side.

5.1.2 I Field Layout

In this layout the solar field is divided into a 2 header pairs, as shown in Figure 5.2, with the power block located at the center of the solar field. Cold and hot header run East-West direction. Each collector loop consists of 16 LS-2 solar collectors. As in H solar field layout, the LS-2 collectors are arranged in series with two rows. The dimensions and properties of LS-2 and LS-3 solar collectors are shown in Appendix B.
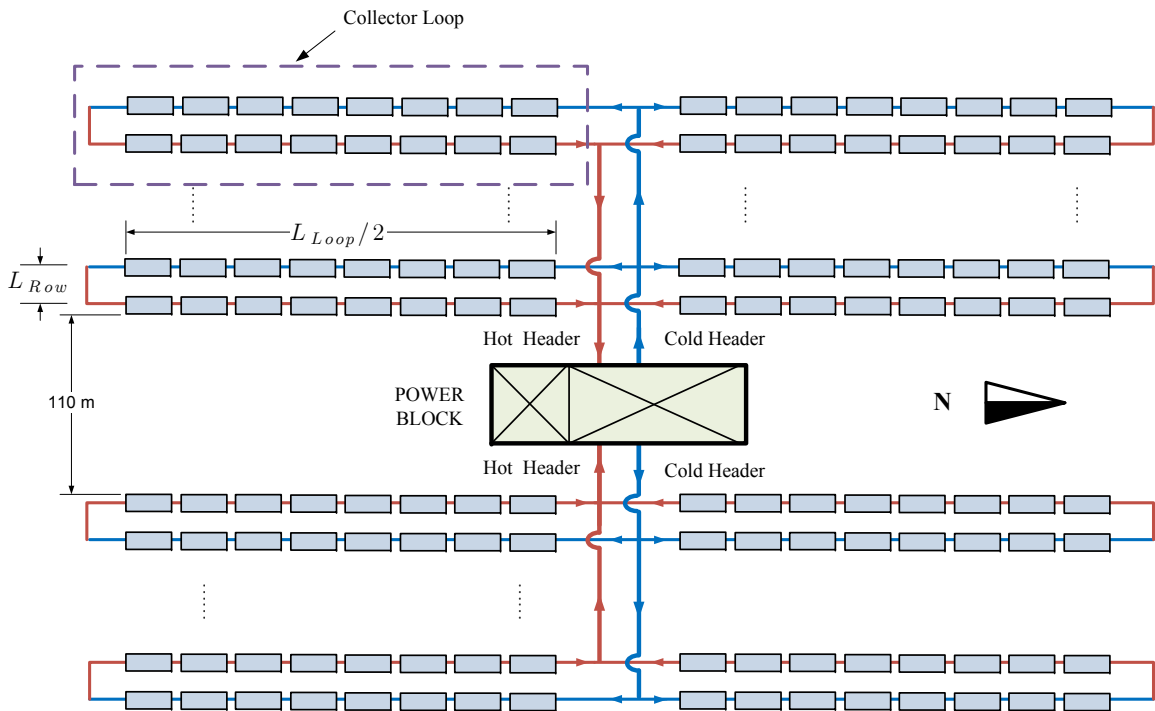
Figure 5.2 I solar field layout. Adapted from [3]

For both layouts, the maximum pressure drop is given by the longest path in the HTF circuit. This pressure drop is calculated for the solar field and the power block (heat exchangers, internal piping, etc.).

5.2 Pressure Drop in the Solar Field

The pressure drop in the solar field depends on: the HTF, mass flow rate, inner diameter of the pipes and fittings (elbow, cross, reduction, expansion, valves, etc.). Initially, it is necessary to determine the optimum diameter for each section. The calculations are based on the optimum flow velocity for minimizing of the piping costs given by NREL [141], which is in the range of 2-4 m/s. A flow velocity of 2 m/s, also used in [16], was selected for all the piping modeling. The pipe in each section must meet the flow conditions (optimum velocity) and the pressure requirements. For the pressure requirements the required wall thickness is calculated as [142]:

$$t_{wall} = \frac{(P_{abs} - P_{atm}) \, D_o}{2 \, [S_y + 0.4 \, (P_{abs} - P_{atm})]} \tag{5.1}$$

where P_{abs} is the absolute pressure of HTF in psi, P_{atm} is the atmospheric pressure in psi, D_o is the outside diameter in inches, and S_y is the allowable stress in psi. As recommended by NREL [141], three different pipe materials are used:

- ASTM A106, Grade B, Seamless Carbon Steel pipe

- ASTM A335 P9, Intermediate Alloy Steel

- ASTM TP347, Stainless Steel

The allowable stress for each material is shown in Table 5.1. The inner diameter and wall thickness for different pipe schedules and nominal diameters are shown in Appendix D.

Table 5.1 Maximum allowable stress (ksi) for different materials. Adapted from [143]

Temperature (°F)	Maxi mun Allowable Stress (ksi)		
	A106	TP347	A335
400	...	15.5	...
500	...	14.9	14.4
600	...	14.7	14.2
650	15	14.7	13.9
700	14.4	14.7	13.7
750	13.0	14.7	13.2
800	10.8	14.7	12.8
850	...	14.7	12.1
900	...	14.7	11.4
950	...	14.6	10.6
1000	...	14.0	7.4
1050	...	12.1	5.0
1100	...	9.1	3.3
1150	...	6.1	2.2
1200	...	4.4	1.5

Once the diameter is selected, the flow friction loss is calculated using the Darcy-Weisbach equation [111]:

$$h_i = 2C_f \frac{L_i}{D_i} \frac{V_i^2}{g}$$

(5.2)

where C_f is the friction coefficient (Fanning friction factor), L_i is the length of the pipe section in m, and V_i is the flow velocity in m/s. The friction coefficient can be calculated from the correlation given by Chen [53]:

$$\frac{1}{\sqrt{C_f}} = 3.48 - 1.7372\,Ln\left(2\frac{\varepsilon}{D_i} - \frac{16.2426}{Re_D}\,Ln\,A_2\right)$$

(5.3)

$$A_2 = \frac{(2\varepsilon/D_i)^{1.1098}}{6.0983} + \left(\frac{7.149}{Re_D}\right)^{0.8981}$$

where Re_D is the Reynolds number, ε is the pipe roughness in m. This correlation is valid for $4000 \leq Re_D \leq 10^8$ and $2 \times 10^{-8} \leq \varepsilon/a \leq 0.1$. For all the pipe materials it is assumed that the pipe roughness has a value of $\varepsilon = 0.046$ mm [144]. The pressure drop in a section is given by:

$$\Delta P_{L_i} = \rho_i \, g \, h_i \tag{5.4}$$

The friction losses through the pipe fittings are calculated as:

$$L_{fi} = K \left[\frac{D_i}{2\,C_f}\right] \tag{5.5}$$

where L_{fi} is the pipe length which gives the same pressure drop as the fitting. The pressure drop through the fitting is:

$$h_{fi} = 2\,C_f \, \frac{L_{fi}}{D_i} \frac{V_i^2}{g} \tag{5.6}$$

$$\Delta P_{L_{fi}} = \rho_i \, g \, h_{fi} \tag{5.7}$$

The K factors are given in Table 5.2. The location and number of fittings used was set by the description given by NREL [141]. Table 5.3 and 5.4 summarize the types and locations of the fittings used in each loop as well as the length of the cold and hot header. As seen in Table 5.3 , expansion loops are every other loop to maintain pipe stresses within the limits allowed [140].

Table 5.2 *K* values for different pipe fittings used in the solar field. Adapted from [141]

Fitting	K
Gate Valve	0.19
Globe Valve	10.00
Check Valve	2.50
Standard Elbow	0.90
Medium Elbow	0.75
Long Elbow	0.60
Weldolet	1.80
Ball Joint	4.73
Flexible Hose	20.60

The pressure drop through the solar field is calculated for the longest path traveled by the HTF. The pressure drop is then calculated as:

$$\Delta P_{SF} = \Delta P_H + \Delta P_C + \sum_i \Delta P_{i,loop,H} + \sum_i \Delta P_{i,loop,C} + \Delta P_{in,out} + \Delta P_{collector} \qquad (5.8)$$

where ΔP_H is the pressure drop in the outlet hot header, ΔP_C is the pressure drop in the inlet cold header, $\Delta P_{i,loop,H}$ is the pressure drop in the hot header pipe at the position of the loop i, $\Delta P_{i,loop,C}$ is the pressure drop in the cold header pipe at the position of the loop i, $\Delta P_{in,out}$ is the pressure drop in the inlet and outlet of the solar collector loop, and $\Delta P_{collector}$ is the pressure drop in the solar collector loop. The pressure drop through the power block should be included as well. Table 5.5 shows the typical length and fittings used in a power block unit. The description of each line is as follows:

- Line 1: Expansion vessel or thermal storage tank to pump suction header

- Line 2: Individual pump suction line, from suction header to pump inlet

- Line 3: Individual pump discharge line, from pump discharge to discharge header

Table 5.3 Fittings used in the Heat Collection Element (HCE) loop. Adapted from [141]

Accessories and Pipe	Inlet and Outlet	HCE	To Loop[a]	To Loop	From Loop[a]	From Loop
Pipe Length (m)[b]	$L_{Row} + 40$	$L_{Loop} = L_{HCE} \times n_{SCE}$	$2L_{Row} + 19$	$2L_{Row}$	$2L_{Row} + 19$	$2L_{Row}$
Standard Elbows	2	10	0	0	0	0
Medium Elbows	0	0	0	0	0	0
Long Elbows	0	0	4	0	8	0
Gate Valves	2	0	0	0	0	0
Globe Valves	0	0	0	0	0	0
Check Valves	0	0	0	0	0	0
Loop Weldolets	2	0	0	0	0	0
Loop Control Valves	1	0	0	0	0	0
Ball Joints[c]	0	$2 + n_{SCE}$	0	0	0	0

[a] Every other loop
[b] L_{Row}: Row spacing, $L_{Row} \approx 12 - 15\,\mathrm{m}$ [3]
[c] n_{SCE}: Number of solar collector assemblies, LS-2 $n_{SCE} = 16$, LS-3 $n_{SCE} = 6$ [3]

Table 5.4 Header length and fittings used in the solar field piping layout. Adapted from [143]

	Cold Header	Hot Header
Length (m)		
Position of Power Block	Configuration I	Configuration H
Center	50	$20 + 0.5\,L_{Loop}$
North-South	$20 + 0.5\,L_{Row}$	$50 + 0.5\,L_{Loop}$
East-West	50	$20 + 0.5\,L_{Loop}$
Accessories		
Standard elbows	0	0
Medium elbows	0	0
Long elbows	8	8
Gate valves	1	1
Globe valves	0	0
Check valves	1	0
Loop Weldolets	0	0
Loop control valves	0	0
Ball Joints	0	0

- Line 4: Pump discharge header

- Line 5: Collector field outlet header to expansion vessel or thermal storage tank

- Line 6: Steam generator supply header

- Line 7: Inter steam generator piping

- Line 8: Steam generator exit header to expansion vessel or thermal storage

The total pressure drop in the power block is given by:

$$\Delta P_{PB} = \sum_{i=1}^{7} \Delta P_{Line,i} + \Delta P_{HE} \tag{5.9}$$

Table 5.5 Piping fitting and length used for a typical power block unit. Adapted from [141]

Accessories and Pipe	Line							
	1	2	3	4	5	6	7	8
Pipe Length (m)	20	6	6	10	30	20	25	20
Expansions	1	1	0	0	0	0	0	0
Contractions	0	0	1	0	0	0	0	0
Standard elbows	0	0	0	0	0	0	0	0
Medium elbows	0	0	0	0	0	0	0	0
Long elbows	4	0	4	6	6	6	6	6
Gate valves	1	1	1	0	0	0	0	0
Globe valves	0	0	0	0	0	0	0	0
Check valves	0	0	1	0	0	0	0	0

where ΔP_{HE} is the pressure drop through the heat exchanger, which is assumed to be approximately 4 bar. The total pressure drop is given by:

$$\Delta P_{total} = \Delta P_{SF} + \Delta P_{PB} \qquad (5.10)$$

The pressure drop is iterated until the minimum allowable pressure is reached at the expansion tank. The minimum allowable pressure for various HTFs is shown in Table 5.6.

Table 5.6 Minimum and maximum allowable working temperature and pressure for different HTFs. Adapted from [4, 141]

Fluid	T_{min} (°C)	T_{max} (°C)	P_{min} (bar)
VP-1	37.8	400	15
Dowtherm Q	37.8	330	6
Dowtherm RP	37.8	350	6
Solar Salt	260	621	6
Hitec	149	538	6
Hitec XL	150	500	6

The HTF is circulated in a closed loop by using a variable speed pump [140]. The pump power is the highest parasitic load in the solar plant and therefore a variable speed pump is used to reduce the power requirements when the solar field requires flow rates less than the nominal rate. The pumping requirement is calculated as:

$$\dot{W}_{p,nom} = \rho_{HTF,T_{cold}} \, g \, \Delta P_{total} \tag{5.11}$$

At different speeds, the pump law is used and the pump work is given by [145]:

$$\dot{W}_p = \dot{W}_{p,nom} \left(\frac{\dot{m}_{SF}}{\dot{m}_{SF,nom}} \right)^3 \tag{5.12}$$

where $\dot{m}_{SF}$ is the current mass flow rate, and $\dot{m}_{SF,nom}$ is the mass flow rate at nominal condition. The pump efficiency is affected by the solar field mass flow rate as well:

$$\frac{\eta_{p,SF}}{\eta_{p,SF,nom}} = \alpha_o + 2 \, (1 - \alpha_o) \, \frac{\dot{m}_{SF}}{\dot{m}_{SF,nom}} - (1 - \alpha_o) \left(\frac{\dot{m}_{SF}}{\dot{m}_{SF,nom}} \right)^2 \tag{5.13}$$

with $\alpha_o = -0.4$ as recommended by Lippke [5]. The net electric power required by the solar field pump is:

$$\dot{W}_{net,pump} = \dot{W}_p / \eta_{p,SF} \tag{5.14}$$

During night, the solar field operates at 20% of the nominal flow rate to keep the pipes and solar collectors warm, and avoid thermal shock due to sudden temperature drops or rises. When the temperature drops beyond the minimum allowable temperature, an external heater systems is activated to avoid freezing problems.

5.3 Thermal Losses

Thermal losses take place in the solar field piping owing to the temperature difference between the HTF and the surrounding air. The way to mitigate the thermal losses is by adding insulation to the pipes, but adding too much insulation generates excessive cost with little extra benefits. For this reason, an optimum thickness is calculated at nominal conditions which minimizes the costs and thermal losses. In this chapter, the methodology developed by Bahadori and Vuthaluru [146] is used. This methodology determines the optimum economic thickness of the thermal insulation as a function of the steel pipe diameter and the surface temperature.

As a conservative assumption for insulated pipes, thermal resistances of the pipe walls and the exterior air film are neglected [147]. This assumption simplifies the calculation of thermal losses. The total thermal losses are given by:

$$
\dot{Q}_{piping} = 2\pi \left[\bar{k}_{ins,H} (T_H - T_a) \sum_i \frac{L_i}{\ln \left(\dfrac{D_{oi,pipe} + 2\,\delta_{ins,i}}{D_{oi,pipe}} \right)} + \right.
$$
$$
\left. \bar{k}_{ins,C} (T_C - T_a) \sum_j \frac{L_j}{\ln \left(\dfrac{D_{oj,pipe} + 2\,\delta_{ins,j}}{D_{oj,pipe}} \right)} \right] \tag{5.15}
$$

where $\bar{k}_{ins,H}$ is the thermal conductivity of the pipe insulation evaluated at $\bar{T}_H = (T_H + T_a)/2$, $\bar{k}_{ins,C}$ is the thermal conductivity of the pipe insulation evaluated at $\bar{T}_C = (T_C + T_a)/2$. The above Equation can be rewritten as:

$$
\dot{Q}_{piping} = 2\pi \left[\bar{k}_{ins,H} (T_H - T_a)\, \zeta_H + \bar{k}_{ins,C} (T_C - T_a)\, \zeta_C \right] \tag{5.16}
$$

192

$$\zeta_H = \sum_i \frac{L_i}{\ln\left(\frac{D_{oi,pipe} + 2\,\delta_{ins,i}}{D_{oi,pipe}}\right)}$$

$$\zeta_C = \sum_j \frac{L_j}{\ln\left(\frac{D_{oj,pipe} + 2\,\delta_{ins,j}}{D_{oj,pipe}}\right)}$$

The insulation thickness is a function of the steel outer pipe:

$$\ln\left(\delta_{ins}\right) = \sum_{n=0}^{3} \alpha_n D_o^{-n} \tag{5.17}$$

The coefficients α_n are expressed as functions of the thermal conductivity as follows:

$$\alpha_n = A_n + \frac{B_n}{k_{ins}} + \frac{C_n}{k_{ins}^2} + \frac{D_n}{k_{ins}^3} \tag{5.18}$$

The following interpolation is used for the other surface temperatures:

$$\delta_{ins} = \delta_{ins,T_1} + (T - T_1)\frac{(\delta_{ins,T_2} - \delta_{ins,T_1})}{(T_2 - T_1)} \tag{5.19}$$

where δ_1 and δ_2 are calculated at T_1 and T_2 respectively. Due to the low thermal resistance in the wall pipe, the surface temperature is assumed to be the HTF temperature. The thermal conductivity of typical insulation material used in CSP plants is shown in Table 5.7 for different temperatures. The coefficients, A_n, B_n, C_n and D_n are shown in Table 5.8.

Table 5.7 Thermal conductivity, in kW/m K, of pipe insulation materials. Data taken from [56, 148]

Temperature (°C)	Mineral Wool	Temperature (°C)	Calcium Silicate
38	0.0336	36.9	0.055
93	0.0432	91.9	0.059
149	0.0525	146.9	0.063
204	0.0624	256.9	0.075
260	0.0730	371.9	0.089
316	0.0853	476.9	0.104
371	0.0997	...	...

Table 5.8 Coefficients for calculation of the optimum economic thickness. Adapted from [146]

Coefficients	T_s=100 °C	T_s=300 °C	T_s=500 °C	T_s=700 °C
A_0	-1.619063838	-1.467341621	-1.306428735	-1.50683293
B_0	-6.0440641629 E-2	-9.4579004057 E-3	3.7689223988 E-2	1.6368010607 E-1
C_0	1.2992412636 E-3	-9.0991682769 E-4	-5.7653162538 E-3	-1.9272634157 E-2
D_0	-1.0480516067 E-5	2.1036093111 E-5	1.5920740612 E-4	6.081932874 E-4
A_1	-5.675424778 E-2	5.6420129717 E-3	2.3856855469 E-2	2.1494907991 E-1
B_1	1.1266206576 E-3	-8.1324216389 E-3	-1.7666292295 E-2	-7.236908659 E-2
C_1	-4.5476251244 E-5	3.6013086233 E-4	1.2527015231 E-3	6.2521396767 E-3
D_1	5.4011484658 E-7	-5.0991959691 E-6	-2.9095395202 E-5	-1.7702985302 E-4
A_2	1.287145175 E-3	-1.0914548287 E-3	-2.2442814135 E-3	-1.2571952312 E-2
B_2	-3.1321987972 E-5	3.1336503528 E-4	7.879778678 E-4	3.6872340957 E-3
C_2	1.3585299744 E-6	-1.3704000608 E-5	-5.6411819564 E-5	-3.1830356934 E-4
D_2	-1.6951529528 E-8	1.9239332368 E-7	1.3264010427 E-6	9.0141402462 E-6
A_3	-1.1238180847 E-5	1.4969220576 E-5	3.3668468005 E-5	1.4981731667 E-4
B_3	3.574027836 E-7	-3.3674152566 E-6	-9.9103300792 E-6	-4.2562432156 E-5
C_3	-1.5140460085 E-8	1.4658761606 E-7	7.1509244179 E-7	3.6706099161 E-6
D_3	1.8649575376 E-10	-2.0517177043 E-9	-1.6973934089 E-8	-1.0392224103 E-7

5.4 Expansion Tank

The expansion tank provides space for expansion of the HTF due to the change in volume when the HTF is heated up in the solar field to the operating temperature. The expansion tank is usually installed at the highest point in the solar field next to the pump. This tank is used to vent the moisture that accumulates in the HTF and to create positive head pressure to the pump inlet as well.

The expansion tank should be sized so that it is 25% full at ambient temperature and 75% full at the normal operating temperature [149]. Usually the expansion tank is blanketed with nitrogen to maintain a non-reactive atmosphere and keeping a positive pressure which prevents air and moisture from entering the tank [149]. The heat transfer losses from the tank to the surrounding air are significant and should be taken into account along with the thermal piping losses to calculate the total thermal losses in the solar field. The increment in the HTF volume is given by:

$$
\begin{aligned}
\Delta V_{HTF} &= \left(\frac{\rho_{T_{ref}}}{\rho_{T_C}} - 1 \right) \left(V_c + \frac{1}{4} V_{exp,tank} N_{tank} \right) + \left(\frac{\rho_{T_{ref}}}{\rho_{T_H}} - 1 \right) (V_H + V_{collectors} \\
&\quad + V_{in,out}) + \left(\frac{\rho_{T_{ref}}}{\rho_{T_H}} - 1 \right) V_H
\end{aligned}
\tag{5.20}
$$

$$
V_c = \frac{\pi}{4} \sum_i D_{innner,i}^2 L_i
\tag{5.21}
$$

$$
V_H = \frac{\pi}{4} \sum_j D_{innner,j}^2 L_j
\tag{5.22}
$$

$$
V_{collector} = \frac{\pi}{4} n_{loops} D_{receiver}^2 L_c
\tag{5.23}
$$

where $\rho_{T_{ref}}$ is the density of the HTF calculated at reference condition, 25 °C, ρ_{T_C} is the density of the HTF calculated at cold temperature, ρ_{T_H} is the density of the HTF calculated at hot temperature, V_c is the total volume of the cold header, $V_{in,out}$ is the total volume of the inlet and outlet pipe of the collector loop, and V_c is the total volume of solar receiver.

For the solar field, multiple expansion tanks with a volume of 283 m^3 [140] were selected. The dimensions of this tank are approximately: $D_{tank} = 6$ m and $H_{tank} = 10$ m. The number of tanks is calculated as:

$$N_{tank} = \begin{cases} \Delta V_{HTF} / \frac{1}{2} V_{exp,tank} & \text{if mod}\left(\Delta V_{HTF}, \frac{1}{2} V_{exp,tank} \right) = 0 \\ \text{int}\left(\Delta V_{HTF} / \frac{1}{2} V_{exp,tank} \right) + 1 & \text{if mod}\left(\Delta V_{HTF}, \frac{1}{2} V_{exp,tank} \right) \neq 0 \end{cases} \tag{5.24}$$

The procedure for heat losses in the expansion tank was taken from the methodology developed by Kumana and Kothari [150]. For the heat loss calculation in the expansion tank it is assumed that:

- Fouling factors are negligible

- Radiation losses are negligible

- Temperature in the gas and liquid sections is uniform

- Thermal equilibrium exists between the gas and the liquid fluid

As shown in Figure 5.3, the four individual losses in the tank need to be calculated. The heat loss from each surface is shown below. For dry sidewall:

$$\dot{Q}_d = U_d A_d \left(T_{gas} - T_\infty \right) \tag{5.25}$$

196
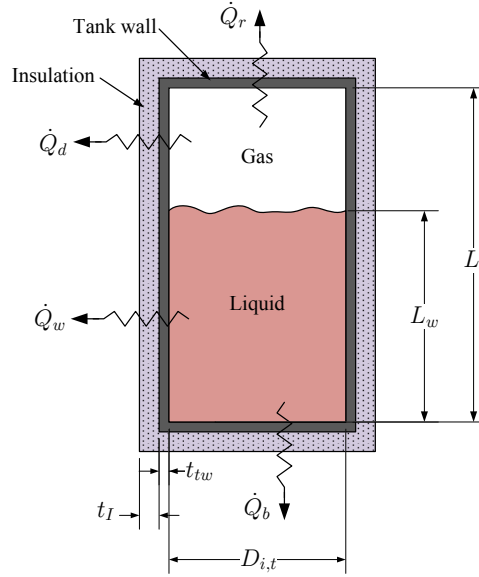
Figure 5.3 Thermal losses from a vertical tank. Adapted from [150]

$$U_d = \left[\frac{1}{h_{\infty,d}} + D_I \frac{\ln\left(D_I/D_{o,t}\right)}{2\,k_I} + D_I \frac{\ln\left(D_{o,t}/D_{i,t}\right)}{2\,k_{tw}} + \frac{1}{h_{gas,d}} \left(\frac{D_I}{D_{i,t}}\right) \right]^{-1} \tag{5.26}$$

$$A_d = \pi\,D_I\,(L - L_w) \tag{5.27}$$

$$D_I = D_{i,t} + 2\,t_{tw} + 2\,t_I \tag{5.28}$$

For wet sidewall:

$$\dot{Q}_w = U_W\,A_{Ww}\left(T_{Liquid} - T_\infty\right) \tag{5.29}$$

$$U_w = \left[\frac{1}{h_{\infty,w}} + D_I \frac{\ln\left(D_I/D_{o,t}\right)}{2\,k_I} + D_I \frac{\ln\left(D_{o,t}/D_{i,t}\right)}{2\,k_{tw}} + \frac{1}{h_{Liquid,w}} \left(\frac{D_I}{D_{i,t}}\right) \right]^{-1} \tag{5.30}$$

$$A_w = \pi\,D_I\,L_w \tag{5.31}$$

For tank bottom:

$$\dot{Q}_b = U_b\,A_b\left(T_{Liquid} - T_\infty\right) \tag{5.32}$$

$$U_b = \left[\frac{1}{h_{\infty,b}} + \frac{t_I}{k_I} + \frac{t_{tw}}{k_{tw}} + \frac{1}{h_{Liquid,b}} \right]^{-1} \tag{5.33}$$

$$A_b = \pi D_{i,t}^2 / 4 \tag{5.34}$$

For tank roof:

$$\dot{Q}_r = U_r A_r \left(T_{Gas} - T_\infty \right) \tag{5.35}$$

$$U_r = \left[\frac{1}{h_{\infty,r}} + \frac{t_I}{k_I} + \frac{t_{tw}}{k_{tw}} + \frac{1}{h_{gas,r}} \right]^{-1} \tag{5.36}$$

$$A_r = \pi D_{i,t}^2 / 4 \tag{5.37}$$

Therefore, the total heat losses are:

$$\dot{Q}_{tank,losses} = \dot{Q}_d + \dot{Q}_w + \dot{Q}_b + \dot{Q}_r \tag{5.38}$$

The convective heat transfer coefficients are detailed below. $h_{\infty,d}$ and $h_{\infty,w}$ are calculated for two cases: wind or no wind condition. For the wind condition a cylinder in cross flow is used. The average Nusselt number recommended for a cylinder in cross flow [53] is given by:

$$Nu_D = c\, Re_D^m\, Pr^n \left(\frac{Pr}{Pr_w} \right)^p \tag{5.39}$$

$$h_{\infty,d} = \frac{Nu_D\, k_{air}}{D_I} \tag{5.40}$$

$$h_{\infty,w} = \frac{Nu_D\, k_{air}}{D_I} \tag{5.41}$$

The constants suggested for this equation are tabulated in Table 3.8. The value of p depends on the heat flux direction: $p = 0.25$ for fluid heating and $p = 0.2$ for fluid cooling. For no

wind condition, natural convection is used and the vertical cylinder can be approximated as a vertical plate, Kakaç et al. [53] recommend to use the following expression:

$$Nu_L = \left\{ 0.825 + \frac{0.387\,Ra_L^{1/6}}{\left[1+(0.492/Pr)^{9/16}\right]^{8/27}} \right\}^2 \quad \left(10^{-1} \leq Ra_L \leq 10^{12}\right) \qquad (5.42)$$

for

$$\frac{D}{L} \geq \frac{35}{Gr_L^{1/4}} \qquad (5.43)$$

with

$$Gr_L = \frac{g\,\beta\,(T_s - T_\infty)\,L^3}{v^2} \qquad (5.44)$$

where L is the high of the cylinder in m, D is the diameter of the cylinder in m, v: Kinematic viscosity in m^2/s. When D/L is not large enough, Kakaç et al. [53] recommend the following correlation:

$$Nu_L = \frac{4}{3} \left[\frac{7\,Gr_L\,Pr^2}{5\,(20+21\,Pr)} \right]^{1/4} + \frac{4\,(272+315\,Pr)}{35\,(64+63\,Pr)}\,(L/D) \qquad (5.45)$$

$$h_{\infty,d} = \frac{Nu_L\,k_{air}}{L - L_w} \qquad (5.46)$$

$$h_{\infty,w} = \frac{Nu_L\,k_{air}}{L_w} \qquad (5.47)$$

The no wind condition is also used for the calculation of $h_{gas,d}$ and $h_{Liquid,w}$. The same cases, wind and no wind condition, are presented for horizontal plates (top and bottom). For no wind condition a flat surface approximation under natural convection is used.

Natural convection , upper surface of hot plate or lower surface of cold plate ($h_{\infty,r}$, $h_{gas,r}$) [111]:

$$Nu_{L_D} = 0.54\, Ra_L^{1/4} \qquad\qquad \left(10^4 \le Ra_L \le 10^7\right) \qquad\qquad (5.48)$$

$$Nu_{L_D} = 0.15\, Ra_L^{1/4} \qquad\qquad \left(10^7 \le Ra_L \le 10^{11}\right) \qquad\qquad (5.49)$$

Natural convection, lower surface of hot plate or upper surface of cold plate ($h_{\infty,b}$, $h_{Liquid,r}$) [111]:

$$Nu_{L_D} = 0.27\, Ra_L^{1/4} \qquad\qquad \left(10^5 \le Ra_L \le 10^{10}\right) \qquad\qquad (5.50)$$

with

$$L_D = \frac{A_s}{P} = \frac{D_{i,t}}{4} \qquad\qquad (5.51)$$

$$Ra_{L_D} = \frac{g\,\beta\,(T_s - T_\infty)\,L_D^3}{\nu\,\alpha} \qquad\qquad (5.52)$$

$$h = \frac{Nu_{L_D}\,k}{L_D} \qquad\qquad (5.53)$$

where A_s and P are the plate surface area and perimeter, respectively. For wind condition ($h_{\infty,b}$ and $h_{\infty,r}$), the wind enhancement factor ζ_w is calculated as [150]:

$$\zeta_w = \frac{h_{\infty,w}\big|_{wind}}{h_{\infty,w}\big|_{no,\,wind}} \qquad\qquad (5.54)$$

and

$$h_{\infty,b}\big|_{wind} = \zeta_w\left(h_{\infty,b}\big|_{no\,wind}\right) \qquad\qquad (5.55)$$

$$h_{\infty,r}\big|_{wind} = \zeta_w\left(h_{\infty,r}\big|_{no\,wind}\right) \qquad\qquad (5.56)$$

In order to calculate the heat transfer coefficients, it is necessary to obtain the wall temperatures which require an iterative procedure. The total heat losses are calculated as:

$$\dot{Q}_{total,tank} = \dot{Q}_{tank,losses,full} N_{tank,full} + \dot{Q}_{tank,losses,partial}$$

$$+ \dot{Q}_{tank,losses,empty} N_{tank,empty} \qquad (5.57)$$

where $\dot{Q}_{tank,losses,full} N_{tank,full}$ is the total heat losses for the tanks completely filled $(0.75\,V_{exp,tank})$, $\dot{Q}_{tank,losses,partial}$ is the total heat losses for the tank partially filled $(V < 0.75\,V_{exp,tank})$, and $\dot{Q}_{tank,losses,empty} N_{tank,empty}$ is the total heat losses for the tanks filled at nominal conditions $(0.25\,V_{exp,tank})$.

5.5 Conclusions

A comprehensive model for the pressure drop and pumping power requirement of a solar field was performed. The model calculates the diameter and pressure drop in each header section based on the pipe stress calculation and HTF flow rate distribution.

A heat losses model was also carried out for the piping system and the expansion tank. The model calculates the thermal losses of the solar field piping for the optimum economic thickness of the thermal insulation in each header section. For the expansion tank, the thermal losses are calculated individually for the gas and liquid sections.

Chapter 6

Integration of System Components

In the previous chapters the different subsystems of the PTC solar power plant were designed for nominal and partial conditions. In the final step, the subsystems must be integrated into the plant and work together. For example, the energy coming from the solar field runs the power block, the power block is affected by the ambient conditions and at the same time the return HTF temperature from the power block affects the output from the solar field. This kind of connection between the subsystems of the solar power plant affect its performance under steady and transient conditions. Initially a preliminary design under steady state conditions is performed, in the following steps:

- Calculation of Direct Normal Radiation (DNI).

- Calculation of the DNI cumulative frequency distribution (CFD), at this step a DNI with 95 % of the cumulative frequency is selected as the reference radiation for the preliminary design.

- Power block design:

  - HTF selection.

  - Conditions of operation of the power block (low pressure, high pressure, turbine efficiency,etc).

202

- Temperature drop and mass flow rate of the HTF.

- Calculation of the parasitic losses in the condenser system.

- Selection of the solar collector.

- Solar collector performance under reference conditions: mass flow rate at nominal conditions and the heat gained.

- Selection of solar field layout and determination of the number of loops.

- Calculation of the maximum pressure drop through the solar field.

- Calculation of pumping power requirement and heat losses.

- Calculation of the expansion tank volume and heat losses.

- Hourly simulation.

- Calculation of the optimum size by LCOE and solar energy utilization .

Figure 6.1 shows a flowchart of the different steps described above.

6.1 Transient Analysis

Although it is commonly assumed that the solar power plant operates under steady state conditions, this assumptions is not true for most of the operation time. In this case, a transient analysis is necessary to incorporate the thermal inertia of the system. The transient energy balance of a Solar Collector Assembly (SCA) is given by [151] (Figure 6.2):

$$\frac{d}{dt}\left(m_{collector}\, C_{HTF}\, T\right) = \dot{m}_{HTF}\, C_{HTF}\, \left(T_{in} - T\right) + \dot{Q}_u \tag{6.1}$$
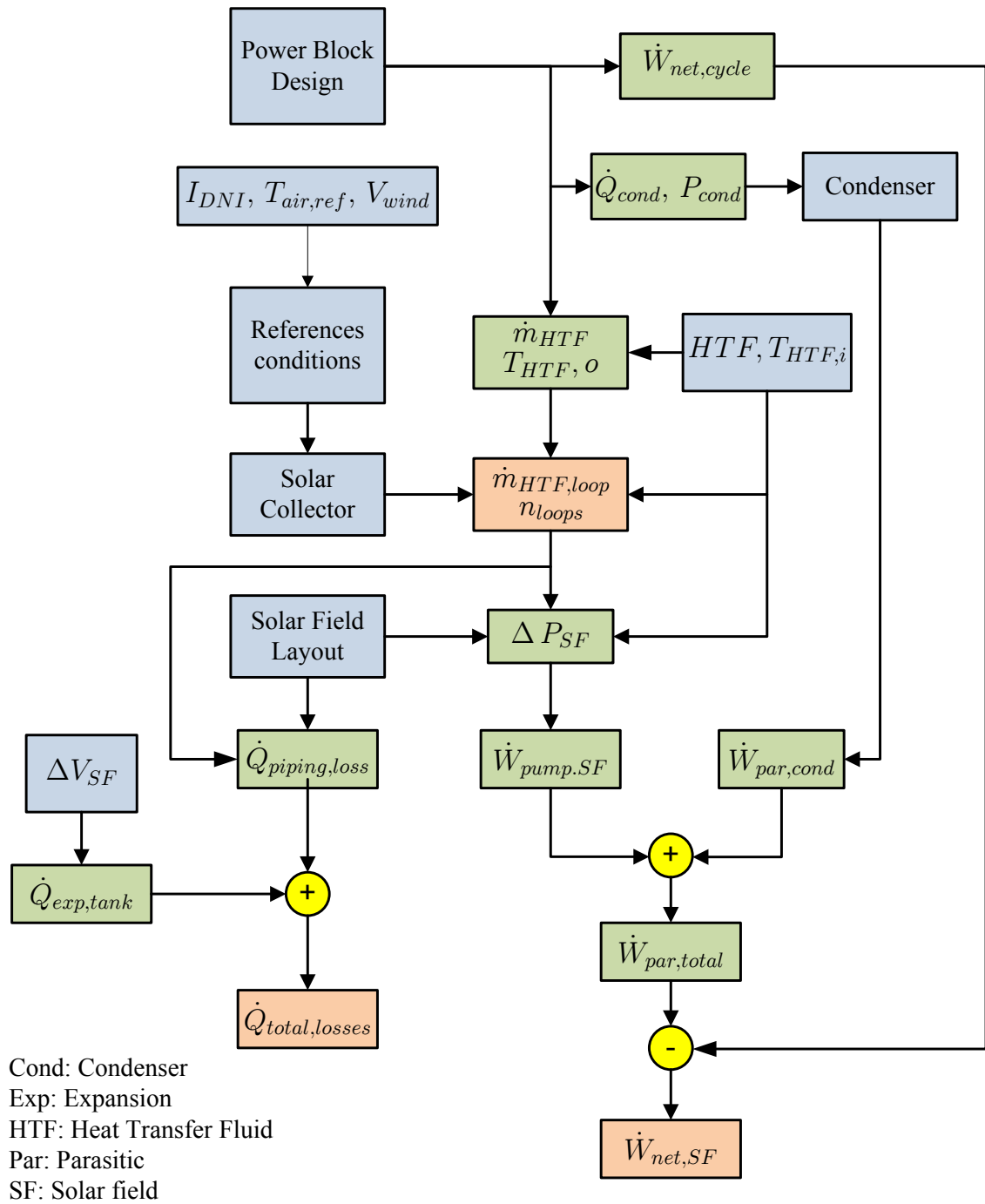
Figure 6.1 Logic flow for the preliminary design of the PTC solar plants

Cond: Condenser
Exp: Expansion
HTF: Heat Transfer Fluid
Par: Parasitic
SF: Solar field
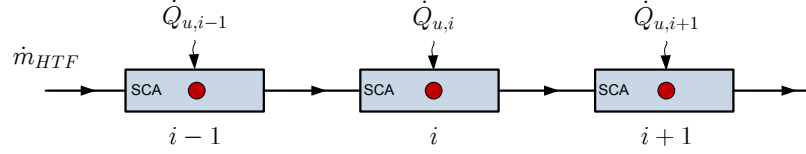
Figure 6.2 Node analysis of the solar collector assembly (SCA)

Integrating the last expression, it is obtained that:

$$\int_{t_1 0}^{t_1 + \Delta t} \frac{dT}{T - T_{in} - \dot{Q}_u / \dot{m}_{HTF} \, C_{HTF}} = -\frac{\dot{m}_{HTF}}{m_{collector}} \int_{t_1 0}^{t_1 + \Delta t} dt \tag{6.2}$$

$$
\begin{aligned}
T\,(t_1 + \Delta t_1) &= \left(T\,(t_1) - T_{HTF,in} - \frac{\dot{Q}_u}{\dot{m}_{HTF}\, C_{HTF}} \right) \exp\left(-\frac{\dot{m}_{HTF}}{m_{collector}} \Delta t \right) \\
&\quad + T_{HTF,in} + \frac{\dot{Q}_u}{\dot{m}_{HTF}\, C_{HTF}}
\end{aligned} \tag{6.3}
$$

Using a nodal notation, the last expression can be rewritten as:

$$
\begin{aligned}
T_i^{n+1} &= \left(T_i^n - T_{i-1}^n - \frac{\dot{Q}_{u,i}}{\dot{m}_{HTF}\, C_{HTF,i}} \right) \exp\left(-\frac{\dot{m}_{HTF}}{V_{SCA}\, \rho_i} \Delta t \right) \tag{6.4} \\
&\quad + T_{i-1}^n + \frac{\dot{Q}_{u,i}}{\dot{m}_{HTF}\, C_{HTF,i}} \tag{6.5}
\end{aligned}
$$

$$V_{SCA} = \frac{\pi}{4} D_{abs}^2 L_c$$

where T_i^{n+1} is the temperature at node i in the next time step.

The same transient analysis is employed for the the pipe header, after applying the energy balance to the system (Figure 6.3) the next ordinary differential equation (ODE) is found:

$$\frac{d}{dt}\,(m_T\, C_T\, T) = \dot{m}_f\, C_{HTF}\,(T_{in} - T) - \dot{Q}_{loss} \tag{6.6}$$
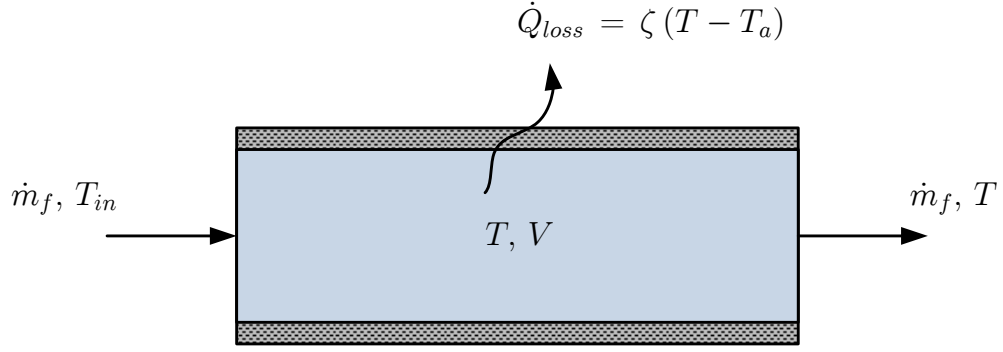
Figure 6.3 Thermal capacitance analysis of the pipe header

$$\dot{Q}_{loss} = \zeta \left(T - T_a \right)$$

Integrating:

$$\int_{t_1 0}^{t_1 + \Delta t} \frac{dT}{T - T_p} = -\frac{\dot{m}_f C_{HTF} + \zeta}{m_T C_T} \int_{t_1 0}^{t_1 + \Delta t} dt \qquad (6.7)$$

$$T_p = \frac{\dot{m}_f C_{HTF} T_{in} + \zeta T_a}{\dot{m}_f C_{HTF} + \zeta}$$

$$T \left(t_1 + \Delta t_1 \right) = T_p + \left(T \left(t_1 \right) - T_p \right) \exp \left(-\frac{\dot{m}_f C_{HTF} + \zeta}{m_T C_T} \Delta t \right) \qquad (6.8)$$

which may be rewritten as:

$$T^{n+1} = T_p + \left(T^n - T_p \right) \exp \left(-\frac{\dot{m}_f C_{HTF} + \zeta}{m_T C_T} \Delta t \right) \qquad (6.9)$$

The last Equation can be used for the thermal capacitance calculation of the hot header, cold heater and expansion tank. The term $m_T C_T$ includes the thermal capacitance of the HTF, pipe walls and insulation. In this simulation, the thermal capacitance of the pipe walls and insulation was distributed uniformly over the solar field. The same assumption was used for the HTF in the hot and cold headers. Figures 6.4 and 6.5 show the distribution

206
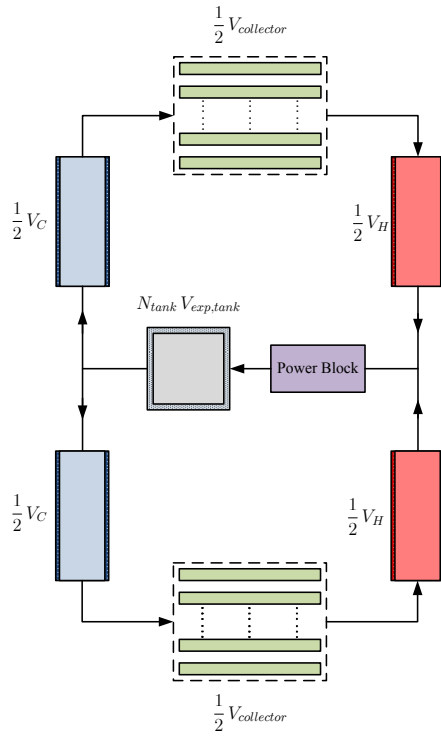
Figure 6.4 Thermal inertia distribution for I layout
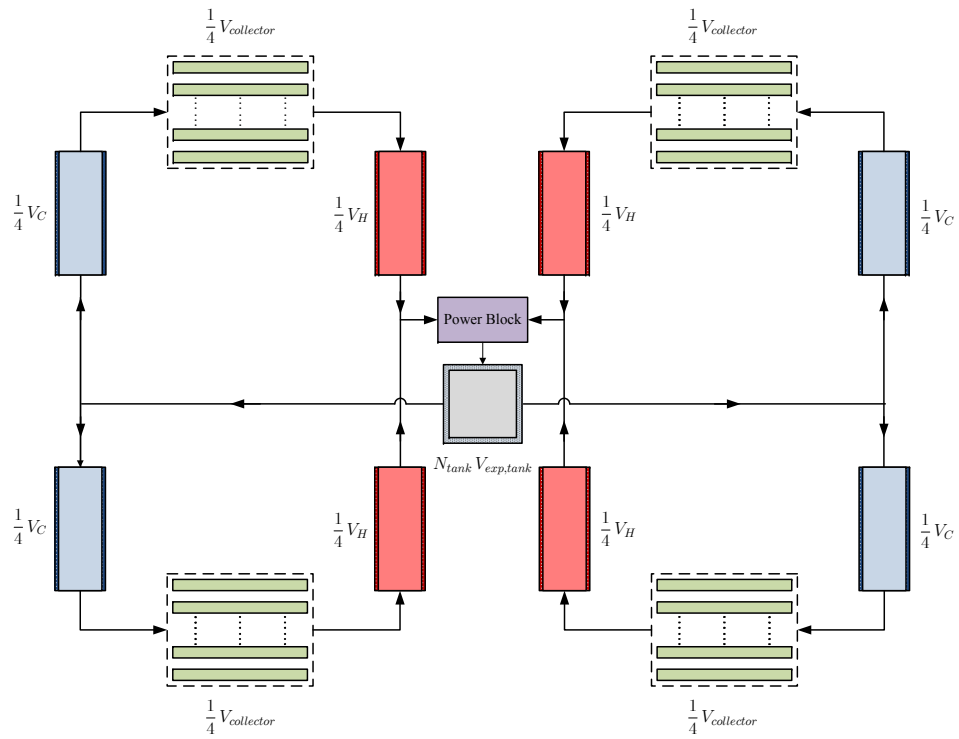
Figure 6.5 Thermal inertia distribution for H layout
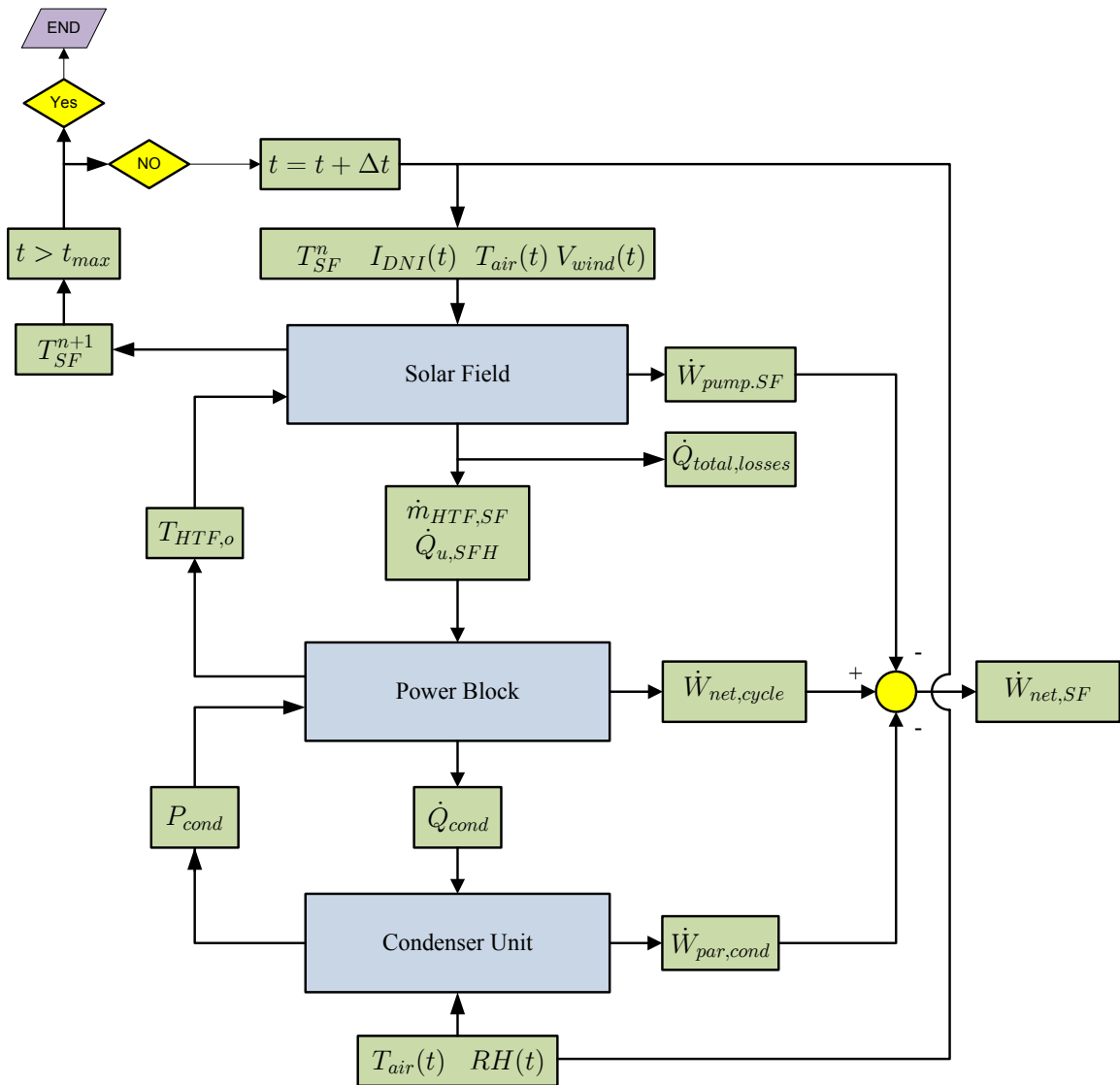
Figure 6.6 Logic flow used for the dynamic simulation of the PTC solar power plant

of the thermal inertia assumed through the solar field for I and H layouts. Figure 6.6 shows the logic flow used for the dynamic simulation of the systems, in this case all the systems should be simultaneously solved.

6.2 Economic Analysis

The levelized cost of energy (LCOE) is the cost that, if assigned to every unit of electricity produced by the solar power plant over the project life, will equal the total life-cycle cost (TLCC) when discounted back to the base year [152]. LCOE is used to compare the cost of electricity generated by a renewable resource (in this case solar energy) with the equivalent fossil fuel unit or to optimize the solar field under different scenarios. The LCOE without incentives is given by [152, 153]:

$$LCOE = \frac{I + \sum_{n=1}^{N} \left[Cost_{annual,n} / (1+d)^n \right] \times (1 - TR)}{\sum_{n=1}^{N} \dot{E}_{annual} (1 - R_d)^n / (1+d)^n} \qquad (6.10)$$

where I is the initial investment, $Cost_{annual}$ is the annual Fuel and O&M costs, d is the discount rate, TR is the tax rate, R_d is the system degradation rate, $\dot{E}_{annual}$ is the net annual power output in kWh, and N is the project life. The total investment is the sum of direct and indirect costs. The direct costs are given by [15, 152]:

$$DC = \left[(SI + SF + HTF_{system}) A_{SF} + C_{storage} + C_{FB} + C_{PB} \right] (1 + F_{contingency}) \qquad (6.11)$$

where SI is the site improvements cost, SF is the solar field cost, HTF_{system} is the cost of the HTF, A_{SF} is the total area of the solar field, $C_{storage}$ is the cost of the storage energy,

C_{FB} is the cost of fossil back up, C_{PB} is the cost of the power block, and $F_{contingency}$ is the contingency factor. The indirect costs are as follows:

$$IC = DC\,(EPC + PLM + ST) \tag{6.12}$$

where EPC is the engineer, procure and construct cost, PLM is the project, land and management cost, and ST is the sale Tax. The annual costs are calculated as:

$$Cost_{annual} = FC + FCC\,P_{nom} + VCG\,\dot{E}_{annual}\,(\text{MWh}) + C_{Fuel} \tag{6.13}$$

where FC is the fixed annual Cost, FCC is the fixed cost by capacity, VCG is the variable cost per generation, and C_{Fuel} is the fuel cost. Table 6.1 shows the values assumed for the economic analysis. The discount rate is used for the calculation of the present value by taking into account the time value. Two different analyses can be performed by accounting for the inflation: nominal discount rate (include inflationary effects), and real discount rate (exclude inflationary effects). Discount rate can be converted from real to nominal and vice versa by using the following formulas [152]:

$$
\begin{aligned}
d_n &= (1+d_r)\,(1+e) - 1 \\
d_r &= [(1+d_r)/(1+e)] - 1
\end{aligned}
\tag{6.14}
$$

where d_n is the nominal discount rate, d_r is the real discount rate, and e is the inflation rate. On the other hand, the effective tax rate, or combined state and federal tax rate is calculated as [152]:

$$TR = STR + FTR\,(1 - STR) \tag{6.15}$$

where STR is the state tax rate, and FTR is the federal tax rate.

210

Table 6.1 Costs, taxes and discount rate assumed for the economical analysis. Values taken from [15, 140, 152]

Direct Cost	Value	Units
Site Improvements	25	$/m^2
Solar Field	295	$/m^2
HTF System	90	$/m^2
Storage	80	$/kWht
Fossil Backup	0	$/kW
Power Block (Wet-Cooled)	940	$/kW
Power Block (Dry-Cooled)	1160	$/kW
Contingency	10	% DC
Indirect Cost		
Engineer, Procure and Construct	15	%DC
Project, Land and Management	3.5	%DC
Sales Tax	7.75	% DC
O&M Cost		
Fixed Annual Cost	0	$/yr
Fixed Cost by Capacity	70	$/kW-yr
Variable Cost per Generation	3	$/MWh
Fuel Cost	0	$/MWh
Taxes, Interest and System Degradation		
Real Discount Rate	8	%
Inflation Rate	2.5	%
Federal Tax Rate	35	%
State Tax Rate	8	%
Annual Degradation Rate	0.5	%
Project Life	30	years

6.3 Results

The solar power plant was simulated every hour by using the monthly average values. Table 6.2 shows the parameters used for the hourly simulation. The solar field size was increased by adding even collector loops to the solar layout, and a parametric analysis was then carried out to get the optimum size.

Table 6.2 Parameter used for the hourly simulation

Nominal Power Output	50 MW$_e$
Hours of Thermal Storage (TES):	0
Solar Radiation Data:	TMY3
Location:	Tampa, Daggett
HTF:	VP1
Solar Collector:	LS-3
Solar Receiver:	UVAC Annulus under vacuum, P = 10^{-4} Torr
Layout:	H
$\eta_{SF,pump}$ [5]:	60%
$\dot{m}_{SF,night}$ [141]:	20%
$\dot{m}_{SF,day,min}$:	20%
Condenser:	Cooling Tower Air Cooled Condenser

The results obtained for the cooling tower used as the cooling system for the power block are presented in Tables 6.3 and 6.4. As it was expected, there is a minimum LCOE which corresponds to the optimum solar plant size. For Tampa this number corresponds to 136 collector loops, while for Daggett the optimum LCOE corresponds to 88 collector loops. The difference in the optimum number of loops is related to the solar radiation distribution.

212

Table 6.3 Results obtained for Tampa. Parameters used for the simulation are given in Table 6.2

A_{SF} (m^2)	n_{loops}	$\dot{W}_{net,cycle}$(kW)	$\dot{W}_{par}$(kW)	C_{Factor}(%)	$LCOE_R$ (¢/kWh)	$LCOE_N$(¢/kWh)	Net Power (GWh)
246343.6	72	49312.8	2344.4	14.3	37.3	45.9	59.0
273715.2	80	49312.8	2532.2	16.3	35.1	43.2	66.8
301086.7	88	49312.8	2678.4	18.2	33.4	41.1	74.7
328458.2	96	49312.8	2863.4	20.3	32.0	39.4	82.6
355829.7	104	49312.8	3020.6	22.1	31.1	38.4	89.7
383201.2	112	49312.8	3202.7	23.8	30.4	37.6	96.4
410572.8	120	49312.8	3367.1	25.5	29.9	37.0	102.8
437944.3	128	49312.8	3555.7	27.1	29.7	36.7	108.8
465315.8	136	49312.8	3760.6	28.5	29.6	36.7	113.8
492687.3	144	49312.8	3899.6	29.6	29.8	36.8	118.2
520058.8	152	49312.8	4112.1	30.8	30.0	37.1	122.3
547430.4	160	49312.8	4294.4	31.8	30.3	37.6	125.7

Table 6.4 Results obtained for Daggett. Parameters used for the simulation are given in Table 6.2

A_{SF} (m^2)	n_{loops}	$\dot{W}_{net,cycle}$(kW)	$\dot{W}_{par}$(kW)	C_{Factor}(%)	$LCOE_R$ (¢/kWh)	$LCOE_N$(¢/kWh)	Net Power (GWh)
191600.6	56	49312.8	2481.3	18.8	24.8	30.3	77.1
218972.2	64	49312.8	2762.6	22.3	22.6	27.7	90.9
246343.7	72	49312.8	3053.1	25.6	21.3	26.1	103.6
273715.2	80	49312.8	3321.5	28.2	20.8	25.6	113.4
301086.7	88	49312.8	3619.3	30.2	20.7	25.5	120.7
328458.2	96	49312.8	3891.9	31.4	21.2	26.1	124.9
355829.8	104	49312.8	4197.1	32.7	21.6	26.7	129.0
383201.3	112	49312.8	4468.3	33.9	22.1	27.2	133.1
410572.8	120	49312.8	4766.8	34.9	22.6	28.0	136.2
437944.3	128	49312.8	5047.6	35.7	23.3	28.9	138.3
465315.8	136	49312.8	5360.0	36.2	24.2	29.9	139.5
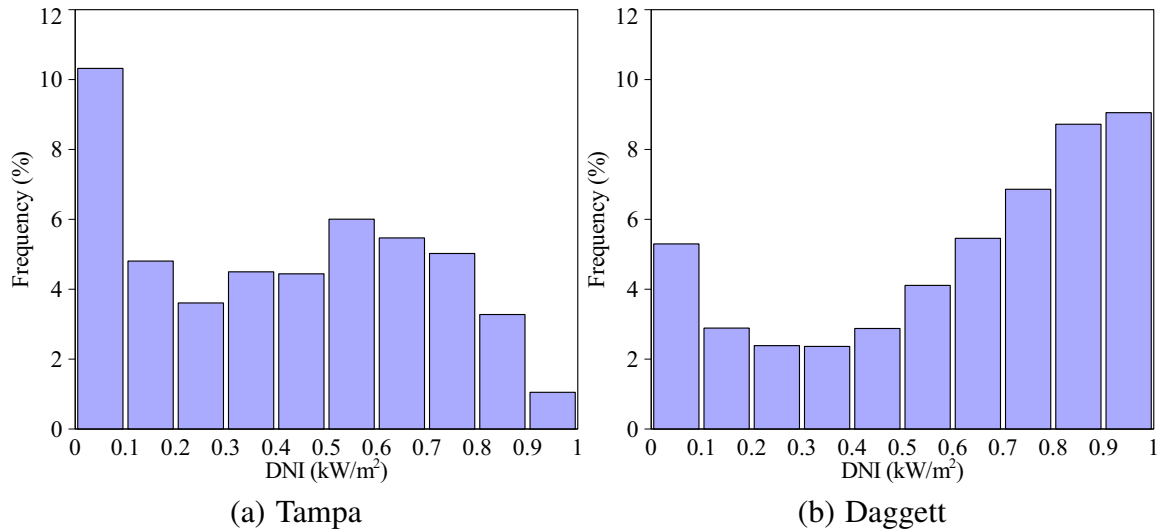
Figure 6.7 Frequency distribution of Direct Normal Irradiance (DNI)

As seen in Figure 6.7, the frequency distribution of Direct Normal Irradiance (DNI) for Tampa shows that its DNI is below 500 W/m^2 for almost 27% of the year the while for Daggett it is only for 15.8 % of the year. This implies that , for Tampa, in order to increase the annual output from the solar field an appreciable increase in the solar field size is required to compensate for those months when the solar radiation is low. For the case of Daggett, higher radiation is obtained during the whole year and therefore the solar field size is smaller as compared with Tampa. This is evidenced by Figure 6.8, which shows that for Daggett a more uniform monthly average net power output is obtained as compared to Tampa.

In order to validate the results obtained from the proposed model, it was compared with a model developed by NREL, the Solar Advisor Model (SAM) [15]. Figures 6.9 and 6.10 show the results obtained, levelized cost of electricity evaluated at real discount rate (LCOE$_R$), and the annual net power output, for Tampa and Daggett respectively. The

215

(a) Tampa

(b) Daggett
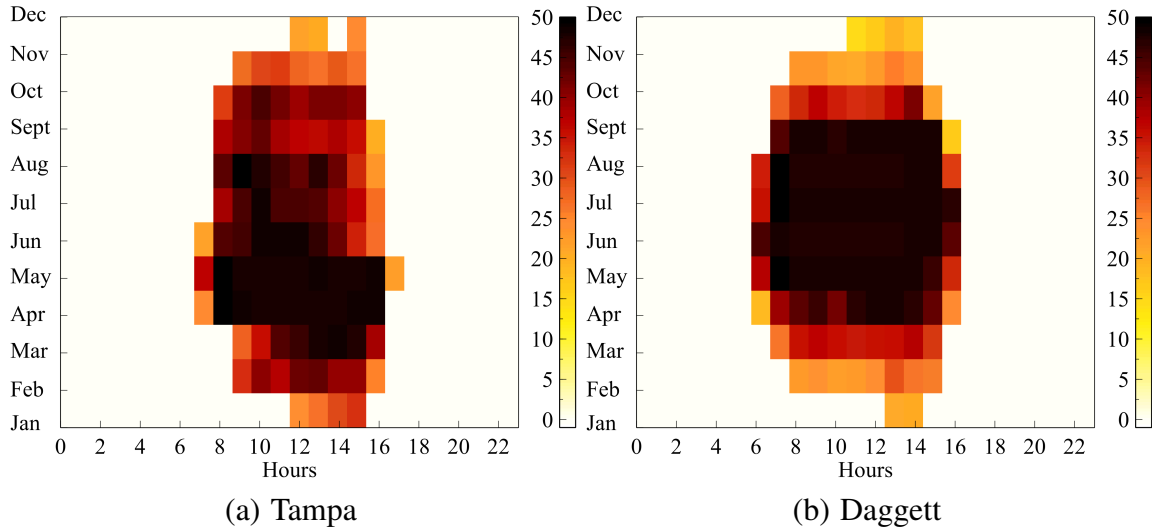
Figure 6.8 Monthly average distribution of the net power output calculated at minimum LCOE$_R$. Parameters used for the simulation are given in Table 6.2

results show that the proposed model follows the trend given by SAM, but there are some discrepancies. The assumptions and modeling of the physical phenomena are different in both of these models, hence it is expected that the results obtained would have some

(a) LCOE$_R$

(b) Annual Net Power Output
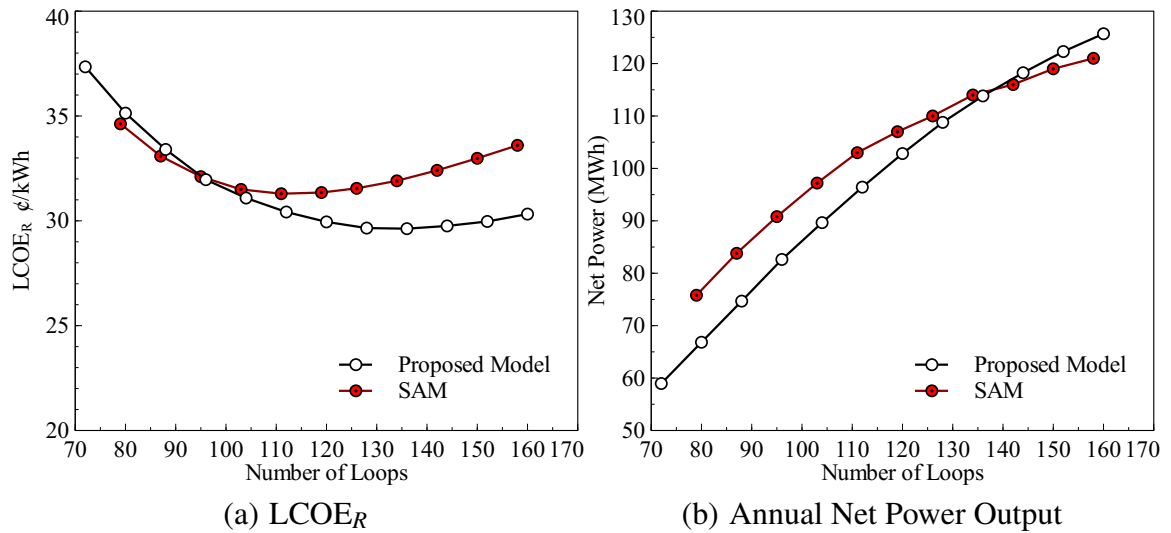
Figure 6.9 Comparison of the LCOE$_R$ and annual net power output between the proposed model and System Advisor Model (SAM) [15], location: Tampa. Parameters used for the simulation are given in Table 6.2

(a) LCOE$_R$ (b) Annual Net Power Output
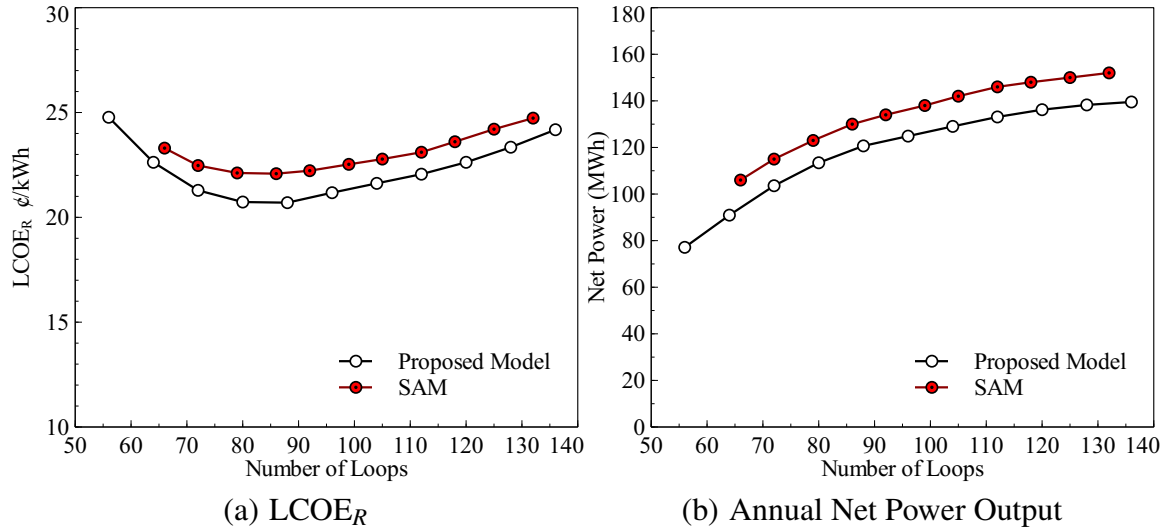
Figure 6.10 Comparison of the LCOE$_R$ and annual net power output between the proposed model and System Advisor Model (SAM) [15], location: Daggett. Parameters used for the simulation are given in Table 6.2

differences. As it was explained in chapter 3, the proposed model is more conservative than the models developed by NREL, which explains why the net power output obtained from the model is lower than the results obtained by SAM in both cities. The LCOE$_R$ calculated from the proposed model is also lower than the values obtained from SAM due to the difference in the annual cost which is proportional to the annual net power output.

Another important parameter for the design of the PTC solar power plant is the utilization of solar energy which is a measure of how much of the collected solar energy is used by the power block [12]. The utilization is defined as:

$$\text{Utilization} = \frac{(\text{Collected-Dissipated})_{Solar\ energy}}{\text{Collected}_{Solar\ energy}} \qquad (6.16)$$

217

(a) Tampa

(b) Daggett
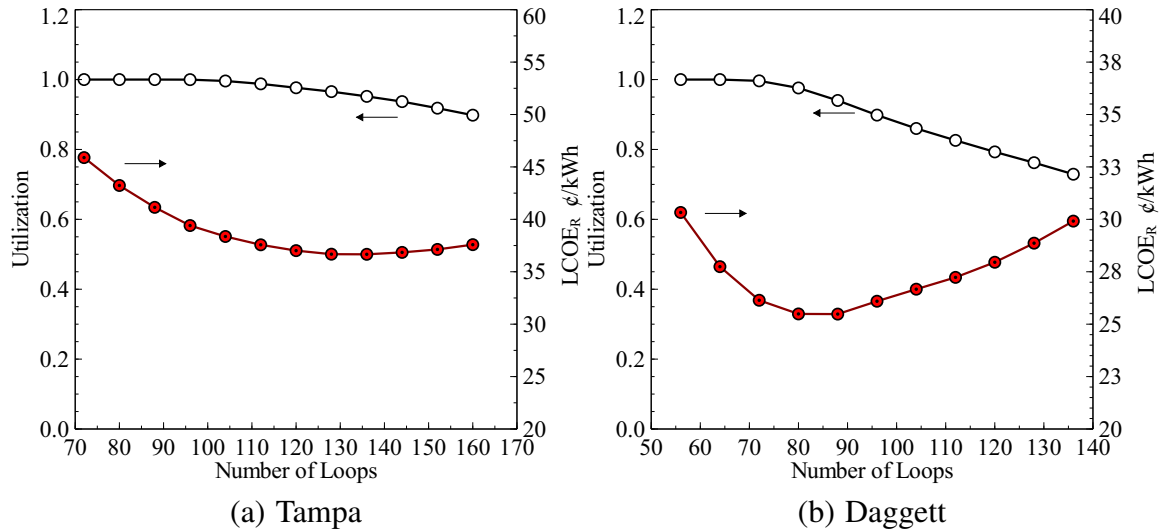
Figure 6.11 Effect of the number of loops on the LCOE$_R$ and the utilization factor. Parameters used for the simulation are given in Table 6.2

A utilization value less than unity means that the collected energy is more than what can be used to run the power block, and therefore a part of the energy collected by the solar field is dumped. Figure 6.11 shows the utilization value as function of the solar field size.

Utilization values equal to unity are obtained for solar field sizes close to the reference conditions, but in order to decrease the LCOE, it is necessary to increase the net power output by increasing the solar field size and consequently the utilization factor decreases due to more energy having to be dumped. This can be avoided by incorporating a storage system to the solar plant or by defocusing the solar collectors at high solar irradiance.

6.3.1 Results for Air Cooled Condensers

After performing the analysis using the convectional wet cooling method for condensers, an analysis of the effect of the alternative condensing method (air cooled condenser) on the solar power plant performance was carried out. Initially the number of air cooled condenser units was determined. The results obtained are presented in Figure 6.12;

218

(a) Tampa (b) Daggett
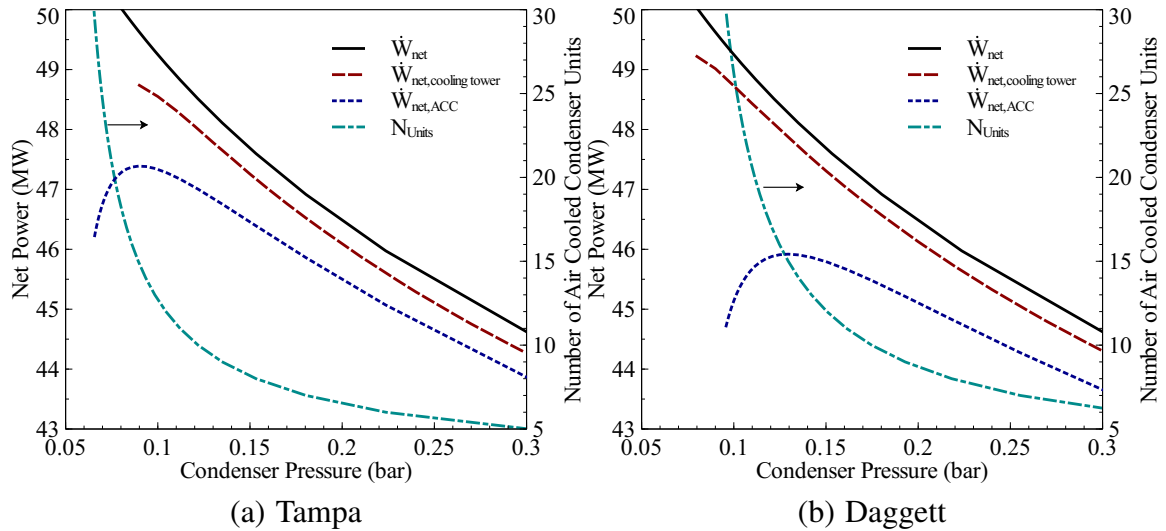
Figure 6.12 Effect of the condensing method on the power cycle performance

the best performance corresponds to the evaporative method since the minimum condensing water temperature is limited by the wet bulb air temperature. For the case of air cooled condenser, the net power output is lower than the evaporative case owing to the high fan power requirement.

As seen in Figure 6.12, the performance of air cooled condenser has an optimum number of condenser units, in which there is a balance between the cycle power output and parasitic losses. For both cities, the optimum number of air cooled condenser units are 15. For the case of Tampa, the condenser pressure near the design conditions (0.08 bar) can be achieved, but for Daggett higher condenser pressures are expected due to its location. Figure 6.13 shows the monthly average distribution of the condenser pressure for the two cooling methods proposed. For Tampa, high relative humidity and relative high air temperature are present during most of the year, therefore air cooled condenser gives a little improvement in the condenser pressure but its high power requirements decrease the net
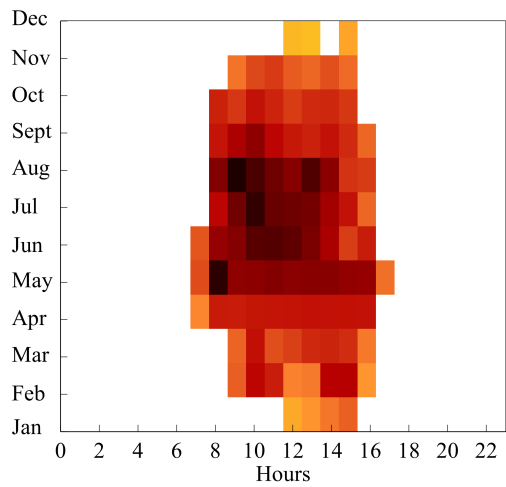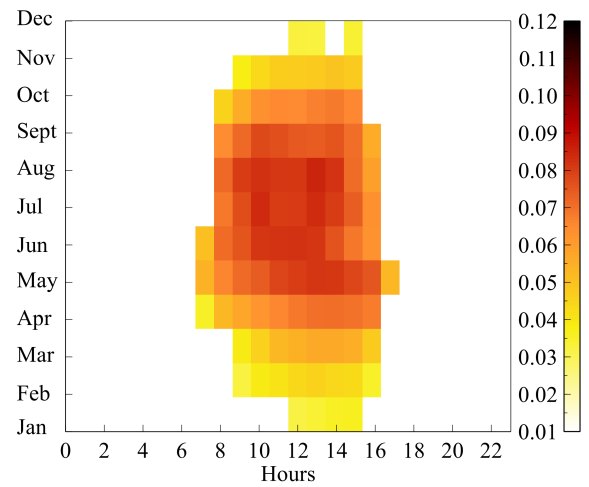
Cooling Tower   Air Cooled Condenser

(a) Tampa
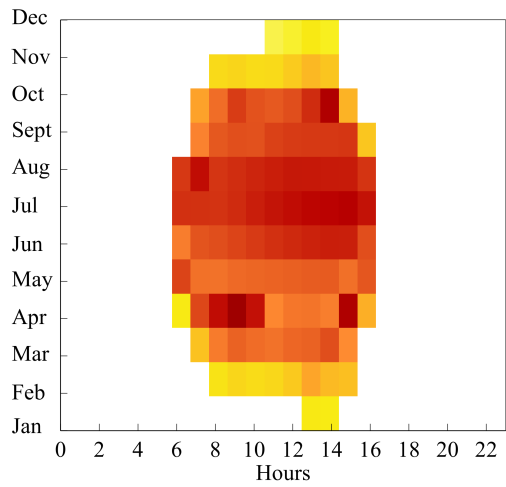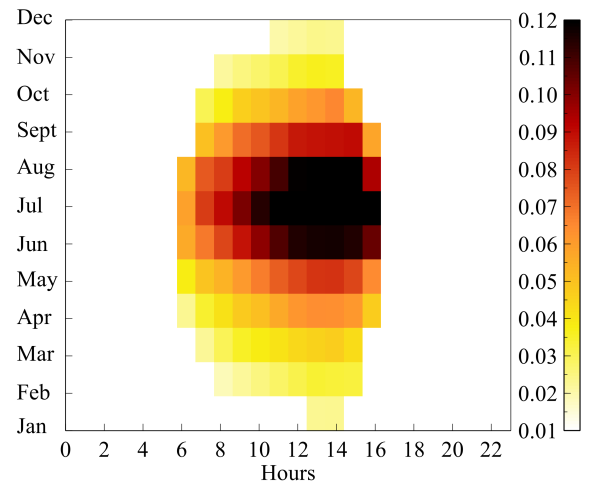
Cooling Tower   Air Cooled Condenser

(b) Daggett

Figure 6.13 Monthly average distribution of the condenser pressure. Parameter used for the simulation are given in Table 6.2

power output. The opposite is seen in Daggett, where low relative humidity and consequently low wet bulb temperature are present; for this location evaporative cooling method provides acceptable condensing pressures to the power block. For Daggett, the air cooled condensers generate a decrease in the cycle performance due to the higher condensing pressures and higher parasitic losses due to the high air temperatures.

The evaluation of the air cooled condenser was performed for the solar field size corresponding to the minimum LCOE. Table 6.5 shows the results obtained for evaporative and air cooled condenser.

Table 6.5 Effect of the condenser type on the annual performance of the PTC solar power plant. Parameters used for the simulation are given in Table 6.2

$\dot{W}_{net,cycle}$(kW)	$\dot{W}_{par}$(kW)	$LCOE_R$ (¢/kWh)	$LCOE_N$(¢/kWh)	Net Power (GWh)
Tampa, Cooling Tower				
49312.8	3760.6	29.6	36.7	113.8
Tampa, Air Cooled Condenser				
49312.8	5088.9	31.9	39.5	110.7
Daggett, Cooling Tower				
49312.8	3619.3	20.7	25.5	120.7
Daggett, Air Cooled Condenser				
49312.8	5363.3	22.8	28.1	116.2

The monthly performance of the PTC solar plant is shown in Figure 6.14. As it was mentioned before, the fan power requirements and the high air temperatures decrease the net power output, the difference is remarkable during summer days.
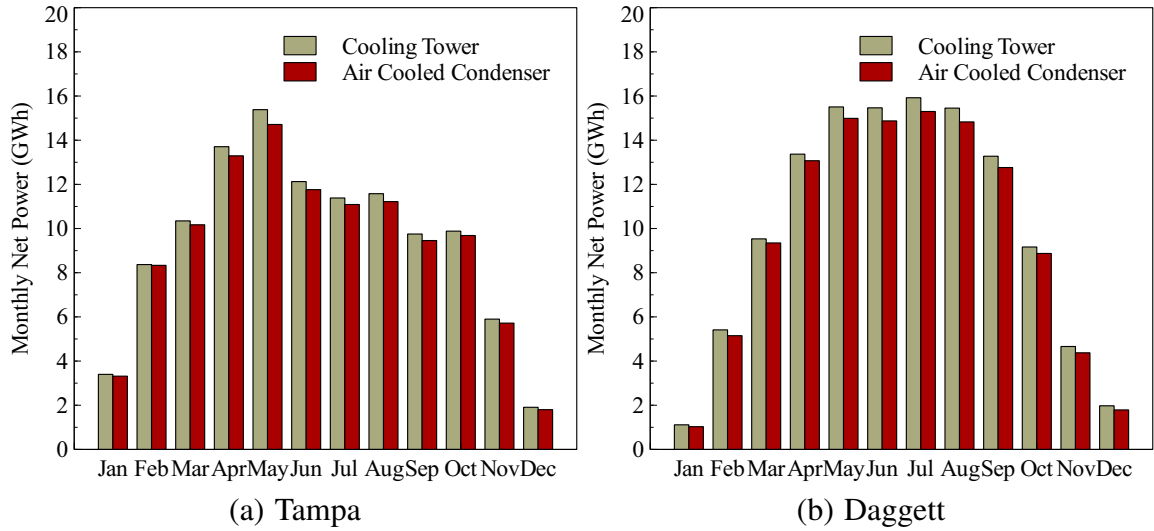
Figure 6.14 Effect of the condenser type on the monthly net power output. Parameter used for the simulation are given in Table 6.2

Figure 6.15 shows the annual output obtained for each cooling method; for Tampa the reduction in the net power output is 2.8% while for Daggett is 3.7%. This reduction in net power output also affects the LCOE, the increase in the LCOE is 7.7% and 10.1% for Tampa and Daggett respectively.
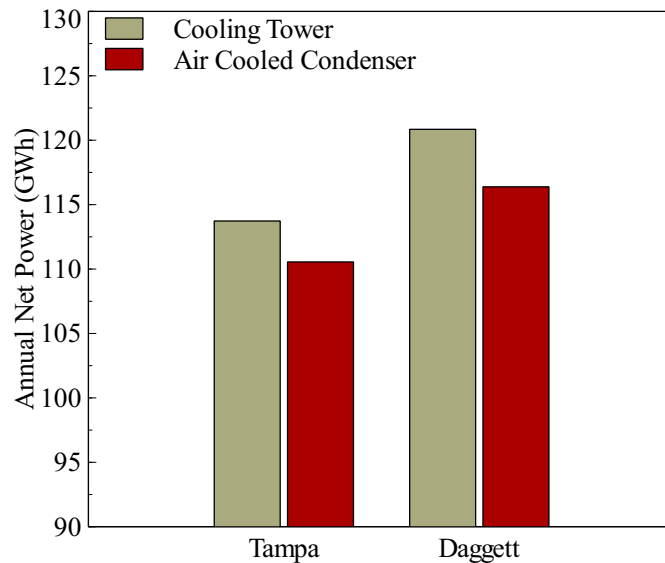
Figure 6.15 Annual net power output for cooling tower and air cooled condenser. Parameter used for the simulation are given in Table 6.2

Chapter 7

Conclusions and Recommendations

In this dissertation a comprehensive methodology for designing parabolic trough solar power plants without thermal storage was developed. The methodology is based on the individual design of different components and subsequent integration of the components into the whole system.

The validation of the results obtained showed that the proposed methodology is suitable for any location and that an optimum configuration can be achieved by sensitivity analysis. In this case, the levelized cost of electricity (LCOE) is a useful parameter for obtaining the optimum size of the solar field. LCOE is one of the main parameters to analyze, but the utilization factor is also important to assure that the solar energy collected is almost totally used by the power block.

On the other hand, the analysis of alternative condensers showed that although air cooled condensers are an excellent alternative, the parasitic losses (fan power requirements) and the higher condensing pressures, especially in hot locations, make this technology less attractive except in certain locations where there is water available.

The following recommendations should be considered for further research in this area:

- In order to simulate the power block at different reference conditions, a correction factor that can be applied to the original power block fitting equation should be determined.

- Alternative and different combinations (bottoming cycles) of power blocks should be studied for maximizing the net power output.

- The design of the air cooled and evaporative condenser should be improved by using more comprehensive models.

- A more detailed cost analysis and LCOE calculation should be included. The cost analysis proposed in the present work is simple and did not include tax incentives and commercial loans.

- Thermal storage model should be included in future work. The heat transfer model used for the thermal expansion tank can be extended for the heat losses in the thermal storage system.

- More realistic control strategies should be implemented in the program to keep the collector outlet temperature almost constant without dumping energy.

List of References

[1] Administration, U. E. I., 2010. International energy outlook. Tech. Rep. DOE/EIA-0484(2010), Office of Integrated Analysis and Forecasting, U.S. Department of Energy, Washington, DC.

[2] Administration, U. E. I., 2010. Annual energy review. Tech. Rep. DOE/EIA-0484(2010), Office of Integrated Analysis and Forecasting, U.S. Department of Energy, Washington, DC.

[3] Goswami, D., and Kreith, F., 2008. *Energy conversion*. CRC.

[4] Price, H., Lüpfert, E., Kearney, D., Zarza, E., Cohen, G., Gee, R., and Mahoney, R., 2002. "Advances in parabolic trough solar power technology". *Journal of Solar Energy Engineering, Transactions of the ASME, 124*(2), pp. 109–125.

[5] Lippke, F., 1995. Simulation of the part-load behavior of a 30 MWe SEGS plant. Tech. rep., SAND–95-1293, Sandia National Labs., Albuquerque, NM (United States).

[6] Forristall, R., 2003. *Heat Transfer Analysis and Modeling of a Parabolic Trough Solar Receiver Implemented in Engineering Equation Solver*. National Renewable Energy Laboratory (NREL), Colorado.

[7] Jones, S., Pitz-Paal, R., Schwarzboezl, P., Hohe, L., Blair, N., and Cable, R., 2001. "TRNSYS Modeling of the SEGS VI Parabolic Trough Solar Electric Generating System". In Proceedings of Solar Forum 2001: Solar Energy: The Power to Choose, Washington, DC, USA, p. 405.

[8] Stuetzle, T. "Automatic control of the 30 MWe SEGS VI parabolic trough plant". Master's thesis, University of Wisconsin-Madison, College of Engineering, 2002.

[9] Stuetzle, T., Blair, N., Mitchell, J., and Beckman, W., 2004. "Automatic control of a 30 MWe SEGS VI parabolic trough plant". *Solar energy, 76*(1-3), pp. 187–193.

[10] Quaschning, V., Kistner, R., and Ortmanns, W., 2002. "Influence of direct normal irradiance variation on the optimal parabolic trough field size: A problem solved with technical and economical simulations". *Journal of Solar Energy Engineering, 124*, pp. 160–164.

[11] Price, H., 2003. A parabolic trough solar power plant simulation model. Tech. Rep. NREL/CP-550-33209, National Renewable Energy Laboratory (NREL), Golden, Colorado.

[12] Stine, W. B., and Harrigan, R. W., 1985. *Solar Energy Fundamentals and Design: With Computer Applications*. Wiley-Interscience, Apr.

[13] Patnode, A. M. "Simulation and performance evaluation of parabolic trough solar power plants". Master's thesis, University of Wisconsin-Madison., College of Engineering, 2006.

[14] Blair, N., Mehos, M., and Christensen, C., 2008. Sensitivity of Concentrating Solar Power trough performance, cost, and financing with the Solar Advisor Model. Tech. Rep. NREL/CD-550-42709, NREL.

[15] National Renewable Energy Laboratoty (NREL), Solar Advisor Model CSP Reference Manual for Version 3.0, 2009.

[16] Montes, M., Abánades, A., Martínez-Val, J., and Valdés, M., 2009. "Solar multiple optimization for a solar-only thermal power plant, using oil as heat transfer fluid in the parabolic trough collectors". *Solar Energy, 83*(12), pp. 2165 – 2176.

[17] Rolim, M. M., Fraidenraich, N., and Tiba, C., 2009. "Analytic modeling of a solar power plant with parabolic linear collectors". *Solar Energy, 83*(1), pp. 126–133.

[18] Mittelman, G., and Epstein, M., 2010. "A novel power block for CSP systems". *Solar Energy, 84*(10), pp. 1761–1771.

[19] Harrigan, R., 1981. Handbook for the conceptual design of parabolic trough solar energy systems process heat applications. Tech. rep., NASA STI/Recon Technical Report N,.

[20] Gueymard, C., 2004. "The sun's total and spectral irradiance for solar energy applications and solar radiation models". *Solar energy, 76*(4), pp. 423–453.

[21] Goswami, D. Y., Kreith, F., Kreider, J. F., and Kreith, F., 2000. *Principles of Solar Engineering*. second ed., Taylor & Francis, Philadelphia, PA.

[22] Woolf, H. M., 1968. "On the Computation of Solar Evaluation Angles and the Determination of Sunrise and Sunset Times". *National Aeronautics and Space Administration Report NASA TM-X-164, USA*.

[23] Gueymard, C., 1995. SMARTS2: A Simple Model of the Atmospheric Radiative Transfer of Sunshine: Algorithms and Performance Assessment. Tech. Rep. FSEC-PF-270-95, Florida Solar Energy Center Cocoa, FL, USA.

[24] Chandler, W., Whitlock, C., and Stackhouse Jr, P. Surface meteorology and solar energy. a renewable energy resource web site (release 6.0).

[25] Gueymard, C., 2000. "Prediction and performance assessment of mean hourly global radiation". *Solar Energy, 68*(3), Mar., pp. 285–303.

[26] Collares-Pereira, M., and Rabl, A., 1979. "The average distribution of solar radiation-correlations between diffuse and hemispherical and between daily and hourly insolation values". *Solar Energy, 22*(2), pp. 155–164.

[27] Gueymard, C., 1986. "Mean daily averages of beam radiation received by tilted surfaces as affected by the atmosphere". *Solar Energy, 37*(4), pp. 261–267.

[28] Liu, B., and Jordan, R., 1960. "The interrelationship and characteristic distribution of direct, diffuse and total solar radiation* 1". *Solar Energy, 4*(3), pp. 1–19.

[29] Gueymard, C., 1986. "Monthly averages of the daily effective optical air mass and solar related angles for horizontal or inclined surfaces". *J. Solar Energy Engng. Trans. ASME, 108*, pp. 320–324.

[30] Duffie, J. A., and Beckman, W. A., 1980. *Solar Engineering of Thermal Processes*. Wiley, New York.

[31] Collares-Pereira, M., and Rabl, A., 1979. "Simple procedure for predicting long term average performance of nonconcentrating and of concentrating solar collectors". *Solar Energy, 23*(3), pp. 235–253.

[32] NREL Electric Systems Center. National Solar Radiation Data Base 1991- 2005 Update: Typical Meteorological Year 3.

[33] Whitaker, J., 2011. The Matplotlib Basemap Toolkit User's Guide. Matplotlib Basemap Toolkit documentation, February.

[34] Lutz, M., 2006. *Programming python*. O'Reilly Media, Inc.

[35] Edenburn, M. W., 1976. "Performance analysis of a cylindrical parabolic focusing collector and comparison with experimental results". *Solar Energy, 18*(5), pp. 437 – 444.

[36] Pope, R., and Schimmel, W., 1973. "An analysis of linear focused collectors for solar power". In Eighth Intersociety Energy Conversion Engineering Conference , Philadelphia, PA, pp. 353–359.

[37] Ratzel, A., Hickox, C., and Gartling, D., 1979. "Techniques for reducing thermal conduction and natural convection heat losses in annular receiver geometries". *J Heat Transfer Trans ASME, 101*(1), pp. 108–113.

[38] Clark, J., 1982. "An analysis of the technical and economic performance of a parabolic trough concentrator for solar industrial process heat application". *International Journal of Heat and Mass Transfer, 25*(9), pp. 1427–1438.

[39] Dudley, V., Kolb, G., Sloan, M., and Kearney, D., 1994. *SEGS LS2 Solar Collector-Test Results*. Report of Sandia National Laboratories, SAN94-1884.

[40] Thomas, A., and Thomas, S., 1994. "Design data for the computation of thermal loss in the receiver of a parabolic trough concentrator". *Energy Conversion and Management, 35*(7), pp. 555–568.

[41] García-Valladares, O., and Velázquez, N., 2009. "Numerical simulation of parabolic trough solar collector: Improvement using counter flow concentric circular heat exchangers". *International Journal of Heat and Mass Transfer, 52*(3-4), pp. 597–609.

[42] Cheng, Z., He, Y., Xiao, J., Tao, Y., and Xu, R., 2010. "Three-dimensional numerical study of heat transfer characteristics in the receiver tube of parabolic trough solar collector". *International Communications in Heat and Mass Transfer, 37*(7), pp. 782 – 787.

[43] He, Y., Xiao, J., Cheng, Z., and Tao, Y., 2011. "A MCRT and FVM coupled simulation method for energy conversion process in parabolic trough solar collector". *Renewable Energy, 36*, pp. 976–985.

[44] Gong, G., Huang, X., Wang, J., and Hao, M., 2010. "An optimized model and test of the China's first high temperature parabolic trough solar receiver". *Solar Energy*, p. doi: 10.1016/j.solener.2010.08.003.

[45] Cohen, G., and Kearney, D., 1994. "Improved parabolic trough solar electric systems based on the SEGS experience". In Proceedings of the ASES Annual Conference, SOLAR 94, pp. 147–150.

[46] Heidemann, W., Spindler, K., and Hahne, E., 1992. "Steady-state and transient temperature field in the absorber tube of a direct steam generating solar collector". *International Journal of Heat and Mass Transfer, 35*(3), pp. 649–657.

[47] Odeh, S., Morrison, G., and Behnia, M., 1996. "Thermal analysis of parabolic trough solar collectors for electric power generation". In Proceedings of ANZSES 34th annual conference, Darwin, Australia, pp. 460–467.

[48] Odeh, S., Morrison, G., and Behnia, M., 1998. "Modelling of parabolic trough direct steam generation solar collectors". *Solar energy, 62*(6), pp. 395–406.

[49] Kreith, F., and Goswami, D. Y., 2007. *Handbook of Energy Efficiency and Renewable Energy*. first ed., CRC.

[50] Özişik, M. N., 1973. *Radiative Transfer and Interactions with Conduction and Convection*. Wiley, New York.

[51] Modest, M., 2003. *Radiative Heat Transfer*, 2 ed. Academic Press, Feb.

[52] Moran, M. J., and Shapiro, H. N., 2004. *Fundamentals of Engineering Thermodynamics*, 5 ed. Wiley, Apr.

[53] Kakaç, S., Shah, R. K., and Aung, W., 1987. *Handbook of Single-Phase Convective Heat Transfer*. John Wiley & Sons, New York.

[54] Gnielinski, V., 1976. "New equations for heat and mass transfer in turbulent pipe and channel flow". *International chemical engineering, 16*(2), pp. 359–368.

[55] Rohsenow, W. M., Hartnett, J. P., and Cho, Y. I., 1998. *Handbook of Heat Transfer*, 3 ed. McGraw-Hill Professional, May.

[56] Incropera, F. P., 2006. *Fundamentals of Heat and Mass Transfer*. sixth ed., Wiley.

[57] Kays, W., Crawford, M., and Weigand, B., 2005. *Convective heat and mass transfer*. McGraw-Hill Science/Engineering/Math.

[58] Schlunder, E. U., 1983. *Heat Exchanger Design handbook (HEDH)*. Hemisphere Publishing Corporation.

[59] Gnielinski, V., 2009. "Heat Transfer Coefficients for Turbulent Flow in Concentric Annular Ducts". *Heat Transfer Engineering, 30*(6), pp. 431–436.

[60] Petukhov, B. S., and Roizen, L. I., 1964. "Generalized relationships for heat transfer in a turbulent flow of gas in tubes of annular section". *High Temperature, 2*, pp. 65–68.

[61] Jones Jr, O. C., and Leung, J. C. M., 1981. "An improvement in the calculation of turbulent friction in smooth concentric annuli". *Journal of Fluids Engineering, 103*, pp. 615–623.

[62] Shah, R. K., and London, A. L., 1978. *Laminar flow forced convection in ducts: a source book for compact heat exchanger analytical data*. Academic Press, Inc.

[63] Davis, J. R., 2000. *Alloy Digest Sourcebook: Stainless Steels*. ASM International, Materials Park, Ohio.

[64] Thomas, J. R., 1979. *Heat Conduction in Partial Vacuum*. Virginia Polytechnic Institute and State University. Blacksburg, Virginia: U.S. Department of Energy, EM-78-C-04-5367.

[65] Dushman, S., 1962. *Scientific Foundations of Vacuum Technique*. second ed., Wiley, New York.

[66] Lide, D. R., 2007. *CRC Handbook of Chemistry and Physics, 88th Edition*, 88 ed. CRC, Oct.

[67] Kaye, G. W. C., and Laby, T. H., 1995. *Tables of Physical and Chemical Constants and Some Mathematical Functions*, 16 sub ed. Longman Sc & Tech, Oct.

[68] Saxena, S. C., and Joshi, R. K., 1989. *Thermal Accommodation and Adsorption Coefficients of Gases*. CINDAS data series on material properties. Hemisphere Pub. Corp, New York.

[69] Rader, D., Trott, W., Torczynski, J., Castañeda, J., and Grasser, T., 2005. Measurements of thermal accomodation coefficients. Tech. Rep. SAND2005-6084, Sandia National Laboratories, Albuquerque, New Mexico.

[70] Trigg, G. L., 2002. *Digital Encyclopedia of Applied Physics*. Wiley, New York.

[71] Harding, G. L., and Window, B., 1981. "Free molecule thermal conduction in concentric tubular solar collectors". *Solar Energy Materials, 4*, pp. 265–278.

[72] Zohar, Y., 2002. *Heat Convection in Micro Ducts*, 1 ed. Springer, Oct.

[73] Kuehn, T. H., and Goldstein, R. J., 1976. "Correlating equations for natural convection heat transfer between horizontal circular cylinders". *Int. J. Heat Mass Transfer, 19*, pp. 1127–1134.

[74] Siegel, R., and Howell, J. R., 1971. *Thermal Radiation Heat Transfer*. McGraw-Hill, New York.

[75] Reid, R. L., and Tennant, J. S., 1973. "Annular ring view factors.". *AIAA Journal, 11*(10), pp. 1446–1448.

[76] Tso, C. P., and Mahulikar, S. P., 1999. "View factors between finite length rings on an interior cylindrical shell". *Journal of Thermophysics and Heat Transfer, 13*(3), pp. 375–379.

[77] Kreith, F., 1962. *Radiation heat transfer for spacecraft and solar power plant design*.

[78] Kraus, A. D., Aziz, A., and Welty, J., 2001. *Extended Surface Heat Transfer*, 1 ed. Wiley-Interscience.

[79] Farber, E. A., and Rennat, H. O., 1957. "Variation of Heat Transfer Coefficient with Length". *Industrial and Engineering Chemistry, 49*(3), pp. 437–440.

[80] Al-Arabi, M., and Khamis, M., 1982. "Natural convection heat transfer from inclined cylinders". *International Journal of Heat and Mass Transfer, 25*(1), pp. 3–15.

[81] Jaluria, Y., 1980. *Natural Convection: Heat and Mass Transfer*. No. v. 5 in HMT–the science & applications of heat and mass transfer. first ed., Pergamon Press, Oxford.

[82] Clemes, S. B., Hollands, K. G. T., and Brunger, A. P., 1994. "Natural convection heat transfer from long horizontal isothermal cylinders". *Journal of heat transfer, 116*(1), pp. 96–104.

[83] Sparrow, E., Abraham, J., and Tong, J., 2004. "Archival correlations for average heat transfer coefficients for non-circular and circular cylinders and for spheres in cross-flow". *International Journal of Heat and Mass Transfer, 47*(24), pp. 5285–5296.

[84] Igarashi, T., 1985. "Heat transfer from a square prism to an air stream". *International journal of heat and mass transfer, 28*(1), pp. 175–181.

[85] Assael, M., Gialou, K., Kakosimos, K., and Metaxa, I., 2004. "Thermal conductivity of reference solid materials". *International Journal of Thermophysics, 25*(2), pp. 397–408.

[86] Howell, J. R., 2001. *A Catalog of Radiation Heat Transfer Configuration Factors*. second ed., Department of Mechanical Engineering, University of Texas at Austin.

[87] Tang, R., Etzion, Y., and Meir, I. A., 2004. "Estimates of clear night sky emissivity in the negev highlands, israel". *Energy Conversion and Management, 45*(11-12), July, pp. 1831–1843.

[88] Berdahl, P., and Fromberg, R., 1982. "The thermal radiance of clear skies". *Solar Energy, 29*(4), pp. 299–314.

[89] Berdahl, P., and Martin, M., 1984. "Emissivity of clear skies". *Solar Energy, 32*(5), pp. 663–664.

[90] Berger, X., Buriot, D., and Garnier, F., 1984. "About the equivalent radiative temperature for clear skies". *Solar Energy, 32*(6), pp. 725–733.

[91] Price, H., Forristall, R., Wendelin, T., Lewandowski, A., Moss, T., and Gummo, C., 2006. "Field Survey of Parabolic Trough Receiver Thermal Performance". In Proceedings of ASME International Solar Energy Conference 2006,.

[92] Bialobrzeski, R. W. "Optimization of a SEGS solar field for cost effective power output". Master's thesis, Department of Mechanical Engineering,Georgia Institute of Technology, 2007.

[93] Swinbank, W., 1963. "Long-wave radiation from clear skies". *Quarterly Journal of the Royal Meteorological Society, 89*(381), pp. 339–348.

[94] Gaul, H., and Rabl, A., 1980. "Incidence-angle modifier and average optical efficiency of parabolic trough collectors". *Journal of Solar Energy Engineering, 102*, pp. 16–21.

[95] Kalogirou, S., 2004. "Solar thermal collectors and applications". *Progress in energy and combustion science, 30*(3), pp. 231–295.

[96] Geyer, M., Lüpfert, E., Osuna, R., Esteban, A., Schiel, W., Schweitzer, A., Zarza, E., Nava, P., Langenkamp, J., and Mandelberg, E., 2002. "EUROTROUGH-Parabolic Trough Collector Developed for Cost Efficient Solar Power Generation". In Proceedings 11th SolarPACES Int. Symp. Conc. Solar Power and Chemical Energy Technologies, September.

[97] Rabl, A., 1985. *Active solar collectors and their applications*. Oxford University Press, USA.

[98] , 2009. SCHOTT Solar Inc. schott ptr®70 receiver the next generation.

[99] Burkholder, F., and Kutscher, C., 2009. Heat Loss Testing of Schott's 2008 PTR70 Parabolic Trough Receiver. Tech. rep., NREL/TP-550–45633.

[100] Touloukian, Y. S., and DeWitt, D. P., 1972. *Thermophysical Properties of Matter-The TPRC Data Series Vol. 8., Thermal Radiative Properties-Nonmetallic Solids*. IFI/Plenum, New York.

[101] Özişik, M. N., 1994. *Finite difference methods in heat transfer*. CRC Press, Inc, Boca Raton, FL.

[102] Jones, E., Oliphant, T., and Peterson, P. SciPy: Open source scientific tools for Python, 2001.

[103] Cox, C. H., and Raghuraman, S. C., 1985. "Design considerations for flat-plate-photovoltaic/thermal collectors". *Solar energy, 35*(3), pp. 227–241.

[104] Dow, 2001. *SYLTHERM 800, Silicone Heat Transfer Fluid. Product Information*.

[105] Naeeni, N., and Yaghoubi, M., 2007. "Analysis of wind flow around a parabolic collector (1) fluid flow". *Renewable Energy, 32*(11), pp. 1898–1916.

[106] Naeeni, N., and Yaghoubi, M., 2007. "Analysis of wind flow around a parabolic collector (2) heat transfer from receiver tube". *Renewable Energy, 32*(8), pp. 1259–1272.

[107] Stodola, A., and Loewenstein, L., 1927. *Steam and gas turbines, with a supplement on The prospects of the thermal prime mover*, Vol. 1. Peter Smith, New York.

[108] Kostyuk, A., and Frolov, V., 1988. *Steam and gas turbines*. Mir Publishers.

[109] Pye, J., 2010. Freesteam 2.0.

[110] Kakaç, S., 1991. *Boilers, evaporators, and condensers*. Wiley-Interscience.

[111] Cengel, Y. A., 2002. *Heat Transfer: A Practical Approach*, 2nd ed. McGraw-Hill Companies, Nov.

[112] Wagner, M., 2008. "Simulation and predictive performance modeling of utility-scale central receiver system power plants". Master's thesis, University of Wisconsin–Madison.

[113] Nag, P., 2002. *Power plant engineering*. Tata McGraw-Hill.

[114] Drbal, L., Boston, P., and Westra, K., 1996. *Power plant engineering*. Kluwer Academic Pub.

[115] Habib, M., Said, S., and Al-Zaharna, I., 1999. "Thermodynamic optimization of reheat regenerative thermal-power plants". *Applied Energy, 63*(1), pp. 17–34.

[116] Dincer, I., and Al-Muslim, H., 2001. "Thermodynamic analysis of reheat cycle steam power plants". *International Journal of Energy Research, 25*(8), pp. 727–739.

[117] Leyzerovich, A., 1997. *Large power steam turbines: design and operation*, Vol. 1. PennWell Publising Company.

[118] Marcelle, K., Chiang, K., Houpt, P., and Bonissone, P., 2002. "Optimal load cycling of large steam turbines". In Fuzzy Systems, 1994. IEEE World Congress on Computational Intelligence., Proceedings of the Third IEEE Conference on, IEEE, pp. 667–672.

[119] Bartlett, R., 1958. *Steam turbine performance and economics*. McGraw-Hill.

[120] Kelly, B., 2006. Nexant Parabolic Trough Solar Power Plant Systems Analysis; Task 2: Comparison of Wet and Dry Rankine Cycle Heat Rejection,. Tech. Rep. NREL/SR-550-40163, National Renewable Energy Laboratory (NREL), Golden, CO.

[121] Green, D., and Perry, R., 2007. *Perry's Chemical Engineers' Handbook, Eighth Edition*, 8 ed. McGraw-Hill Professional, Oct.

[122] Fraas, A., 1989. *Heat exchanger design*. Wiley-Interscience.

[123] Cheremisinoff, N. P., and Cheremisinoff, P. N., 1981. *Cooling towers selection, design and practice*. Ann Arbor Science, Ann Arbor, MI.

[124] Leeper, S. A., 1981. Wet cooling towers: rule-of-thumb design and simulation. Tech. Rep. EGG-GTH-5775, Idaho National Engineering Laboratory, U.S. Department of Energy, July.

[125] Cengel, Y., Boles, M., and He, Y., 2002. *Thermodynamics: an engineering approach*, Vol. 930. McGraw-Hill New York.

[126] Mohiuddin, A., and Kant, K., 1996. "Knowledge base for the systematic design of wet cooling towers. Part II: Fill and other design parameters". *International journal of refrigeration, 19*(1), pp. 52–60.

[127] Mohiuddin, A., and Kant, K., 1996. "Knowledge base for the systematic design of wet cooling towers. Part I: Selection and tower characteristics". *International Journal of Refrigeration, 19*(1), pp. 43–51.

[128] Braun, J., 1988. "Methodologies for the design and control of central cooling plants". PhD thesis, University of Wisconsin-Madison.

[129] Jaber, H., and Webb, R., 1989. "Design of cooling towers by the effectiveness-NTU method". *Journal of Heat Transfer, 111*, pp. 837–843.

[130] IMTE AG, Switzerland Power Consulting Engineers, 2004. Dry systems for power plant cooling. Tech. rep., May.

[131] Mayer, D., Arnold, E., and Allemann, R., 1979. Potential use of dry cooling in support of advanced energy generation systems. Tech. rep., PNL-3149, Battelle Pacific Northwest Labs., Richland, WA (USA).

[132] Kröger, D., 2004. *Air-cooled heat exchangers and cooling towers: thermal-flow performance evaluation and design*, Vol. 2. Pennwell Corp.

[133] Serth, R., 2007. *Process heat transfer: principles and applications*. Academic Press.

[134] Gas Processors Suppliers Association (GPSA), 2004. *Engineering Data book*, 12th ed., Vol. I.

[135] Pieve, M., and Salvadori, G., 2011. "Performance of an air-cooled steam condenser for a waste-to-energy plant over its whole operating range". *Energy Conversion and Management, 52*(4), pp. 1908–1913.

[136] Wilber, K., and Zammit, K., 2005. "Development of procurement guidelines for air-cooled condensers". In Advanced Cooling Strategies/Technology Conference, Sacramento CA, USA, Vol. 11, pp. 8–9.

[137] Kakaç, S., and Liu, H., 2002. *Heat exchangers: selection, rating, and thermal design*. CRC.

[138] Kröger, D., 2004. *Air-cooled heat exchangers and cooling towers: thermal-flow performance evaluation and design*, Vol. 1. Pennwell Corp.

[139] Kroshko, D. L., 2010. OpenOpt 0.32. http://openopt.org/, December.

[140] Turchi, C., 2010. Parabolic Trough Reference Plant for Cost Modeling with the Solar Advisor Model (SAM). Tech. rep., National Renewable Energy Laboratory (NREL), Golden, CO.

[141] Kelly, B., and Kearney, D., 2006. Parabolic Trough Solar System Piping Model. Tech. rep., National Renewable Laboratory, NREL/SR-550-40165, July.

[142] Megyesy, E. F., 2001. *Pressure Vessel Handbook 12th ed*, 12th ed. Pressure Vessel Publishing, Oct.

[143] American Society of Mechanical Engineers (ASME), 2004. *ASME B31.1-2004, American National Standard, ASME Code for Pressure Piping*.

[144] White, F., 2000. *Fluid Mechanics*. Boca Raton, Fl:CRC Press.

[145] Logan, E., 1993. *Turbomachinery: Basic theory and applications*. CRC.

[146] Bahadori, A., and Vuthaluru, H., 2010. "A simple correlation for estimation of economic thickness of thermal insulation for process piping and equipment". *Applied Thermal Engineering, 30*(2-3), pp. 254–259.

[147] Cao, E., 2010. *Heat transfer in process engineering [electronic resource]*. McGraw-Hill, New York. Eduardo Cao. : Eduardo Cao.; 50012 Description based on print version record.; 50411 Includes bibliographical references and index.

[148] Specialty Products & Insulation Co., 2005. Mineral wool pipe insulation, May.

[149] Solutia, 1999. Therminol information bulletin no 4. heat transfer system expansion tank design. Tech. rep., Solutia.

[150] Kumana, J., and Kothari, S., 1982. "Predict Storage-Tank Heat Transfer Precisely.". *Chemical Engineer, 89*(6), pp. 127–132.

[151] Wagner, M., Blair, N., and Dobos, A., 2010. Detailed Physical Trough Model for NREL's Solar Advisor Model: Preprint. Tech. Rep. NREL/CP-5500-49368, National Renewable Energy Laboratory (NREL), Golden, CO., October.

[152] Short, W., Packey, D., and Holt, T., 1995. A manual for the economic evaluation of energy efficiency and renewable energy technologies. Tech. rep., National Renewable Energy Lab., Golden, CO (United States).

[153] Campbell, M., Aschenbrenner, P., Blunden, J., Smeloff, E., and Wright, S., 2008. The drivers of the levelized cost of electricity for utility-scale photovoltaics. Tech. rep., SUNPOWER Corporation.

[154] SkyFuel, 2010. Skytrough brochure.

[155] Solutia Inc., 2008. Therminol vp-1, vapor phase/ liquid phase heat transfer fluid 54 ºf to 750 ºf. technical bulletin 7239115c. Tech. rep.

[156] Dow, 2001. Dowtherm Q, Synthetic Organic Heat Transfer Fluid. Product Information. Tech. rep., Dow.

[157] Dow, 2001. Dowtherm RP, Synthetic Organic Heat Transfer Fluid. Product Information. Tech. rep., Dow.

[158] Zavoico, A. B., 2001. Solar Power Tower Design Basis Document. Tech. rep., Sandia National Laboratories, SAND2001-2100.

[159] Coastal Chemical Co., HITEC® Heat Transfer Salt. Tech. rep., Brenntag Company.

[160] Kirst, W. E., Nagle, W. M., and Castner, J. B., 1940. "A new heat transfer medium for high temperatures". *Transactions of the American Institute of Chemical Engineers, 36*, pp. 371–394.

Appendices

Appendix A: Thermophysical Properties of Gases

The specific heats, absolute viscosities, and thermal conductivities are only function of the temperature. To obtain the density of a gas, the perfect gas law may be used [55]:

$$P = \rho R T \qquad (A.1)$$

Specific heat ($kJ/kg\,K$), absolute viscosity ($\mu\,Pa \cdot s$), and thermal conductivity ($W/m\,K$) are defined by [55]:

$$C_p = \sum_{i=0}^{N} A_i\,T^i \qquad (A.2)$$

$$\mu = \sum_{i=0}^{N} B_i\,T^i \qquad (A.3)$$

$$k = \sum_{i=0}^{N} C_i\,T^i \qquad (A.4)$$

where T is in K

Appendix A: (Continued)

Physical properties of air [55]:

- Molecular weight (kg/mol): 28.966

- Gas Constant R ($kJ/kg\,K$): 0.287040

- Critical Temperature T_c (K): 132.6

- Critical Pressure P_c (Mpa): 3.77

Table A.1 Thermophysical coefficients of air (Equations (A.2)-(A.4)). Adapted from [55] [(1)] $250 \leq T < 1050\,K$, [(2)] $250 \leq T < 600\,K$, [(3)] $600 \leq T < 1050\,K$

i	A_i [(1)]	B_i [(2)]	B_i [(3)]	C_i [(1)]
0	1.03409	-9.8601×10^{-1}	4.8856745	-2.276501×10^{-3}
1	$-0.2848870 \times 10^{-3}$	9.080125×10^{-2}	5.43232×10^{-2}	1.259848×10^{-4}
2	0.7816818×10^{-6}	$-1.17635575 \times 10^{-4}$	$-2.4261775 \times 10^{-5}$	-1.481523×10^{-7}
3	$-0.4970786 \times 10^{-9}$	1.2349703×10^{-7}	7.9306×10^{-9}	1.735506×10^{-10}
4	$0.1077024 \times 10^{-12}$	$-5.7971299 \times 10^{-11}$	-1.10398×10^{-12}	$-1.066657 \times 10^{-13}$
5	0	0	0	2.476630×10^{-17}
6	0	0	0	0

Appendix A: (Continued)

Physical properties of hydrogen [55]:

- Molecular weight (kg/mol): 2.016

- Gas Constant R ($kJ/kg\,K$): 4.124289

- Critical Temperature T_c (K): 33.3

- Critical Pressure P_c (Mpa): 1.3

Table A.2 Thermophysical coefficients of hydrogen (Equation (A.2)). Adapted from [55]
$^{(1)}$ $250 \leq T < 425\,K$, $^{(2)}$ $425 \leq T < 490\,K$, $^{(3)}$ $490 \leq T < 1050\,K$

i	A_i $^{(1)}$	A_i $^{(2)}$	A_i $^{(3)}$
0	5.00662530	14.4947	14.920082
1	$1.01569422 \times 10^{-1}$	0	$-1.996917584 \times 10^{-3}$
2	$-6.02891517 \times 10^{-4}$	0	2.540615×10^{-6}
3	$2.73758940 \times 10^{-6}$	0	$-4.7588954 \times 10^{-10}$
4	$-8.47582750 \times 10^{-9}$	0	0
5	$1.43800374 \times 10^{-11}$	0	0
6	$-9.80724030 \times 10^{-15}$	0	0

Appendix A: (Continued)

Table A.3 Thermophysical coefficients of hydrogen (Equations (A.3)-(A.4)). Adapted from [55]

$^{(1)}$ $250 \leq T < 500\,K$, $^{(2)}$ $500 \leq T < 1050\,K$

i	$B_i{}^{(1)}$	$B_i{}^{(2)}$	$C_i{}^{(1)}$	$C_i{}^{(2)}$
0	-0.135666	2.72941	2.01×10^{-2}	0.108
1	$6.84115878 \times 10^{-2}$	2.3224377×10^{-2}	3.23×10^{-4}	2.21×10^{-4}
2	-3.928747×10^{-4}	$-7.6287854 \times 10^{-6}$	2.16×10^{-6}	2.26×10^{-7}
3	1.8996×10^{-6}	2.92585×10^{-9}	-6.49×10^{-9}	-1.74×10^{-10}
4	-5.23104×10^{-9}	$-5.2889938 \times 10^{-13}$	5.52×10^{-12}	4.65×10^{-14}
5	$7.4490972 \times 10^{-12}$	0	0	0
6	$-4.250937 \times 10^{-15}$	0	0	0

Appendix A: (Continued)

Physical properties of argon [55]:

- Molecular weight (kg/mol): 39.948

- Gas Constant R ($kJ/kg\,K$): 0.208129

- Critical Temperature T_c (K): 150.8

- Critical Pressure P_c (Mpa): 4.87

Table A.4 Thermophysical coefficients of argon (Equations (A.2)-(A.4)). Adapted from [55]
[1] $200 \leq T < 1600\,K$, [2] $200 \leq T < 1000\,K$, [3] $200 \leq T < 540\,K$, [4] $540 \leq T < 1000\,K$

i	A_i [1]	B_i [2]	B_i [3]	C_i [4]
0	0.52034	$-5.2839462 \times 10^{-4}$	1.22573	4.03764
1	0	$7.60706705 \times 10^{-5}$	5.9456964×10^{-2}	7.3665688×10^{-2}
2	0	$-6.4749393 \times 10^{-8}$	1.897011×10^{-4}	-3.3867×10^{-5}
3	0	$5.41874502 \times 10^{-11}$	-8.171242×10^{-7}	1.127158×10^{-8}
4	0	$-3.22024235 \times 10^{-14}$	1.2939183×10^{-9}	$-1.585569 \times 10^{-12}$
5	0	$1.17962552 \times 10^{-17}$	$-7.5027442 \times 10^{-13}$	0
6	0	$-1.86231745 \times 10^{-21}$	0	0

Appendix A: (Continued)

Physical properties of nitrogen [55]:

- Molecular weight (kg/mol): 28.013

- Gas Constant R ($kJ/kg\,K$): 0.296798

- Critical Temperature T_c (K): 126.2

- Critical Pressure P_c (Mpa): 3.4

Table A.5 Thermophysical coefficients of nitrogen (Equations (A.2)-(A.4)). Adapted from [55]
[1] $280 \leq T < 590\,K$, [2] $590 \leq T < 1080\,K$, [3] $250 \leq T < 1050\,K$

i	A_i [1]	A_i [2]	B_i [3]	C_i [3]
0	1.08804	1.405507	2.5465×10^{-2}	-1.523178×10^{-3}
1	-3.55968×10^{-4}	-2.189456×10^{-3}	7.533653×10^{-2}	1.1887996×10^{-4}
2	7.290760×10^{-7}	4.785289×10^{-6}	$-6.5156624 \times 10^{-5}$	-1.209284×10^{-7}
3	$-2.886155 \times 10^{-10}$	-4.54016×10^{-9}	4.34945×10^{-8}	$1.1556780 \times 10^{-10}$
4	0	$2.0849125 \times 10^{-12}$	$-1.562245 \times 10^{-11}$	$-6.3653734 \times 10^{-14}$
5	0	$-3.790303 \times 10^{-16}$	2.24966×10^{-15}	$1.4716702 \times 10^{-17}$
6	0	0	0	0

Appendix B: Data of Parabolic Trough Collectors

Table B.1 Geometrical and optical data for parabolic trough collectors. Adapted from [4]

Collector	$w^{(1)}$ (m)	$f^{(2)}$ (m)	$L_e^{(3)}$ (m)	$L_c^{(4)}$ (m)
LS-1	2.55	0.94	6.3	50.2
LS-2	5.00	1.49	8	49.0
LS-3	5.76	1.71	12	99.0
IST $^{(8)}$	2.30	0.76	6.1	49.0
EuroTrough	5.76	1.71	12	150.0
SkyTrough $^{(9)}$	6.00	1.71	13.9	115.0

Collector	Mirror area (m^2)	$D^{(5)}$ (m)	$C^{(6)}$	$\eta_o^{(7)}$ (%)
LS-1	128	0.04	61:1	71
LS-2	235	0.07	71:1	76
LS-3	545	0.07	82:1	80
IST $^{(8)}$	424	0.04	50:1	78
EuroTrough	817	0.07	82:1	80
SkyTrough $^{(9)}$	750	0.08	75:1	77

$^{(1)}$ Aperture width
$^{(2)}$ Focal length
$^{(3)}$ Length per element
$^{(4)}$ Length per collector
$^{(5)}$ Receiver diameter
$^{(6)}$ Geometric concentration
$^{(7)}$ Peak optical efficiency
$^{(8)}$ Industrial Solar Technology
$^{(9)}$ Taken from: [154]

Appendix C: Thermophysical Properties of Heat Transfer Fluid (HTF)

Density (kg/m^3) is defined by:

$$\rho = \sum_{i=0}^{N} a_i T^i \tag{C.1}$$

where T is in ℃

Table C.1 Coefficients for use in Equation (C.1)

HTF	a_0	a_1	a_2	a_3
VP-1 [1] [155]	1083.22	−0.902	7.369×10^{-4}	-2.287×10^{-6}
D- Q [1] [156]	982.18	−0.776	4.827×10^{-5}	0
D- RP [1] [157]	1042.39	−0.668	-1.924×10^{-4}	0
Solar Salt [1] [158]	2090.18	−0.640	0	0
Hitec [1] [159, 160]	2081.44	−0.728	0	0
Hitec XL [2] [15]	2240.00	−0.826	0	0

[1] $R^2 = 0.99$

[2] R^2 is not given
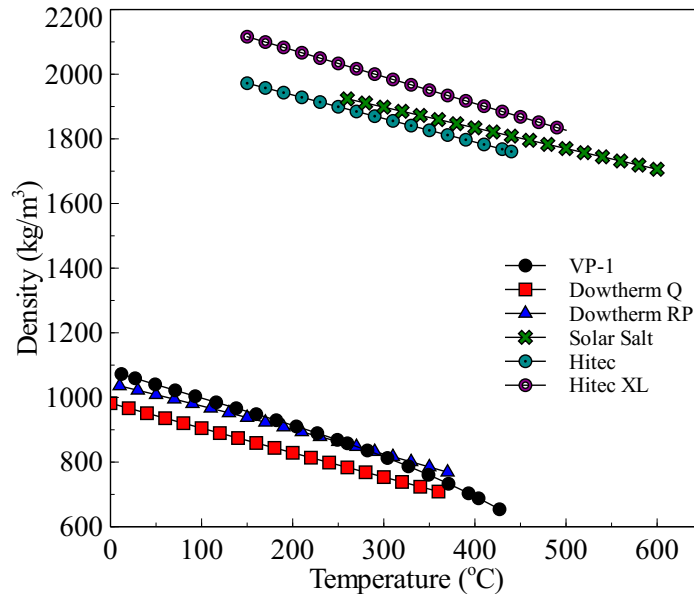
Figure C.1 Density for different HTFs

Appendix C: (Continued)

Specific heat at constant pressure ($kJ/kg\,K$) is defined by:

$$C_p = \sum_{i=0}^{N} b_i\, T^i \qquad (C.2)$$

where T is in ºC

Table C.2 Coefficients for use in Equation (C.2)

HTF	b_0	b_1	b_2	b_3	b_4
VP-1 [1] [155]	1.471	3.497×10^{-3}	-4.817×10^{-6}	8.400×10^{-9}	0
D- Q [1] [156]	1.589	3.198×10^{-3}	-5.288×10^{-7}	0	0
D- RP [1] [157]	1.561	2.975×10^{-3}	0	0	0
Solar Salt [1] [158]	1.093	3.755×10^{-3}	-1.322×10^{-5}	2.112×10^{-8}	-1.2×10^{-11}
Hitec [159, 160]	1.560	0	0	0	0
Hitec XL [2] [15]	1.536	-2.624×10^{-4}	-1.139×10^{-7}	0	0

[1] $R^2 = 0.99$

[2] R^2 is not given
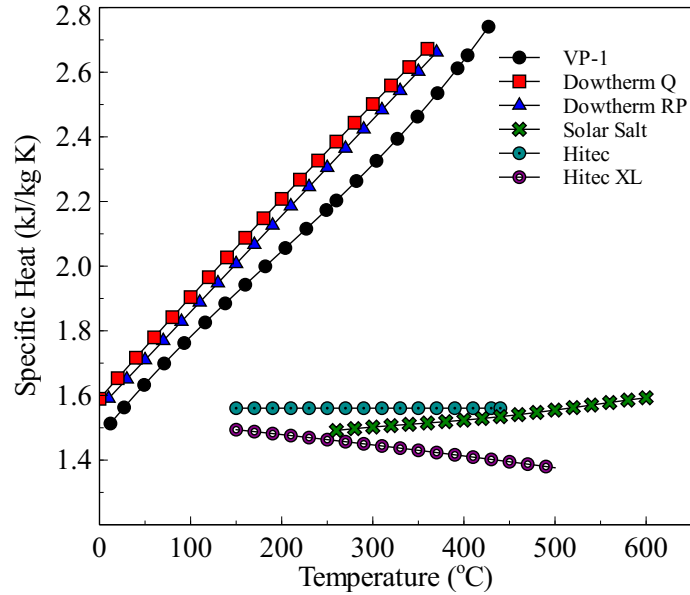
Figure C.2 Specific heat at constant pressure for different HTFs

Appendix C: (Continued)

Specific enthalpy (kJ/kg) is defined by:

$$h = \sum_{i=0}^{N} c_i T^i \tag{C.3}$$

where T is in ºC

Table C.3 Coefficients for use in Equation (C.3)

HTF	c_0	c_1	c_2	c_3
VP-1 [1] [155]	-18.977	1.513	1.2908×10^{-3}	1.201×10^{-7}
D-Q [1] [156]	53.671	1.589	1.599×10^{-3}	-1.762×10^{-7}
D-RP [1] [157]	-15.759	1.561	1.4875×10^{-3}	0
Solar Salt [1] [158]	-354.845	1.092	1.877×10^{-3}	-4.409×10^{-6}
Hitec [159, 160]	-232.360	1.560	0	0
Hitec XL [2] [15]	0	1.536	-1.312×10^{-4}	-3.796×10^{-8}

			c_4	c_5
VP-1 [1] [155]			0	0
D- Q [1] [156]			0	0
D-RP [1] [157]			0	0
Solar Salt [1] [158]			5.282×10^{-9}	-2.4×10^{-12}
Hitec [159, 160]			0	0
Hitec XL [2] [15]			0	0

[1] $R^2 = 0.99$
[2] R^2 is not given
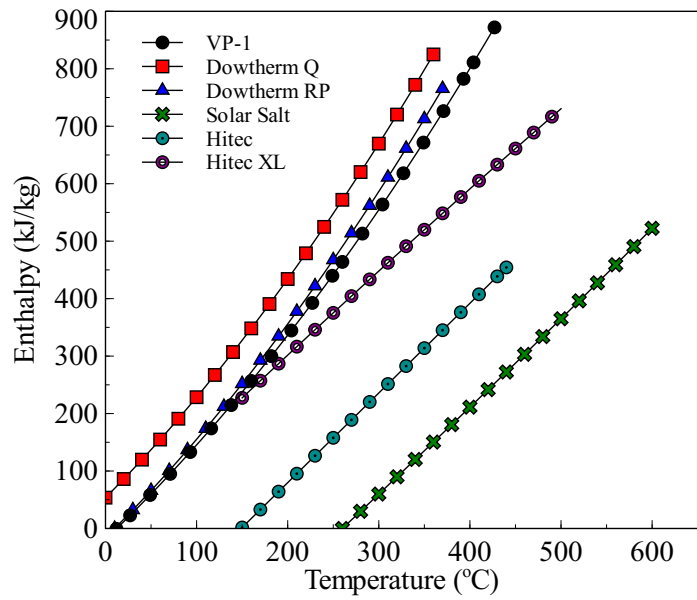
Figure C.3 Specific enthalpy for different HTFs

Appendix C: (Continued)

Thermal conductivity (W/mK) is defined by:

$$k = \sum_{i=0}^{N} d_i T^i \qquad (C.4)$$

where T is in ºC

Table C.4 Coefficients for use in Equation (C.4)

HTF	d_0	d_1	d_2	d_3	d_4
VP-1 [1] [155]	0.138	-8.738×10^{-5}	-1.720×10^{-7}	0	0
D-Q [1] [156]	0.124	-1.239×10^{-4}	-6.320×10^{-8}	0	0
D-RP [1] [157]	0.133	-1.296×10^{-4}	0	0	0
Solar Salt [1] [158]	0.441	1.953×10^{-4}	0	0	0
Hitec [159, 160]	0.221	3.457×10^{-4}	-3.669×10^{-7}	-4.165×10^{-9}	6.07×10^{-12}
Hitec XL [141]	0.519	0	0	0	0

[1] $R^2 = 0.99$
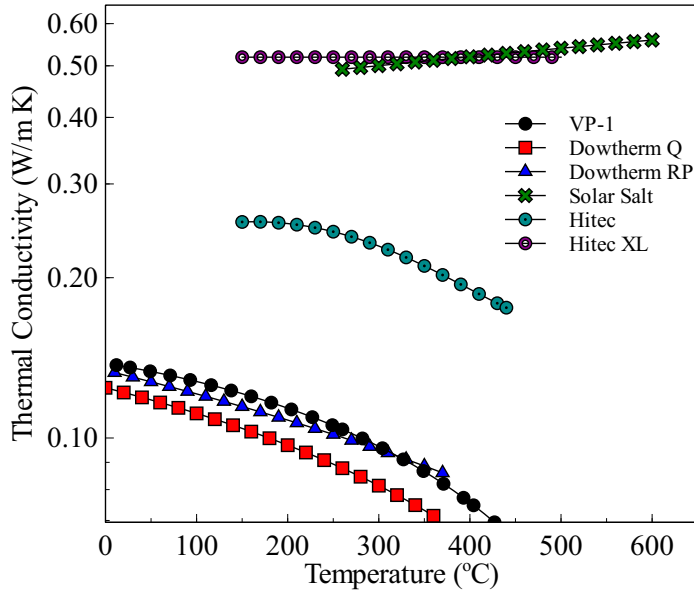
Figure C.4 Thermal conductivity for different HTFs

Appendix C: (Continued)

Absolute viscosity (cP) is defined by:

$$\ln \mu = \sum_{i=0}^{N} e_i T^i \tag{C.5}$$

For Hitec and Hitec XL the next equation is used:

$$\ln \mu = \sum_{i=0}^{N} e_i (\ln T)^i \tag{C.6}$$

For solar salt:

$$\mu = \sum_{i=0}^{N} e_i T^i \tag{C.7}$$

where T is in °C

Table C.5 Coefficients for use in Equations (C.5)-(C.7)

HTF	e_0	e_1	e_2	e_3	e_4
VP-1 [1] [155]	2.008	-2.989×10^{-2}	1.207×10^{-4}	-2.714×10^{-7}	2.370×10^{-10}
D-Q [1] [156]	2.125	-3.960×10^{-2}	2.090×10^{-4}	-5.935×10^{-7}	6.460×10^{-10}
D-RP [1] [157]	5.147	-7.174×10^{-2}	3.981×10^{-4}	-1.087×10^{-6}	1.108×10^{-9}
Solar Salt [1] [158]	22.713	-1.200×10^{-1}	2.281×10^{-4}	-1.474×10^{-7}	0
Hitec [1] [159, 160]	33.324	-9.270	6.364×10^{-1}	0	0
Hitec XL [2] [141]	14.132	-3.364	0	0	0

[1] $R^2 = 0.99$
[2] R^2 is not given
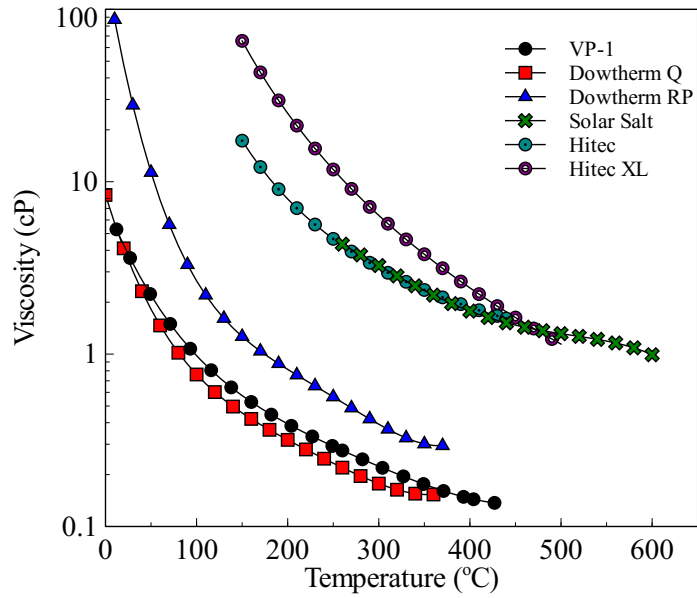
Figure C.5 Absolute viscosity for different HTFs

Appendix C: (Continued)

Vapor pressure (*kPa*) is defined by:

$$P_v = \sum_{i=0}^{N} f_i T^i \tag{C.8}$$

where T is in ℃

Table C.6 Coefficients for use in Equation (C.8)

HTF	f_0	f_1	f_2	f_3	f_4
VP-1 [(1)] [155]	0.789	-1.379×10^{-1}	3.783×10^{-3}	-3.387×10^{-5}	1.056×10^{-7}
D-Q [(1)] [156]	24.738	-7.325×10^{-1}	8.525×10^{-3}	-4.684×10^{-5}	1.080×10^{-7}
D-RP [(2)] [157]	-354.560	4.768	-2.155×10^{-2}	3.318×10^{-5}	0

[(1)] $R^2 = 0.99$
[(2)] $R^2 = 1.00$
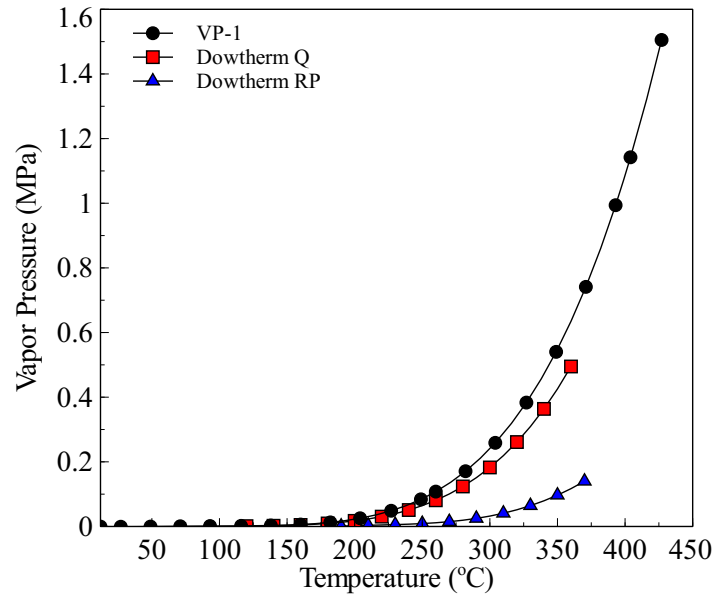
Figure C.6 Vapor pressure for different HTFs

Appendix D: Pipe Geometry

Table D.1 Wall thickness, in mm, for different nominal pipe sizes (Pipe Schedule A-G). Adapted from [141]

Nominal	Pipe Schedule						
Pipe Size, in	A	B	C	D	E	F	G
2.5	2.11	3.05	5.16	7.01	9.53	14.02	…
3	2.11	3.05	5.49	7.62	11.13	15.24	…
4	2.11	3.05	3.96	4.78	6.02	8.56	11.13
6	2.77	3.40	4.78	7.11	10.97	14.27	18.26
8	2.77	3.76	6.35	7.04	8.18	10.31	12.70
10	3.40	4.19	4.78	6.35	7.80	9.27	12.70
12	3.96	4.57	6.35	8.38	9.53	10.31	12.70
14	4.78	6.35	7.92	9.53	11.13	12.70	15.09
16	4.78	6.35	7.92	9.53	12.70	14.35	21.44
18	4.78	6.35	7.92	9.53	11.13	12.70	14.27
20	5.54	6.35	9.53	12.70	15.09	20.62	26.19
22	6.35	9.53	12.70	22.23	28.58	34.93	41.28
24	6.35	9.53	12.70	14.27	17.48	24.61	30.96
26	7.92	9.53	12.70	…	…	…	…
28	7.92	9.53	12.70	15.88	…	…	…
30	7.92	9.53	12.70	15.88	…	…	…
32	7.92	9.53	12.70	15.88	17.48	…	…
34	7.92	9.53	12.70	15.88	17.48	…	…
36	7.92	9.53	12.70	15.88	19.05	…	…
42	9.53	12.70	15.88	19.05	…	…	…
48	9.53	12.70	19.05	25.40	…	…	…
54	9.53	12.70	19.05	25.40	…	…	…
60	9.53	12.70	19.05	25.40	…	…	…
66	9.53	12.70	19.05	25.40	…	…	…
72	9.53	12.70	19.05	25.40	…	…	…

Appendix D: (Continued)

Table D.2 Wall thickness, in mm, for different nominal pipe sizes (Pipe Schedule H-M). Adapted from [141]

Nominal	Pipe Schedule					
Pipe Size, in	H	I	J	K	L	M
2.5	…	…	…	…	…	…
3	…	…	…	…	…	…
4	13.49	17.12	…	…	…	…
6	21.95	…	…	…	…	…
8	15.09	18.26	20.62	22.23	23.01	…
10	15.09	18.26	21.44	25.40	28.58	…
12	14.27	17.48	21.44	25.40	28.58	33.32
14	19.05	23.83	27.79	31.75	35.71	…
16	26.19	30.96	36.53	40.49	…	…
18	19.05	23.83	29.36	34.93	39.67	45.24
20	32.54	38.10	44.45	50.01	…	…
22	47.63	53.98	…	…	…	…
24	38.89	46.02	52.37	59.54	…	…
26	…	…	…	…	…	…
28	…	…	…	…	…	…
30	…	…	…	…	…	…
32	…	…	…	…	…	…
34	…	…	…	…	…	…
36	…	…	…	…	…	…
42	…	…	…	…	…	…
48	…	…	…	…	…	…
54	…	…	…	…	…	…
60	…	…	…	…	…	…
66	…	…	…	…	…	…
72	…	…	…	…	…	…

Appendix D: (Continued)

Table D.3 Inside diameter, in mm, for different nominal pipe sizes (Pipe Schedule A-G). Adapted from [141]

Nominal	Pipe Schedule						
Pipe Size, in	A	B	C	D	E	F	G
2.5	68.8	66.9	62.7	59.0	54.0	45.0	...
3	84.7	82.8	77.9	73.7	66.6	58.4	...
4	110.1	108.2	106.4	104.7	102.3	97.2	92.0
6	162.7	161.5	158.7	154.1	146.3	139.7	131.7
8	213.5	211.6	206.4	205.0	202.7	198.5	193.7
10	266.2	264.7	263.5	260.4	257.5	254.5	247.7
12	315.9	314.7	311.2	307.1	304.8	303.2	298.5
14	346.0	342.9	339.8	336.6	333.3	330.2	325.4
16	396.8	393.7	390.6	387.4	381.0	377.7	363.5
18	447.6	444.5	441.4	438.2	434.9	431.8	428.7
20	496.9	495.3	489.0	482.6	477.8	466.8	455.6
22	546.1	539.8	533.4	514.4	501.7	489.0	476.3
24	596.9	590.6	584.2	581.1	574.6	560.4	547.7
26	644.6	641.4	635.0	...	...	...	...
28	695.4	692.2	685.8	679.5	...	...	...
30	746.2	743.0	736.6	730.3	...	...	...
32	797.0	793.8	787.4	781.1	777.8	...	...
34	847.8	844.6	838.2	831.9	828.6	...	...
36	898.6	895.4	889.0	882.7	876.3	...	...
42	1047.8	1041.4	1035.1	1028.7	...	...	...
48	1200.2	1193.8	1181.1	1168.4	...	...	...
54	1352.6	1346.2	1333.5	1320.8	...	...	...
60	1505.0	1498.6	1485.9	1473.2	...	...	...
66	1657.4	1651.0	1638.3	1625.6	...	...	...
72	1809.8	1803.4	1790.7	1778.0	...	...	...

Table D.4 Inside diameter, in mm, for different nominal pipe sizes (Pipe Schedule H-M). Adapted from [141]

Nominal	Pipe Schedule					
Pipe Size, in	H	I	J	K	L	M
2.5	…	…	…	…	…	…
3	…	…	…	…	…	…
4	87.3	80.1	…	…	…	…
6	124.4	…	…	…	…	…
8	188.9	182.5	177.8	174.6	173.1	…
10	242.9	236.5	230.2	222.3	215.9	…
12	295.3	288.9	281.0	273.1	266.7	257.2
14	317.5	307.9	300.0	292.1	284.2	…
16	354.0	344.5	333.3	325.4	…	…
18	419.1	409.5	398.5	387.4	377.9	366.7
20	442.9	431.8	419.1	408.0	…	…
22	463.6	450.9	…	…	…	…
24	531.8	517.6	504.9	490.5	…	…
26	…	…	…	…	…	…
28	…	…	…	…	…	…
30	…	…	…	…	…	…
32	…	…	…	…	…	…
34	…	…	…	…	…	…
36	…	…	…	…	…	…
42	…	…	…	…	…	…
48	…	…	…	…	…	…
54	…	…	…	…	…	…
60	…	…	…	…	…	…
66	…	…	…	…	…	…
72	…	…	…	…	…	…

About the Author

Ricardo Vasquez Padilla was born in Barranquilla, Colombia in March 1978. He pursued his bachelor and master at Universidad del Norte in Mechanical Engineering. After he got married with his beloved Jennifer, he began doctoral studies at University of South Florida under the guidance of Dr. Yogi Goswami and Dr. Elias Stefanakos in the Clean Energy Research Center (CERC). Initially, he worked in the experimental and theoretical analysis of the Goswami cycle and then on the design of parabolic trough (PTC) solar power plants. In August 2010 his first son Noah was born. Upon graduation, the author will return to Universidad del Norte, there he will work as faculty member in the Department of Mechanical Engineering in the area of renewable energy.